Mechanistic study of the ethanol oxidation reaction on carbon supported Pt-, Rh- and SnO2-based electrocatalysts in acidic medium

Antoine Bach Delpeuch

UNIVERSITÉ DE GRENOBLE

THÈSE

Pour obtenir le grade de

DOCTEUR DE L'UNIVERSITÉ DE GRENOBLE

Spécialité : **Matériaux, Mécanique, Génie civil, Electrochimie**

Arrêté ministériel : 7 août 2006

Présentée par

Antoine BACH DELPEUCH

Thèse dirigée par **Prof. Marian CHATENET** et
Co-encadrée par **Dr. Carsten CREMERS**

préparée au sein du **Fraunhofer Institute for Chemical Technology (ICT) (Pfinztal, Allemagne)**

dans **l'École Doctorale Ingénierie - Matériaux Mécanique Energétique Environnement Procédés Production (Grenoble, France)**

Etude mécanistique de la réaction d'oxydation de l'éthanol sur électrocatalyseurs à base de Pt, Rh, SnO_2 sur support carboné en milieu acide

Thèse soutenue publiquement le **« 24 Novembre 2014 »**,
devant le jury composé de :

Mr., Jean-Pierre PETIT
Professeur, Grenoble INP, Grenoble (FR), Président
Mr., Vito DI NOTO
Professeur, Università di Padova, Padova (I), Rapporteur
Mr. Plamen ATANASSOV
Professeur, University of New Mexico, Albuquerque (USA), Rapporteur
Mr. Claude LAMY
Professeur, IEM, Montpellier (FR), Examinateur
Mr. Marian CHATENET
Professeur, Grenoble INP, Grenoble (FR), Directeur de thèse
Mr. Carsten CREMERS
Chargé de recherche, Fraunhofer ICT, Pfinztal (DE), Co-encadrant

Acknowledgements

This PhD thesis has been achieved at the Fraunhofer Institut für chemische technologie (ICT) in the department of applied electrochemistry lead by Dr. Jens Tübke and Dr. Karsten Pinkwart within the fuel cell group. This work has also been accomplished in collaboration with the Laboratoire d'électrochimie et de Physico-chimie des matériaux et interfaces (LEPMI) lead by Pr. Ricardo Nogueira.

First and foremost, I would like to thank Dr. Carsten Cremers, leader of the fuel cell group, for his supervision for those almost three years, as well as Dr. Jens Tübke and Dr. Karsten Pinkwart for making this PhD possible.

I would also like to express my sincere gratitude to Pr. Marian Chatenet for his staunch support and excellent advices during the whole PhD. Besides, thanks to him and Frederic Maillard for bearing me during my three weeks holidays in Grenoble. I do not forget Gwenn, Drielly, Luis, Cleyton, Anicet, Marc and Pyo for their warm welcoming and Camille for the couch!

I am also grateful to my colleagues, Sophie, Birgit, Stanislas, François, Nils, Christiane, Tilman and the others for the excellent atmosphere in the offices and laboratories. Special thanks to Martin Joos, who I interacted with for mass spectrometry and who was always available to fix the MS when it was needed.

I would also like to thank Marjorie and Tristan for the quality of their work they have done during their internship at the Fraunhofer ICT. It has been a great pleasure working with them.

I would also like to thank the professors of Grenoble INP who taught me everything that I know now and also the professors Pr. Tsukasa Torimoto and Pr. Fabio Lima, who welcomed me and supervised me in their lab at Nagoya University and at the University of São Paulo, respectively.

Special thanks also to my girlfriend Jana who never complained during the long week-ends I was working on my manuscripts!

Last but not least, big thanks to my parents and my brother for their cheering presence and unconditional support.

Table of contents

Table of contents

Glossary

a:	Lattice parameter, Å
A:	Geometric surface
AL:	Active layer
BOR	Borohydride oxidation reaction
BP:	Bipolar plate
b:	Tafel slope
C_{dl}:	Double layer capacitance, C
CA:	Chronoamperometry
CB:	Carbon black
CCE	CO_2 current efficiency
CV:	Cyclic volammetry
d_{Elec}:	Average cristallite size deduced from ECSA estimation, nm
d_{hkl}:	Distance between two adjacent lattice plans (hkl), Å
d_N:	Number-averaged diameter, nm
d_S:	Surface-averaged diameter, nm
d_V:	Volume-averaged diameter, nm
d_{XRD}:	Average nanoparticle size (XRD) deduced from XRD data, nm
DEFC:	Direct ethanol fuel cell
DEMS:	Differential electrochemical mass spectrometry
D_x:	Diffusion coefficient of x-species, $cm^2\ s^{-1}$
E:	Electrical potential, V
$E°$:	Electrical standard potential, V
E_a:	Activation energy, $J\ mol^{-1}$
ECSA:	Electrochemical active surface area, cm^2
EG:	Ethylene glycol
EOR:	Ethanol oxidation reaction
F:	Faraday constant (96485 $C\ mol^{-1}$)
FC:	Fuel cell
GC:	Glassy carbon
GDL:	Gas diffusion layer
(hkl):	Miller indices
HOR	Hydrogen oxidation reaction
I:	Current density, $A\ cm^{-2}$
ICP-AES:	Inductively coupling plasma – Atomic emission spectroscopy
m_x:	Mass of x-species, g
M_x:	Molar mass of x-species, $g\ mol^{-1}$
MEA:	Membrane electrode assembly
MSCV	Mass spectrometric cyclic voltammetry

n_{e^-}:	Number of electrons
ORR	Oxygen reduction reaction
PAFC:	Phosphoric acid fuel cell
PEMFC:	Proton exchange membrane fuel cell
PTFE:	Polytetrafluoroethylene
R:	Perfect gas constant (8.315 J K^{-1})
R_Ω:	Ohmic resistance, Ω
RHE:	Reversible hydrogen electrode
SEM:	Scanning electron microscopy
T:	Temperature, °C
TEM:	Transmission electron microscopy
TGA:	Thermogravimetry analysis
W_e:	Electrical work, J
[X]:	Concentration of x-species, mol L^{-1}
X_{ad}:	Adsorbed X-species
XRD:	X-ray diffraction
$\Delta G_r°$:	Gibbs free energy, J mol^{-1}
$\Delta H_r°$:	Standard reaction enthalpy, J mol^{-1}
$\Delta S°$:	Standard entropy, J mol^{-1}
δ:	Diffusion layer thickness, cm
Ɛ:	Yield, %
η:	Overpotential, V
λ:	Wavelength, nm
θ:	Angle, °
ν:	Scan rate, mV s^{-1}

Chapter I.

Introduction on the Direct Ethanol Fuel Cell

A brief summary of the history of fuel cells is broached in this section followed by an overview of the fuel cell components and the reactions occurring in the direct ethanol fuel cell.

I.1. Context

The depletion of fossil fuel resources and the environmental damages caused by their exploitation have recently raised international concerns as can evidence the establishment of the Kyoto protocol in 1998. On the one hand, fossil fuels now constitute about 80 % of the world energy demand. But their resources are becoming scarcer, thus creating a situation where the demand will one day exceed the production [1]. On the other hand, environmental damages induced by the exploitation of fossil fuels are already resulting in phenomena such as global warming, climate change and local destruction of the ozone layer. The ever-growing energy demand calls for a greater effort and new advances in energetics.

In that global energetic context, fuel cells (FC) constitute a high prospect as alternative power source. Their ability to generate electricity from electrochemical reactions makes them exempted from the Carnot cycle limitations. As such, the fuel cell can benefit from higher energetic efficiency compared to internal combustion engines or thermal power plants. Moreover, the use of hydrogen (ideally of renewable origin) and oxygen as fuel and oxidant makes fuel cells the cleanest energy source.

Public projects in cooperation with industry partners have started to be implemented for the last 5-10 years in order to facilitate the introduction of fuel cells on the market. For instance, the Japanese government started in 2009 its Ene-Farm scheme, which consists in deploying adapted fuel cell systems for domestic micro combined heat and power (micro-CHP). As main effect, the scheme permitted selling the largest amount of fuel cell units in the world for a single purpose. 20 000 units were sold in 2012, that is to say 90% more than in 2011, and 500 000 were planned to be sold in 2013. More precisely, 80 % PEMFC and 20 % SOFC systems represent so far the fleet distribution. The fuel cells are developed by Panasonic in collaboration with Tokyo Gas. A second example is the development of hydrogen fuel stations in Europe by the horizon of 2015. It is well known now that automakers (Daimler, Ford, General Motors, Honda, Hyundai-Kia, Renault-Nissan and Toyota) will start commercializing fuel cell electric vehicles (FCEV) in Europe, especially in Germany, by the horizon of 2015 [2]. But the proper operation of FCEV relies entirely on the implementation of hydrogen refilling stations: the largest European project (*ca.* 40 million €) of the sort, HyFive, aims at implementing no more than 110 hydrogen refueling stations dispatched in six European cities (Bolzano, Copenhagen, Innsbruck, London, Munich, Stuttgart). The project is achieved in cooperation with gas suppliers (OMV, Linde, ITM Power, Air products…) and auto manufacturers (BMW, Daimler, Honda, Hyundai and Toyota) [3].

I.2. Brief history of fuel cells

After the discovery of the working principle of the fuel cell by C.F. Schönbein in 1838, the first fuel cell concept was invented by W.R. Grove in 1839, who succeeded in

producing electricity from hydrogen oxidation and oxygen reduction at two platinum stripes dipped in an sulfuric acid solution. Despite this fundamental (but premature?) discovery, no further development for the industry was carried out, as heat conversion systems, combustion and steam engines were significantly more performent at that time.

The first real fuel cell system was the alkaline fuel cell (AFC) of F.T. Bacon (an English mechanical engineer), which generated a usable current density of 13 mA cm^{-2} at 0.89 V cell voltage. Following developments enabled him to assemble 6 kW stacks for forklifts and welding equipment. Alkaline fuel cells were then developed for space applications where batteries were found too heavy. They were embarked between 1961 and 1970 for the Apollo missions and later in the space shuttles, both for electric power generation and drinkable water processing.

In parallel W.T. Grubb, engineer at General Electric, developed the first proton exchange membrane fuel cell (PEMFC) in 1955. But its performance compared to the AFC was modest because of the high degradation rate and low durability of the membrane (sulfonated polystyrene). The breakthrough of Dupont in membranes with its Nafion® ionomer in 1955 attracted once again attention on PEMFC systems and was followed by other innovations: elaboration in the 80s of carbon-supported platinum electrocatalysts and the combined structuration of composite thin-film electrodes blended by such Pt/C and ionomer [4].

Direct alcohol fuel cells (DAFCs) do not have a so long history as the PEMFCs and the AFCs. Up to now, only the direct methanol fuel cell (DMFC), among the different DAFCs, is commercialized. The advantage of this fuel cell in regards to AFCs or PEMFCs is that the oxidation of a methanol molecule can theoretically generate up to 6 e^-, that is to say three times more than hydrogen. As such, DAFCs present very large volumic energy densities, combined with an easier fuel storage and transportation. However, numerous obstacles hinder their performance such as the fuel (*e.g.* methanol) cross-over, electrodes contamination by carbon monoxide and, above all, the high fuel oxidation activation overpotential. K. Kordesch and A. Marko were the first to suggest the direct methanol fuel cell in 1951. Nonetheless first applications did not see daylight before the 1960s and a 100 W system developed by Esso Research and Engineering for the US army. Since then, multiple DMFC systems have been developed over the past 50 years, such as the first DMFC using platinum and ruthenium at the anode by Hitachi in 1983 for golf cart application or, more recently, a 3kW DMFC for go-cart by Daimler in 2001, or a 100 mW self-breathing DMFC for mobile phones and MP3 players from Toshiba in 2004. Lately, a 7 kW DMFC hybrid system developed for forklift applications demonstarted 20 000 h of lifetime, well above the economic system requirements (10 000 h) [5].

A variety of fuel cells has been developed so far, differing from their materials, their temperature range, sometimes their electrochemical reactions... They are ranked in five different categories according to their type of electrolyte: PEMFC, AFC, PAFC, MCFC and SOFC (see Table 1). The DAFC (among which the DMFC) is included in the PEMFC category, as the membrane remains the same.

The present work focuses on a special type of PEMFC, which is directly fed with ethanol: the direct ethanol fuel cell (DEFC).

Table 1. Classification of fuel cells

Fuel cell	electrolyte	Operating temperature	Electrode reactions
PEMFC	Polymer membrane ionomer	60 - 100 °C	Anode: $H_2 \rightarrow 2\ H^+ + 2\ e^-$ Cathode: $½\ O_2 + 2\ H^+ + 2\ e^- \rightarrow H_2O$
AFC	Potassium hydroxide aqueous solution	80 - 200 °C	Anode: $H_2 + 2\ OH^- \rightarrow 2\ H_2O + 2\ e^-$ Cathode: $½\ O_2 + H_2O + 2\ e^- \rightarrow 2\ OH^-$
PAFC	Phosphoric acid gelified solution	150 - 200 °C	Anode: $H_2 \rightarrow 2\ H^+ + 2\ e^-$ Cathode: $½\ O_2 + 2\ H^+ + 2\ e^- \rightarrow H_2O$
MCFC	Lithium/Potassium carbonate melts	600 - 700 °C	Anode: $H_2 + CO_3^{2-} \rightarrow H_2O + CO_2 + 2\ e^-$ Cathode: $½\ O_2 + CO_2 + 2\ e^- \rightarrow CO_3^{2-}$
SOFC	Yittra stabilized zirconium oxide	800 - 1000 °C	Anode: $H_2 + O^{2-} \rightarrow H_2O + 2\ e^-$ Cathode: $½\ O_2 + 2\ e^- \rightarrow O^{2-}$

I.3. Overview of a fuel cell

I.3.1. Overall operation

A fuel cell is a power generator which converts chemical energy (contained in the fuel) in electrical energy. It is composed of a positive pole (cathode), a negative pole (anode) and a membrane (or electrolyte) that separates them. A singular difference with a battery is that the fuel is not stored inside the fuel cell, as for the battery, but outside; it is therefore regularly (on-time) provided by a continuous flow inward the system. Typical reactants of a fuel cell are hydrogen (anodic fuel or reducer) and oxygen (cathodic fuel or oxidant): this situation corresponds to the PEMFC. However, in the case of the DEFC, the anodic fuel is ethanol. An overview of the working operation of a fuel cell is given in Fig. 1.

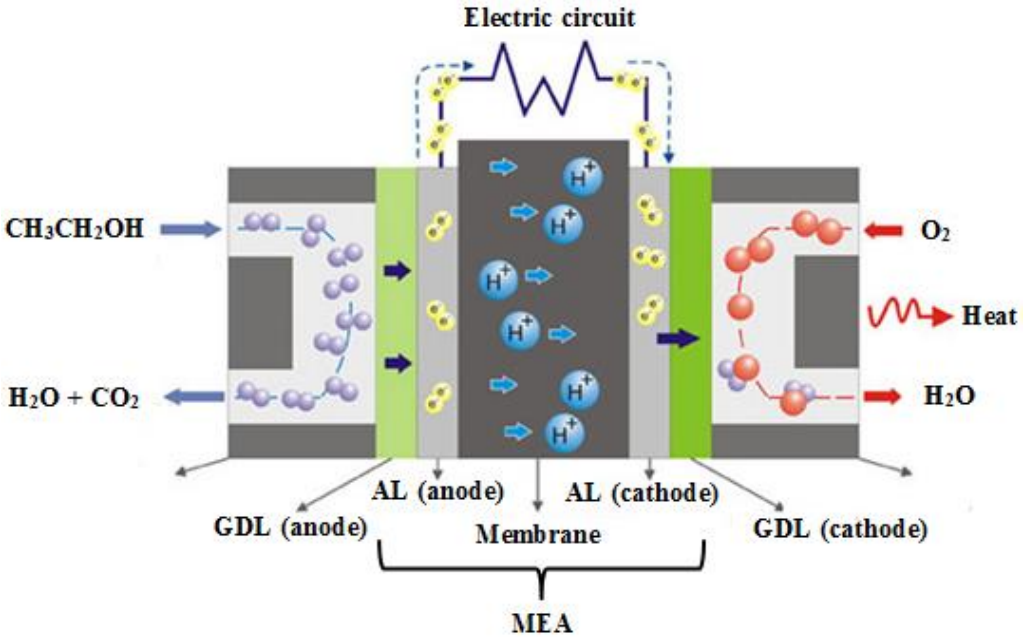

Fig. 1. Operation scheme of a DEFC [6].

I.3.2. Fuel cell components

The unit fuel cell is generally composed of end plates, current collectors, bipolar plates, gas diffusion layers, active layers located at each side a membrane (the electrolyte) separating the two compartments, as illustrated in Fig. 2. Knowing that this elementary unit delivers *ca.* 1 V or less (this value decreasing when the output current increases), a fuel cell must be assembled in series (FC stack). Such stacks needs auxiliaries to operate, *e.g.* for the fuel storage and delivery, the current collection and power management [7].

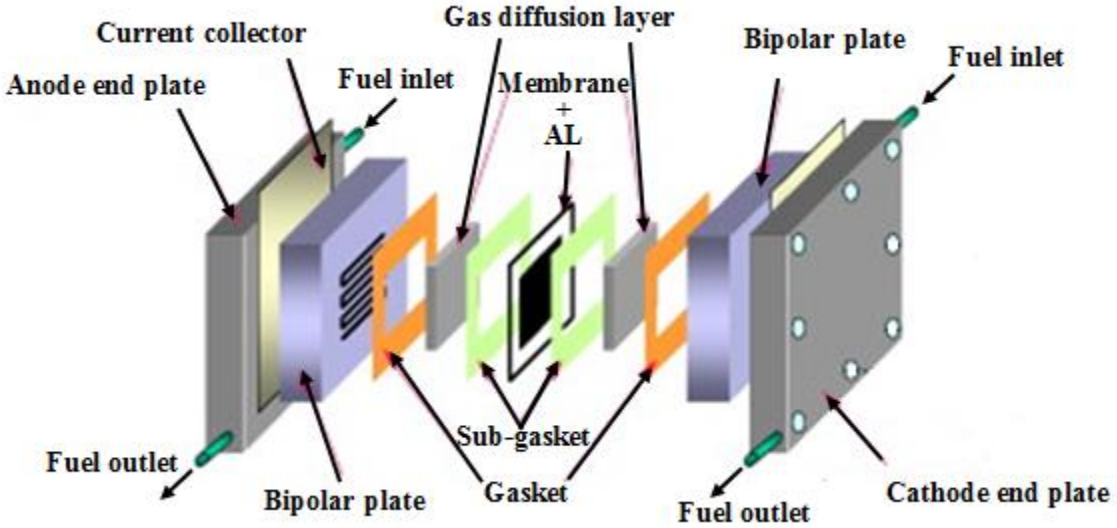

Fig. 2. Scheme of a unit fuel cell assembly [8].

(a) The bipolar plates (BPs) ensure the uniform gas distribution to the system *via* a network of gas channels. They have to be thermal and electrical conductive and to provide a good chemical and mechanical stability. Typical bipolar plates are graphitic or metallic.

(b) The gas diffusion layers (GDLs) guarantee the reactants feeding and products draining to/from the electrodes. They also act as current collectors and should stand thermal and mechanical constraints. GDLs are made of non-woven carbon fiber paper or woven carbon cloth. They are generally coated with polytetrafluoroethylene (PTFE) to improve the hydrophobicity and avoid clogging of the pores by water droplets.

(c) The active layers (ALs), directly sputtered or coated on the GDLs (or on the membrane), are the location of the electrochemical reactions. Three phases compose each AL:

- Metallic nanoparticles deposited on an electrical, conductive support (typically carbon black) act as catalyst for the electrochemical reactions.
- A proton conductive ionomer serves as binder for the supported electrocatalytic nanoparticles on their carbon support and proton conductors to/from the membrane.
- Pores guarantee the gas supply to/from the electrocatalytic sites.

The so-called triple contact is reached when the reagent supply, the ionic and electronic conduction are ensured simultaneously in the same region of the AL.

(d) The membrane is the element separating the anode from the cathode compartments. As such, the reagents integrity (no contamination) and circulation is preserved. In a DEFC, the membrane ensures the protons (typically H^+) transport from the anode to the cathode side. Besides, it is an electronic insulator. A typical membrane of the PEMFC is the Nafion®, a perfluorosulfonated polymer. Indeed, its ability to conduct protons from the anode to the cathode *via* its sulfonic groups at low temperature (< 100°C) makes it unique. However, Nafion® becomes dehydrated above 100°C and thus looses its conductivity, which makes it improper for use at so "high" temperatures. The association GDL-AL-membrane is called the membrane-electrode assembly (MEA).

I.4. Electrochemical reactions: DEFC

I.4.1. Anode side

A fuel cell is an energy converter which directly generates electricity from electrochemical reactions. At the anode, ethanol is oxidized to produce CO_2 gas, protons and a fair amount of electrons in theory (n_{e^-} = 12 e^-):

$C_2H_5OH + 3\ H_2O \rightarrow 2\ CO_2 + 12\ H^+ + 12\ e^-$ ($E_{an}° = 0.085$ V *vs.* RHE) Eq.I.1

E°_{an}, the standard reaction potential, is calculated from the standard energy of formation of the species involved in the reaction:

$$E^\circ_{an} = \frac{-\Delta G^\circ_{r,an}}{n_{e-}\ F} \quad \text{Eq.I.2}$$

with:

$$\Delta G^\circ_{r,an} = 2\ \Delta G^f(CO_2) - \Delta G^f(C_2H_5OH) - 3\ \Delta G^f(H_2O) \quad \text{Eq.I.3}$$

and:

$\Delta G^f(H_2O_{(l)}) = 237.1$ kJ mol^{-1}; $\Delta G^f(CO_{2(g)}) = 394.4$ kJ mol^{-1}; $\Delta G^f(C_2H_5OH_{(l)}) = 174.8$ kJ mol^{-1} [9].

Thus:

$$E^\circ_{an} = \frac{2 \times 394.4 - 174.8 - 3 \times 237.1}{12 \times 96485} = 0.085\ \text{V}\ vs.\ \text{RHE}$$

I.4.2. Cathode side

While the generated electrons circulate through an external circuit and make their way to the other side of the cell, the produced protons are transported through the membrane. Both protons and electrons then react with O_2 gas flowing at the cathode in a reduction reaction producing water:

$3\ O_2 + 12\ H^+ + 12\ e^- \rightarrow 6\ H_2O$ ($E^\circ_{ca} = 1.229$ V *vs.* RHE) Eq.I.4

E°_{ca} was obtained similarly to E°_{an}, with $n_{e-} = 12$, $\Delta G^f(H_2O_{(l)}) = 237.1$ kJ mol^{-1}, $\Delta G^f(O_{2(g)}) = 0$ kJ mol^{-1}.

I.4.3. Global reaction

Hence, the global reaction can be written:

$C_2H_5OH + 3\ O_2 \rightarrow 2\ CO_2 + 3\ H_2O$ ($\Delta E^\circ_{eq} = 1.145$ V) Eq.I.5

ΔE°_{eq} corresponds to the electromotive force of the system at the thermodynamic equilibrium and can be obtained as follows:

$$\Delta E^{\circ}_{eq} = E^{\circ}_{ca} - E^{\circ}_{an} = 1.229 - 0.085 = 1.144 \text{ V} \quad \text{Eq.I.6}$$

The associated Gibbs free energy also equals:

$$\Delta G^{\circ}_{r} = \Delta G^{\circ}_{r,an} - \Delta G^{\circ}_{r,cat} = 97.3 - 1422 = -1325 \text{ kJ mol}^{-1} \quad \text{Eq.I.7}$$

Besides, the specific energy can be evaluated as follows:

$$W_e = \frac{-\Delta G^{\circ}_{r}}{3600\, M} = \frac{1325}{3600 \times 0.046} = 8.00 \text{ kWh kg}^{-1} \quad \text{Eq.I.8}$$

with *M* the molar mass of ethanol.

In comparison, the specific energy of methanol is: W_e = 6.00 kWh kg^{-1} and the specific energy of gasoline is *ca.* W_e = 13 kWh kg^{-1} [10].

I.5. Energy efficiency

The energetic efficiency corresponds to the ratio between the (useful) energy leaving the system and the energy going to the system. The energy output is the electricity produced during the electrochemical reactions occurring inside the fuel cell system. The energetic efficiency of a fuel cell is expressed as the product of three efficiencies:

$$\varepsilon = \varepsilon_{Th}\, \varepsilon_{F}\, \varepsilon_{v} \quad \text{Eq.I.9}$$

ε_{Th}: thermodynamic efficiency; ε_{F}: faraday efficiency; ε_{V}: potential efficiency

I.5.1. Thermodynamic efficiency

The thermodynamic efficiency is equal to the ratio between Gibbs free energy and the standard enthalpy of reaction:

$$\varepsilon_{Th} = \frac{\Delta G^{\circ}_{r}}{\Delta H^{\circ}_{r}} \quad \text{Eq.I.10}$$

On the one hand, Gibbs free energy was estimated in section I.5.3: $\Delta G_r^\circ = -1325$ kJ mol^{-1}.

On the other hand, the standard reaction enthalpy is: $\Delta H_r^\circ = -1370$ kJ mol^{-1}.

The reversible yield of the reaction can thus be determined:

$$\mathcal{E}_{Th} = \frac{1325}{1370} = 96.7\ \%$$

The reversible yield of a DEFC is comparable to the DMFC ($\mathcal{E}_{Th,DEMFC}$ = 96.6 %) but larger than the PEMFC ($\mathcal{E}_{Th,PEMFC}$ = 83.0 %) [11] (all values determined at 25°C).

In comparison, the yield of combustion engines is limited by the Carnot cycle:

$$\mathcal{E}_{Th} = 1 - \frac{T_{out}}{T_{in}} \approx 40\ \% \qquad \text{Eq.I.11}$$

with T_{out} and T_{in} the output and input temperature.

I.5.2. Potential efficiency

However when the system leaves its equilibrium state and starts debiting a current, the appearance of an overpotential at the anode ($\eta_a > 0$) and cathode side ($\eta_c < 0$) is inevitable: these overpotentials reflect the kinetics hindrances associated to the electrochemical reactions and the mass-transport of their reactants. Moreover, an ohmic resistance implied by the electrolyte, the electrodes and their interfaces ($R_\Omega\ I$) has to be added. The resulting potential imposed between the anode and the cathode is:

$$E\ (I) = E^\circ - \eta_a - (-\eta_c) - R_\Omega I \qquad \text{Eq.I.12}$$

For the DEFC, it can be considered that η_a = 0.4 V and η_c = 0.2 V for a density current of I = 100 mA cm^{-2}. The real electromotive force can be thus evaluated to *ca.* $E\ (I)$ = 0.5 V.

Hence the practical electrical yield becomes:

$$\mathcal{E}_V = \frac{E(I)}{E_{I=0}} = \frac{0.5}{1.145} \approx 44\ \% \qquad \text{Eq.I.13}$$

I.5.3. Faraday yield

On Pt/C electrocatalysts, the actual number of electrons exchanged during the EOR at room temperature is not equal to $n_{e^-} = 12$, but can be as small as $n_{e^-} = 2$ (formation of acetaldehyde), which can dramatically lower the faraday efficiency:

$$\varepsilon_F = \frac{n_{exp}}{n_{theo}} = \frac{2}{12} \approx 17\ \% \qquad \text{Eq.I.14}$$

I.5.4. Overall energy

In conclusion, the actual efficiency of a DEFC at room temperature can be as low as $\varepsilon = 7\ \%$:

$$\varepsilon = \varepsilon_{Th}\, \varepsilon_V\, \varepsilon_F = 0.97 \times 0.44 \times 0.17 = 7.3\ \% \qquad \text{Eq.I.15}$$

I.6. Ethanol oxidation reaction

I.6.1. Problematic

The use of ethanol as fuel for the anode side of the fuel cell system presents several advantages. Indeed, ethanol can be produced from biomass fermentation [12,13], is non-toxic and is easy to store: at room temperature and under normal pressure conditions, ethanol is stable as liquid and thus can easily be stored in pre-existing infrastructure. In addition, ethanol presents, in theory, a high energy density (8 kWh kg^{-1}) [14].

Nevertheless, all those advantages do not counterbalance the drawbacks of the DEFC, which dramatically hinder its performances:

- *Electrocatalyst corrosion:* The use of an acidic electrolyte coupled with operating temperature above room temperature accelerates the corrosion of the electrocatalyst and hence deteriorates the durability of the system. The corrosion operates both on the metal nanoparticles and on the carbon support constituting the electrocatalyst. Mitigating the degradation of the electrocatalyst is a burning issue and can be performed by multiple strategies: for example, modification of the carbon support surface by alteration of its physical characteristics (thermal treatment) or by addition/removal of chemical groups (chemical treatment). More information on this topic can be found in [15].

- *Metal cost and poisoning:* The use of platinum is primordial in a DEFC. Indeed, in acid medium, platinum demonstrated is one of the pure metals with the highest electrocatalytic performances towards the ethanol oxidation reaction (EOR) [16]. Besides, platinum is also remarkably corrosion-resistant compared to other metals.

Yet, platinum is very costly and its use would therefore hinder the fuel cell commercial viability. Moreover, pure platinum electrodes are rapidly poisoned by the EOR intermediates such as CO_{ad} and $CH_{x,ad}$ [17], overall leading to sluggish EOR kinetics and low potential efficiency (even with electrodes highly-loaded with Pt electrocatalysts).

- *Crossover of the membrane:* Due to Nafion® hydrophilic proprieties, ethanol can cross the membrane and contaminate the cathode side [18]. As a consequence, the presence of the alcohol at the cathode sets up a mixed cathodic potential, which results in the drop of the PEMFC performances. Ethanol cross-over was however reported slower than that of methanol due to its longer carbon chain [19,20].

- *Faraday (and overall system) efficiency:* As seen earlier, the faraday efficiency is very low considering that incomplete ethanol oxidation can lead to 2 e^- (toxic acetaldehyde generation) or to 4 e^- (acetic acid) instead of a maximum of 12 e^-.

Although all those issues are of primary importance, this work will predominantly focus on the faraday and potential efficiency issues of EOR, *via* a survey of the EOR mechanism.

I.6.2. Mechanism of the EOR in acidic medium on platinum

The EOR is a complex mechanism which can follow different reaction pathways. A scheme, issued from [21], summarizes the possible reactions of the EOR (Fig. 3). This scheme was chosen because it gives a good overall view of the mechanism on platinum and gives as well a good illustration of the complexity of the EOR mechanism.

The main EOR pathway, also known as the complete ethanol oxidation reaction, involves the generation of 12 electrons and the production of CO_2 as final reaction product (see Eq. I.1). This reaction, which generates up to 12 electrons, can obviously not happen in a single step. On the contrary, it is a kinetically slow electrochemical reaction [22–24], which is divided in a succession of elemental reactions which require the participation of different reaction intermediates. Some steps are more difficult to operate than others. Among them, the cleavage of the C-C bond of the ethanol molecule accounts as the most difficult one [22,25–27].

Due to this difficulty, the ethanol electrooxidation operates through easier parallel pathways leading to other reaction products. In this way, the EOR may proceed partially, yielding a number of electrons below the maximum 12 electrons. These incomplete reactions can produce, on the one hand, acetaldehyde (with 2 electrons exchanged during the electrooxidation reaction) and, on the other hand, acetic acid (4 electrons) [22,26–28].

In any case, the first step of the EOR mechanism involves the dehydrogenation of the ethanol molecule leading to the formation of acetaldehyde (Eq.I.17). Two electrons are produced during the process(*):

$$CH_3CH_2OH_{ad} \rightarrow CH_3CHO_{ad} + 2\ H^+ + 2\ e^- \qquad \text{Eq.I.16}$$

(*): The notation used in (Eq.I.17) and in the following equations (in this section only) is consciously wrong and is used for the reader's comprehension in order to match with the notations used in Fig. 3.

In the complete ethanol oxidation pathway, the adsorbed acetaldehyde dissociates into CO_{ad}- and $CH_{x,ad}$-species (Eq.I.18):

$$CH_3CHO_{ad} \rightarrow CO_{ad} + CH_{x,ad} + (4\text{-}x)\ H^+ + (4\text{-}x)\ e^- \qquad \text{Eq.I.17}$$

The parallel formation of CO_{ad}- and $CH_{x,ad}$-species can also be obtained through the direct dissociative adsorption of ethanol:

$$CH_3CH_2OH_{ad} \rightarrow CO_{ad} + CH_{x,ad} + (6\text{-}x)\ H^+ + (6\text{-}x)\ e^- \qquad \text{Eq.I.18}$$

Then, adsorbed CH_x-species react with water to give CO_{ad}:

$$CH_{x,ad} + H_2O \rightarrow\ CO_{ad} + (2+x)\ H^+ + (2+x)\ e^- \qquad \text{Eq.I.19}$$

The CO_2 generation is finally achieved by the oxidation of CO_{ad}-species with water:

$$CO_{ad} + H_2O \rightarrow CO_2 + 2\ H^+ + 2\ e^- \qquad \text{Eq.I.20}$$

Hence, two different pathways can lead to the formation of CO_2 and to the creation of 12 e^-:

- Eq.I.17 → Eq.I.18; Eq.I.20 → Eq.I.21
- Eq.I.19 → Eq.I.20 → Eq.I.21

However, these two pathways require splitting the C-C bond, which is a process of high activation energy. As such, other pathways, more energetically feasible, are favored during the EOR.

The most encountered one is the direct release of adsorbed acetaldehyde in the solution (Eq.I.22) without further oxidation:

$$CH_3CHO_{ad} \rightarrow CH_3CHO_{sol} \qquad \text{Eq.I.21}$$

This pathway is also the most unwished one as it only implies the production of two electrons. Acetaldehyde toxicity and suspected carcinogenicity makes it even more undesired.

Another competitive pathway is the further oxidation of acetaldehyde with adsorbed OH-species into acetic acid (Eq.I.23):

$$CH_3CHO_{ad} + H_2O \rightarrow CH_3COOH + 2\,H^+ + 2\,e^- \qquad \text{Eq.I.22}$$

According to Lai et al., the reaction could occur either by direct reaction of adsorbed acetaldehyde with hydroxide species to form an intermediate adsorbed acetate species or by aqueous acetaldehyde hydrolysis reaction which further produces 1,1-ethane-diol as reaction intermediate [21].

Although this pathway generating acetic acid ($4e^-$) offers a much higher faradaic efficiency than acetaldehyde formation ($2e^-$), it does not allow a full exploitation of ethanol.

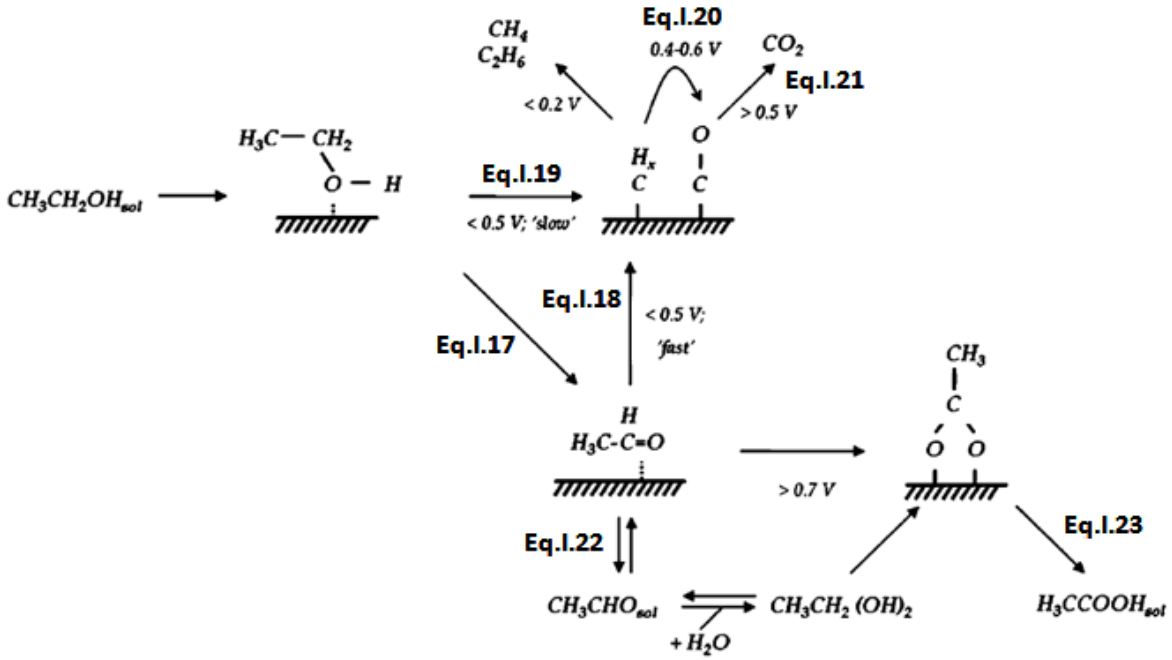

Fig. 3. Scheme of the ethanol oxidation reaction [21].

I.6.3. Ethanol adsorption modes

According to Iwasita and Pastor [29], ethanol adsorption on the Pt electrocatalyst surface forms four different adsorbates represented in Fig. 4:

- (a) Pt-CO (33 %) and Pt-CH_x
- (b) Pt-OCH_2-CH_3 (32 %)
- (c) Pt-$COCH_3$ (29 %)
- (d) $(Pt)_2$=COH-CH_3 (5 %)

As demonstrated in this FTIR and DEMS study using labeled carbon ($^{12}CH_3{}^{13}CH_2OH$), almost all ^{13}C remains on the Pt surface after four successive reductions between *ca.* E = 0.35 and 0 V *vs.* RHE while half of the ^{12}C are reduced in methane (the other half remaining at the electrode surface). It was interpreted from these results that the methane generation is favored by the adsorption mode (–CO-CH_3) whereas (–OCH_2-CH_3) was stable during the reduction scans.

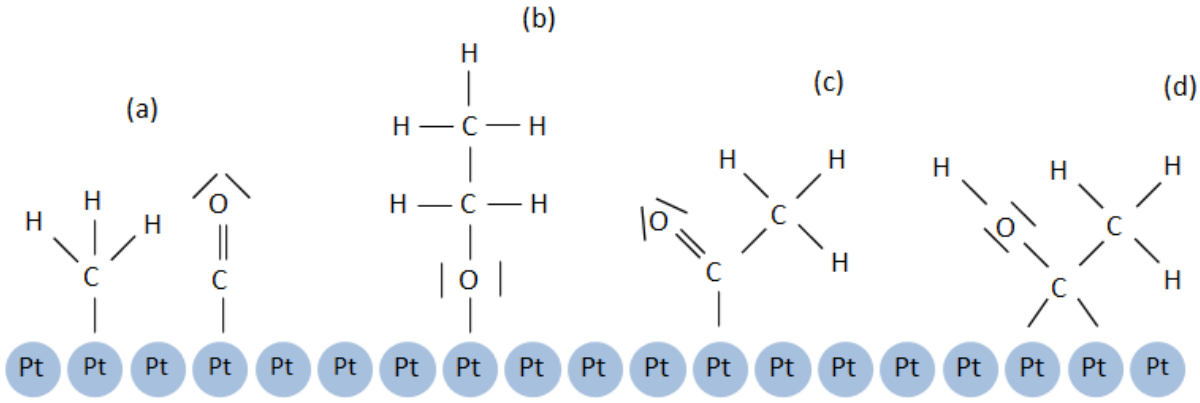

Fig. 4. Adsorption modes of ethanol adsorbates on Pt.

I.6.4. Ethanol dehydrogenation

The ethanol dehydrogenation is the first step of the EOR and also one of the most crucial ones. Indeed, this reaction controls acetaldehyde production that is to say the formation of the main product of the EOR at room temperature on platinum electrocatalysts [22,23,30–32]. As written in section I.5., the EOR initiates thermodynamically at potentials as low as E = 0.085 V *vs.* RHE. However, no current is witnessed below *ca.* E = 0.3 V *vs.* RHE on platinum [31,33–36]. Besides, the reaction do not only suffers overpotentials over 200 mV but also slow kinetics until *ca.* E = 0.6 V *vs.* RHE [22–24].

The causes of this high overpotential are not certain. Some studies attribute this high overpotential to a blockage of the electrocatalytic surface by adsorbed hydrogen species [37,38], similarly to what is also observed for methanol [39]. Bergamaski et al. highlighted the appearance of a new peak during a cyclic voltammetry after introduction of ethanol at E = 0.05 V *vs.* RHE which was ascribed to ethanol dehydrogenation [39]. The addition of a second transition metal (rhodium) to platinum enabled a negative shift of this reaction initiation. More conclusive, Wang et al. discovered that ethanol dissociative adsorption was hindered in the H_{UPD} region compared to higher potentials (E = 0.31 V *vs.* RHE). Besides the hindrance by H_{ad}-species, the EOR is also impeded by the electrocatalyst surface poisoning by C_2- and CO-adsorbates, which do not start oxidizing below the potential onset of the Pt-oxides formation [40].

I.6.5. C-C bond splitting

As mentioned in section I.15.1, the C-C bond splitting is considered as the most difficult step of the EOR on platinum and thus as the main obstacle to the complete EOR into CO_2. The low amount of CO_2 generated during the EOR at room temperature is the main illustration of this challenging reaction.

IR-studies [22,26,27] revealed by means of semi-quantitative techniques that CO_2 constitutes a minor EOR product compared to acetaldehyde and acetic acid. Besides, quantitative studies using on-line differential electrochemical mass spectrometry (DEMS) demonstrated that CO_2 current efficiency (CCE) values are relatively low on Pt/C [30,32,41]: Wang et al., Cantane et al. and Bergamaski et al. found out a CCE closed to 2.7 % [30], 3.5 % [32] and 8% [41] respectively in 0.1 M EtOH on Pt/C electrocatalysts.

These observations are supported by on-line DEMS studies with associated activation energy (E_a) estimations for the recorded EOR and for the sole complete EOR to CO_2 (m/z = 22) [23,42,43]. The C-C bond breaking has also been investigated by means of DFT calculations [25,44,45]. Wang et al. found that the C-C bond breaking step has the highest energetic barrier in comparison to the other ethanol electrooxidation reaction steps (C-O and C-H bond dissociation steps) on the investigated Pt(111) and Pt (211) surfaces [25].

I.6.6. CO-stripping

Carbon monoxide oxidation has been the subject of a significant amount of publications [46–57]. The topic is of importance as CO traces present in reformed H_2 gas used as fuel at the anode (of a classical PEMFC) is a constant source of contamination of the Pt electrocatalyst, intolerant to CO, which results in the fuel cell sinking performances [50,58–60]. CO is also encountered in direct alcohol fuel cells (DAFC) as a strongly adsorbed reaction intermediate. The problem is inherent in PEMFCs and DAFCs (in the present case,

DEFCs), where the practical operating low temperatures and potentials hinder the electrooxidation of strongly adsorbed carbon monoxide.

The CO oxidation reaction likely operates through a Langmuir-Hinshelwood mechanism, *i.e.* with the participation of two adsorbed species, where the adsorbed CO reacts with adsorbed hydroxide (issued from water dissociative adsorption):

$$H_2O \rightarrow OH_{ad} + H^+ + e^- \quad \text{Eq.I.23}$$

$$CO_{ad} + OH_{ad} \rightarrow CO_2 + H^+ + e^- \quad \text{Eq.I.24}$$

Although its standard potential is located at around E = - 0.1 V *vs.* RHE, the reaction is limited by water dissociation (Eq.I.24), which initiates at *ca.* E = 0.6 V *vs.* RHE on Pt electrocatalysts. This reaction is the rate determining step of carbon monoxide oxidation and highly depends on the electrocatalyst structure [56,57,61].

I.6.7. Acetaldehyde oxidation reaction

The acetaldehyde oxidation reaction (AOR) has been seldom reviewed in the literature in comparison to the EOR [26,62–66]. Yet, its study is of high interest. Indeed, acetaldehyde is a C_2-species with one of the simplest structure and, as such, can be considered as a model molecule for the study on the C-C bond cleavage. Moreover, acetaldehyde has been repeatedly reported as the major product of the ethanol oxidation reaction [22,23,30–32]. Therefore, the AOR study may also help understanding the processes occurring during the EOR.

The following mechanism summarizing the different pathways and reactions constituting the AOR on platinum in acid medium is adapted from the one proposed by Farias et al. [66]:

$$CH_3CHO_{sol} \rightarrow CO_{ad} + CH_{x,ad} + (4\text{-}x)\ H^+ + (4\text{-}x)\ e^- \quad \text{Eq.I.25}$$

$$CO_{ad} + H_2O_{ad} \rightarrow CO_2 + 2\ H^+ + 2\ e^- \quad \text{Eq.I.26}$$

$$CH_{x,ad} + 2\ H_2O_{ad} \rightarrow CO_2 + (x+4)\ H^+ + (x+4)\ e^- \quad \text{Eq.I.27}$$

$$CH_3CHO_{sol} + H_2O_{ad} \rightarrow CH_3COOH_{aq} + 2\ H^+ + 2\ e^- \quad \text{Eq.I.28}$$

As it can be seen, this AOR mechanism is very similar to the one in section I.15.1 for the EOR. Like the latter, the electrooxidation of bulk acetaldehyde leads to the production of either acetic acid or CO_2 as reaction products. Besides, similarly to the EOR [22], low acetaldehyde concentrations favor the pathway leading to CO_2. Moreover, the AOR and the EOR seem to have the same onset potential (*ca.* 0.4 V *vs.* RHE in [21,22,66]).

However, the AOR contrasts on some points with the EOR. The onset potential of the acetic acid formation (corresponding to Eq.I.24) is located at slightly higher potentials than with the EOR. Moreover, this reaction is more favored than during the EOR.

A comparison between the AOR and EOR mechanism may also give information on the nature of the improvement operated on the latter due to the addition of a transition metal alloyed to platinum, in other words, which step of the EOR has been facilitated or not: ethanol dehydrogenation, C-C bond breaking…

I.6.8. Acetic acid or ethyl acetate

One uncertainty concerning the EOR relies in the formation of one of the reaction products: acetic acid.

On the one hand, according mainly to IR-studies, acetic acid would be the third reaction product besides CO_2 and acetaldehyde [26,27,67–69]. The simultaneous detection of bands at *ca.* 1715, 1400 and 1280 cm^{-1} [68,70], all of them characteristic of acetic acid, could only correspond to this molecule (for more details on the identity of these bands, please refer to chapter III).

On the other hand, mass spectrometric studies preferentially mention ethyl acetate ($CH_3COOCH_2CH_3$) as possible third EOR product [30,32,71]. Wang et al. were among the first to propose ethyl acetate as EOR product [71]. They notably used the mass-to-charge signal m/z = 73 ($[CH_3CH(OC_2H_5)_2)^+]$) (which cannot physically be attributed to acetic acid) among others to identify the formation of this species. They explained its formation by the reaction of freshly produced acetic acid (Eq.I.30) with bulk ethanol:

$$CH_3COOH_{sol} + CH_3CH_2OH_{sol} \rightarrow CH_3COOCH_2CH_3 + H_2O \qquad \text{Eq.I.29}$$

This reaction does actually not exclude the electrochemical formation of acetic acid during the EOR, but suggests that acetic acid is not an EOR final product as it is the case for example in the mechanism proposed in section I.15.1, which does not mention the possible formation of ethyl acetate.

For the sake of clarity, the notion of acetic acid will be preferentially used in the present work. Although the latter is not directly detected by mass spectrometry, its presence as EOR product was identified by IR-techniques.

I.6.9. Pt-M alloys

As written earlier, although the highest EOR electroactivity is demonstrated on platinum electrocatalysts, the reaction suffers multiple obstacles which hinder its performances. One way to overcome these issues is the development of bi- and tri-metallic Pt-based electrocatalysts. A particular effort has been done during the past decades in order to develop multi-metallic electrocatalysts: Pt-Ru/C [33,72–74], Pt-Rh/C [41,75,76], Pt-SnO_2/C [30,77,78], Pt-Rh-SnO_2/C [79,80], Pt-Ir-SnO_2/C [81], Pt-Ru-Mo/C [82], Pt-Sn-Mo/C [83].

This work focuses most particularly on Pt-Rh/C, Pt-SnO_2/C and Pt-Rh-SnO_2/C. The reasons explaining this choice are given below.

I.6.9.1. Pt-SnO_2/C

First and foremost, it has to be precised why the notation "SnO_2" instead of "Sn" is used throughout the presented work. Higuchi et al. demonstrated using XPS analysis the absence of peak assigned to the $3d_{3/2}$ and $3d_{5/2}$ of Sn^0, whereas peaks of this doublet could be found for Sn^{4+} [84]. In other words, tin does not exist as such, in its zerovalence form, in this study, but as oxide. It can be argued that the synthesis method used in this reference is different than the one used in this work. Tin state most likely depends on the synthesis conditions: an air atmosphere would definitely lead to the formation of tin oxide whereas an inert gas environment could hinder this formation. However, although the reduction step of the polyol synthesis used in this work occurs under argon, it is believed that the heat treatment at 80°C in an air atmosphere and the subsequent use of aqueous electrolytes lead to the formation of tin oxide (more details about the synthesis are given in section II.8.). When other studies are referred, the notation "SnO_2" will be preferred, even though the original notation is "Sn". Although blameworthy, this choice was made for the convenience of the readers.

One peculiar feature of tin oxide is its oxophilic character, *i.e.* its ability to bring adsorbed OH-species to the system at low potentials. For this reason, this metal has largely been investigated associated to platinum for the CO_{ad}-electrooxidation [46,49–51,85,86] and for the MOR [85,87–92]. However, its effects on the two reactions were singularly different.

On the one hand, large negative potential shifts of the CO electrooxidation in CO-containing electrolyte and to a minor extent in CO-free electrolyte (CO-stripping experimental conditions) were reported on the bi-metallic Pt-SnO_2/C compared to Pt/C and Pt-Ru/C [50]. According to Wang et al. [85], the competition between OH_{ad} and CO_{ad} formation during CO_{ad} electrooxidation (in a CO containing electrolyte) on Pt-Ru/C results in a positive shift *versus* a CO_{ad}-stripping (in a CO-free electrolyte) where this competition does not take place. On the contrary, Pt-SnO_2/C does not suffer from the concurrence between the two reactions. This explains the difference in CO-containing electrolytes. In CO-stripping

conditions, the higher overpotential on Pt-Ru/C may be due to the initial state of coverage of the electrocatalysts: in Pt-Ru/C, platinum and ruthenium are covered by CO_{ad}-species. On the contrary, in Pt-SnO_2/C, tin oxide is never covered by CO_{ad}-species and can provide OH_{ad} all along the stripping-CV.

On the other hand, Pt-SnO_2/C did not display any enhancement of methanol electrooxidation against Pt/C or to a larger extent to Pt-Ru/C [93–95] (even if this affirmation is biased by the presence of contradictory results in the literature [46,85,92,96,97]). The higher CO_{ad} coverage of platinum in Pt-SnO_2 systems compared to pure Pt or Pt-Ru systems evidenced in [85] could justify the phenomenon: the higher CO_{ad} coverage of Pt on Pt-SnO_2/C would prevent methanol dehydrogenation (the first step of the MOR mechanism) which requires free electroactive sites in order to take place. This would result in higher overpotentials than Pt-Ru/C.

Pt-SnO_2/C electrocatalysts has already been thoroughly studied for the EOR in the literature [78,98–102]. Comparisons between Pt-SnO_2/C and Pt/C revealed a higher EOR electroactivity on the former than on the latter [78,84,99–103]. Adding tin to the electrocatalyst material leads to a negative shift of the EOR onset potential and also improves the selectivity of the ethanol electrooxidation toward acetic acid formation [99–101]. The last reaction is favored by tin ability to bring adsorbed OH-species to the system at low potentials.

It was also thought that tin oxophilicity could help oxidizing adsorbed CO during the alcohol oxidation at lower potential than on Pt/C and could improve the CO_2 current efficiency. However, no study ever reported so far any improvement of the CCE for Pt-SnO_2/C compared to Pt/C [98,99]. This could be explained by the electrocatalyst inability to ease the C-C bond cleavage.

To go beyond the existing literature, the presented work will focus on Sn particular role in Pt-SnO_2/C electrocatalysts in the ethanol oxidation reaction.

I.6.9.2. Pt-Rh/C

Pt-Rh/C has been less extensively reviewed than Pt-SnO_2/C with respect to CO_{ad}-electrooxidation [104–109] and to MOR [110–113]. According to Tokarz et al., CO_{ad}-stripping displays a limited negative shift of the oxidation initiation on Pt-Rh/C compared to Pt/C [110]. Similarly, in the same study, the methanol electrooxidation presents at slightly lower overpotential on Rh/C and Pt-Rh/C against Pt/C [110].

Pt-Rh/C has been the subject of more studies in regard to the EOR [32,35,41,75,114]. On the one hand, Rh metal demonstrated encouraging performances in the achievement of C-C bond breaking [115,116] and, consequently, Pt-Rh/C alloys showed promising results in the improvement of the selectivity of the EOR toward the CO_2 formation [75,114]. Alloying Rh

to Pt seems to modify the electronic structure of the latter, leading to a down-shift of the Pt 5d-band center caused by the interactions in the lattice between Pt and Rh atoms [117]. As a result, the adsorption strength of the adsorbates on the electrocatalyst may diminish, therefore easing their oxidation. Moreover, the presence of rhodium, which is also an oxophilic metal, in the lattice also likely suggests a faster supply in OH-species helping the oxidation of adsorbed CO. On the other hand, results on the better electroactivity of Pt-Rh/C compared to Pt/C remain controversial. Indeed, Lima et al. [35] and Cantane et al. [32] found a higher faradaic current on Pt/C than on Pt-Rh/C or Pt_2Rh_1/C, whereas Sen Gupta [118] registered higher currents on $Pt_{25}Rh_{75}$/C and $Pt_{75}Rh_{25}$/C. Similarly, some studies show a higher CCE on Pt-Rh/C than on Pt/C [35,114,119], while others demonstrate similar performances regarding the C-C bond splitting [32]. The lower EOR onset potential on Pt-Rh/C electrocatalyst compared to Pt/C is however generally admitted [32,35,37,114,119,118]. A reason could be the better dehydrogenation of the ethanol molecule at low potentials on Pt-Rh/C than on Pt/C [37].

In situ FTIR measurements on Rh/C are scarce [115,120] and on Pt-Rh/C even more [120]. Tacconi et al. showed that rhodium discriminates ethanol electrooxidation into acetaldehyde as main product and, on the opposite, favors the dissociative ethanol adsorption and CO_2 generation against iridium [115]. Besides, acetaldehyde was proposed as reaction intermediate to the formation of acetic acid, but its presence could not be confirmed by FTIR. On the contrary, Li et al. found that acetaldehyde was the main reaction product on Rh/C against acetic acid on Pt/C in a thin layer configuration [120]. Besides, the EOR on Pt-Rh/C did proceed to a higher extent than Pt/C toward the CO_2 production.

An important difference that should be kept in mind between rhodium and tin oxide is that the latter does not have any affinity toward CO adsorption while the reaction proceeds easily on rhodium. As a result, contrary to rhodium, tin oxide is never blocked by the CO_{ad} formation and can always supply OH_{ad} to the system. To that extent, Pt-Rh/C and Pt-SnO_2/C should be considered as completely different electrocatalysts.

To some extent, rhodium can be better compared to ruthenium, as the two metals are oxophilic and can be blocked by CO-adsorbates. However, contrary to ruthenium, rhodium presents the ability to enhance the cleavage of the C-C bond.

I.6.9.3. Pt-Rh-SnO_2/C

Pt-Rh-SnO_2/C has first been investigated by Colmati et al. [121]. It was reported that the EOR electroactivity was higher at $E > 0.45$ V *vs.* RHE on the tri-metallic electrocatalyst than on Pt-SnO_2/C and Pt/C but lower at $E < 0.45$ V *vs.* RHE against Pt-SnO_2/C.

More recently, Pt-Rh-SnO_2/C has been thoroughly studied by means of IR-techniques [120,122,123]. Besides, demonstrating a large negative shift of the EOR onset potential as well as a higher activity compared to Pt/C and Pt-SnO_2/C, the tri-metallic electrocatalyst

displays also the best selectivity toward the EOR complete pathway leading to CO_2 generation. The better performances obtained on the electrocatalysts are attributed to:

- ethanol dehydrogenation on platinum.

- the enhanced C-C bond cleavage on rhodium electroactive sites.

- the supply in OH-species guaranteed by tin oxide at low potentials (necessary for the oxidation of formed CO-adsorbates into CO_2), which in parallel prevent from OH-species adsorption on platinum and rhodium due to the OH-OH interactions [124]. In this way, the rhodium and platinum surface will be free to interact with ethanol molecules and be able to ensure their role in the EOR mechanism.

Based on DTF calculations, the same authors proposed that the complete EOR occurs through the formation of a reaction intermediate ($CH_2CH_2O_{ad}$) which would favor the CO_2 formation [122]. This mechanism would significantly differ from the EOR mechanism on Pt/C presented above [21] which operates *via* the formation of adsorbed acetaldehyde or the direct ethanol dissociative adsorption.

Finally, Silva-Junior et al. found a higher potentiostatic electroactivity of the EOR at E = 0.6 V *vs.* RHE on Pt-Rh-SnO_2/C against $Pt_{91}Rh_{09}$/C, $Pt_{57}Rh_{23}$/C and $Pt_{28}Rh_{72}$/C [125]. Based on an FTIR analysis, they attributed the better performances on the tri-metallic electrocatalyst to facilitated adsorption and oxidation steps during the EOR. However, they did not conclude on the better EOR selectivity toward the CO_2 formation, as both CO_2 and acetic acid generation were qualitatively higher against their Pt-Rh/C electrocatalysts [79].

Due to the scarce number of publications on the EOR on Pt-Rh-SnO_2/C [120–123,125,126], and regarding the promising performances of the EOR on the tri-metallic electrocatalysts, it has been found of relevance and of interest to study further the EOR on this electrocatalyst.

I.7. Overview of the investigations carried out in this thesis

The following investigations have the double objective to examine the performances of 20 wt.% carbon supported Pt-, Rh- and SnO_2-based electrocatalysts (Pt/C, Rh/C, Pt-Rh/C, Pt-SnO_2/C and Pt-Rh-SnO_2/C) regarding the EOR, as well as to understand the positive and negative impact of each metal on the mechanism of the ethanol electrooxidation.

Chapter II is dedicated on the thorough description of the synthesis method employed for the preparation of the studied home-made electrocatalysts. The experimental techniques

employed to characterize physically and electrochemically the EOR are subsequently detailled.

Chapter III is separated in two distinct sections. In the first one, some experimental parameters, such as the scan rate and the thickness layer, were investigated on 20 wt.% Pt/C by means of DEMS and RDE, in order to understand how their variation impacts the EOR. In the second section, the EOR was studied on Pt-, Rh- and SnO_2-based electrocatalysts by means of DEMS and *in situ* FTIR. The results were confronted to highlight the similarities and disparities between the two techniques.

In chapter IV, the influence of the presence of H- and OH-adsorbates on the ethanol and acetaldehyde electrooxidation has been investigated in order to evaluate their action (inhibition/intensification effect) on the reaction initiation and CO_2 current efficiency. The study was performed on Pt/C, Rh/C, Pt-Rh/C, Pt-SnO_2/C and Pt-Rh-SnO_2/C, so as to point out the role of rhodium or/and tin oxide in the ethanol dehydrogenation and complete electrooxidation into CO_2.

Chapter V presents a study of the stripping of ethanol and acetaldehyde adsorbates in an alcohol-free solution on Pt-, Rh- and SnO_2-based electrocatalysts in order to give further insights into the EOR mechanism on the different electrocatalysts.

Chapter VI focuses on the influence of the temperature on the EOR on Pt/C, Pt-Rh/C and Pt-Rh-SnO_2/C *via* potentiostatic and potentiodynamic techniques. A special attention is drawn on the change in rate determining steps with the increase of the temperature.

A conclusion finally summarizes all the different results and discussions of this work and some ideas are proposed as possible research perspectives for the future.

Chapter II.

Experimental section

This chapter summarizes in the first place the preparation of the electrocatalysts used in the different sections of this thesis. Detailed information is then provided on the experimental techniques used for the physical and electrochemical characterization of the electrocatalysts.

II.1. Synthesis of the carbon-supported electrocatalysts by the polyol method

The studied carbon-supported electrocatalysts were prepared using a modified polyol method. In a typical procedure, 100 mg of 10 or 20 wt. % metal loaded electrocatalysts was prepared. The calculated amount of metal precursors, H_2PtCl_6, $RhCl_3.xH_2O$ and $SnCl_2$ (Aldrich), was dissolved in a 20 mL solution containing milli-Q water and ethylene glycol (EG) (volume ratio 1:1), prior to the addition of carbon black particles (Vulcan XC-72R, Cabot) dispersed in 20 mL of the same mixture (10 mL EG, 10 mL water) by sonication. 20 mL EG was then added to the solution in order to get in the end a 2:1 EG:water ratio. The pH of the whole solution was subsequently adjusted to pH = 12 using a 0.5 M NaOH solution (diluted in EG + water (1:1)) and let under vigorous stirring for one hour at ambient temperature under argon atmosphere. Thereafter the solution was heated up to 160°C (still under argon atmosphere), maintained at this temperature for three hours and cooled down overnight in air. The pH of the solution was then fixed to pH = 3 using a 0.5 M H_2SO_4 aqueous solution and stirred for 24 h. Finally, the electrocatalyst powder was filtered, washed copiously with milli-Q water and dried overnight in an oven at 80°C.

A considerable advantage of this colloidal method is its high simplicity and the ability to control the size of the nanoparticles.

The polyol synthesis requires the presence of only one chemical, ethylene glycol, which plays the role of the solvent and of the reducing agent. In our procedure, milli-Q water was added to the process as it was found that additional water was helping CB dispersion and the dissolution of the metal salts. No additional stabilizing agent is needed in the synthesis solution to prevent from the possible nanoparticles agglomeration, as it can be found for other colloidal syntheses such as the Bönnemann method [127–132] or methods using borohydride as reducing agents [111,133–136].

Although this method is well employed [123,137–155], very few studies focused on the reactions occurring during the synthesis [148,153–155].

Heating up the synthesis solution to 130°C (ethylene glycol boiling point) engage the solvent oxidation into glycolic acid which remains stable in the alkaline solution as glycolate anions. The reaction frees one electron per oxidized ethylene glycol molecule which is further used in the reduction of the metal salts in zerovalent metal atoms. The stabilization of the metal colloids is believed to be carried out by the glycolate anions [143,148].

Diverse temperatures from 130°C to 180°C are reported in the literature [123,139,143,152] for the synthesis. No accurate control of the temperature is usually operated as this factor is believed to be neutral. A home study investigated the effects of the temperature during the synthesis on the electrocatalysts state and concluded that this parameter does indeed not impact the nanoparticle size or the metal loading [156]. Nonetheless, a study from Fievet et al. [155] shows that the particles size decreases with the temperature increase. The effects of the temperature were however investigated above 160°C. Besides, it must be precised that the particles size in this study was comprised between 0.1

and 1 µm *i.e.* well above the diameters reached here. No similar study on the temperature effect on the nanoparticles size was found in the literature.

In colloidal synthesis methods in general, the nucleation phase initiates after the metal atoms concentration reaches a "supersaturation concentration" during the metal salts reduction and should take place in a very short time interval (almost instantaneously) to ensure the particles size homogeneity [157]. After the formation of the nuclei, the metal atoms concentration drops below a concentration threshold. From this moment, the number of nuclei remains constant while they start growing until the consumption of all the zerovalent atoms.

The polyol method is no exception and follows the same principle: The first step (the reduction of the metal salts resulting in the formation of zerovalent metal atoms) occurs after an induction time after the temperature is raised to 160°C (temperature chosen in the protocol). Once the metal atoms supersaturation is reached, the nucleation step initiates and stops before the nuclei starts growing until consumption of all the metal atoms in the solution. These three steps (metal salts reduction, nucleation and nuclei growth) all occur at 160°C. The three hours fixed in the protocol (see above) correspond to a sufficient duration for the reduction of the metal salts and the growth of the nuclei, and can be found in many studies [138,143,144,146]. However, alike the temperature, this parameter varies in the literature from two to five hours [142,145].

The adsorption of the formed nanoparticles on the carbon support takes place afterward during the overnight cooling step. After the cooling procedure, another step was added to the polyol method, which consists of lowering the pH to pH = 3, likewise to the protocol in [144] in order to improve the nanoparticles adsorption. Oh et al. investigated the effects of the pH on the zeta potential of the carbon support and Pt nanoparticles [144]. They found out that, after the synthesis at pH = 12, the zeta potential of the carbon support and the metal nanoparticles is negative. However, after the pH adjustment down to pH = 3, the zeta potential of the carbon support changes and becomes positive while the zeta potential of the nanoparticles remains negative. The authors assumed that the glycolate anions are more strongly adsorbed on the nanoparticles than on the carbon support, which would hinder the modification of the nanoparticles zeta potential. As a consequence, the authors believed that it could help the electrostatic attraction of the nanoparticles with the carbon support and thus render their adsorption more homogeneous on the carbon surface. Other publications added similar steps in their synthesis protocol but without explaining the reason [123,146].

The gas environment of the synthesis solution is also an influent parameter which impacts significantly the yield of the total deposited nanoparticles mass on the carbon support. Oh et al. [143] discovered that when the complete synthesis (at 160°C and after at room temperature) is carried out in an inert gas atmosphere, the control of the nanoparticles size is good but the metal loading on the carbon support poor. On the opposite, an entire process in open air results in a good metal loading but in the presence of agglomerates on the carbon support. Finally, the optimum result (good particle size control + good metal loading) was obtained in inert gas during the three-hour step at 160°C and in open air during the next steps

at room temperature. No conclusions were drawn related to the impact of the gas environment on the reactions occurring during the synthesis.

A significant advantage of the polyol process is the good control on the metal nanoparticle size by pH adjustment. The decrease of the nanoparticles size by increasing NaOH concentration (and *a fortiori* the pH) was already reviewed in the literature [143,148,154,158]. According to Fievet et al. [154], an increase of the pH by NaOH addition in the synthesis solution leads to faster kinetics of the metal salt reduction, which would result in the formation of a larger number of nuclei. As a consequence, the nuclei growth would be hindered. pH = 12 was chosen for the experiments in the present study in order to hinder the formation of agglomerates (and the decrease of the electrocatalyst specific area) which could occur at low pH and the formation of too small nanoparticles (and their increased stability on the carbon support) at too high pH (for the sake of concision, the impact of the nanoparticles size on electrochemical reactions is introduced in section III).

This synthesis method was finally chosen among others due principally to its simple operability, the use of only one chemical (EG) as reducing and stabilizing agent and the good control of the nanoparticle size.

II.2. Physical characterisations

II.2.1. ICP-AES

Inductively coupled plasma atomic emission spectroscopy (ICP-AES) enables the quantitative determination of elemental chemical compounds present in a solution. Two distinct elements constitute the ICP-AES: the plasma and the photodetector.

The ignition of an argon gas constrained in a strong electromagnetic field results in inelastic collisions between argon neutral atoms and ions, which in return gives rise to a stable plasma, the temperature of which is in the order of 7000 K.

A solution containing the sample is pumped into the ICP device where it is evaporated by a nebulizer before being introduced inside the plasma. There, the sample molecules/atoms/ions enter in collision with the ions and electrons constituting the plasma and break into exited ions which further stabilize after photon emission. The emitted radiation, unique for each element, is then analyzed and quantified by a photodetector.

The ICP-AES analysis was used to determine the metal-carbon and metal-metal ratio in the bi- and tri-metallic electrocatalysts. The device employed for the measurements was a iCAP 6300 Thermo.

II.2.2. Thermogravimetric analysis

The thermogravimetric analysis (TGA) allows recording continuous material mass changes as a function of the temperature during a thermal treatment (the temperature usually varies linearly against the time at *ca.* 5-10 K min^{-1}). The pressure and the atmosphere (air, inert gas…) in the analysis chamber are also important parameters which impact the profile of the material mass evolution.

The mass variations of the sample, placed on a micro-balance, are recorded by measuring the voltage required to maintain the micro-balance in its initial position. The variation of the balance position is determined by a photo-sensor which permits to adjust the voltage response of the induction coils located at two extremities of the micro-balance. The voltage is then converted to mass during the experiments.

Concretely, the metal loading on the carbon support of the synthesized electrocatalysts was measured by TGA. Due to the high melting point of the investigated metals (Pt and Rh melting point are over 1500°C), only the carbon mass loss can be measured and thus the carbon-metal ratio estimated (the maximal temperature reached by the device is *ca.* 1200°). For tin oxide containing electrocatalysts (Pt-SnO_2/C, Pt-Rh-SnO_2/C), this ratio could not be estimated due to tin low melting point (T ≈ 200°C). Thus, the use of ICP-AES was primordial for the knowledge of the metal-metal and carbon-metal ratio. The TGA analyses were carried out with a Q 5000 from TA Instruments apparatus.

II.2.3. Transmission Electron Miscroscopy

The principle of the transmission electron miscroscopy (TEM) relies in electrons-atoms interactions. Depending on the TEM mode, information related to the studied sample either concerns its topography or its chemical contrast.

Primary electrons are generated by a thermo-electronic source, typically a tungsten or a LaB_6 filament, and expulsed from the anode with an energy up to *ca.* 200 kV. The beam is then directed through a column where its focus is ensured magnetically by the presence of one or several condensers, before being finally directed on the sample by the objective lenses. The primary electrons pass trough the sample owing to its small thickness (< 100 nm). The imaging contrast is ensured by the the thickness of the sample, its chemical composition (in this case, between the Pt nanoparticles and the carbon support) and by the sample cristallinity (deflection of the inciding electrons on the sample diffraction planes).

Other analyses such as the energy dispersive X-ray spectroscopy (X-EDS or EDX) are enabled by TEM. The collision of primary electrons with highly energetic electrons of the sample atoms can engender the ionization of the latter. The hole in their valence band will be replaced by an electron of an upper layer which will in return emit energy in the form of a photon. This energy in the X-range will subsequently be detected by a sensor. Information on the chemical composition of the sample is thus made possible since each atom has its own X-ray spectrum.

The preparation of the samples is trouble-free and only consists of dipping a properly-cleaned copper grid baring a thin carbone membrane inside the studied electrocatalyst powder. A Jeol 2010 TEM was employed for this characterization (1.9 Å point-to-point resolution at 200 kV).

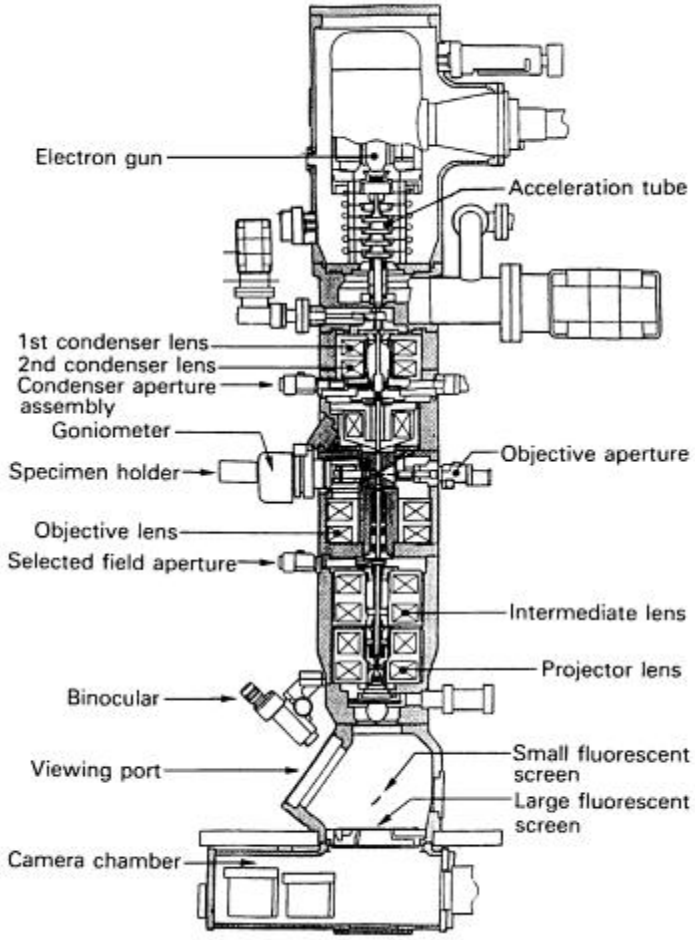

Fig. 5.TEM Scheme [159].

Determination of the particle size distribution (PSD) was performed from TEM imaging. This evaluation was performed measuring manually the diameter of *ca.* 400-500 nanoparticles visualized on *ca.* 20 different TEM images randomly taken on the sample, which usually provides data with sufficient statistics. Those images were photographed in four distinct areas of the studied sample (five images per sample area), which themselves were shot at × 200 000 magnification.

For each sample, the number-averaged (d_N), the surface-averaged (d_s) and the volume-averaged diameter (d_V) were calculated as follows:

$$d_N = \frac{\sum n_i \times d_i}{\sum n_i} \qquad \text{Eq.II.1}$$

$$d_S = \frac{\sum n_i \times d_i^3}{\sum n_i \times d_i^2} \quad \text{Eq.II.2}$$

$$d_V = \frac{\sum n_i \times d_i^4}{\sum n_i \times d_i^3} \quad \text{Eq.II.3}$$

with n_i the number of nanoparticles and d_i their respective diameter.

The knowledge of these three parameters is essential as it enables verifying that the surface- (d_S) and volume-averaged diameter (d_V) match with d_{Elec} and d_{XRD} respectively (introduced hereafter).

II.2.4. X-Ray Diffraction (XRD)

X-Ray Diffraction (XRD) permits identifying the crystalline structure of the studied sample. The XRD analysis was also used to evaluate the volume-average cristallite size and the lattice parameter of the corresponding electrocatalysts.

The X-radiation originates from the violent collision of electrons, bombarded from a tungsten filament, with a copper anode emitting heat and X-rays in the process. More precisely, these X-rays correspond to the photons emitted by the electrons from the L shell replacing the vacancies let by the electrons from the K shell ejected from their Cu atoms as a result of the W filament electrons collision with the copper anode. The electrons from the other electron shells (M, N…) emit too-low-energy photons to be functional (they are rapidly absorbed in the air). Only the K_α and K_β X-photons can be detectable at the exit of the X-ray tube. A monochromator is placed between the source and the sample in order to select the photons with the highest energy (K_α: $K_{\alpha1}$ and $K_{\alpha2}$).

The incident X-photons issued from the source collide the atoms of the sample and are diffracted following three conditions:

- The 1st Snell-Descartes law should be respected: incident and diffracted rays and the line perpendicular to the crystallographic planes should be contained in the same plane.
- The angle (θ) between the incident rays with the crystallographic planes and between the diffracted rays with the crystallographic planes (θ') should be equal (θ' = θ).
- The diffraction angle (θ) should verify Bragg's law (Eq.II.4):

$$n\,\lambda = 2\,d_{hkl}\sin\theta \quad \text{Eq.II.4}$$

with λ the wavelength of the incident ray, *n* the diffraction order and d_{hkl} the distance between the crystallographic planes with (*hkl*) orientation (*h*, *k* and *l* are also known as the Miller indices) of the crystalline lattice (see Fig. 6).

Finally, the diffracted X-photons are collected by a detector which also forms a θ angle with the crystallographic planes. During the acquisition, the sample support is rotated on itself so that the different sample diffraction planes can be detected.

A Bruker AXS D8 diffractometer was used to analyze the studied electrocatalysts from 2θ = 15° to 90° with a scan rate of *ca.* 0.74° min^{-1}.

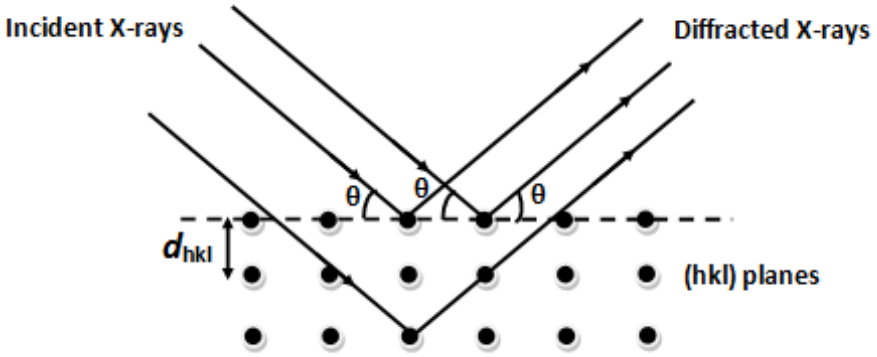

Fig. 6. X-ray diffraction scheme on the crystallographic (*hkl*) planes.

The average cristallite size was estimated using Scherrer's equation:

$$d_{\mathrm{XRD}} = \frac{0.9\,\lambda_{\mathrm{K}\alpha}}{B\cos\theta_{\mathrm{max}}} \qquad \text{Eq.II.5}$$

with $\lambda_{K\alpha}$ the wavenumber of the incident ray and θ_{max} the angular position and *B* the width at half-maximum of the (111) and of the (220) peaks.

The (111) and (220) diffraction peaks were used because of their high intensity. Inaccuracies can be found in the determination of *B* due to the possible overlap of the carbon support peak and the Pt (111) diffraction peak. In case of a sample with a large nanoparticle size distribution, the average size value can be biased because of the presence of the bigger nanoparticles, which impacts the diffraction peaks width. Accurate determination of the average size may also render difficult or even impossible in case of exclusive presence of very small nanoparticles, which will broaden the diffraction peaks.

Discrepancies between d_V with d_{XRD} can regularly be witnessed and often reflect the formation of heterogeneous nanoparticles (in shape, size…), which can only be observed by TEM. Due notably to the weak reflection by small nanoparticles of the incident X-ray beam, XRD spectra are more sensitive to the presence of small fractions of larger nanoparticles in the sample, which results in the formation of sharper diffraction peaks.

II.3. Electrochemical characterization

II.3.1. Three electrode assembly

A three electrode assembly was used to carry out electrochemical experiments. The system is constituted with a working electrode (WE), a counter electrode (CE) and a reference electrode (RE). The electrochemical reactions of interest generally occur at the working electrode. The cell voltage is generally measured as the difference between the WE potential and the RE potential. The latter should not be polarized so as to provide a reliable comparison to the WE and should be located as close as possible from the latter in order to minimize the ohmic drop engendered by the electrolyte resistance. Its position should however not interfere with the ions/molecules mass-transport. The CE serves only as a current sink. In other words, it helps the current flow through the cell. The reactions occurring at the counter electrode are usually of no concern (in aqueous electrolyte, it is usually predominantly H_2 or O_2 evolution).

II.3.2. Cyclic voltammetry

This technique allows measuring the current variation at the working electrode while the potential applied at the latter linearly changes *vs*. time. The cyclic voltammetry starts at an initial potential and ends at a final one. The reversible potential marks the scan direction switch. The scan rate $\nu = \frac{dE}{dt}$ indicates the tempo of the potential variation. Typical ν values vary from a few mV s^{-1} to a few V s^{-1} but can also go up to a few kV s^{-1} in a study with ultra-microelectrodes (UME).

The measured current is equal to the addition of two distinct terms: I_f and I_{dl}. The faraday current I_f originates from the electron transfer coming from electrochemical reactions occurring at the working electrode. I_{dl} stands for the double layer (or capacitive) current and corresponds to the current generated by the capacitive ion charges movement operating at the interface electrode/electrolyte when the applied potential varies. I_{dl} can be written as followed:

$$I_{dl} = C_{dl}\, A\, \upsilon \qquad \text{Eq.II.6}$$

with A the working electrode surface, ν the scan rate and C_{dl} the double layer capacitance. C_{dl} values are approximately 20 μF cm^{-2} for glassy carbon electrodes and can be much higher when specific adsorption occurs (*i.e*. typically for Pt electrodes in the so-called hydrogen and oxide regions). The CV is often the first method carried out to electrochemically study a new system.

II.3.3. Chronoamperometry

A chronoamperometry is a potentiostatic method which enables measuring the current as a function of the time after application of a potential step. Like in a cyclic voltammetry, the current response to the step potential accounts for the contribution of a capacitive and a faradaic current. The capacitive current, only occurring at short times, corresponds to the double layer charging. It decays exponentially with time more or less rapidly depending on the values of the double layer capacity C_{dl} and the solution resistance R_{Ω}.

The evolution of the faraday current follows a trend in two steps. At short times, the faraday current shrinks due to the concentration gradient sinking with time before the establishment of a steady-state value.

II.3.4. Rotating Disc Electrode

The rotating disc electrode (RDE) is a powerful tool used in a three-electrode assembly (see II.2.1.) which permits to study reactions limited by mass-transport, under quasi-stationary conditions, and to access possibly some kinetics parameters (number of exchanged electrons during a reaction, diffusion coefficient, kinetic rate constants…) provided by an adequate mathematical treatment of the electrochemical data.

In RDE, a disc electrode plugged in an insulated Teflon rod rotates at a fixed rotation rate on its axis; this creates a vortex, which continously provides reactant by convection to the electrocatalyst surface, before dragging it out perpendicular to the electrode surface (see Fig. 7).

In a RDE study, a new term appears in the expression of the limited faraday current, which is proportional to the square root of the electrode rotation speed (Levich law - Eq II.7):

$$I_{lim} = 0.62\, n_{e^-}\, F\, D^{2/3}\, C\, \upsilon^{-1/6}\, \omega^{1/2} \qquad \text{Eq.II.7}$$

where I_{lim} is the limiting current, n_{e^-} the number of exchanged electrons, F the Faraday constant, D the diffusion coefficient, C the species concentration, υ the kinematic viscosity and ω the rotation speed.

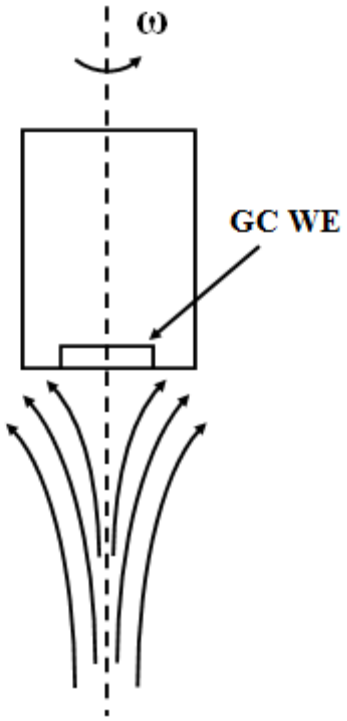

Fig. 7. Flow profile at a rotating disc electrode (RDE).

II.3.5. Evaluation of the electrochemical active surface area

The electrochemical active surface area (ECSA) is the surface of the metal nanoparticles which participates in the electrochemical reactions, *i.e.* in the transformation of chemical energy in electrical energy. The CO stripping enables the ECSA evaluation based on the calculation of the charge required to oxidize a carbon monoxide monolayer adsorbed on the electrocatalyst surface (for more convenience, the ECSA was noted A_m with *m* the metals constituting the different studied electrocatalysts):

$$A_{\mathrm{m}} = \frac{A_{\mathrm{CO,m}}}{\nu\, Q_{\mathrm{Pt}}} \qquad \text{Eq.II.8}$$

with ν the scan rate, Q_{Pt} Pt specific charge and $A_{CO,m}$ the area of the CO_{ad} monolayer electrooxidation. This area $A_{CO,m}$ is obtained by subtraction of the 1st cycle during which the CO_{ad} monolayer oxidizes and the 2nd cycle (see Fig. 8):

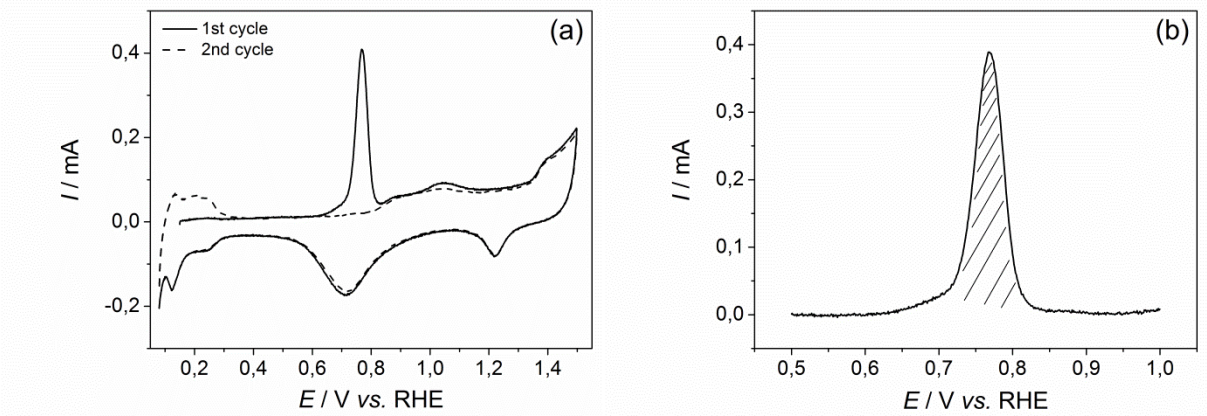

Fig. 8. (a) 1st (solid) and 2nd cycle (dash) of a CO stripping CV in 0.5 M H_2SO_4 in the DEMS flow cell and associated (b) substraction of the 1st cycle by the 2nd one.

Based on the assumption that the nanoparticles have a cubooctahedral shape, their size can be evaluated using the following equation:

$$d_{\mathrm{Elec}} = \frac{6\left(3+\sqrt{3}\right) W_{\mathrm{m}}}{5\, A_{\mathrm{m}}\, \rho_{\mathrm{m}}} \qquad \text{Eq.II.9}$$

with W_{m} the mass of deposited metal nanoparticles and ρ_{m} the metals density.

Inconsistencies between d_{S} and d_{Elec} can originate from the non-utilization of some nanoparticles, due for example to the presence of non-supported nanoparticles, to large nanoparticles/agglomerates, the sole surface of which is electrochemically active (not their volume), or also to the presence of surfactants on the electrocatalyst surface blocking the active sites of the nanoparticles.

II.3.6. Normalization of the current

The results presented hereafter are normalized either by the ECSA or by the total metal mass. The normalization by the ECSA was found more convenient for the comparison between the Pt electrocatalysts (in section III). On the contrary, the normalization by the metal mass was favored for the comparison between the Pt-based multi-metallic electrocatalysts. Indeed, the CO-stripping could suffer some inexactitudes:

- CO_{ad} quantitative electrooxidation starts at low potentials on Pt-SnO_2/C and Pt-Rh SnO_2/C electrocatalysts (between E = 0.2 and 0.3 V *vs.* RHE). CO_{ad} desorption during the chronoamperometry step prior the CV is thus possible.

- CO does not adsorb on tin/tin oxide.

- Overlap of the current originating from the CO-stripping (1st cycle) and the oxide formation (2nd cycle) on rhodium and rhodium-containing electrocatalysts is possible.

- Electronic interactions between metals may modify CO adsorption affinity.

II.4. Coupled physical and electrochemical techniques

II.4.1. *In situ* Fourier Transform InfraRed spectroscopy

In situ Fourier Transform InfraRed (FTIR) spectroscopy is a technique which enables the coupled electrochemical and physical characterization of the electrode/solution interface: solution and adsorbed species can be identified via their unique infrared spectrum fingerprint under potential control conditions.

The principle is based on the absorption of an incident infrared polychromatic beam by the studied species present in the solution or adsorbed on the electrocatalysts. The light absorbed at punctual wavenumbers corresponds to the energy necessary for the vibration of specific dipolar covalent bonds. Thus, the identity of the bonds but, more important, the identity of the molecules can be identified. [4000 cm^{-1}; 400 cm^{-1}] generally corresponds to the spectral window for the vibration of molecules in a FTIR.

After absorption of the required energy of the incident beam by the different molecules adsorbed on the electrocatalyst or present in the solution, the beam is reflected by the surface of the working electrode before reaching the detector. The latter then measures the light reflected by the sample. The raw data are then converted using the Fourier transform in order to give the amount of light absorbed per wavelength (or wavenumber).

The nature of the window separating the FTIR compartment from the cell containing the studied system influences the range of the infrared spectrum and the amplitude of the bands. For example, a ZnSe window permits to have information at low wavenumbers (at high wavelengths) from 4000 cm^{-1} to 650 cm^{-1} whereas a CaF_2 window can only give access to wavelengths until 1000 cm^{-1} (limits are defined by the beam absorption of the window itself).

The role of the aperture is to settle the intensity of the incident beam. The wider the opening, the larger the intensity of the incident beam (and as a consequence the intensity of the reflected beam); it should however not exceed a maximum value to avoid the deterioration of the detector.

Finally, a polarizer is positioned after the transmitter and permits to filter the incident beam. It lets only the electromagnetic waves with an electric field perpendicular to the metallic wires, constituting the polarizer, go through the grid. As a result, electromagnetic waves with a specific orientation can be selected and give more precise information. p- and s-polarization correspond respectively to electromagnetic waves perpendicular and parallel to

the surface of the working electrode. A p-polarization (0° on the polarizer) allows identifying the species adsorbed on the electrode but also some species in the solution (depending on their orientation), while an s-polarization (90°) enables only the detection of the species present in the solution. Indeed, in the case of adsorbed species, the bond linking the atoms together is perpendicular to the surface of the working electrode and can only reflect the p-polarized beam.

Fig. 9 shows the electrochemical cell adapted for the *in situ* FTIR experiments. The different inlets were employed for the three electrodes as well as for the inert gas (Ar) or CO bubbling depending on the electrochemical procedure. A last inlet was used to evacuate the gas. The counter electrode was a Pt grid and the reference electrode a RHE. The working electrode was either an Au electrode (for the CO-stripping study) or a GC electrode (for the EOR study). In order to minimize the infrared beam absorption by the aqueous solution, the working electrode was pressed by a glass rod against the CaF_2 optical window used for the *in situ* FTIR experiments allowing us to work in a thin layer configuration.

Each FTIR spectrum was obtained under p-polarization and acquired during 30 s as an average of 256 interferograms. The spectra were recorded every 100 mV from E = 0.25 to 1.15 V *vs.* RHE and are represented hereafter as R/R_{Ref}, with R_{Ref} the spectrum recorded at E = 0.15 V *vs.* RHE.

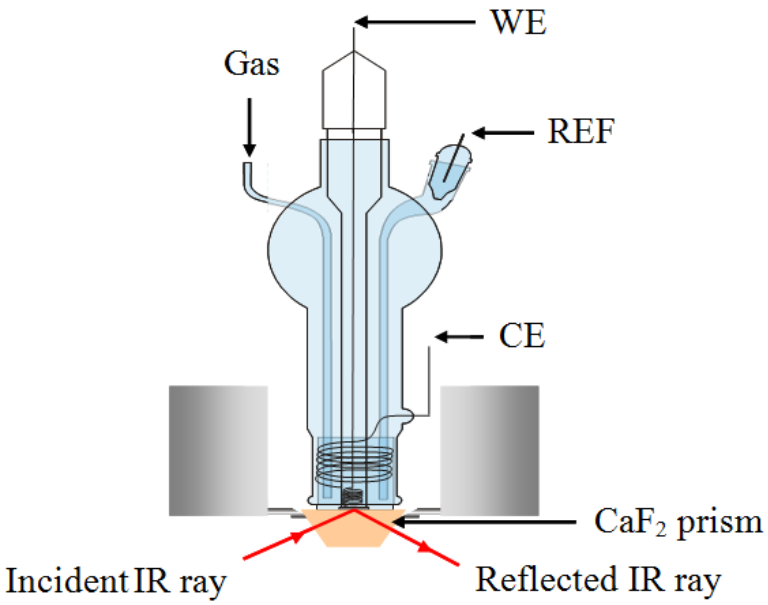

Fig. 9. Standard scheme of an *in situ* FTIR cell

II.4.2. Differential Electrochemical Mass Spectrometry (DEMS)

II.4.2.1. Basics of operation

Mass spectrometry (MS) analysis allows identifying gas and volatile molecules using their mass-to-charge signature. A typical mass spectrometer is composed of three components: an an ion source, a mass analyzer and a detector. It is connected to a pre-vacuum compartment (*ca.* 8.10^{-2} mbar) *via* a gas inlet which ensures a constant supply in the studied gas phase molecules pumped from the electrochemical cell.

In differential electrochemical mass spectrometry (DEMS), the gas inlet is going through two vaccum compartments maintained at differential pressures (*ca.* 10^{-3} mbar and then 10^{-6} mbar). This cascade of vaccum enables "ballistic" transport of the gases and very low transition times. As a result, the MS detector sees the molecules formed at the working electrode less than *ca.* 0.5 s after their generation (corresponding to on time-detection).

The ionization process operates through the collision between electrons and the absorbed gas and volatile molecules. Electrons are generated by thermionic emission from a heated tungsten filament in a vacuum. The emitted electrons accelerated up to 70 eV collide with absorbed gas molecules entering in the ion source chamber in a perpendicular direction to the electron beam. The collision results in the ionization of the molecules or/and their possible defragmentation(s).

Positive ionized molecules are then transported by an extracting diaphragm to a quadrupole mass analyzer through a repeller electrode where they are separated according to their mass-to-charge ratio (*m/z*). The qualizer is composed of four cylindrical rods, parallel from one another, imposing a variable electrical and magnetic field to the flowing ionized molecules. The latter adopts in this environment an ellipsoidal trajectory, the amplitude and speed of which depend on the characteristics of the electromagnetic field (parameters *E* and *B*) as well as the mass-to-charge ratio of the ionized molecules. Because of their singular speed and trajectory, each molecule can be sorted according to their mass-to-charge ratio.

The detector, located at the end of the mass analyzer, finally records the intensity resulting from the impact of the ionized molecules on the surface of the detector. Typical mass intensity values vary between 10^{-14} and 10^{-5} A. A maximum of 64 channels enables to measure the different mass-to-charge signals that are relevant to the experiment.

The dwell time for each signal varies between 0.1 s and 60 s. The longer the detection time, the more accurate the precision of the signal; however, a too long detection time can also result in a too important delay between the electrochemical and the mass spectrometric measurements ruining the interest of the differential pumping. That is why a compromise has to be found to get as precise information as possible during the electrochemical measurements: in the following studies, eight mass-to-charge signals (see Table 2) were studied during 2.5 s overall. A *ca.* 20 mV delay could be observed between the electrochemical and mass spectrometric experiments.

The Quadstar software was employed to parameter and run the measurements with the QMS 200 mass spectrometer from former Balzers.

Table 2. Studied molecules and associated mass-to-charge signals.

m/*z* signals	Molecules	Formula	Detected ions	Dwell time / s
2	Dihydrogen	H_2	$[H_2]^+$	0.1
15	Ethanol, acetaldehyde, methane	CH_3CH_2OH, CH_3CHO, CH_4	$[CH_3^+]$	0.1
22	Carbon dioxide	CO_2	$[CO_2^{++}]$	1
29	Ethanol, acetaldehyde	CH_3CH_2OH, CH_3CHO	$[CHO^+]$	0.1
30	Ethane	CH_3CH_3	$[CH_3CH_3^+]$	0.1
44	Ethanol, acetaldehyde, carbon dioxide	CH_3CH_2OH, CH_3CHO, CO_2	$[CO_2^+]$, $[CH_3CHO^+]$	0.1
60	Acetic acid	CH_3COOH	$[CH_3COOH^+]$	0.5
61	Ethyl acetate	$CH_3COOCH_2CH_3$	$[CH_3CH_2OO^+]$	0.5

A flow cell setup is exploited for the purpose of *in situ* differential electrochemical mass spectrometry (DEMS) measurements. The geometry of the polychlortrifluorethylene (PCTFE) cell represented in Fig. 10 is the one of a wall-jet cell with one inlet for the studied solutions and two outlets, one for the reference electrode and one for the counter electrode. The solution is fed to the cell under a constant flow rate (the latter was always maintained between *ca.* 1.9 and 2.3 mL min^{-1}) in order to prevent any current fluctuation during the electrochemical measurements. The reference hydrogen electrode (RHE) is located in a compartment containing the electrolyte solution (0.5 M H_2SO_4), while the platinum wire counter electrode is positioned at the cell outlet. Finally, the working electrode is constituted of a hydrophobic Gore-Tex membrane (60 µm thickness, 0.02 µm mean pore size, 50 % porosity) on which an inert gold thin layer (*ca.* 75 nm) is sputtered in order to render the membrane electrically conductive.

Gas phase molecules coming from the flowing solution and produced during the electrochemical reactions are pumped to the pre-pump compartment through a glass frit located below the working electrode.

With the cell directly in contact to the mass spectrometer without any capillary intermediates, the delay time between the electrochemical measurements and the mass spectrometry signals can be minimized.

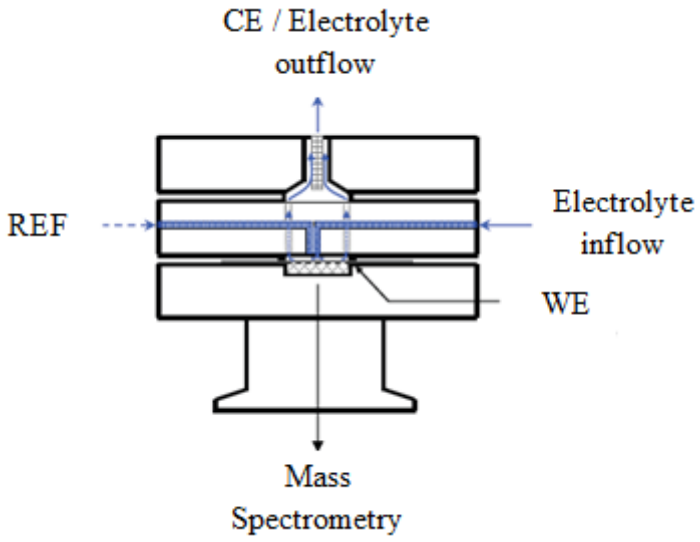

Fig. 10. Scheme of the electrochemical DEMS flow cell [160].

II.4.2.2. MS calibration

In order to quantify the amount of CO_2 produced during the EOR and detected by the DEMS, a calibration of the mass-to-charge signal *m/z* = 22 regarding the corresponding faraday current has to be achieved [161]. For that purpose, the CO stripping is used as a calibration reaction, as it involves the sole production of CO_2 from a known CO_{ad} monolayer (Eq. I.18):

$$CO_{ads} + H_2O \rightarrow CO_2 + 2\,H^+ + 2\,e^- \qquad \text{Eq.II.10}$$

The mass to charge signal *m/z* = 22 is the only signal in the present experimental conditions (oxidation of ethanol) that can be ascribed solely to the production of CO_2 (doubly ionized [CO_2^{++}]). Indeed, the signal *m/z* = 44 (ionized [CO_2^+]) is compromised by the presence of acetaldehyde (ionized [CH_3CHO^+]), a known by-product of the EOR.

Eq.II.11 correlates the ionic current for the mass to charge signal *m/z* = 22 and the faradaic current:

$$K_{22}^* = \frac{2\,I_{m/z=22,CO}}{I_{f,CO}} \qquad \text{Eq.II.11}$$

where $I_{m/z=22,co}$ is the ionic charge of the mass-to-charge signal *m/z* = 22, $I_{f,co}$ the faradaic charge, 2 the number of electrons exchanged during the electrooxidation of adsorbed CO in CO_2 and K_{22}^* the calibration constant of the signal *m/z* = 22. The current value of the CO-stripping peak and of the signal *m/z* = 22 peak were used to determine K_{22}^*. The latter was then checked with two or three other (faraday and ionic) current values in the ascending part

of the CO-stripping. The 20 mV delay between the electrochemical and mass spectrometric measurements was taken into account for the choice of these values (Fig. 11):

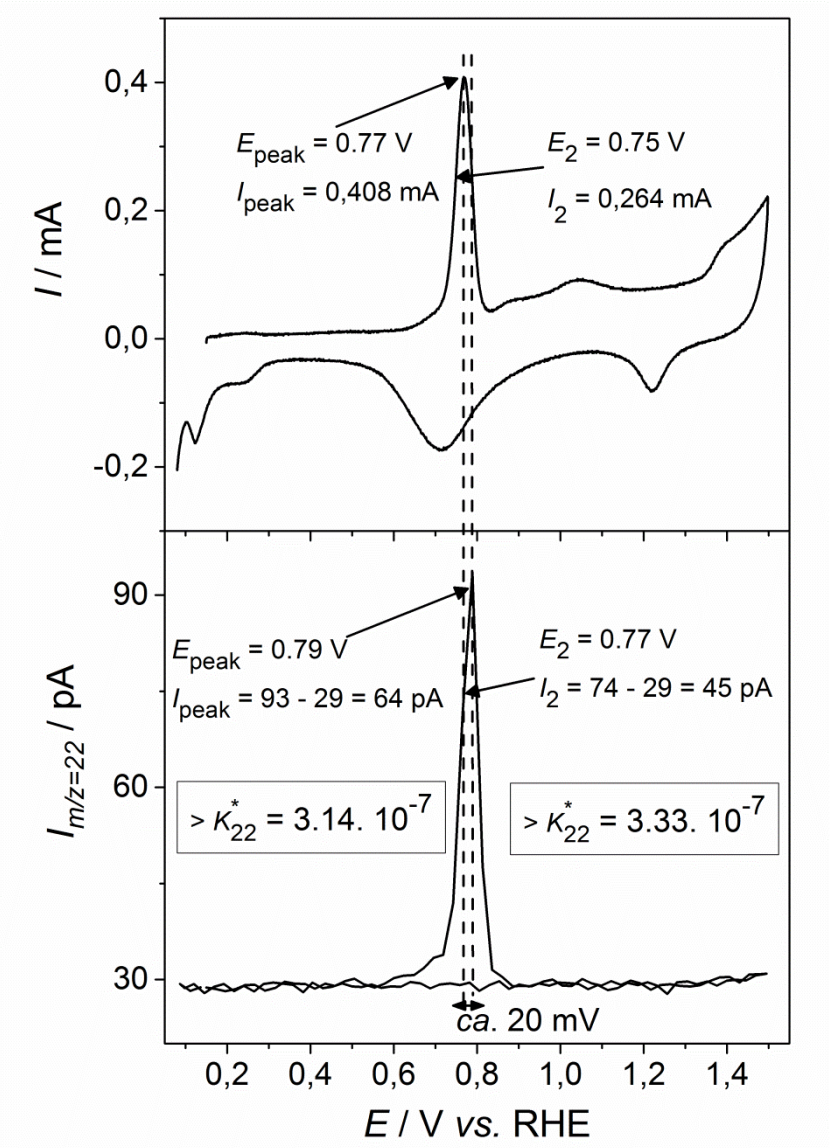

Fig. 11. K_{22}^{*} calibration using a CO-stripping CV in 0.5 M H_2SO_4 on Pt/C and its associated mass-to-charge signal *m*/*z* = 22.

The CO_2 current efficiency (CCE) can then be deduced using the faradaic and ionic current values obtained during the ethanol oxidation (see Fig. 12):

$$CCE = \frac{6}{K_{22}^{*}} \frac{I_{\mathrm{m/z=22}}}{I_{\mathrm{f}}} \qquad \text{Eq.II.12}$$

with 6 the number of electrons exchanged for the production of one CO_2 molecule.

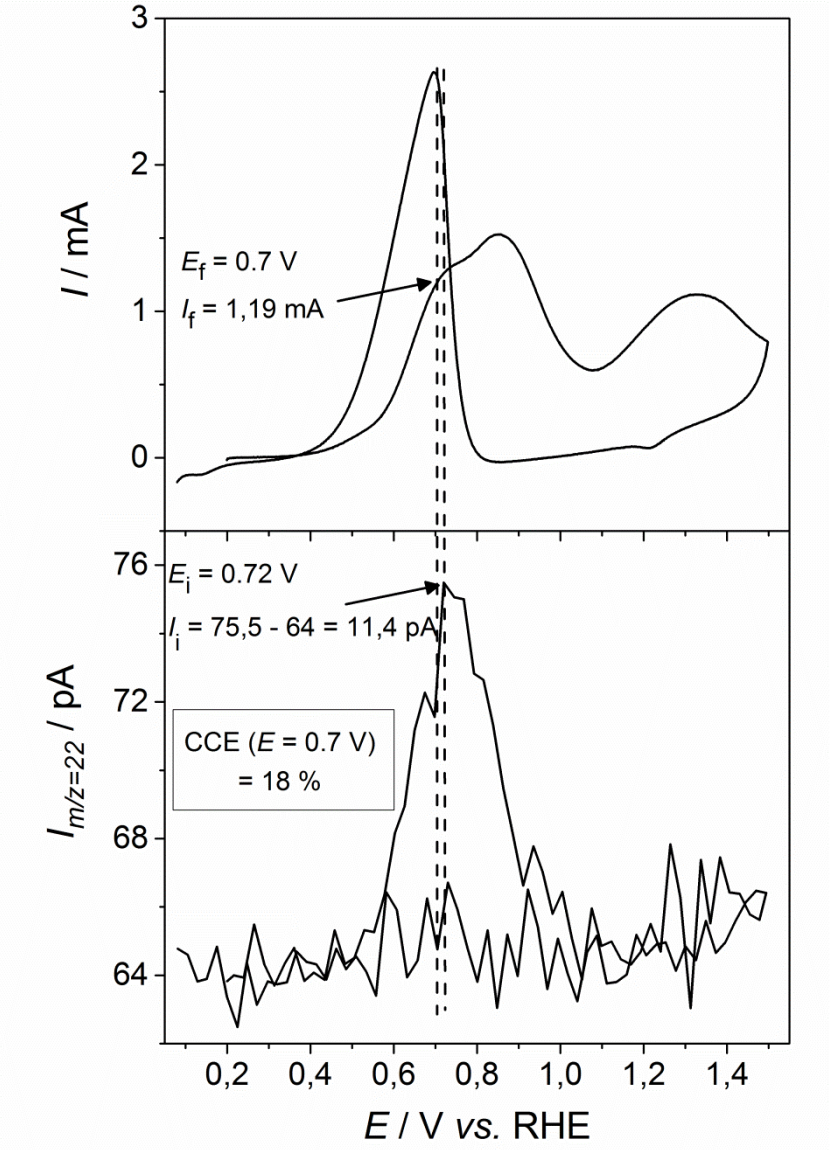

Fig. 12. EOR CCE calculation at E = 0.7 V *vs.* RHE in 0.5 M H_2SO_4 + 0.1 M EtOH.

For the study on the stripping of organic species (see section V), a calibration was required to estimate the number of electrons exchanged during the reactions producing CO_2 as final product. Both mass-to-charge signals m/z = 22 and m/z = 44 could be used for this purpose (no acetaldehyde or ethyl acetate emission during stripping-CVs), but the signal m/z = 44 was favored as the latter had a better signal-to-noise ratio and thus could enable a more accurate determination of the number of exchange per CO_2 molecule. The calibration was carried out using charges ($Q_{f,CO}$ and $Q_{m/z\,=\,44,CO}$) instead of currents ($I_{f,CO}$ and $I_{m/z\,=\,22,CO}$), in Eq. II.11. The number of exchanged electrons per CO_2 molecule could then be deduced using the faraday ionic charge values obtained during the stripping of ethanol and acetaldehyde adsorbates:

$$n_{e-} = K_{44}^{*} \frac{Q_f}{Q_{m/z=44}}$$ Eq.II.13

with Q_f the faradaic charge and $Q_{m/z=44}$ the ionic charge of the signal *m/z* = 44 from the ethanol or acetaldehyde adsorbates oxidation.

II.5. Conclusions

Different physical, electrochemical and coupled (physical-electrochemical) characterization techniques were described in this section. These methods were employed throughthout the thesis to characterize the electrocatalysts developed for the EOR study.

The polyol method was chosen in order to synthesize the Pt-based electrocatalysts due to the advantages offered by this method: easy applicability, use of only one chemical which plays both the role of the reducing and stabilizing agent and control of the nanoparticles size.

The electrocatalysts were then physically characterized by TGA or/and ICP-AES so as to accurately determine the metal-carbon and metal-metal ratio. TEM imaging revealed how well the dispersion of the nanoparticles operated on the carbon support and enabled the determination of the particle size distribution. XRD gave information on the crystalinity of the synthesized electrocatalysts.

The described electrochemical techniques were used throughout the presented work in order to highlight how efficient the different electrocatalysts are regarding the EOR and how they impact on the reaction.

Finally, the two coupled techniques (*in situ* FTIR and DEMS) are used combined with the electrochemical characterization in order to better understand and additionally give physical proves of the phenomena occurring during the multi-step/multi-pathway ethanol electrooxidation.

Chapter III.

Ethanol Oxidation Reaction (EOR) investigation on Pt/C, Rh/C, and Pt-based bi- and tri-metallic electrocatalysts: a DEMS and FTIR study

The aim of this section is to identify the changes in the EOR mechanism and in the product distribution induced by the variation of some experimental factors and the use of different electrocatalysts. To that purpose, a first study was carried out on the influence of the scan rate and of the thickness layer of a 20 wt.% Pt/C electrocatalyst on the EOR by means of DEMS and RDE. A combined DEMS and *in situ* FTIR investigation of the EOR was then performed on 20 wt.% Pt/C, Rh/C, Pt-Rh/C, Pt-SnO_2/C, Pt-Rh-SnO_2/C electrocatalysts. Above all, the state of the art on Pt-based multi-metallic electrocatalysts is thoroughly recalled and a special emphasis is given on the effects induced by the addition of rhodium and tin to platinum in the electrocatalyst composition. The results obtained by means of DEMS and *in situ* FTIR are subsequently displayed and meticulously addressed in view of the present knowledge on the field.

III.1. Influence of the Pt/C electrode structure on the EOR

III.1.1. Introduction

Investigating the effect of the electrocatalytic surface structure on the EOR mechanism, a surface sensitive mechanism, can allow its better understanding. For example, studies on monocrystalline electrocatalysts give precious information on the different EOR pathways [34,45,162–170]. It was found that the C-C bond cleavage occurs mainly on surface steps [163,164,166], whereas no influence of the terrace was observed [164]. Besides, the increase of the step density seems to result in an increase of the EOR electroactivity [163], which can be paralleled to the faster CO-oxidation kinetics at the defects of agglomerated Pt/C nanoparticles [57]. Colmati et al. discovered that the effect of the steps on the EOR could be separated in two potential regions: one below and one above E = 0.7 V *vs.* RHE [164]. Using FTIR techniques, they found that both the C-C bond breaking and CO_{ad} electrooxidation are enhanced at low potentials, whereas a competition with acetaldehyde and acetic acid formation takes place at high potentials.

Although information brought by these studies is of high interest, monocrytals are not representative of the practical electrocatalysts used in fuel cell applications. Investigating the EOR on polycrystalline and carbon-supported nanoparticle electrocatalysts appears thus as a necessity. Despite the growing interest in direct ethanol fuel cells, a very low amount of studies exists on the effect of the structure of such electrocatalysts on the EOR [35,42,158,171–173]. According to Perez et al., Pt nanoparticles size of *ca*. 2.5 nm are considered offering a good compromise between their geometric features (smaller crystallites have a large electrochemical surface area, a positive effect, but a decreased stability, a negative effect) and their oxophilicity (smaller Pt nanoparticles exhibit more oxophilic surfaces than larger ones) to get optimal EOR performances. On the contrary, Li et al. found the highest EOR specific activity on their smallest Pt nanoparticles (*ca.* 1.7 nm) against nanoparticles of *ca.* 2.4 and 4.0 nm [158]. Gomes et al. investigated the presence of agglomerates and small nanoparticles in electrocatalyst of constant mean particle size: they observed a higher EOR peak in presence of large nanoparticles but determined lower CCE with the same sample [173]. The effect of the loading was also investigated by Chumillas et al. who recorded lower EOR electroactivity at higher Pt loadings. They attributed these results to a lowered diffusion of the reactants in the internal parts of the electrocatalyst layer with increase of the metal loading [171]. Finally, the investigation on the influence of the electrocatalyst thickness on the EOR brought out the rise of the CO_2 current efficiency with the increase of the electrocatalyst thickness [42], an effect which is expected for complex and multiple-step reactions, such as the CO electrooxidation [174], ORR [175,176] and BOR [177,178].

III.1.2. Physical characterization

The metal loadings of the four Pt/C electrocatalysts, determined by TGA, ranged from 18.7 wt.% to 22 wt.%. A representation of their XRD-pattern is displayed in Fig. 13.

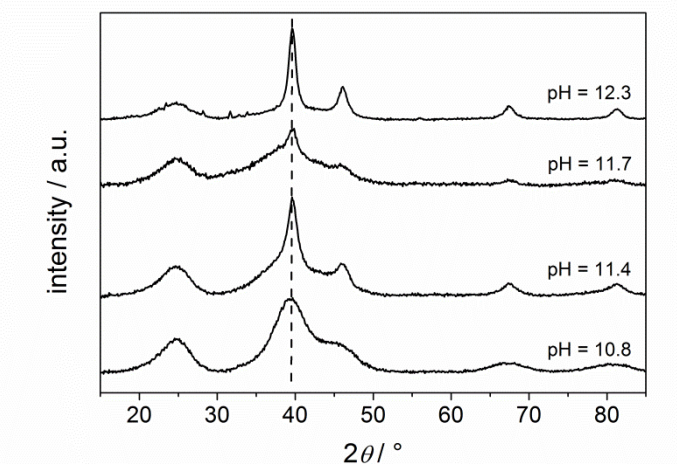

Fig. 13. XRD pattern of the carbon supported Pt/C electrocatalysts prepared by Polyol method at pH = 12.3, 11.7, 11.3 and 10.7.

III.1.3. Effect of the mass-transport

The influence of the mass-transport on the potentiodynamic ethanol electrooxidation was investigated by means of RDE. Fig. 14 displays cyclic voltammetries in 0.5 M H_2SO_4 + 0.1 EtOH on Pt/C at different rotation speeds: ω = 0, 100, 225, 400, 900, 1600, 2500 rpm. Three separate current rises are attributed to the EOR: the first one between E = 0.3 and 1 V *vs.* RHE, a second one at E > 1.1 V *vs.* RHE and a last one located between E = 0.8 and 0.4 V *vs.* RHE during the cathodic scan.

It can be observed that the current between E = 0.3 and 0.85 V *vs.* RHE increases together with the rise of the rotation speed. The reactions occurring in this potential range are mass-transport limited. Besides, the potential of the peak current ($I_{p,a1}$) shifts toward lower values with the rise of the rotation speed. This phenomenon, also observed for formic acid and formaldehyde, is however opposite to the methanol oxidation reaction (MOR) [179]: the different behavior of the methanol electrooxidation is attributed to an enhancement of the formaldehyde formation over the CO_2 production in increased mass-transport conditions, which thus induce a reduction of the number of exchanged electrons.

Interestingly, a non-linear dependence of the peak curren t between E = 0.3 and 1 V *vs.* RHE ($I_{p,a1}$) and between E = 0.8 and 0.4 V *vs.* RHE ($I_{p,c}$) against the square root of the rotation speed is observed in Fig. 14b. This result was expected and illustrates the complexity of the ethanol electrooxidation (inducing slow kinetics), which is a multi-step reaction

yielding up to 12 electrons. In particular, the reaction rate may not only depend on the access to bulk reactant (linear behavior of the "limiting current" *vs.* $\omega^{1/2}$, Levich equation) but also to the formation/desorption/poisoning of adsorbed species, therefore giving this peculiar behavior (quasi-absence of limiting current, presence of multiple peaks with activation/inhibition regions).

The oxidation current at E > 1.1 V *vs.* RHE does not observe the same tendency. Besides a rise of the peak current between ω = 0 and 100 rpm, the current remains quasi-constant independently of the electrode rotation. Actually, it reaches a threshold at 100 rpm which does not vary with increasing rotation speeds. This trend shows that the reaction occurring in this potential region is independent on the electrolyte mass-transport and likely corresponds to the electrooxidation of ethanol adsorbates which cannot oxidize between E = 0.3 and 0.9 V *vs.* RHE. Indeed, it is hardly believable that some new species adsorbed at E = 1.1 V *vs.* RHE on the fully blocked electrocatalyst surface (mostly by OH-adsorbates but also by ethanol adsorbates formed at lower potential values). The presence of strong ethanol adsorbates oxidizing only at E > 0.9 V *vs.* RHE has been demonstrated in [17,38,72].

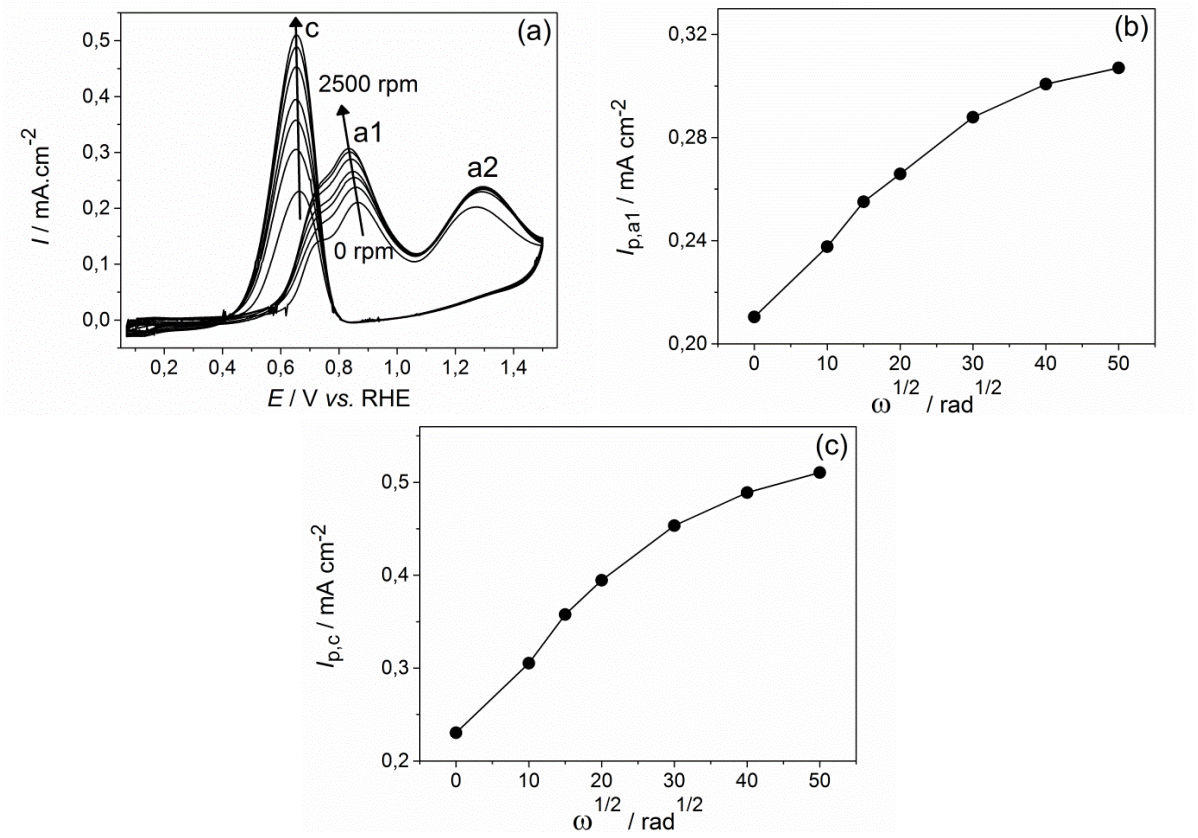

Fig. 14. (a) CV in 0.5 M H_2SO_4 + 0.1 EtOH on Pt/C (metal loading: 9.9 μg) on a RDE at different rotation speeds: 0, 100, 225, 400, 900, 1600, 2500 rpm; Evolution of the peak current between (b) E = 0.3 and 1 V *vs.* RHE ($I_{p,a1}$) and between (c) E = 0.8 and 0.4 V *vs.* RHE ($I_{p,c}$) against the rotation speed; v = 10 mV s^{-1}; T = 25°C.

III.1.4. Influence of the electrocatalyst thickness

III.1.4.1. Thickness determination

The electrocatalyst thickness (L) was evaluated assuming a uniform deposition on the electrode surface and following the relation proposed by Gloaguen et al. [180]:

$$\frac{\gamma}{L} = (1 - \theta)\, \rho\, m\, S \times 10^4 \qquad \text{Eq. III.1}$$

with L the electrocatalyst thickness, γ the ECSA / geometric area ratio, θ the Nafion volume fraction (in the present experiments, $\theta = 0.42$), ρ the electrocatalyst powder density ($\rho = 2.2$ g cm^{-3}), m the electroactive mass fraction in the electrocatalyst powder (m = 20 wt. %) and S the specific electrocatalyst area (ECSA / metal mass ratio). Table 3 summarizes the parameters used for the determination of the thickness.

Table 3. Structural parameters of the electrocatalyst

Metal loading / μg	ECSA / cm^2	Specific area (S) / m^2 g^{-1}	Thickness (L) / μm
19.8	9.79	49.4	10.8
14.9	6.67	44.9	8.1
9.9	4.79	48.4	5.4
4.95	2.52	50.1	2.7

III.1.4.2. Effect of the thickness on the EOR

III.1.4.2.1. DEMS

Fig. 15 shows the potentiodynamic EOR in 0.5 M H_2SO_4 + 0.1 M EtOH and the corresponding mass-to-charge signals m/z = 29, 22 and 61 on the same Pt/C electrocatalyst with a different thickness layer: 10.8, 8.1, 5.4 and 2.7 μm.

Fig. 15a shows that the intensity of the peak current at *ca.* E = 0.8 V *vs.* RHE rises with the decrease of the electrocatalyst thickness; I_p (L = 2.7) > I_p (L = 5.4) > I_p (L = 8.1) > I_p (L = 10.8). The same tendency can be seen in Fig. 15b where the CVs are normalized by the ECSA, which discards any experimental uncertainties (the normalization by the ECSA was kept in Fig. 15c and Fig. 15d). In Fig. 15c, the mass-to-charge signal m/z = 29 follows the same trend and shows that the higher currents is due to a higher acetaldehyde formation. Looking at the normalized mass-to-charge signal m/z = 22 displayed in Fig. 15d, the amount of CO_2 generated during the EOR remains almost unchanged depending on the electrocatalyst

thickness. As a consequence, the lower faraday currents reported in Fig. 15a and Fig. 15b on thicker electrocatalysts combined to the similar CO_2 generation reported in Fig. 15d shows qualitatively that the amount of ethanol oxidizing completely into CO_2 is higher on thicker electrocatalysts.

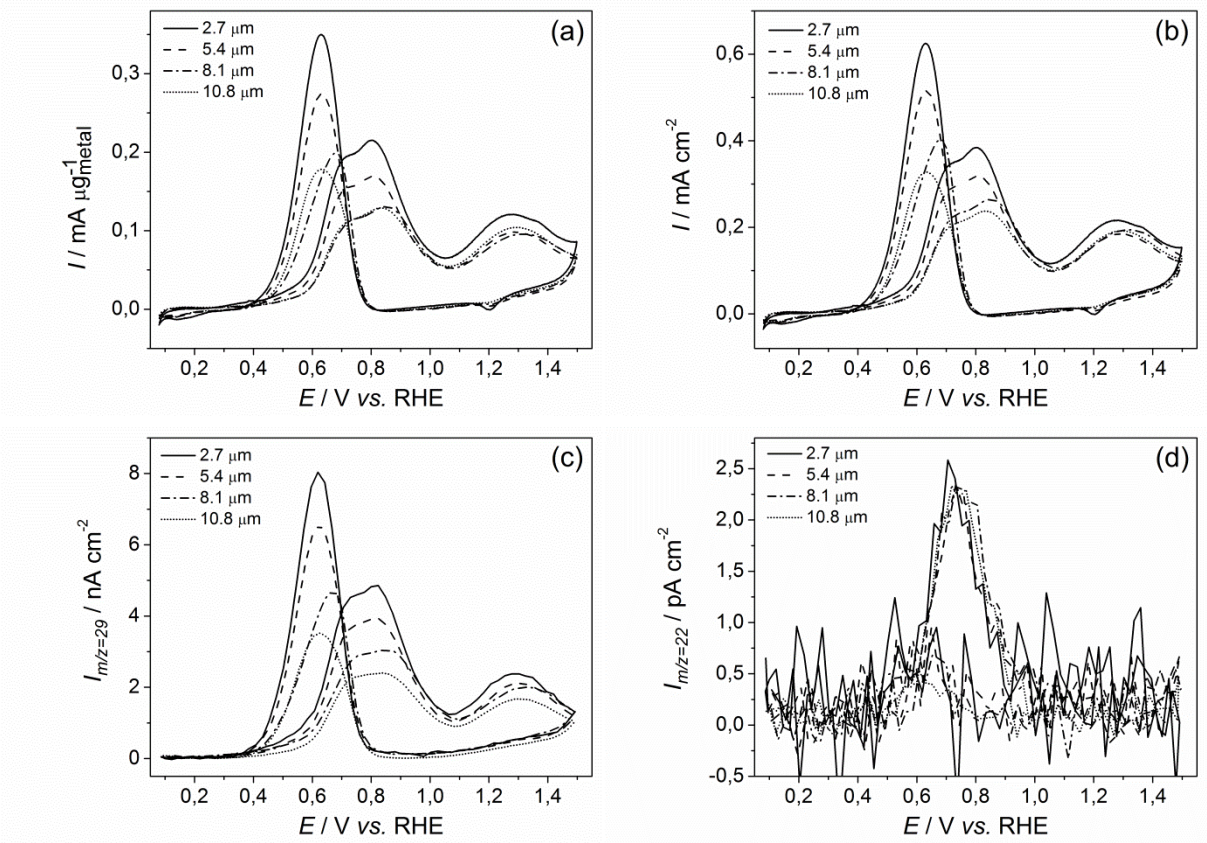

Fig. 15. (a) CV of the EOR in 0.5 M H_2SO_4 + 0.1 M EtOH on Pt/C (L = 2.7, 5.4, 8.1 and 10.8 μm) normalized by the (a) metal loading and (b) ECSA and corresponding MSCV for mass-to-charge ratio (c) m/z = 29 and (d) m/z = 22 (normalized by the ECSA); v = 10 mV s^{-1}; T = 25°C.

To confirm this tendency, the CO_2 current efficiency (CCE) was evaluated to quantify the amount of ethanol oxidizing completely into CO_2. Fig. 16 displays the evolution of the CCE *versus* the electrocatalyst thickness (Fig. 16a) and the applied potential (Fig. 16b). First and foremost, independently of the thickness, it can be seen that the highest CCE is reached for each thickness either at E = 0.6 V *vs.* RHE. At E > 0.6 V *vs.* RHE, the CO_2 generation starts shrinking. It can be assumed that above a certain potential, the ever-growing presence of OH-adsorbates and of remaining ethanol adsorbates discriminate the CO_2 formation over other simpler and faster reactions (acetaldehyde or acetic acid formation).

When comparing the CCE values obtained for different electrocatalyst thicknesses in Fig. 16a, the CCE is clearly increasing when the thickness gets larger. A similar trend was

found by Rao et al. during their MEA tests [42]. An improvement of the CCE due to the rise of the residence time with the electrocatalysts thickness is likely suggested by these results. Moreover, it is suggested that a longer residence time of the reaction products, and more particularly of acetaldehyde (which constitutes most of the produced species during the EOR), would favor the re-adsorption of the latter on the electrocatalyst surface which would oxidize to give CO_2.

It can finally be observed that although the complete ethanol electrooxidation is favored in thicker electrocatalysts, the current produced during the cyclic voltammetry does not increase, but actually decreases. This behavior, which could appear contradictory in regard to the number of electrons exchanged during the complete EOR to CO_2 (12 e^-) compared to the incomplete EOR (up to 4 e^-), can be explained by a weaker utilization of the electrocatalyst and more particularly by a hindered mass-transport of the electrolyte in the internal part of the electrocatalyst. Chumillas et al. found a similar trend for the formic acid electrooxidation and interpreted the lower electrooactivity to the dreadful mass-transport inside the electrocatalyst thickness [171].

However, this behavior can also be interpreted kinetically. The production of CO_2 coming from desorbed/re-adsorbed acetaldehyde (from the ethanol dehydrogenation step) is a kinetically slow reaction which occupies at least one electrocatalytic site. In comparison, ethanol dehydrogenation into acetaldehyde should be a kinetically fast reaction. As such, even if one adsorbed acetaldehyde molecule generates 10 electrons in the reaction leading to CO_2, the fast kinetics of the ethanol dehydrogenation may enable more than one ethanol molecule to dehydrogenate and deliver, in the end, more current per Pt electrocatalytic sites per unit of time. This assumption is supported by the fact that, when acetaldehyde re-adsorbs, the molecule oxidation leads to the generation of either CO_2 (*ca.* at E > 0.6 V *vs.* RHE) or acetic acid (*ca.* at E > 0.9 V *vs.* RHE). The last reaction is not only limited by the number of exchanged electrons (2 e^- for acetic acid formation instead of 10 e^- for CO_2 formation - see Eq. I.26 to Eq. I.29), but also by its high overpotentiel (the reaction starts at *ca.* E > 0.9 V *vs.* RHE). Finally, acetaldehyde re-adsorption may lead to more CO_2 production and to higher CCE values (see Fig. 16), but it may also contaminate the electrocatalyst surface, hinder the ethanol dehydrogenation and *in fine* impede the current generation (in other words, the Pt sites turnover frequency of ethanol oxidation into acetaldehyde may exceed by a large extent that of acethyaldehyde into further oxidized products, such as CO_2).

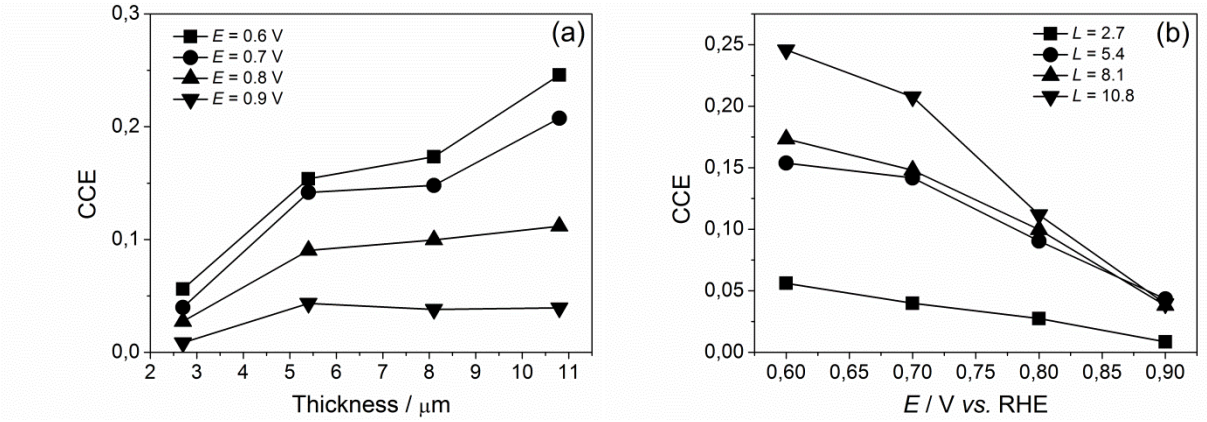

Fig. 16. Evolution of the EOR CO_2 current efficiency (CCE) against (a) the electrocatalyst thickness and (b) the applied potential calculated from cyclic voltammetries run in 0.5 M H_2SO_4 + 0.1 M EtOH (represented in Fig. 15a) and corresponding MSCVs (Fig. 15b) on Pt/C.

III.1.4.2.2. RDE

Fig. 17 displays comparative RDE CVs carried out in 0.5 M H_2SO_4 + 0.1 M EtOH on the same Pt/C electrocatalyst with various layer thicknesses (L = 10.8, 8.1, 5.4 and 2.7 μm) at different rotation speeds: ω = 0 rpm (Fig. 17a), 400 rpm (Fig. 17b) and 2500 rpm (Fig. 17c). Similarly to what was observed in the DEMS study, the current seems to drop against the rise of the thickness of the electrocatalyst layer, although the difference is not as marked as in Fig. 15. More specifically, the peak current values are almost the same for thickness layers between L = 2.7 and 8.1 μm, but are distinctly lower for L = 10.8 μm. This observation is confirmed in Fig. 18, which displays the evolution of the peak current against the square root of the rotation speed. Besides, the peak current values during the anodic and cathodic scan seem to be more sensitive to the effect of the mass-transport at low thickness layers than at high ones, which induce a larger gap of the peak current between the layer at L = 10.8 μm and the other three at ω = 2500 rpm. This tendency shows that the lower EOR electroactivity in the thickest layer of electrocatalyst may not be due to some mass-transport limitation inside the thick layer (as it was proposed for the DEMS study). On the contrary, the increase of the rotation speed, which quickens the supply of bulk ethanol to the electrocatalyst surface, may intensify the poisoning of the electrocatalyst. Indeed, the enhancement of the mass-transport will help supply fresh bulk ethanol species to the electrocatalytic sites freed during the electrooxidation reactions. However, as the ethanol dehydrogenation is enhanced due to the better mass-transport conditions, it will also accelerate the re-adsorption of acetaldehyde, which slowly produces CO_2 and which block during this time Pt sites for other ethanol dehydrogenation reactions. Yet, as seen in the previous section, thick layers of electrocatalyst are believed to promote the re-adsorption/oxidation of acetaldehyde into CO_2. As such, the

acceleration of the scan rate enhances more ethanol dehydrogenation on thin catalyst layers whereas it will favor the poisoning on thick layers.

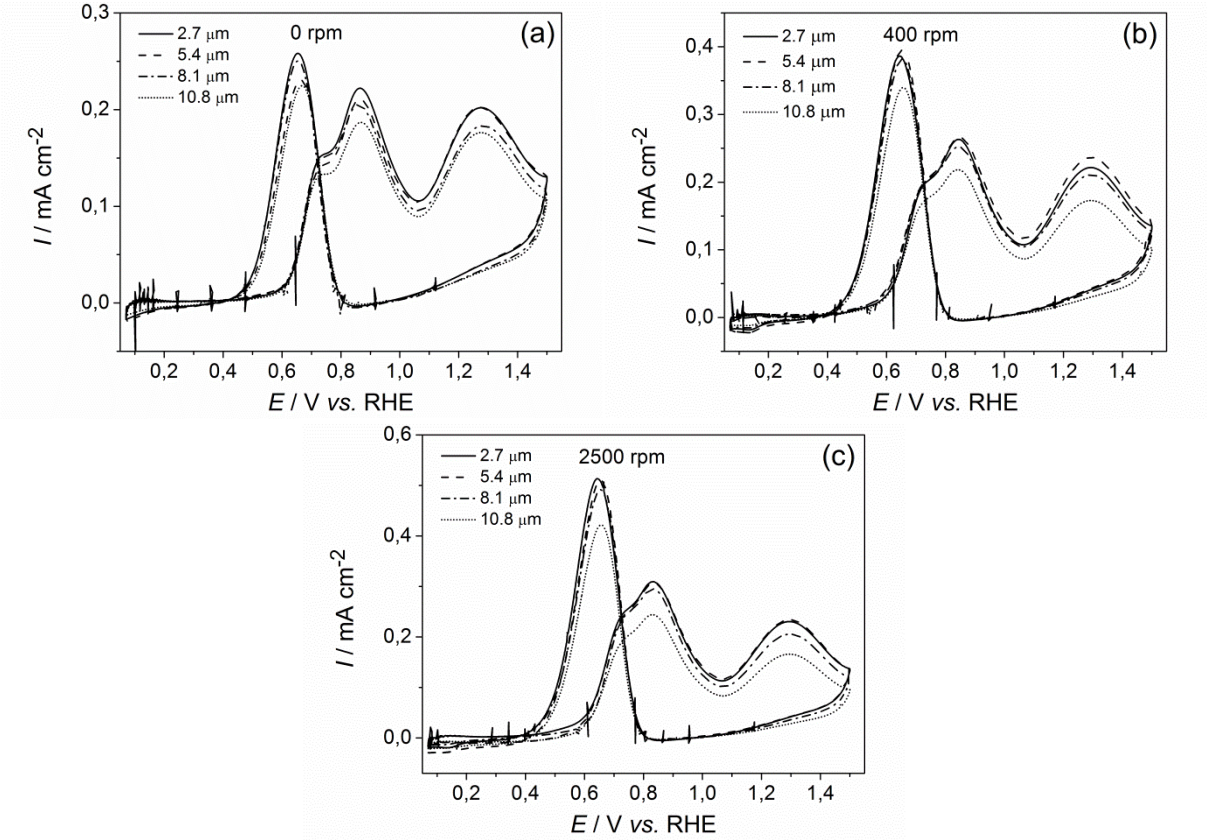

Fig. 17. CV in 0.5 M H_2SO_4 + 0.1 EtOH on Pt/C (L = 2.7, 5.4, 8.1 and 10.8 μm) on a RDE at different rotation speeds: ω = (a) 0, (b) 400 and (c) 2500 rpm; v = 10 mV s^{-1}; T = 25°C.

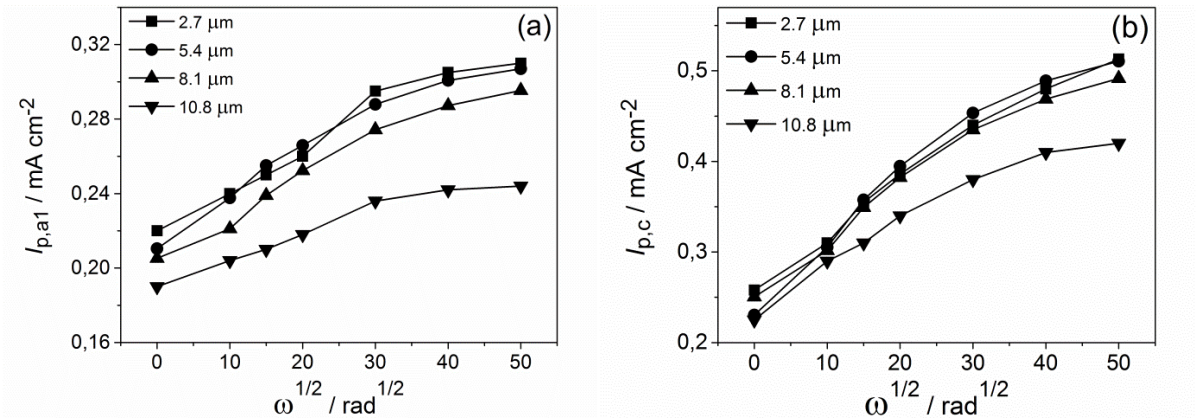

Fig. 18. Evolution of the peak current between (a) E = 0.3 and 1 V *vs.* RHE and (b) E = 0.8 and 0.4 V *vs.* RHE against the rotation speed.

Chronoamperometries were also carried out at E = 0.7 V *vs.* RHE in order to verify if the trend observed in potentiodynamic conditions is the same in potentiostatic ones. This potential was chosen as the CCE is quite high and the CO_2 formation happens quantitatively (according to the DEMS study). Fig. 19 shows the CAs run at ω = 0, 100, 225, 400, 900, 1600 and 2500 rpm on Pt/C at different thickness layers: L = 2.7, 5.4, 8.1 and 10.8 μm. Regarding the results obtained in potentiodynamic conditions, a constant rise of the current against the increase of the RDE rotation, as well as against the decrease of the thickness layer would have been expected. However, as it can be more clearly viewed in Fig. 20, which describes the evolution of the current recorded at the end of the CA (t_f = 630 s) at E = 0.7 V *vs.* RHE, no such trend is observed. Indeed, unlike the cyclic voltammograms where the highest currents were reached on the thinnest electrocatalyst, the highest current values are obtained on the thickest electrocatalyst under the potentiostatic conditions. Moreover, the rotation speed at which the maximum current is reached on each electrocatalyst is dependent on the layer thickness: the maximum current is reached at ω = 100, 225, 900, 1600 rpm for the layers thickness of L = 2.7, 5.4, 8.1 and 10.8 μm respectively.

More precisely, the evolution of the current against the rotation speed can be separated in two regions: a first one, at low rotation speeds, where the current is in an ascending phase, and a second one at higher rotation speeds, where the current slowly decreases or stabilizes. The limits of the first region, defined by the maximal current value, depend highly on the electrocatalyst thickness and shifts to higher rotation speeds *versus* the increase of the thickness layer: at L = 2.7 μm, the highest current value is reached at ω = 100 rpm against ω = 1600 rpm at L = 10.8 μm. Similarly, the amplitude of the current increase, in this first rotation speed region, is also dependent on the electrocatalyst thickness layer: the thicker the layer, the larger the current rise. In the second rotation speed region, the current decreases steeper for the lowest thickness layers and more slowly for the thickest layers. This tendency demonstrates that the thicker the electrocatalyst layer, the more positive the current response to the improved mass-transport conditions. In this case and contrary to what was observed under potentiodynamic conditions (RDE and DEMS), it can be assumed that, while the enhanced mass-transport of the electrolyte (by rotation of the disc-electrode) improved its supply inside the electrocatalyst thickness, the potentiostatic conditions favored ethanol complete oxidation into CO_2. Indeed, E = 0.7 V *vs.* RHE corresponds to a potential at which the CCE is quite high and the CO_2 formation happens quantitatively. However, although this explanation could justify the rise of the current, when the rotation speed increases for the thickest layer of electrocatalyst, it does not take into account the drop of the current by faster rotation speed for the thinnest electrocatalysts. For this reason, results in Fig. 19 and Fig. 20 are tentatively attributed to the enhanced poisoning of the thiner layers, a poisoning which is (independently of the thickness of the electrocatalyst) intensified when the rotation speed rises, *i.e.* when the experimental conditions become stationnary.

Unfortunately, the opposite behaviors between the cyclic voltammograms (Fig. 15 and Fig. 17), where the thicker layers of electrocatalyst demonstrated more dramatic poisoning,

and the chronoamperograms (Fig. 19), where the thinner layers were the most poisoned, could not be rationalized to date.

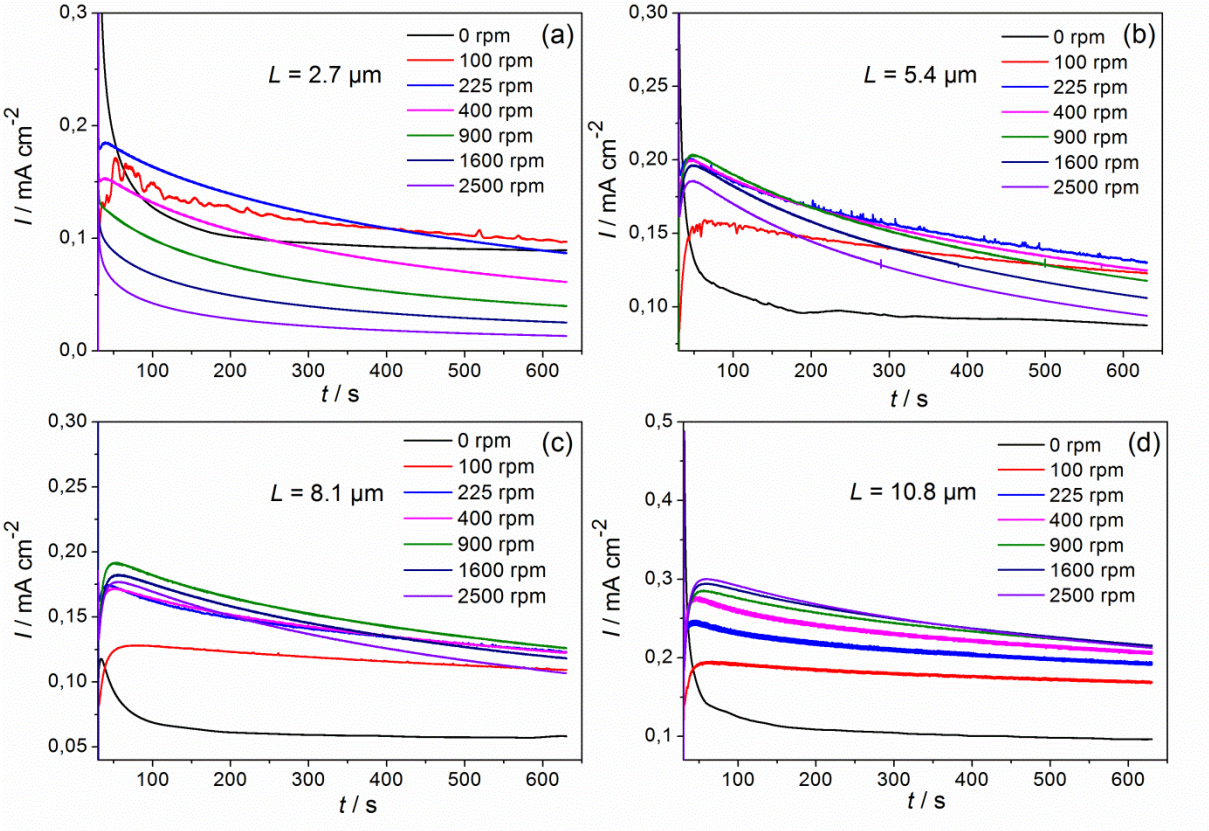

Fig. 19. CA on a RDE at different rotation speeds (ω = 0, 100, 225, 400, 900, 1600 and 2500 rpm) in 0.5 M H_2SO_4 + 0.1 EtOH on Pt/C at different thickness layers: L = (a) 2.7, (b) 5.4, (c) 8.1 and (d) 10.8 µm; v = 10 mV s^{-1}; T = 25°C.

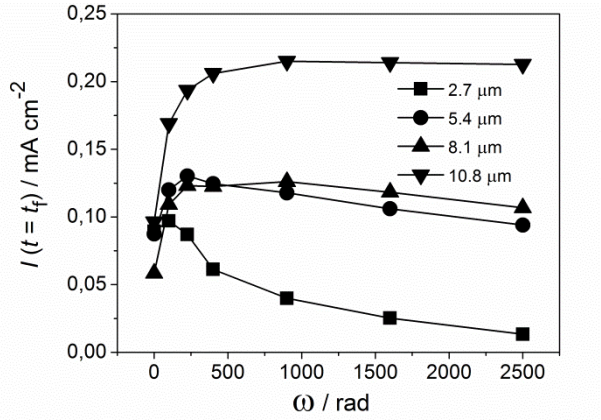

Fig. 20. Evolution of the potentiostatic current (CA at E = 0.7 V *vs.* RHE) recorded at t_f = 630 s against the rotation speed.

III.1.5. Effect of the scan rate

III.1.5.1. CO-stripping CVs

Fig. 21 compares substracted CO-stripping CVs in 0.5 M H_2SO_4 at υ = 2, 5 and 10 mVs^{-1}. The CVs have been amplified in order to take into account the influence of the scan rate on the current [181]. The rise of the sweep rate from υ = 2 mV s^{-1} to 10 mV s^{-1} results in a positive shift of the CO-stripping onset and peak potential, in agreement with the literature [181–183]. Moreover, a similar trend was found in Fig. 21c by use of the mass-to-charge ratio m/z = 22 (ascribed to CO_2). According to Maillard et al., the onset potential of the CO-stripping at υ = 2 mV s^{-1} is close to the equilibrium potential of the OH_{ad} formation [181]. However, as the scan rate increases and the reactions take place deeper in non-stationary conditions, the onset potential, which is believed to be controlled by CO_{ad} + OH_{ad} interactions, shifts positively due to the low mobility of the CO_{ad} on Pt surface, and more particularly Pt terraces.

Besides the potential onset, a sharper soar of the ascending current can also be observed in Fig. 21a and Fig. 21b at low scan rates giving the CO-stripping ascending and descending part a more symmetric profile. The apparent slower kinetics at υ = 10 mV s^{-1} against υ = 2 mV s^{-1} can be induced by the slow diffusion of the CO_{ad} on the Pt surface, as the latter is believed to limit the reaction kinetics of the CO-stripping reaction [181], or by the limiting water dissociation [184].

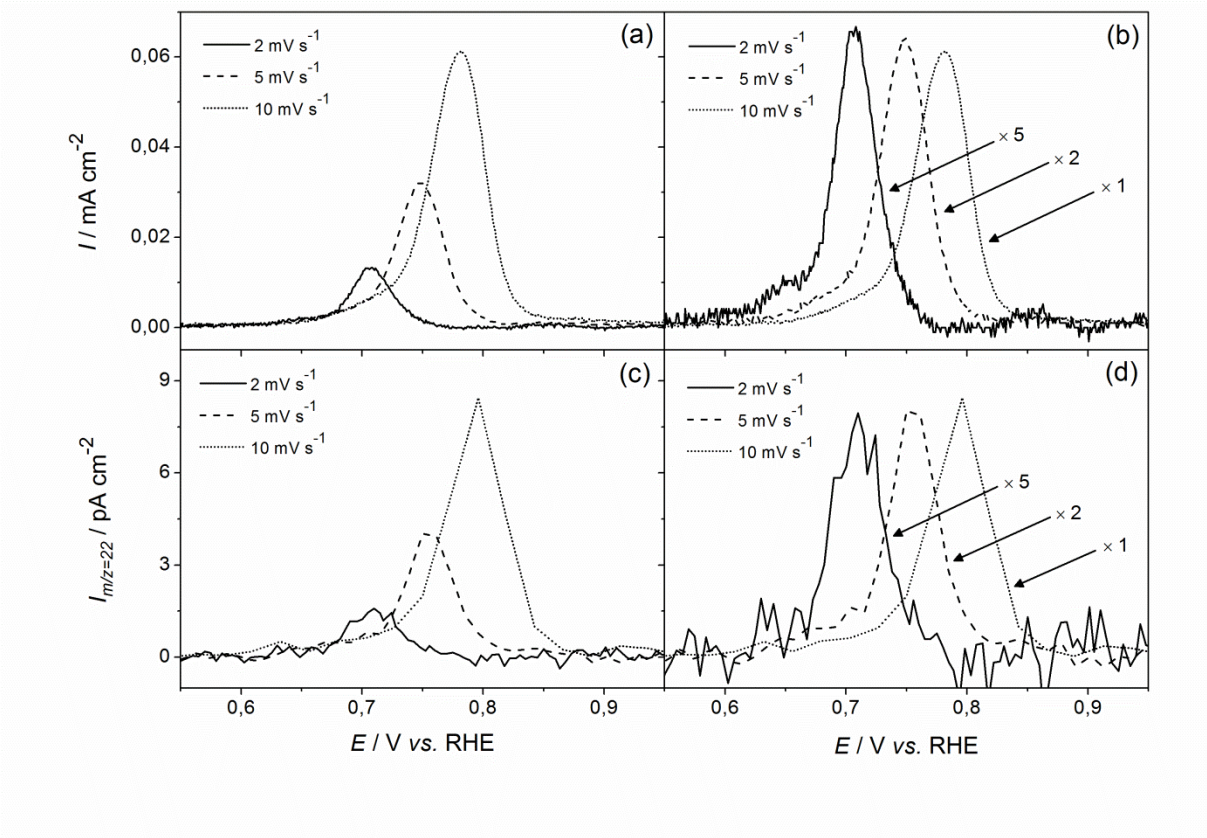

Fig. 21. Substracted (a) non-amplified and (b) amplified CO-stripping CVs in 0.5 M H_2SO_4 on Pt/C (metal loading: 9.9 µg) and corresponding (c) non-amplified and (d) amplified MSCVs for mass-to-charge ratio m/z = 22 multiplied by a number indicated in brackets; T = 25°C.

III.1.5.2. EOR CVs

Fig. 22 displays cyclic voltammograms of the EOR performed at different scan rates: ν = 2, 5 and 10 mV s^{-1} on Pt/C. A usual increase of the peak current, as well as a positive shift of the peaks potential, at *ca.* E = 0.86 V *vs.* RHE and E = 1.3 V *vs.* RHE against the scan rate can be observed in Fig. 22a. The associated mass-to-charge signals m/z = 29 (acetaldehyde) and m/z = 22 (CO_2) are represented in Fig. 22b and Fig. 22c. The feature of the signal m/z = 29 is similar to the CV in Fig. 22a, showing that the generated current mainly corresponds to ethanol dehydrogenation into acetaldehyde. The signal m/z = 22 represented in Fig. 22c seems also to depend on the scan rate. The dashed line centered on the ionic peak current at ν = 5 mV s^{-1} helps discerning a shift of the peak current toward lower potentials with the decrease of the scan rate: the peak potential is located at *ca.* E = 0.65, 0.70 and 0.71 V *vs.* RHE at ν = 2, 5 and 10 mV s^{-1} respectively. This trend shows that the CO_2 generation gets hindered at lower potential when the experimental conditions are quasi-stationary. This hindrance is likely

caused by the adsorption of poisoning species which occupy the electrocatalytic sites and prevent from the dissociative ethanol adsorption, mandatory for any CO_2 generation. The low scan rate would give them more time to block the electrocatalystic surface at lower potential than in non-stationary conditions. These adsorbates are most probably ethanol adsorbates and hydroxide species. The behavior of the CO_2 production during the EOR contrasts with the electrooxidation of adsorbed CO using the mass-to-charge signal m/z = 22. Indeed, although the peak potential of the CO_2 generation depends on the scan rate similarly to the CO-stripping, the extent of the shift is much lower in the case of the EOR and finds other causes: The CO-stripping peak current is attributed to a lack of CO_{ad}-species at the electrocatalyst surface (progressive consumption on the CO_{ad} monolayer, half of it being removed at the CO-stripping peak) whereas the CO_2 peak of the EOR in Fig. 22c is likely due to the poisoning of the surface by ethanol and hydroxide adsorbates. Besides, the positive shift of the CO-stripping initiation with the rise of the scan rate is attributed to CO slow mobility, while the onset potential of the CO_2 formation during the EOR (Fig. 22c) seems to remain constant. This independence of the reaction initiation against the scan rate shows that the reaction is not limited by CO mobility (like in a CO-stripping), but probably by the C-C bond cleavage or the supply in hydroxide species.

An interesting trend can be noticed when comparing the two peak currents of the anodic sweep at *ca.* E = 0.86 V *vs.* RHE and E = 1.3 V *vs.* RHE. Indeed, the ratio $I_{p,a1}$ / $I_{p,a2}$ decreases with the rise of the scan rate: $I_{p,a1}$ / $I_{p,a2}$ = 2.03, 1.62 and 1.38 at υ = 2, 5 and 10 mV s^{-1} respectively. This relative evolution of the two peak currents against the scan rate is assigned to a lower increase of $I_{p,a1}$ than to a larger one of $I_{p,a2}$ with the rise of the scan rate and is rather explained by slow reaction kinetics than a slow species diffusion. The first reason is privileged, as a scan rate of ν = 10 mV s^{-1} still allows quasi-stationnary conditions and should be slow enough to avoid mass-transport limitations by diffusion. Moreover, as the current issued from ethanol complete electrooxidation into CO_2 represents a larger part of the total current at ν = 10 mV s^{-1} than at ν = 2 mV s^{-1} (see CCE values in Fig. 23), the slow kinetics of the reaction should be responsible for the lower increase of $I_{p,a1,}$ when the scan rate rises.

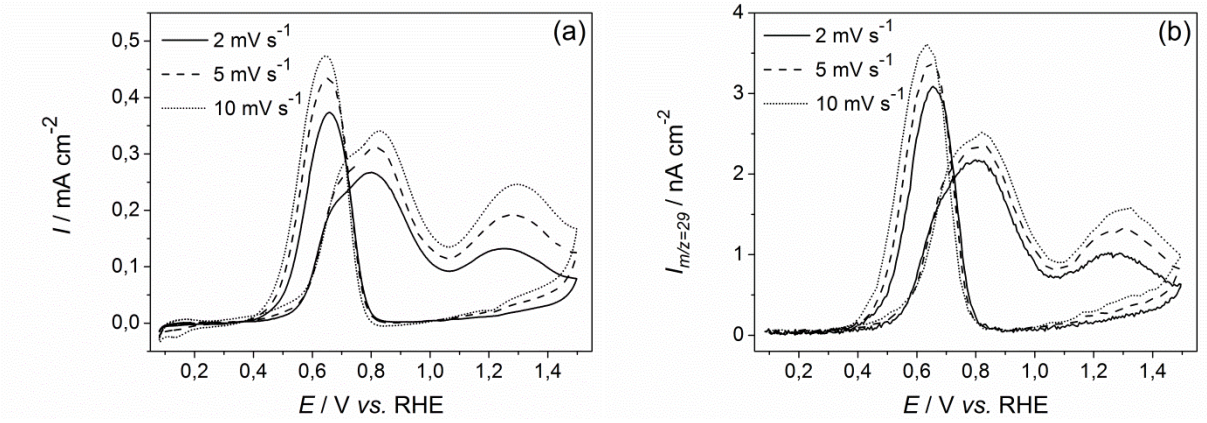

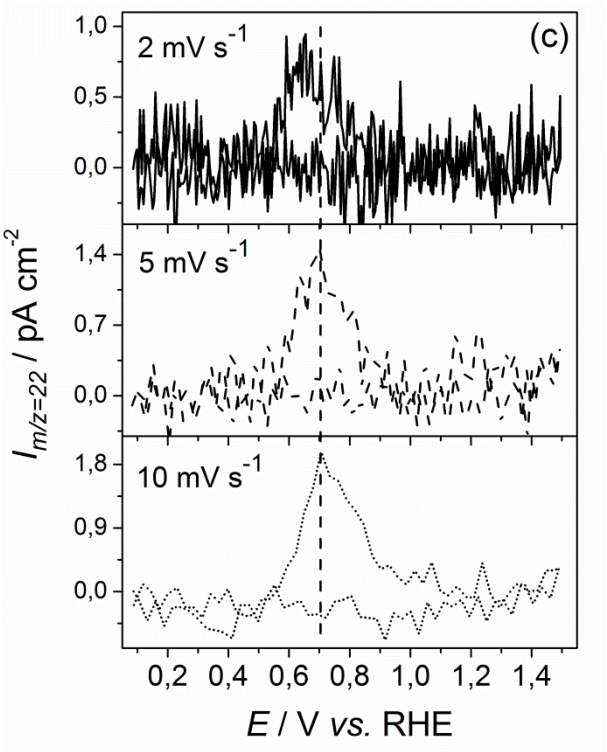

Fig. 22. (a) CV of the EOR in 0.5 M H_2SO_4 + 0.1 M EtOH on Pt/C and corresponding MSCV for mass-to-charge ratio (b) m/z = 29 and (c) m/z = 22; at v = 2, 5 and 10 mV s^{-1}; T = 25°C.

The evolution of the CCE against the potential is represented in Fig. 23. The drop of the CCE *versus* the rise of the applied potential has already been observed in Fig. 16b and was attributed to the growing contamination of the electrocatalyst surface by ethanol and hydroxide adsorbates, which hinders the dissociative adsorption of ethanol. The maximal value obtained at E = 0.6 V *vs.* RHE is very similar for each scan rate, which rules out its influence (at least between υ = 2, 5 and 10 mV s^{-1}) on this value. This result contrasts with what was expected. Indeed, ethanol adsorbates stripping studies have shown that the C-C bond breaking can occur at potentials as low as E = 0.05 V *vs.* RHE [38,185] (more details in section V). As such, a longer time between E = 0.07 (CV initial potential) and E = 0.6 V *vs.* RHE (CO_2 generation initiation), induced by a slower scan rate of the CV, was expected to enhance ethanol dissociative adsorption and boost the amount of CO-like adsorbates at the electrocatalyst surface at the beginning of the CO_2 generation. At $E \geq 0.7$ V *vs.* RHE, the degree at which the CCE decreases against the potential is rather different depending on the sweep rate: the CCE at E = 0.7 V *vs.* RHE is twice lower at υ = 2 mV s^{-1} (CCE = 0.09) than at υ = 10 mV s^{-1} (CCE = 0.18). This is explained by the blockage of the electrocatalyst surface at lower potentials by the mentioned poisoning adsorbates due to the lower scan sweep, which gives more time to the process to operate.

Finally, it would have been of interest to lead this study at higher scan rates, to see wether the trend observed under quasi-stationary conditions were confirmed under non-

stationary ones. However, higher scan rates would have led to longer delays between the CVs and MSCVs and would have corrupted the reliability of the results.

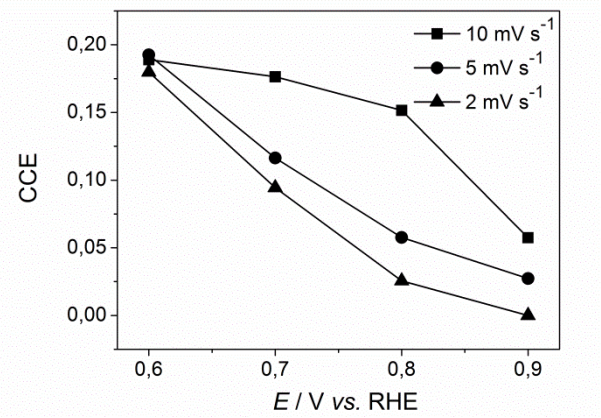

Fig. 23. CO_2 current efficiency (CCE) values calculated from cyclic voltammetries run in 0.5 M H_2SO_4 + 0.1 M EtOH (represented in Fig. 22a) at ν = 2, 5 and 10 mV s^{-1} and corresponding MSCVs (Fig. 22b) on Pt/C.

III.1.6. Discussions

As particularly seen in this investigation, the potentiodynamic electrooxidation of ethanol (in 0.5 M H_2SO_4 + 0.1 M EtOH) presents two different oxidation regions during the positive scan: one between *ca.* E = 0.4 and 1.1 V *vs.* RHE and a second one between E = 1.1 and 1.5 V *vs.* RHE. In most studies present in the literature, the attention is paid on the first oxidation, as this is of higher interest for fuel cell applications (it gives an idea of the DEFC performances and of the work still to accomplish to reduce the anodic overpotential). However, almost no discussion was undertaken about this second oxidation at high potential [186]. Its study is of importance as it suggests the presence of "strong ethanol adsorbates" on the electrocatalyst surface, which cannot oxidize at lower potentials, as it is suspected from the results in Fig. 14, which shows a quasi non-dependence of the reaction on mass-transport effects. An attempt to identify the reaction occurring at E > 1.1 V *vs.* RHE and the species involved in this reaction will be undertaken.

As observed in Fig. 15 and in the literature [32,71,98,99], the main reaction products detected by mass spectrometry during the second oxidation of the anodic scan correspond to acetaldehyde and ethyl acetate (CO_2 does not seem to be produced or, at least, not quantitatively). Their formation is however not evidenced during ethanol adsorbates stripping-CVs [38,185]. If the adsorbates were indeed the same between the EOR CVs and adsorbates stripping-CVs, this would suggest that the adsorbates react with bulk ethanol to produce acetaldehyde and ethyl acetate. A possibility would be that ethyl acetate (m/z = 61) is formed through a one-step reaction:

"Strong adsorbate" + $CH_3CH_2OH_{sol} \rightarrow CH_3COOCH_2CH_{3,sol}$ Eq. III.2

This assumption suggests that the volatile species observed with the signals m/z = 15, 29, 44 (detected simulatenously to m/z = 61, at least at high potential) correspond to the fragments of ethyl acetate only. This is not in contradiction with the ethyl acetate MS spectrum shown in [187], although the signal m/z = 44 is very low on the spectrum in comparison to the other signals.

A second possibility is that Eq. III.2 takes place in two steps, *via* the formation of acetic acid (as the latter is detected by IR-techniques – see section I.6.3) which further reacts with bulk ethanol (Eq. III.3 - Eq. III.4) and, simultaneously, acetaldehyde formation and further reaction, once in the solution, with ethanol to produce ethyl acetate (Eq. III.5 - Eq. III.6):

"Strong adsorbate" + $OH_{ad} \rightarrow CH_3COOH_{sol}$ Eq. III.3

$CH_3COOH_{sol} + CH_3CH_2OH_{sol} \rightarrow CH_3COOCH_2CH_{3,sol}$ Eq. III.4

"Strong adsorbate" + $OH_{ad} \rightarrow CH_3CHO_{sol}$ Eq. III.5

$CH_3CHO_{sol} + CH_3CH_2OH_{sol} \rightarrow CH_3COOCH_2CH_{3,sol}$ Eq. III.6

If acetic acid and acetaldehyde are indeed produced at high potentials (before being consumed in the solution), their formation reaction (Eq. III.3 and Eq. III.5 respectively) should be realizable in stripping conditions (OH_{ad} is solely required). Yet, no ethyl acetate and no acetaldehyde are detected during the stripping-CVs, which could discard Eq. III.3 to Eq. III.6. However, a possible diffusion and re-organisation of the ethanol adsorbates on the electrocatalyst surface during the potentiostatic step in 0.5 M H_2SO_4 preceeding the stripping-CV (more details on the experimental protocol in section V and in [38,185]) is not excluded and could result in the existence of different ethanol adsorbates between the potentiodynamic ethanol electrooxidation and the ethanol adsorbates stripping-CVs.

Although the characterization techniques (DEMS, RDE) used in this work do not allow a proper identification of such "strong ethanol adsorbate(s)", this topic will be discussed in the light of the literature and particularly of a study from Iwasita et al. [29].

As written in section I.6.3, Iwasita et al. [29] proposed four different ethanol adsorbates which were illustrated in Fig. 4. As (=CHOH-CH_3) ((d) in Fig. 4) represents only 5 % of the overall ethanol adsorbates, this adsorbate will not be considered as candidate for the "strong ethanol adsorbate(s)".

Among the three other candidates, it is hardly believable that an adsorption by an O-atom ((b) in Fig. 4) leads to any acetaldehyde formation during the EOR at 0.3 < E < 0.9 V *vs.*

RHE. Indeed, the bonds Pt-O and O-C prevent the formation of the double bond C=O characteristic of the acetaldehyde. It is more likely that an adsorption by the C-atom generates acetaldehyde: (-CO-CH_3) would be a good candidate ((c) in Fig. 4). The adsorption by the C-atom would make ethyl acetate generation easier: the sole OH_{ad} presence at proximity of the adsorbed molecule would be necessary for the reaction. Regarding the O-atom electronegativity, it is also conceivable that the adsorption by the O-atom is more stable than by a C-atom. Moreover, the ethyl group in (–OCH_2-CH_3) is also relatively stable. As such, it is conceivable that (–OCH_2-CH_3) oxidizes at higher potentials than (-CO-CH_3) and that it corresponds to the "strong ethanol adsorbate" in Eq. III.3 to Eq. III.6. The relative stability of the (–OCH_2-CH_3) adsorption mode is believed to grow always more unstable with the potential rise and to start reacting at E > 1.1 V *vs.* RHE in order to produce ethyl acetate (as seen in Eq. III.7):

$$-OCH_2CH_3 + CH_3CH_2OH \rightarrow CH_3COOCH_2CH_3 \qquad \text{Eq. III.7}$$

Finally, the formation of acetaldehyde at E > 1.1 V *vs.* RHE as proposed in Eq. III.5 seems unlikely because of the reasons stated earlier: the bond Pt-O and O-C hinder the formation of the acetaldehyde double bond characteristic. A one-step production of ethyl acetate (Eq. III.2) is believed to take place, but a formation in two steps *via* an intermediate acetic acid generation (Eq. III.3 and Eq. III.4) is not discarded.

III.1.7. Conclusions

The influence of Pt electrocatalysts structure, and more specifically the thickness, on the EOR was investigated. In parallel, the effects of the mass-transport by RDE (convection) and of the scan rate (diffusion) on the EOR were studied.

The nanoparticle average diameters were estimated by XRD and CO-stripping (TEM could not be performed to verify these figures). The electrocatalyst thickness estimation completed the physical characterisation.

The study of the electrocatalyst thickness reveals qualitatively and quantitatively that a larger amount of ethanol oxidizes completely into CO_2 in thicker layers of electrocatalyst. A longer residence time likely enhances the further adsorption and electrooxidation of produced acetaldehyde into CO_2. However, the generated faraday current decreases with the rise of the layer thickness which is believed to be due more to a stronger gradual poisoning of the thick layers than to a non-optimized utilization of the electrocatalyst.

The variation of the scan rate showed a contamination of the electrocatalyst surface enhanced at low scan rate, which hinders dramatically the CO_2 formation. Comparisons between the CO-stripping and the EOR showed that the reactions were likely limited by different phenomena.

III.2. Effect of Rh- and Sn- addition on the Pt-based electrocatalyst on the EOR

III.2.1. Physical characterization

Representative XRD spectra of the carbon-supported Pt/C, Rh/C, Pt-Rh/C, Pt-SnO_2/C and Pt-Rh-SnO_2/C electrocatalysts are displayed in Fig. 24. The sharpness of Pt/C and Pt-Rh-SnO_2/C patterns show well crystallized nanoparticles. The diffraction peaks of Pt/C at *ca*. 40, 46.5, 67.8, 82, 86 are assigned respectively to the (111), (200), (220), (311), (222) planes, characteristic of a face-centered cubic (fcc) structure. Rh/C and Pt-based bi- and tri-metallic electrocatalysts were also found to crystallize in the fcc structure. An evaluation of the average particle size was carried out using the Scherrer's law on the (111) diffraction peak. The lattice parameters and the average particle sizes are summarized in Table 4.

Pt/C and Rh/C are loaded at 20 wt. % and 21.1 wt. %, respectively, as revealed by TGA. ICP-AES analyses showed the presence of 17.07 wt.% Pt and 7.46 wt.% Rh for Pt-Rh/C (24.5 wt.% $Pt_1Rh_{0.8}$/C), 15.01 wt.% Pt and 2.69 wt.% SnO_2 for Pt-SnO_2/C (17.7 wt.% $Pt_1(SnO_2)_{0.8}$/C) and 13.38 wt.% Pt, 4.03 wt.% Rh and 2.73 wt.% SnO_2 for Pt-Rh-SnO_2/C (20.14 wt.% $Pt_1Rh_{0.58}(SnO_2)_{0.35}$/C).

The electrocatalysts morphology and the particle size distribution (PSD) were further characterized by TEM. Fig. 25 displays a uniform dispersion of relatively small nanoparticles on the carbon support for most of the electrocatalysts. Yet, the TEM investigation on Pt-SnO_2/C revealed the presence of larger nanoparticles. The associated PSD histograms in Fig. 25 reveal a narrow particle size distribution with a very similar mean particle size for the electrocatalysts (from 2.1 to 2.4 nm), except for Pt-SnO_2/C (3.3 nm). The presence of some agglomerates was observed on Pt-Rh/C and to a larger extent on Pt-SnO_2/C.

The surface-averaged diameter d_s estimated from the PSD histograms can be compared to the mean particle size (d_{Elec}) calculated from the electrochemically active surface area (A) estimated from the charge of CO-stripping (Eq.2.9).

Table 4 points out a good correspondence between the TEM and XRD mean particle diameter, d_V and d_{XRD} respectively, for Rh/C, Pt-Rh/C and Pt-Rh-SnO_2/C whereas the presence of agglomerates on Pt/C and Pt-SnO_2/C explains the discrepancies. The same reason can explain the inconsistency between d_{Elec} and d_s values for Pt/C and the multi-metallic electrocatalysts. Moreover, for the latter, an alloy effect may have impacted CO_{ad} adsorption/electrooxidation and the resulting electrochemical active surface area (ECSA). More specifically, the ECSA from Pt-SnO_2/C and Pt-Rh-SnO_2/C may be underestimated (and thus d_{Elec} overestimated) due to CO_{ad} electrooxidation probably occurring during the chronoamperometry at E_{ad} = 0.15 V *vs.* RHE preceding the CV.

Table 4. Structural proprieties of Pt/C, Rh/C, Pt-Rh/C, Pt-SnO_2/C and Pt-Rh-SnO_2/C electrocatalysts obtained by XRD and TEM.

Electrocatalyst	Effective composition by ICP-AES	a / Å	d_{XRD} / nm	d_{Elec} / nm	d_N / nm	d_S / nm	d_V / nm
Pt/C	-	3.93	6.2	4.8	2.3	2.6	2.9
Rh/C	-	3.84	2.9	3.8	2.1	2.4	2.7
Pt-Rh/C	$Pt_1Rh_{0.8}$/C	3.91	3.2	4.2	2.3	3.3	3.9
Pt-SnO_2/C	$Pt_1(SnO_2)_{0.3}$/C	3.97	4.8	9.4	3.3	5.8	7.8
Pt-Rh-SnO_2/C	$Pt_1Rh_{0.58}(SnO_2)_{0.35}$/C	3.91	3.3	4.8	2.4	2.6	2.8

a: lattice parameter; d_{XRD} : mean nanoparticle size (XRD); d_{Elec}: electrochemical mean particle size; d_N: number-averaged diameter (TEM); d_S: surface-averaged diameter (TEM); d_V: volume-averaged diameter (TEM)

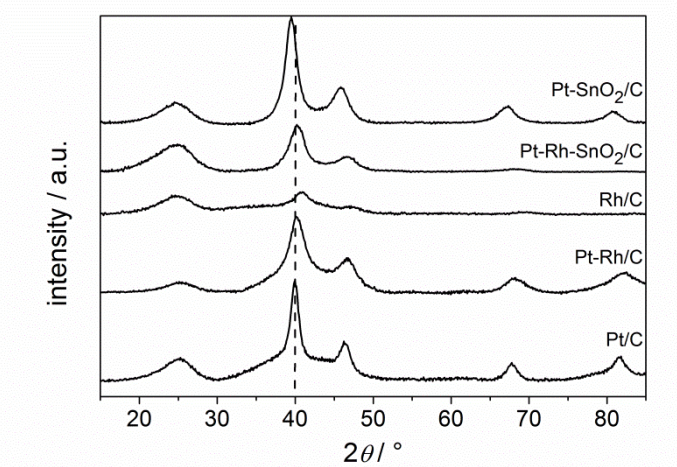

Fig. 24. XRD pattern of carbon supported 20 wt.% Pt/C, Rh/C, Pt-Rh/C, Pt-SnO_2/C and Pt-Rh-SnO_2/C electrocatalysts prepared by Polyol method.

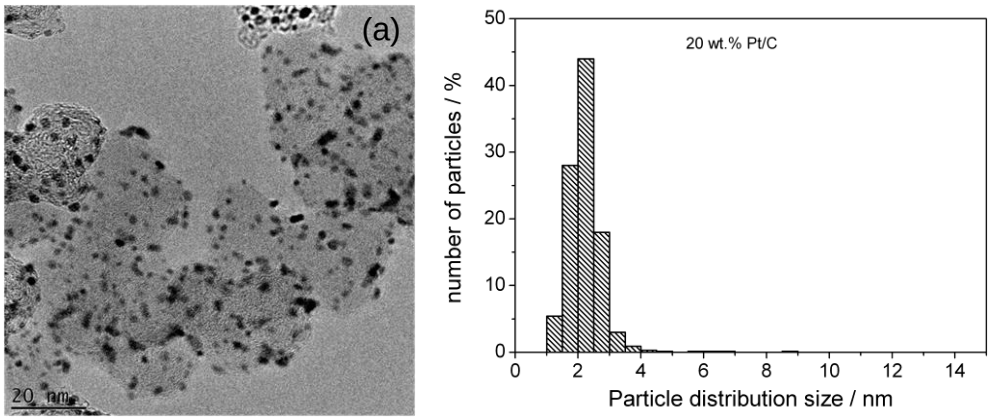

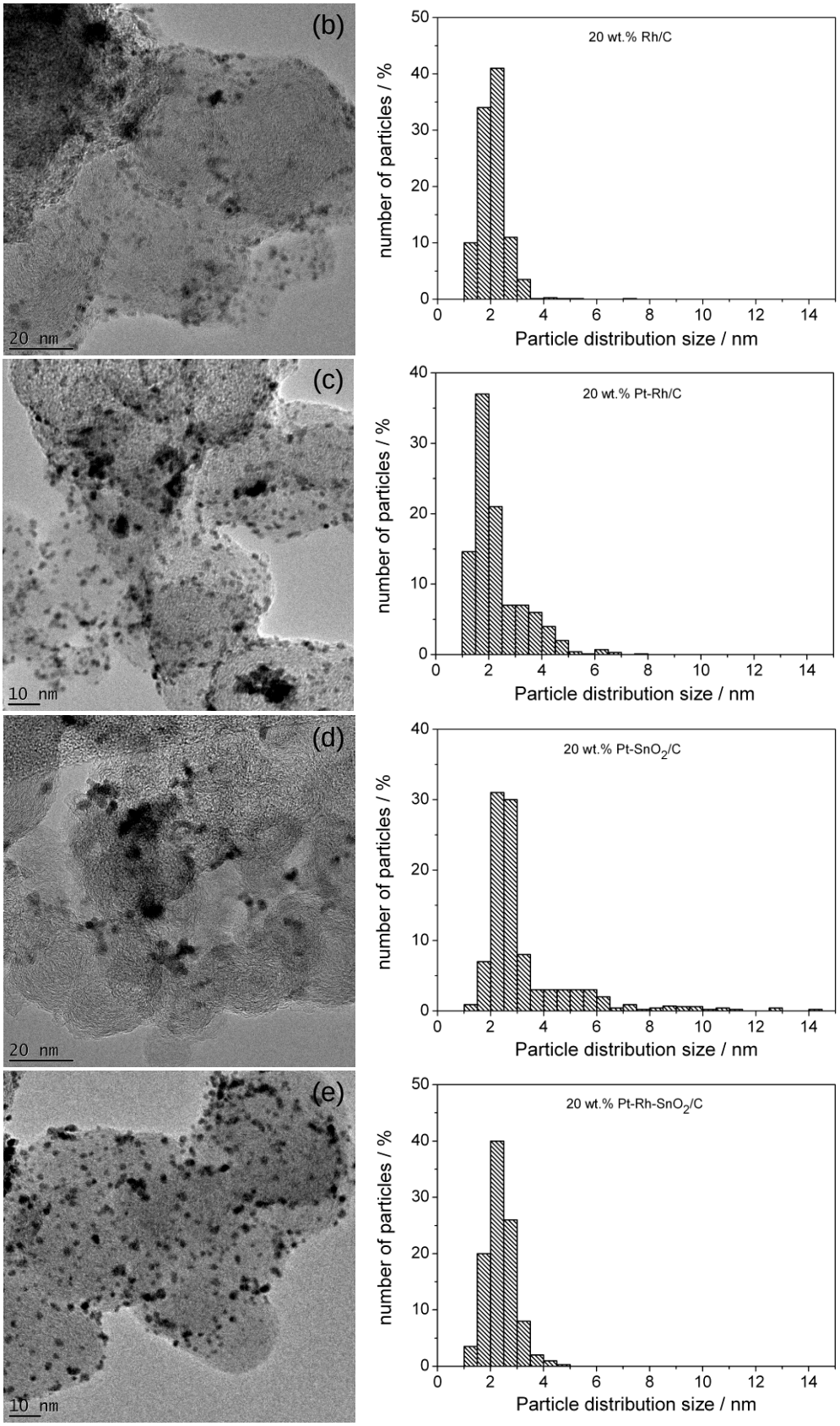
(b)
20 nm
20 wt.% Rh/C
number of particles / %
Particle distribution size / nm
(c)
10 nm
20 wt.% Pt-Rh/C
number of particles / %
Particle distribution size / nm
(d)
20 nm
20 wt.% Pt-SnO2/C
number of particles / %
Particle distribution size / nm
(e)
10 nm
20 wt.% Pt-Rh-SnO2/C
number of particles / %
Particle distribution size / nm

Fig. 25. Typical TEM images at × 200 000 magnification and associated particle size distribution of the (a) Pt/C, (b) Rh/C, (c) Pt-Rh/C, (d) Pt-SnO_2/C and (e) Pt-Rh-SnO_2/C electrocatalysts.

III.2.2. CV in base electrolyte

Fig. 26 presents cyclic voltammograms in supporting electrolyte (0.5 M H_2SO_4) on Pt/C, Rh/C, Pt-Rh/C, Pt-SnO_2/C and Pt-Rh-SnO_2/C. The usual features of the so-called hydrogen and oxygen regions of Pt-based electrodes can be observed. On the one hand, the oxide region on Rh- and Sn-based electrocatalysts, *i.e.* on Rh/C, Pt-Rh/C, Pt-SnO_2/C and Pt-Rh-SnO_2/C, starts at much lower potentials than on Pt/C (E = 0.8 V *vs.* RHE). The lower onset potential for the former electrocatalysts versus Pt/C may be ascribed to the oxophylic character of rhodium and tin. Electronic interactions between Pt and the non-noble metals may also modify the electronic structure of Pt and, as a consequence, favor its affinity toward water dissociation. The oxide reduction also starts at lower potentials on Rh- and Sn-based electrocatalysts, showing the higher oxides stability on the electrocatalysts. On the other hand, the hydrogen starts adsorbing at lower potential on Pt-Rh-based bi- and tri-metallic electrocatalysts than on Pt/C (E = 0.06 V *vs.* RHE). As it can be seen in Fig. 26, this phenomenon can be attributed to the lower adsorption potential of a hydrogen monolayer on Rh/C (E = 0.03 V *vs.* RHE); in other words, H-adsorbates seem less stable at Rh-containing surfaces than at Pt surfaces, because Rh may modify the electronic structure of Pt in the multi-metallic electrocatalysts. Likewise, it can be seen that the oxidation peak corresponding to adsorbed hydrogen oxidation on Pt/C is located at *ca.* E = 0.13 and 0.21 V *vs.* RHE (the H-desorption occurs in two peaks on Pt/C) versus E = 0.13 V *vs.* RHE on Pt-Rh/C, Pt-SnO_2/C and Pt-Rh-SnO_2/C. On Rh/C, the surface dehydrogenation even operates at E = 0.09 V *vs.* RHE.

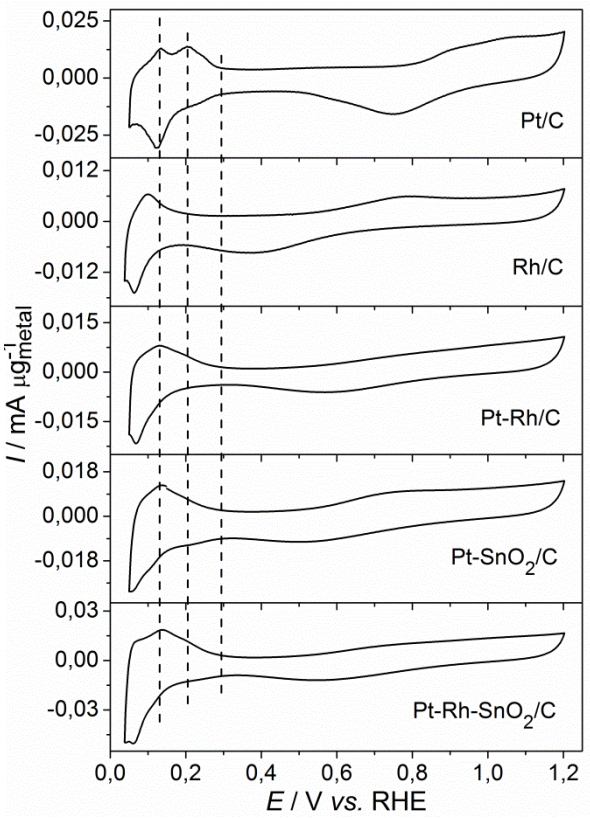

Fig. 26. CV in 0.5 M H_2SO_4 on Pt/C, Rh/C, Pt-Rh/C, Pt-SnO_2/C and Pt-Rh-SnO_2/C electrocatalysts; v = 10 mV s^{-1}; T = 25°C.

III.2.3. CO stripping CV

III.2.3.1. On-line DEMS

Fig. 27 displays the CO-stripping voltammograms recorded on Pt/C, Rh/C, Pt-Rh/C, Pt-SnO_2/C and Pt-Rh-SnO_2/C. A first comparison between Pt/C and Rh/C shows that the CO-stripping initiates at lower potentials on the latter than on the former: the supply in OH-adsorbates proceeds at lower potential on Rh/C than on Pt/C (see Fig. 26), which may ease CO_{ad} electrooxidation into CO_2.

The electrooxidation of CO adsorbates on Rh/C (E = 0.56 V *vs.* RHE), Pt-Rh/C (E = 0.58 V *vs.* RHE), Pt-SnO_2/C (E = 0.25 V *vs.* RHE) and Pt-Rh-SnO_2/C (E = 0.30 V *vs.* RHE) initiates at lower potential than on Pt/C (E = 0.65 V *vs.* RHE). The presence of tin and rhodium, two oxophilic metals, in the lattice of the bi- and tri-metallic electrocatalysts likely suggests a faster (more efficient at low potential) supply in OH_{ad}-species, that helps the oxidation of adsorbed CO (bi-functional mechanism, often mentioned for CO and methanol oxidation reactions [188]). Besides, their presence possibly induces a ligand effect on the

electronic structure of Pt. This is in agreement with the fact that water dissociation into adsorbed OH-species starts at lower potentials on Pt-Rh-SnO_2/C and Pt-Rh/C than on Pt/C. Besides, alloying Rh and Sn with Pt presumably leads to a down-shift of the Pt 5d-band center caused by the interactions in the lattice between Pt and Rh atoms [189]. This phenomenon would result in a weaker adsorption of CO on Pt atoms of the alloy and thus in the acceleration of the kinetics on Pt-Rh/C.

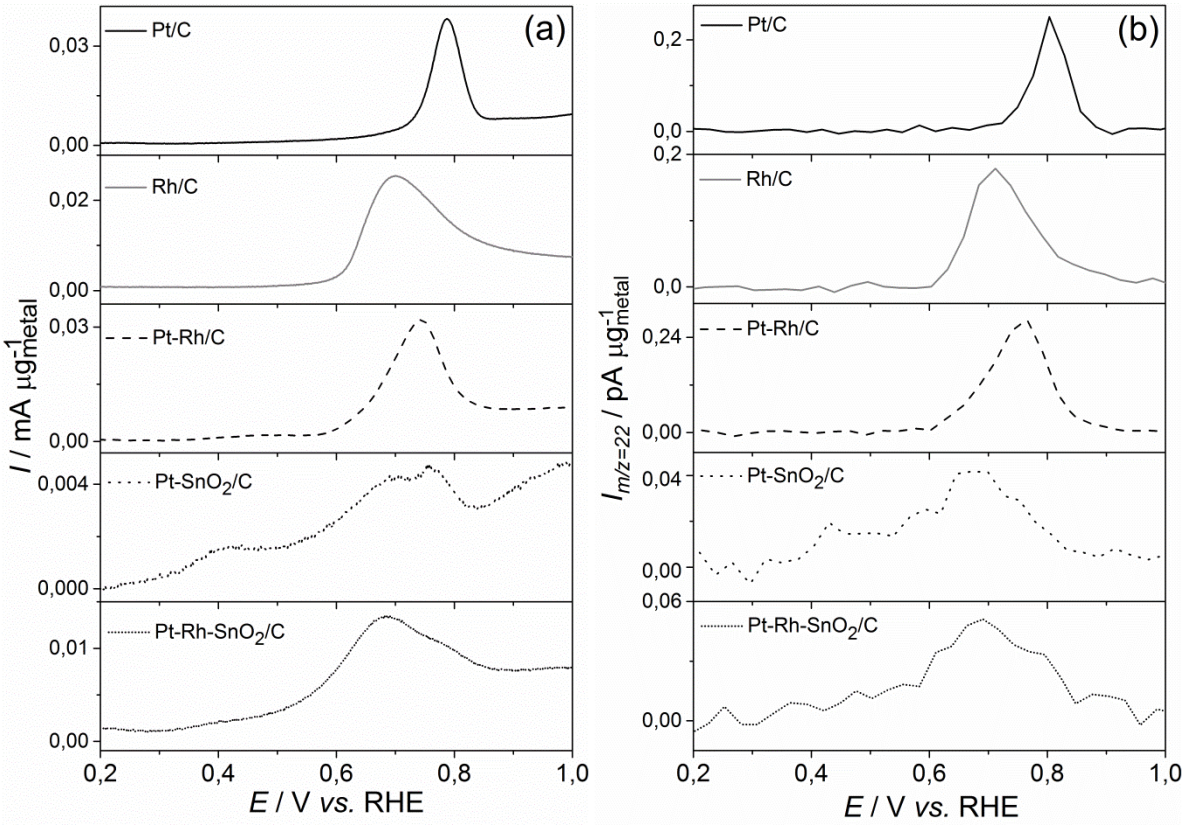

Fig. 27. (a) CO-stripping CV in 0.5 M H_2SO_4 in and (b) corresponding MSCV for mass to charge ratio m/z = 22 on Pt/C, Rh/C, Pt-Rh/C, Pt-SnO2/C and Pt-Rh-SnO_2/C; v = 10 mV s^{-1}; T = 25°C.

III.2.3.2. *In situ* FTIR

Fig. 28 shows typical IR-spectra features of a CO_{ad} monolayer electrooxidation on Pt/C, Rh/C, Pt-Rh/C, Pt-SnO_2/C and Pt-Rh-SnO_2/C recorded between E = 0.25 and 1.15 V *vs.* RHE (in any case, the reference spectrum was obtained at E = 0.15 V *vs.* RHE). The band at 2343 cm^{-1} which signals CO_2 formation is attributed to the O-C-O asymmetric stretching mode [190]. Two additional bands are usually observed during a CO-stripping: linearly bonded CO_L (C-O) and bridge-bounded CO_B (C=O). These bands are regularly located at *ca.*

2055 cm^{-1} and 1820-1840 cm^{-1} respectively on platinum [191–195]. The appearance of these bands corresponds to the initiation of the electrooxidation of the CO_{ad} monolayer into CO_2. As it can be seen in Fig. 28, the CO_B is hardly visible in the IR-spectrum of Pt/C. A favored adsorption of on-top CO on Pt/C could rationalize the quasi-absence of band between 1820 and 1840 cm^{-1}. An additional explanation could be that water H-O-H bending mode [196] overlaps the CO_B band. The latter can however be guessed at E = 0.85 and 0.95 V *vs.* RHE centered at 1830 cm^{-1}. On the contrary, CO_L and CO_B bands can be perfectly observed on Rh/C despite the superimposition with the water band. It seems qualitatively that the ratio between on-top and two-fold bridge CO_{ad} is more balanced than on Pt/C. On Pt-Rh/C and Pt-SnO_2/C, the CO_B is probably ascribed to the broad band between 1900 and 1750-1700 cm^{-1}. Pt-Rh-SnO_2/C presents a CO_L band of particularly low intensity compared to the other electrocatalysts. It can be assumed that CO_L low band intensity is due to the lower CO_{ad} coverage on Pt-Rh-SnO_2/C (50 at.% Pt) than on the other electrocatalysts. Pt-SnO_2/C has three Pt atoms for one Sn atom and Pt-Rh/C has one Pt atom for one Rh atom, but CO adsorbs on both platinum and rhodium metals contrary to tin oxide. Silva-Junior et al. observed a similar phenomenon on Pt-Rh-SnO_2/C compared to Pt-Rh/C [125].

When comparing the position of the CO_L bands on Pt/C and Rh/C, it can be noticed that the band position on the latter (at 2015 cm^{-1}) is located at much lower wavenumbers than on Pt/C (at 2055 cm^{-1}). This behavior is analog with ruthenium which displays a CO_L band at similar wavenumbers (at *ca.* 2010 cm^{-1}) [197,198]. The lower band frequency can indicate a stronger CO adsorption on the Rh/C surface in comparison to Pt/C. As for the bi- and tri-metallic electrocatalysts, the CO_L band from Pt-Rh/C (at 2041 cm^{-1}) and Pt-Rh-SnO_2/C (at 2046 cm^{-1}) is red-shifted against Pt/C while the band from Pt-SnO_2/C (at 2056 cm^{-1}) has the same position as Pt/C. These results tend to show that Rh modifies the electronic structure of Pt: alloying Rh with Pt presumably leads to a down-shift of the Pt 5d-band center caused by the interactions in the lattice between Pt and Rh atoms [189] and lower CO_{ad} adsorption strength on the electrocatalyst. On the contrary, SnO_2 does not modify Pt electronic structure and seems only to provide hydroxide species at low potentials in a so-called bi-functional mechanism.

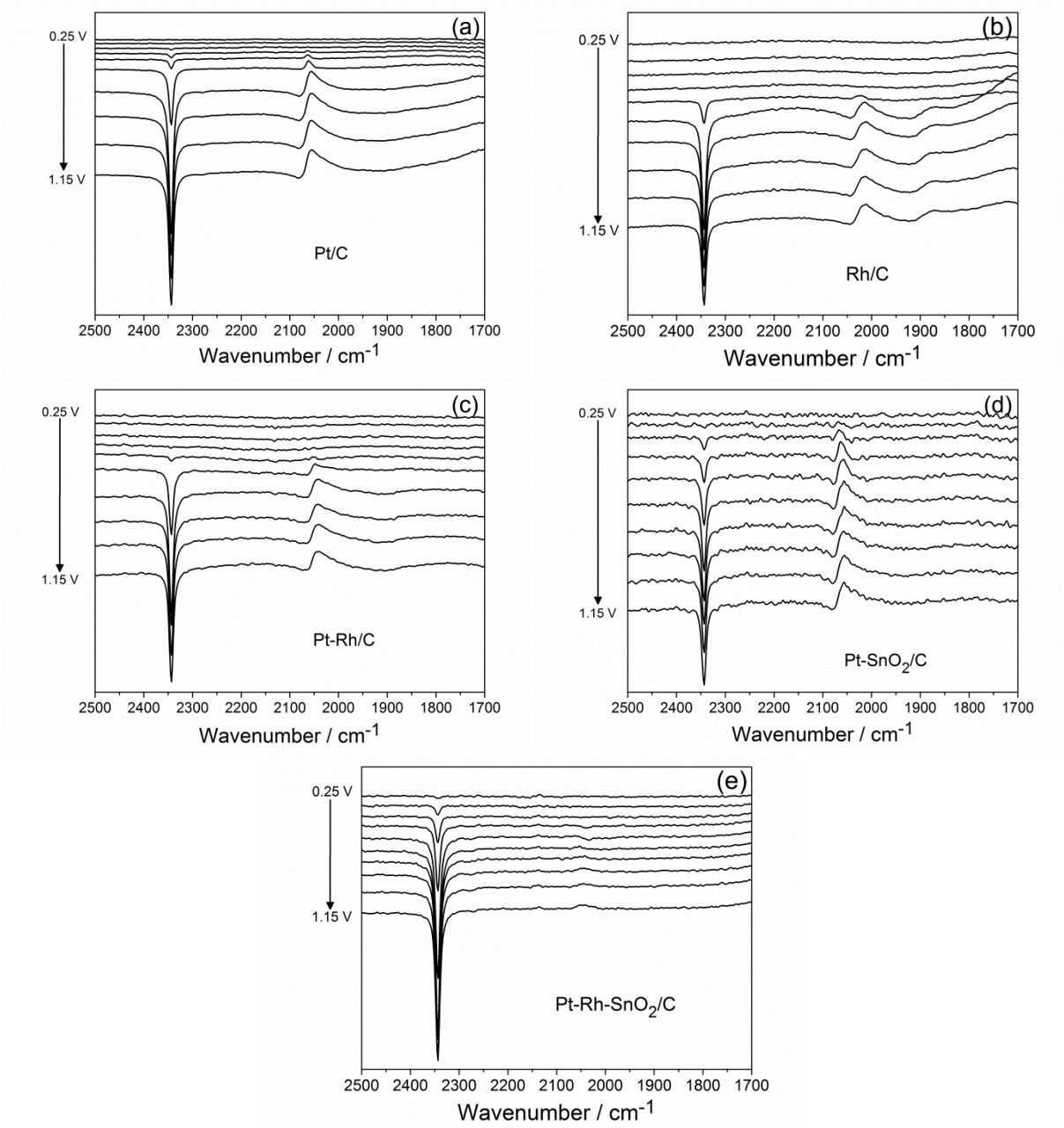

Fig. 28. *In situ* infrared spectra recorded during CO stripping in 0.5 M H_2SO_4 on (a) Pt/C, (b) Rh/C, (c) Pt-Rh/C, (d) Pt-SnO_2/C and (e) Pt-Rh-SnO_2/C; T = 25°C.

It is generally possible to distinguish IR-bands of adsorbed species from solution species by observing the shift of the band position against the potential. This shift of the band frequency with the potential increase can be rationalized by two phenomena [199]: the influence of the potential increase on the electrical field applied on the working electrode and its adsorbates, also commonly called the *Stark effect* [200,201]; the effect of the adsorbates spread on the working electrode surface with increasing potential altering the adsorbates vibrations frequency, also called the *dipole-dipole coupling effect* [199,202], or changing the

chemical bond between the adsorbates and the electrocatalyst, known as the *chemical shift effect* [203]. Fig. 29 illustrates this potential change with the variation of the applied potential on the different electrocatalysts. However, a Stark effect would induce a shift of the frequency toward more positive frequency values. The observed red-shift is therefore most likely due to dipole-dipole coupling interactions: as the CO_{ad}-coverage decreases with the potential increase, the lateral interactions between the CO-adsorbates drop, thus inducing a red-shift of the frequency of the C-O stretch mode [52,204,205].

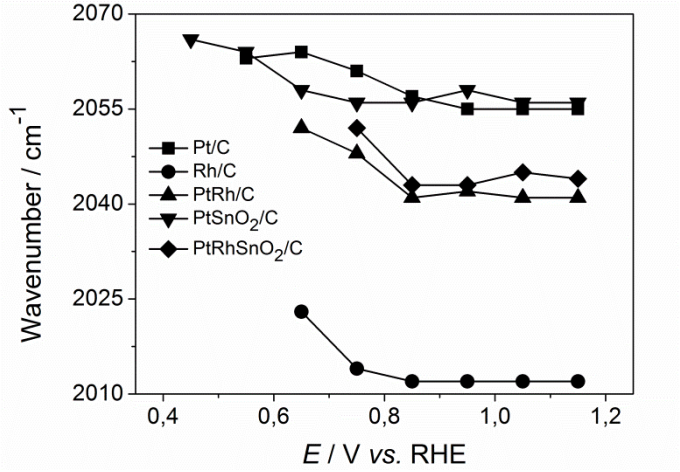

Fig. 29. Variation of the CO_L band wavenumber *versus* potential, measured during the CO stripping in 0.5 M H_2SO_4 on Pt/C, Rh/C, Pt-Rh/C, Pt-SnO_2/C and Pt-Rh-SnO_2/C; T = 25°C.

The charge of the CO_2 band at 2343 cm^{-1} was calculated by integration of the area under the band between 2300 and 2400 cm^{-1}, normalized by the obtained highest charge and further plotted against the applied potential for each electrocatalyst (Fig. 30). A large shift of the CO_{ad} stripping initiation can be observed on Pt-SnO_2/C (E = 0.45 V *vs.* RHE) and Pt-Rh-SnO_2/C (E = 0.35 V *vs.* RHE) compared to Pt/C (E = 0.65 V *vs.* RHE). CO_{ad} electrooxidation is also favored on Rh/C but no striking difference can be reported between Pt/C and Pt-Rh/C. The CO_{ad} electrooxidation at more negative potentials on Pt-SnO_2/C and Pt-Rh-SnO_2/C is ascribed to SnO_2 oxophylic character, which supplies OH-species at low potentials on the electrocatalyst surface helping the oxidation of the adsorbed CO as well as a ligand effect operated on Pt electronic structure (bi-functional mechanism, often mentioned for CO and methanol oxidation reactions [188]).

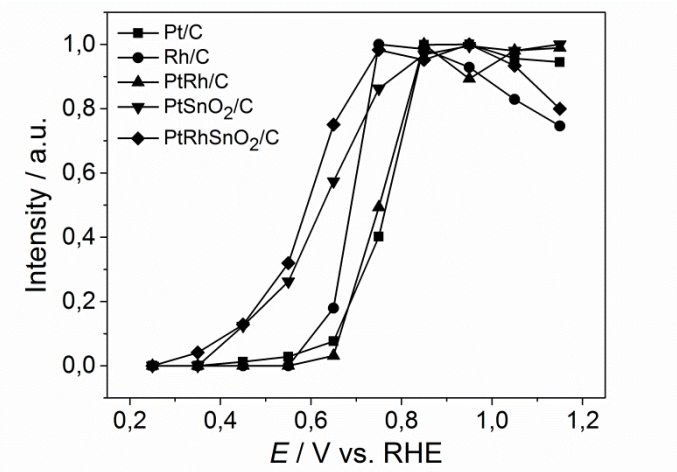

Fig. 30. (a) CO stripping in 0.5 M H_2SO_4 - CO_2 band intensity against potentials on Pt/C, Rh/C, Pt-Rh/C, Pt-SnO_2/C and Pt-Rh-SnO_2/C; T = 25°C.

III.2.4. Comparison of the *in situ* FTIR and on-line DEMS measurements

A comparison between the *in situ* FTIR and on-line DEMS results is displayed in Fig. 31 in order to check the correlation (or not!) between the results obtained in the two very different experimental conditions: thin layer *versus* flow configuration. To that goal, the evolution of the CO_2 band at 2343 cm^{-1} (shown in Fig. 30) was plotted in parallel to the CO-striping CVs and their associated MS signal m/z = 22 represented in Fig. 27. One aim of such comparison is to identify whether the reaction intermediates and products detected by FTIR play a role in the potentiodynamic current evolution.

Looking at the potential onset of the stripping CVs, symbolized approximately by the dash line, it seems to be always located where the CO_2 band starts to be detected in the spectra for all electrocatalysts. An exception maybe for Pt-SnO_2/C can be observed in Fig. 31. Indeed, the onset potential of the CO-stripping is apparently located at slightly lower potentials in the CV than the potential at which first appears the CO_2 IR-band. Possible mass-transport limitation of the OH^--species at the surface of the working electrode seems to be excluded, as this phenomenon is not observed for the other electrocatalysts. A possible explanation could be given based on the physical morphology of this electrocatalyst. Indeed, the presence of agglomerates was noticed in section III.2.1. It can be reasonably proposed that the presence of these larger nanoparticles impacted on the negative shift of the CO-striping in the CV. A lower proportion of tin oxide species in the electrocatalyst analyzed by FTIR could also shift positively the CO-stripping initiation and thus the appearance of the band at *ca.* 2340 cm^{-1}. However, besides this particular case, the correspondence between the onset potentials of the CO-stripping with the potentials of the CO_2 band first appearance makes the procedure quite reliable for a more complicated reaction like the EOR.

Another location in the stripping-CVs which could be of interest is the CO-stripping peak (symbolized by the second dash line, at upper potential). Fig. 31 shows that the potential of the current maximum recorded during the CV does not match with the maximum obtained during the IR-analysis. This phenomenon is attributed to the thin cavity configuration during the IR-measurements which traps and accumulates the CO_2 produced during the CO-stripping and which thus results in an amplification of the CO_2 band. As a consequence, the peak of the potentiodynamic CO-stripping which corresponds to a limitation by the CO_{ad} presence on the electrocatalyst surface should not be confused with the maximum of the CO_2 band intensity.

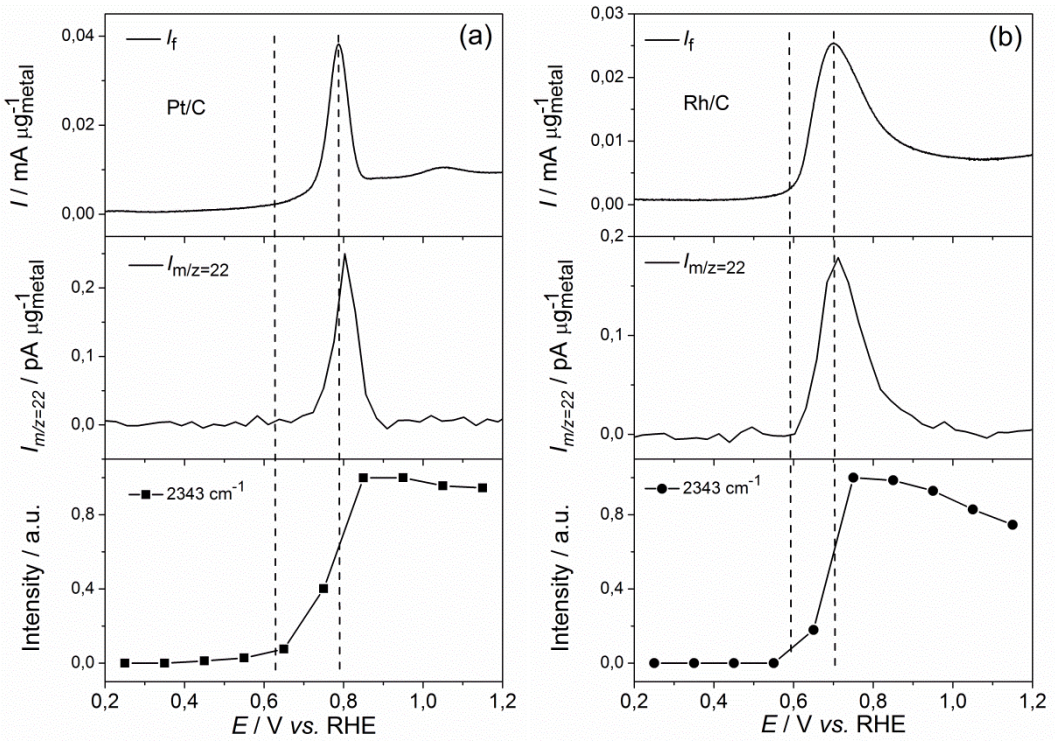

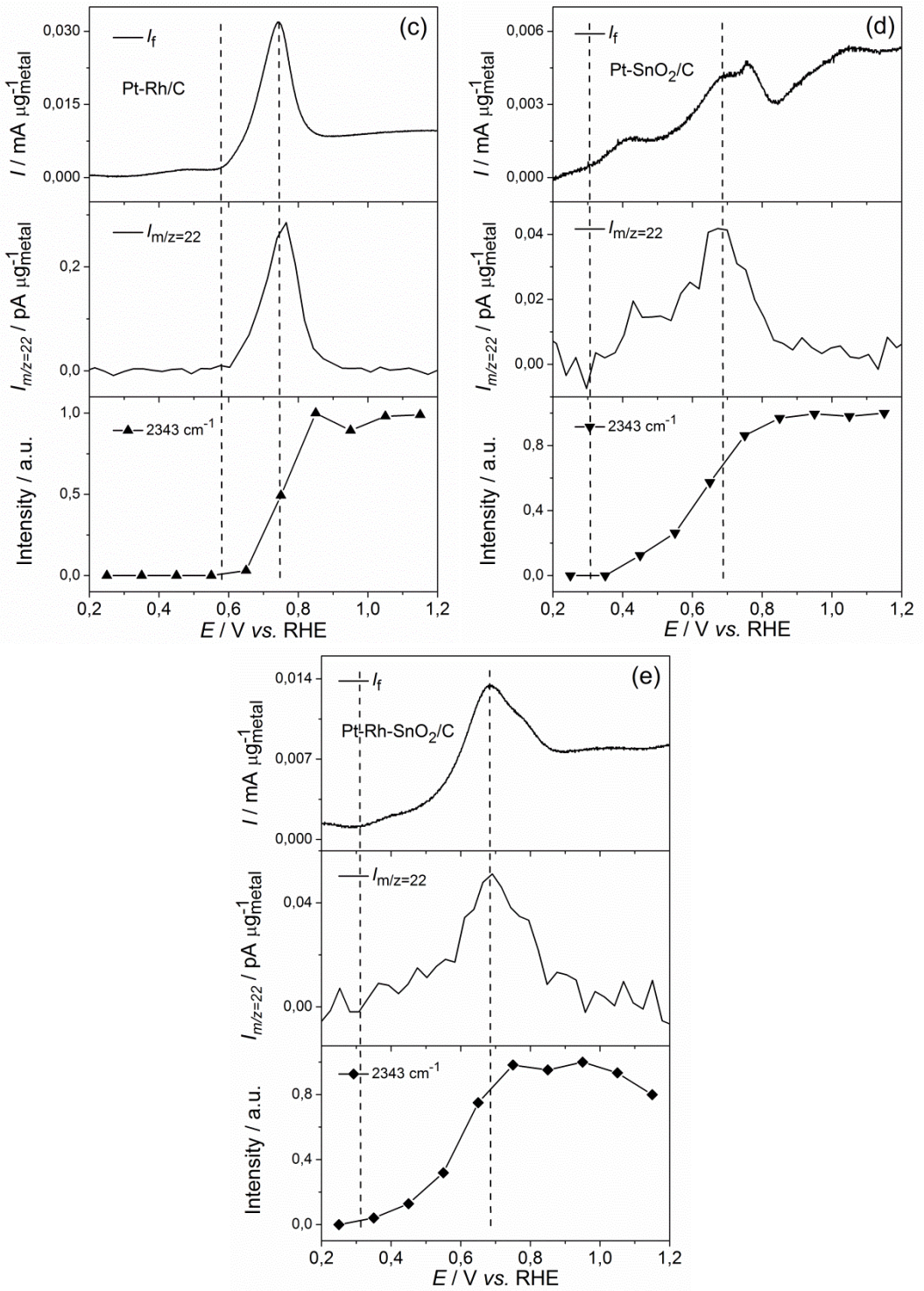

Fig. 31. CO-stripping CV in 0.5 M H_2SO_4, corresponding MS signal *m/z* = 22 and CO_2 band intensity (from Fig. 30) on (a) Pt/C, (b) Rh/C, (c) Pt-Rh/C, (d) Pt-SnO_2/C and (e) Pt-Rh-SnO_2/C; v = 10 mV s^{-1}; T = 25°C.

III.2.5. Ethanol electrooxidation

III.2.5.1. EOR on Pt/C studied by *in situ* FTIR

Fig. 32a shows FTIR-spectra between 2500 cm^{-1} and 1000 cm^{-1} during chronoamperometries run between E = 0.25 and 1.15 V *vs.* RHE by 100 mV step in 0.5 M H_2SO_4 + 1 M EtOH on Pt/C. Down-going bands corresponds to the species production in the thin layer between the working electrode and the optical window compared to the reference spectrum (recorded at E = 0.15 V *vs.* RHE), while up-going bands represent the species consumption/depletion.

One dominant positive band located at 1640 cm^{-1} is present in all spectra and increases together with the applied potential. This band is assigned to water H-O-H bending mode [196]. The associated water band at 3185 cm^{-1} (not represented here) corresponds to interfacial water O-H stretching mode [196]. The particularly broad positive band at *ca.* 1200 cm^{-1} is attributed to the doubly degenerate stretch mode of bisulfate anions [206–210]. This feature has already been largely evidenced in the literature for mono- and polycrystalline electrodes [200,206,207,209–212]. It is interesting to notice that the water band at 1640 cm^{-1} and HSO_4^- band at 1200 cm^{-1} shows an intense rise against the potential. The products of the ethanol electrooxidation (acetaldehyde, acetic acid, CO_2) formed in the thin cavity likely causes the electrolyte depletion thus resulting in a larger increase of the water and bisulfate anions bands. Other positive bands can be observed at 1454 cm^{-1} and 1085 cm^{-1} on the spectra which correspond to ethanol depletion from the thin layer. Two other bands detected at 2908 cm^{-1} and 2983 cm^{-1} (not shown here) are ascribed to ethanol asymmetric CH_2 and CH_3 vibrations respectively [67]. Finally, a broad positive band centered at *ca.* 1915 cm^{-1} appears in Fig. 32a in the medium potential region (E > 0.5 V *vs.* RHE) on all studied electrocatalysts. This band is similar to the one at 1920 cm^{-1} on Pt (100), which Watanabe et al. ascribed to asymmetric bridge-bond species in a CO-stripping study [191]. The authors excluded the dipole-dipole interactions which could not explain the large difference with the usual reported CO_B band at *ca.* 1820-1840 cm^{-1} against this band at *ca.* 1915 cm^{-1}. Although this band is visible on other *in situ* FTIR EOR studies [22,78,82,125,213], the authors did not describe it.

Negative-going bands also compose the spectra features in Fig. 32a. These bands correspond to the formation of reaction intermediates and products, either adsorbed or present in solution in the thin cavity. The bands at 2343 cm^{-1} and 2055 cm^{-1} are the same as in section III.4.2 and represent CO_2 formation and linearly bonded CO_L [191–195]. Unfortunately, the last band could hardly be detected in our experimental conditions. Their presence were however confirmed between E = 0.35 and 0.75 V *vs.* RHE on most of the electrocatalysts. Bands at 1280 cm^{-1}, 1400 cm^{-1} and 1715 cm^{-1} are characteristic of aqueous acetic acid formation [68,70]. They are respectively ascribed to the coupled OH deformation [68] and C-O stretching from -COOH [68,70], to C-O symmetric stretching of adsorbed CH_3COO^- [68,70,214] and C=O stretching mode from -COOH or -CHO [70,190]. Acetaldehyde

characteristic bands are usually found at 933 cm^{-1} (C-C-O asymmetric stretch [26,215] or symmetrical C-C stretch [216]), 1355 cm^{-1} (double band - CH_3 symmetric deformation [68,216]), 1120 cm^{-1} (C-H wagging vibration [68,216]) and 1715 cm^{-1} (stretching mode of carbonyl groups [190]). The feature at 933 cm^{-1} was not observable with the present operating conditions, because the CaF_2 optical window absorbing the incident light below 1000 cm^{-1}. The band at 1715 cm^{-1} ascribed to C=O stretching mode of carbonyl species, in this case acetic acid and acetaldehyde, can generally not be distinguished due to the high proximity of their bands (less than 5 cm^{-1}) too close from the FTIR spectra resolution (4 cm^{-1}). In parallel to the band at 1715 cm^{-1}, the formation of acetates can be seen with a band at 1560-1580 cm^{-1} [67]. A summary of the bands positions is given in Table 5.

Table 5. Band assignment of the EOR products

Frequency (cm^{-1})	Species	References
2343	C-C-O asymmetric stretching	[190]
2055	C-O stretching	[191–195]
1915	C=O asymmetric stretching??	[191]
1715	C=O stretching from -COOH or -CHO	[70,190]
1400	C-O symmetric stretching of adsorbed CH_3COO^-	[68,70,214]
1355	CH_3 symmetric deformation	[68,216]
1280	OH deformation + C-O stretching from -COOH	[68,70]
1120	C-H wagging vibration	[68,216]
930	O-C-O asymmetric stretching / symmetrical C-C stretching	[26,215] / [216]

Fig. 32b shows the evolution of the bands at 2343 cm^{-1}, 1915 cm^{-1}, 1715 cm^{-1}, 1400 cm^{-1} and 1355 cm^{-1} *versus* potential on Pt/C. This graph shows more clearly at which potential the reactions occur, but does not allow a quantitative evaluation of the products generation. CO_2 formation (band at 2343 cm^{-1}) can be observed starting at *ca.* E = 0.55 - 0.65 V *vs.* RHE while acetic acid (1400 cm^{-1}) and acetaldehyde (1355 cm^{-1}) seem to initiate at the same time between E = 0.35 and 0.45 V *vs.* RHE. The detection of acetic acid at so low potentials puts into question the veracity of the equation Eq.I.23. Indeed, adsorbed hydroxide species necessary for the acetic acid formation from acetaldehyde are not quantitatively present on the platinum surface before E = 0.55 - 0.65 V *vs.* RHE (onset potential of the CO_2 formation in Fig. 32b). Assumptions that acetic acid formation does not operate through adsorbed acetaldehyde electrooxidation can be found in the literature [217].

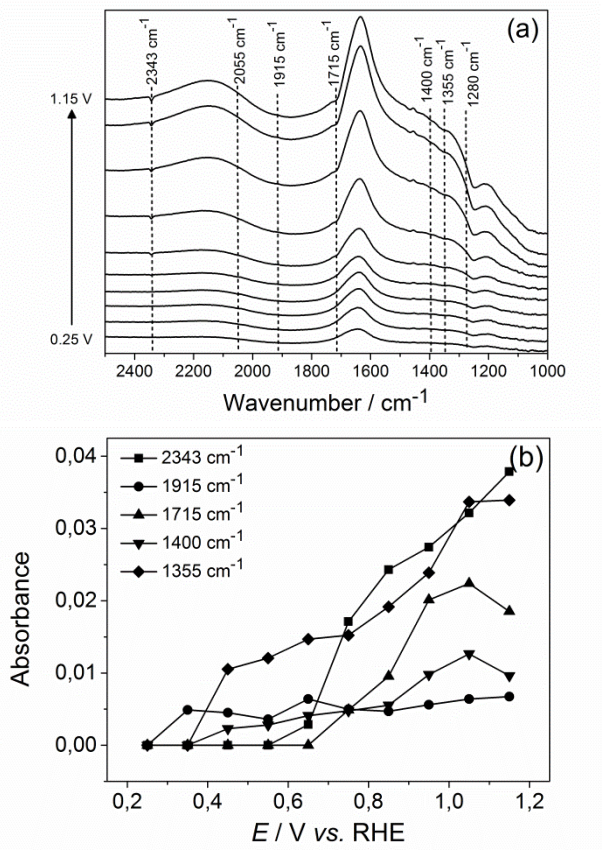

Fig. 32. (a) *In situ* infrared spectra recorded in 0.5M H_2SO_4 + 1M EtOH on Pt/C at room temperature and (b) band intensities evolution (at 2343, 1915, 1715, 1400 and 1355 cm^{-1}) against the applied potential; R_{ref} = 0.15 V *vs.* RHE. Potential range: *E* = 0.25 and 1.15 V *vs.* RHE; Potential step: *E* = 0.1 V.

III.2.5.2. Comparison with on-line DEMS measurements

A direct comparison is carried out in this section between the *in situ* FTIR measurements on Pt/C in section III.5.1 and an on-line DEMS study during a cyclic voltammetry in 0.5 M + 0.1 M EtOH (only the positive scan is shown here). The IR-bands at 1355 cm^{-1} (acetaldehyde), 2343 cm^{-1} (CO_2) and 1400 cm^{-1} (acetic acid) were compared respectively to the mass-to-charge signals *m/z* = 29 (Fig. 33b), *m/z* = 22 (Fig. 33c) and *m/z* = 61 (Fig. 33d) and to the CV profile in Fig. 33a.

The graph is separated in three different regions according to the profile of the cyclic voltammetry. The first one, between *E* = 0.37 and 0.58 V *vs.* RHE corresponds without ambiguity to the initiation of acetaldehyde and acetic acid formation according to the mass-to-charge signals *m/z* = 29 (Fig. 33b) and *m/z* = 61 (Fig. 33d) respectively. Moreover, these reactions are confirmed by the bands at 1355 cm^{-1} and 1400 cm^{-1} corresponding respectively

to the same species. The apparent slow kinetics of the reactions is edifying. At this point, no CO_2 is generated.

The second potential region between E = 0.58 and 0.79 V *vs.* RHE is characterized by the formation of CO_2 (signal m/z = 22) which competes with acetaldehyde and acetic acid formation. The peak of the signal m/z = 22 matches well with the current threshold in the EOR CV at E = 0.75 - 0.79 V *vs.* RHE. The band at 2340 cm^{-1} appears between E = 0.55 - 0.65 V *vs.* RHE which is not in contradiction with the CV and MSCV. The relative flat shape of the bands at 1350 cm^{-1} and 1400 cm^{-1} contrasts significantly with the sharp soar of the signals m/z = 29 (Fig. 33b) and m/z = 61 (Fig. 33d) which both fit closely the shape of the CV. More particularly, both signals present a current threshold at E = 0.75 V *vs.* RHE similarly to the signal m/z = 22.

The third potential region between E = 0.79 and 1.08 V *vs.* RHE corresponds to the maximum current reached during the EOR followed by the current decrease which starts at *ca.* E = 0.84 V *vs.* RHE. According to the mass-to-charge signal m/z = 29, the further ethanol electrooxidation, after the threshold noticed in the second potential region, corresponds to the sole formation of acetaldehyde. Indeed, the signals m/z = 22 and m/z = 61 started plummeting in the second potential region after E = 0.75 V *vs.* RHE. An inconsistency is found again in this potential region with the IR-bands characteristic of acetaldehyde (Fig. 33b), acetic acid (Fig. 33d) and, contrary to the second potential region, CO_2 (Fig. 33c) which all increase quasi-monotonously with the potential while the current is already decreasing.

Three different phenomena (or a combination of them) are suggested to explain this continuous rise in the third potential region:

- A first explanation would be the same as the one accounted for the CO-stripping experiments: the accumulation of products in the solution results in an increase of the three bands conversely to the evolution of the faraday current. However, here, no threshold is found before E > 1.05 V *vs.* RHE in Fig. 33b and Fig. 33d for acetaldehyde and acetic acid. This reason alone does not seem to fully justify the bands evolution.

- Then, it seems that the EOR processes in the third potential region without being limited by the ever growing presence of OH-adsorbates at the electrocatalyst surface (like in Fig. 33a) which prevents bulk ethanol from oxidizing. It can be supposed that the thin layer configuration limits greatly the "contamination" by the OH-species of the electrocatalyst surface due to the lack of support electrolyte. Indeed, the large water depletion from the thin layer illustrated by the large band centered at 1640 cm^{-1} could suggest that not enough OH-species are present in the thin layer to cover the entire electrocatalyst surface (although the amount of electrocatalyst on the GC electrode is pretty low too).

- Finally, the influence of the ethanol concentration which is different in both mass spectrometric and infrared experiments could be at stake to explain these differences. However, the concentration (up to 1 M ethanol, at least) does not seem to change the profile of the CV, but only to shift positively the EOR [22]. Hence, the concentration alone cannot elucidate the continuous rise of the three bands characteristic for acetaldehyde, CO_2 and acetic acid but could be part of the explanation for the bands shape.

A fourth potential region of the EOR could have been defined at E > 1.08 V *vs.* RHE. It would have corresponded to ethanol strong adsorbates electrooxidation (as evidenced in section III.1). Yet, the study of this fourth potential region was beyond the scope of this *in situ* FTIR investigation.

Finally, the great similitudes between the evolution of the bands at 1355 and 1400 cm^{-1} against the applied potential is rather intriguing and makes believe that they could be ascribed to the same species. However, such assumption would be contradictory with three decades of infrared analysis…

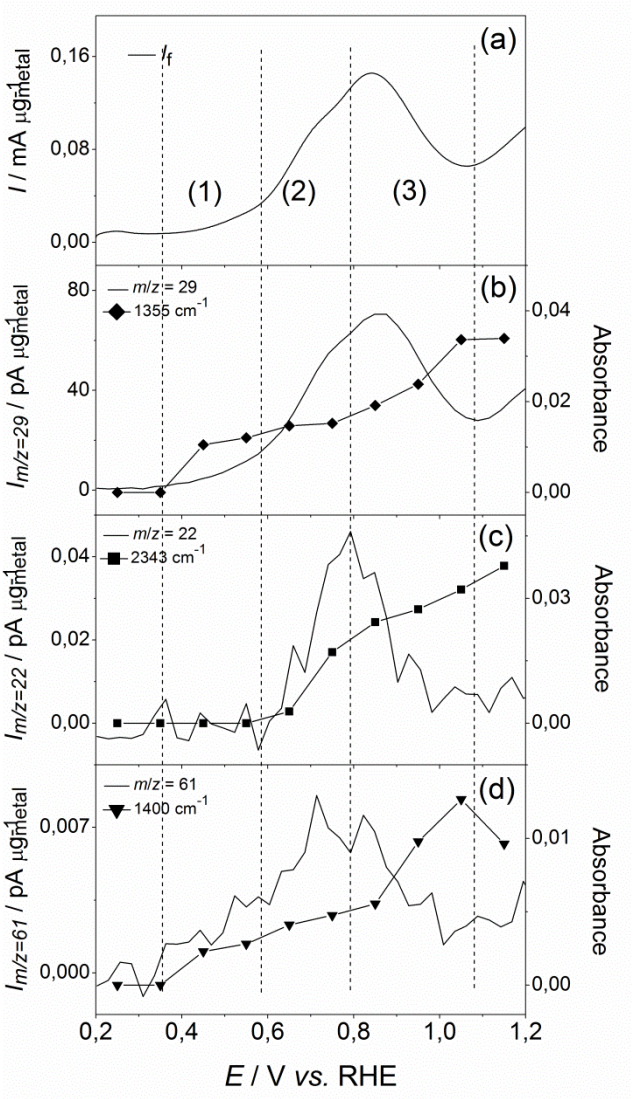

Fig. 33. (a) EOR cyclic voltammetry (in 0.5 M H_2SO_4 + 0.1 M EtOH) and corresponding MSCV associated with EOR infrared bands (from Fig. 32b): (b) *m/z* = 29 + 1355 cm^{-1}, (c) *m/z* = 22 + 2343 cm^{-1} and (d) *m/z* = 61 + 1400 cm^{-1} on Pt/C; *v* = 10 mV s^{-1}; *T* = 25°C.

III.2.5.3. *In situ* FTIR - EOR on Pt- and Rh-based electrocatalysts

Fig. 34 shows FTIR-spectra recorded between 2500 cm^{-1} and 1000 cm^{-1} during chronoamperometries run between *E* = 0.25 and 1.15 V *vs.* RHE by 100 mV step in 0.5 M H_2SO_4 + 0.1 M EtOH on Rh/C, Pt-Rh/C, Pt-SnO_2/C and Pt-Rh-SnO_2/C electrocatalysts.

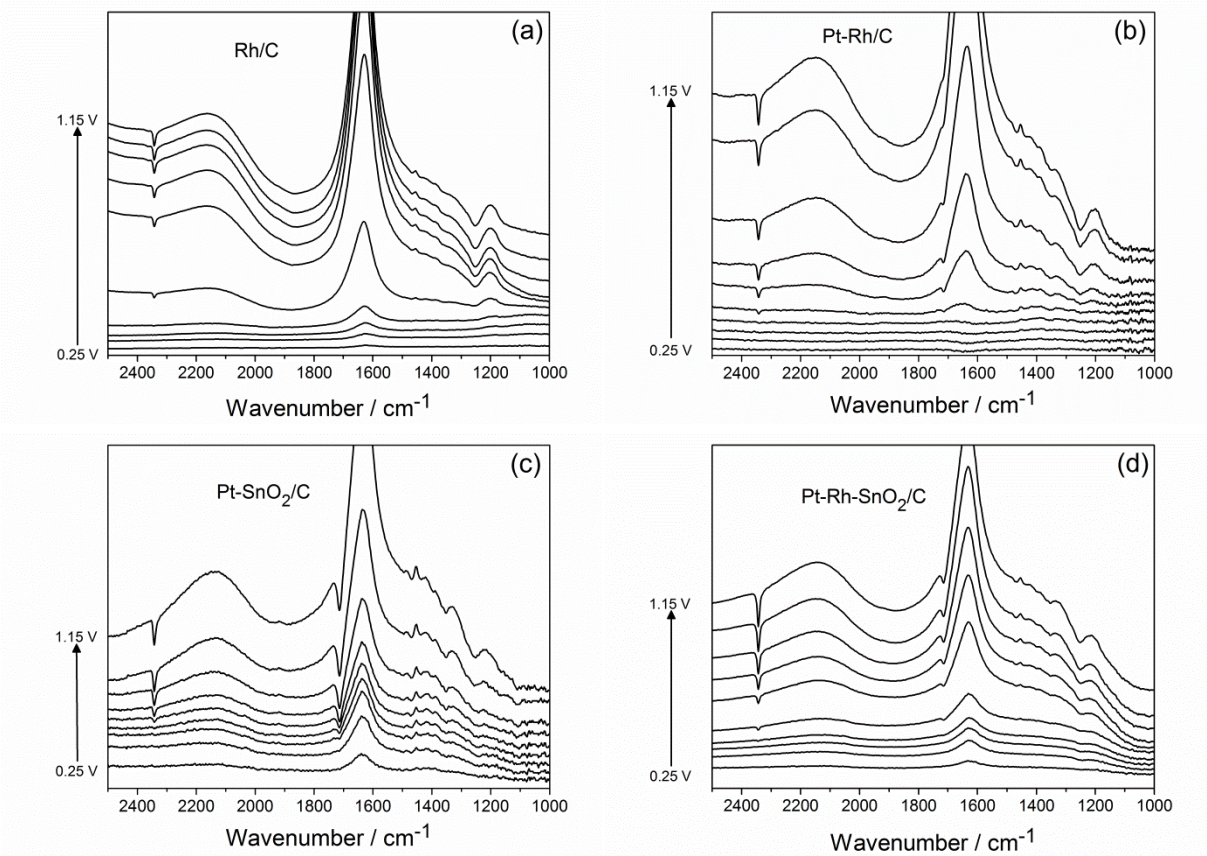

Fig. 34. *In situ* infrared spectra recorded in 0.5M H_2SO_4 + 0.1M EtOH on (a) Rh/C, (b) Pt-Rh/C, (c) Pt-SnO_2/C and (d) Pt-Rh-SnO_2/C at room temperature; R_{ref} = 0.15 V *vs.* RHE. Potential range: *E* = 0.25 and 1.15 V *vs.* RHE; Potential step: *E* = 0.1 V.

Fig. 35 shows the evolution of the bands at 2343 cm^{-1}, 1915 cm^{-1}, 1715 cm^{-1}, 1400 cm^{-1} and 1355 cm^{-1} *versus* potential on Pt/C, Rh/C, Pt-Rh/C, Pt-SnO_2/C and Pt-Rh-SnO_2/C. The evolution of Pt/C bands already shown in Fig. 32b was added in Fig. 35 for the sake of comparison with the other electrocatalysts. It can be seen first that CO_2 generation on Pt-Rh/C and Pt-Rh-SnO_2/C starts at lower potentials (*E* = 0.55 V *vs.* RHE) than on the other electrocatalysts (*E* = 0.65 V *vs.* RHE). These results differ from the CO_{ad} stripping experiments, where Pt-SnO_2/C and Pt-Rh-SnO_2/C displayed the lowest CO_{ad} electrooxidation onsets. The fact that Pt-Rh/C and Pt-Rh-SnO_2/C showed the lowest CO_2 generation initiation demonstrates that rhodium eases the C-C bond cleavage at low potentials and thus allows the complete electrooxidation of ethanol compared to Pt/C or Pt-SnO_2/C. Providing OH-species at low potentials, as does Pt-SnO_2/C, may be necessary to oxidize CO_{ad} formed from ethanol dissociative adsorption, but is not sufficient to facilitate CO_2 generation.

When comparing the different bands with one another, it can be noticed that Pt-Rh-SnO_2/C displays the highest CO_2 band intensity relatively to the other bands ascribed to acetaldehyde and acetic acid formation, followed by Rh/C and Pt-Rh/C. These results suggest that CO_2 formation is favored on Rh-based electrocatalysts and, above all, on Pt-Rh-SnO_2/C.

While Rh helps the cleavage of the C-C bond, SnO_2 provides OH-species at low potential and frees rhodium (and platinum) from the hydroxide adsorbates. As it can be seen in Fig. 35, the addition of tin oxide to Pt does not seem to improve the electrocatalyst ability to break the C-C bond. On the contrary, the large intensity of the bands 1715 cm^{-1} and 1355 cm^{-1} tends to show that acetaldehyde formation was favored on the Pt-SnO_2/C electrocatalyst. This result is a bit contradictory with the literature [99,101,213] where acetic acid formation was found to be favored on Pt-SnO_2/C. The presence of large nanoparticles of Pt-SnO_2/C could explain the divergence of results between this study and the rest of the literature. Conversely, CO_2 formation is slightly promoted on Pt-Rh/C *versus* Pt/C, alike the DEMS results reported in the previous section and in the literature [35,218]. Besides, acetic acid formation seems also hindered on the bi-metallic electrocatalyst.

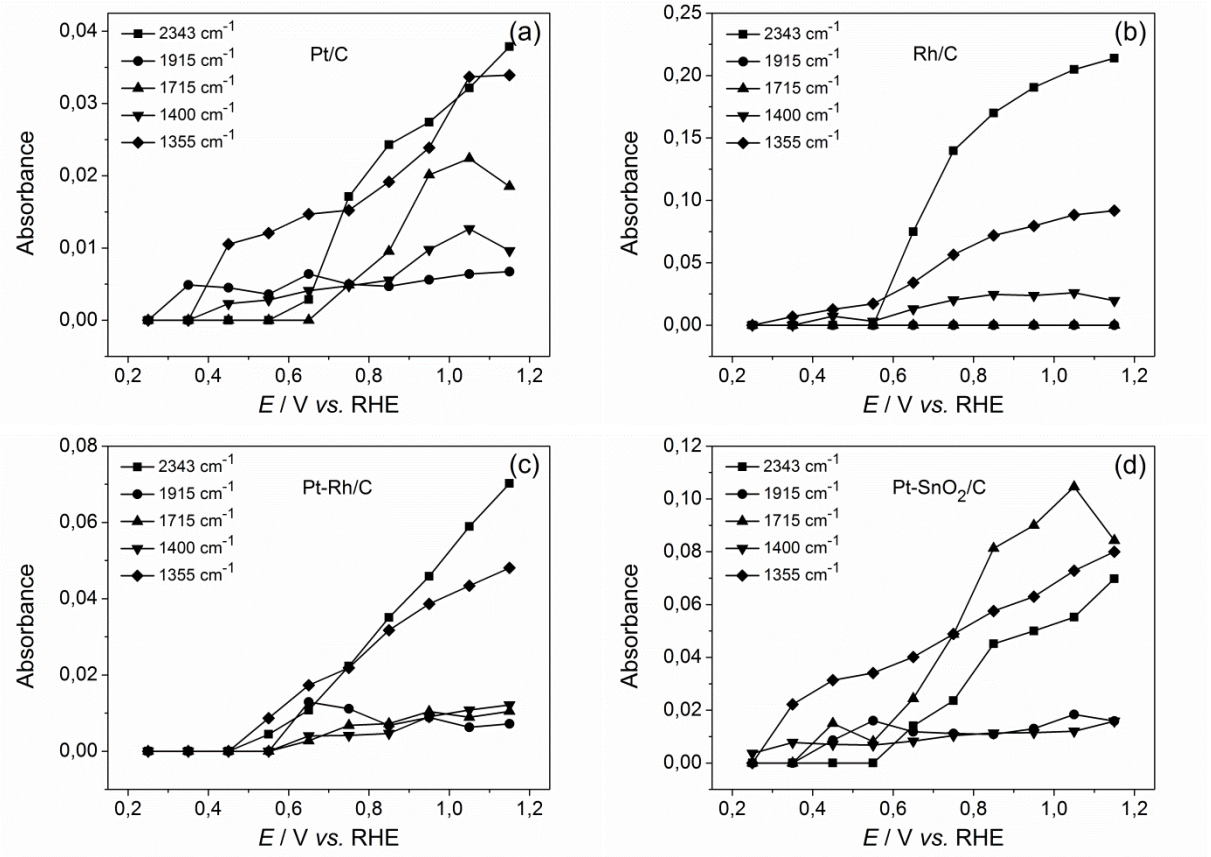

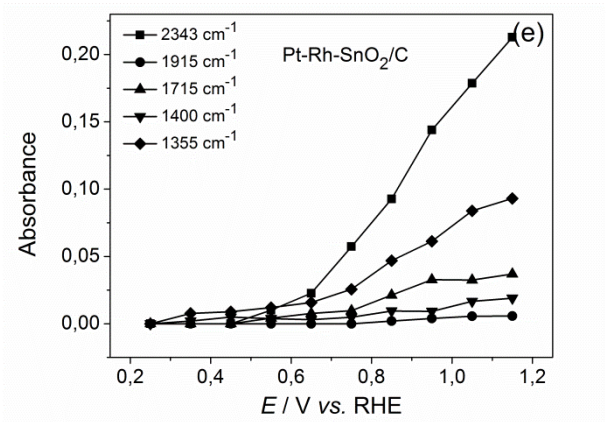

Fig. 35. Evolution of band intensities (at 2343, 1915, 1715, 1400, 1355 cm^{-1}) against applied potential on (a) Pt/C (b) Rh/C, (c) Pt-Rh/C, (d) Pt-SnO_2/C and (e) Pt-Rh-SnO_2/C.

III.2.5.4. Comparison *in situ* FTIR and on-line DEMS measurements

A similar comparison than in Fig. 33 between the EOR CV and corresponding mass-to-charge signals *m/z* = 29, *m/z* = 22 and *m/z* = 61 to the evolution against the potential of the IR-bands at 1355 cm^{-1} (acetaldehyde), 2343 cm^{-1} (CO_2) and 1400 cm^{-1} (acetic acid) is displayed in Fig. 36 on Rh/C, Pt-Rh/C and Pt-SnO_2/C and Pt-Rh-SnO_2/C. The signal *m/z* = 61 of Rh/C is not displayed in Fig. 36A as it remained flat during the CV showing the absence of acetic acid formation during the CV. As represented in Fig. 33, the three potential regions are defined by the different dashed lines. Table 6 summarizes their onset potentials (including Pt/C).

On the one hand, confronting the IR- and MS-results demonstrates the reasonable accordance between the two techniques. Indeed, the values corresponding to the beginning of the first and second potentials region (beginning of ethanol dehydrogenation and CO_2 generation) evaluated with the signals *m/z* = 22 and *m/z* = 29 correlate to the potential values of the bands appearance at 2343 cm^{-1} and at 1355 cm^{-1}. An exception could be noticed however for acetaldehyde band, which appears 200 mV higher compared to the rise of the signal *m/z* = 29 on Pt-Rh/C (Fig. 36B).

On the other hand, the bands evolution seems to be shifted toward positively in regard to the mass spectrometric signals. This observation seems however true on Rh/C (Fig. 36A), Pt-Rh/C (in Fig. 36B) and Pt-Rh-SnO_2/C, but not on Pt-SnO_2/C, for which acetaldehyde and acetic acid bands demonstrate an opposite behavior. This positive shift compared to the MS signals, which seems also present in Fig. 33 for Pt/C, could be ascribed to the discriminating mass-transport conditions in the thin layer configuration which hinder the replenishment of the electrolyte and, more particularly, of the ethanol molecules and of the OH^--species, necessary for CO_2 and acetic acid formation.

In all three Pt-based electrocatalysts and, similarly to Pt/C, the evolution of the CO_2 band at 2343 cm^{-1} is almost linear and keep increasing at the same rate without showing any hindrance at high potentials, as it could be expected when looking at the CVs. On the contrary, the formation of a threshold indicating that much less CO_2 is produced during the CV can be observed for Rh/C at high potentials in Fig. 36A. This observation is supported by the signal m/z = 22: the CO_2 formation starts decreasing between 60 mV and 100 mV earlier than on the Pt-based electrocatalysts at E = 0.69 V *vs.* RHE (see Table 6). It is assumed that the massive adsorption of OH-adsorbates on rhodium surface could stop ethanol electrooxidation at lower potentials than on the Pt-based electrocatalysts (because it leaves no free sites for ethanol adsorption).

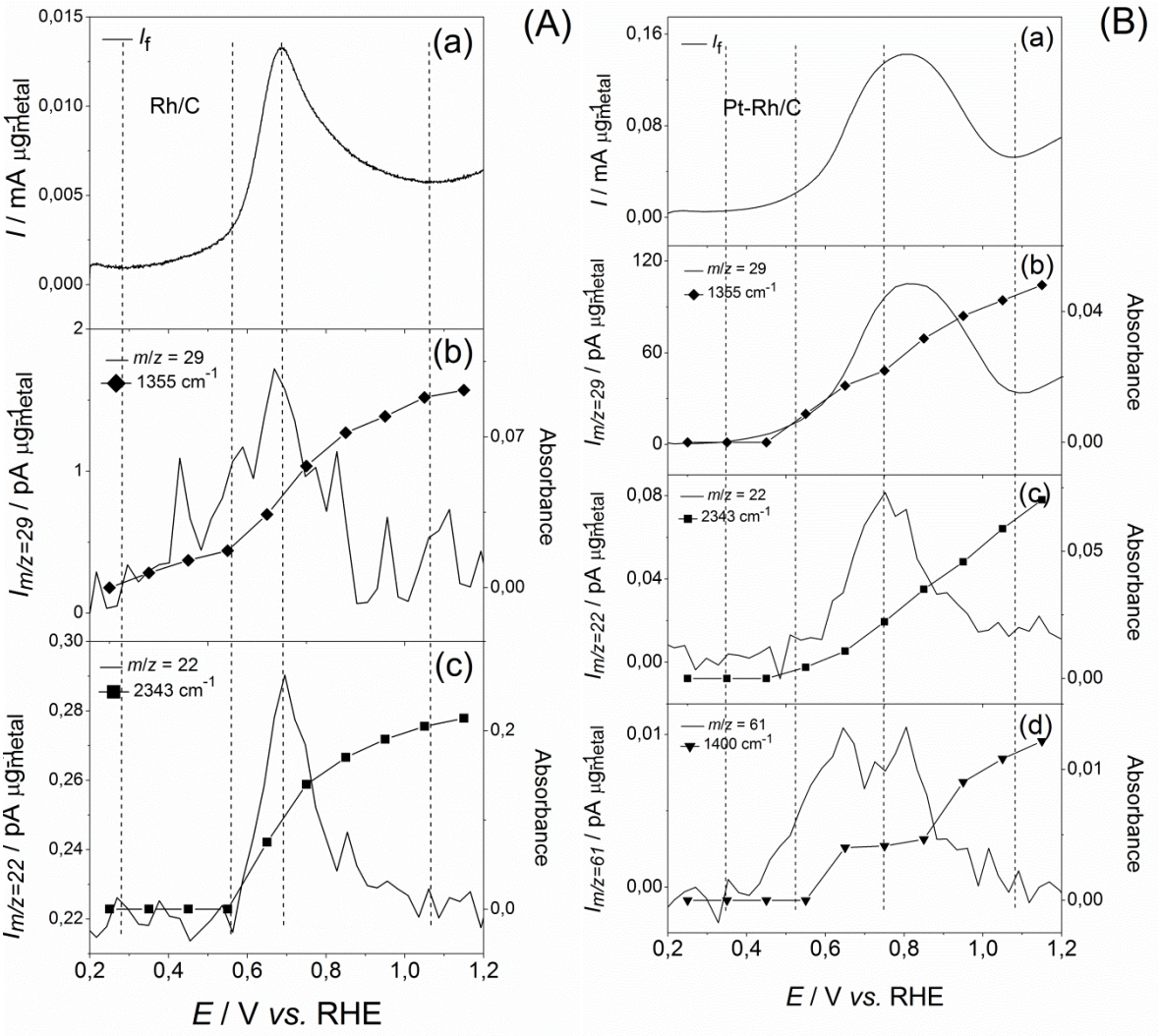

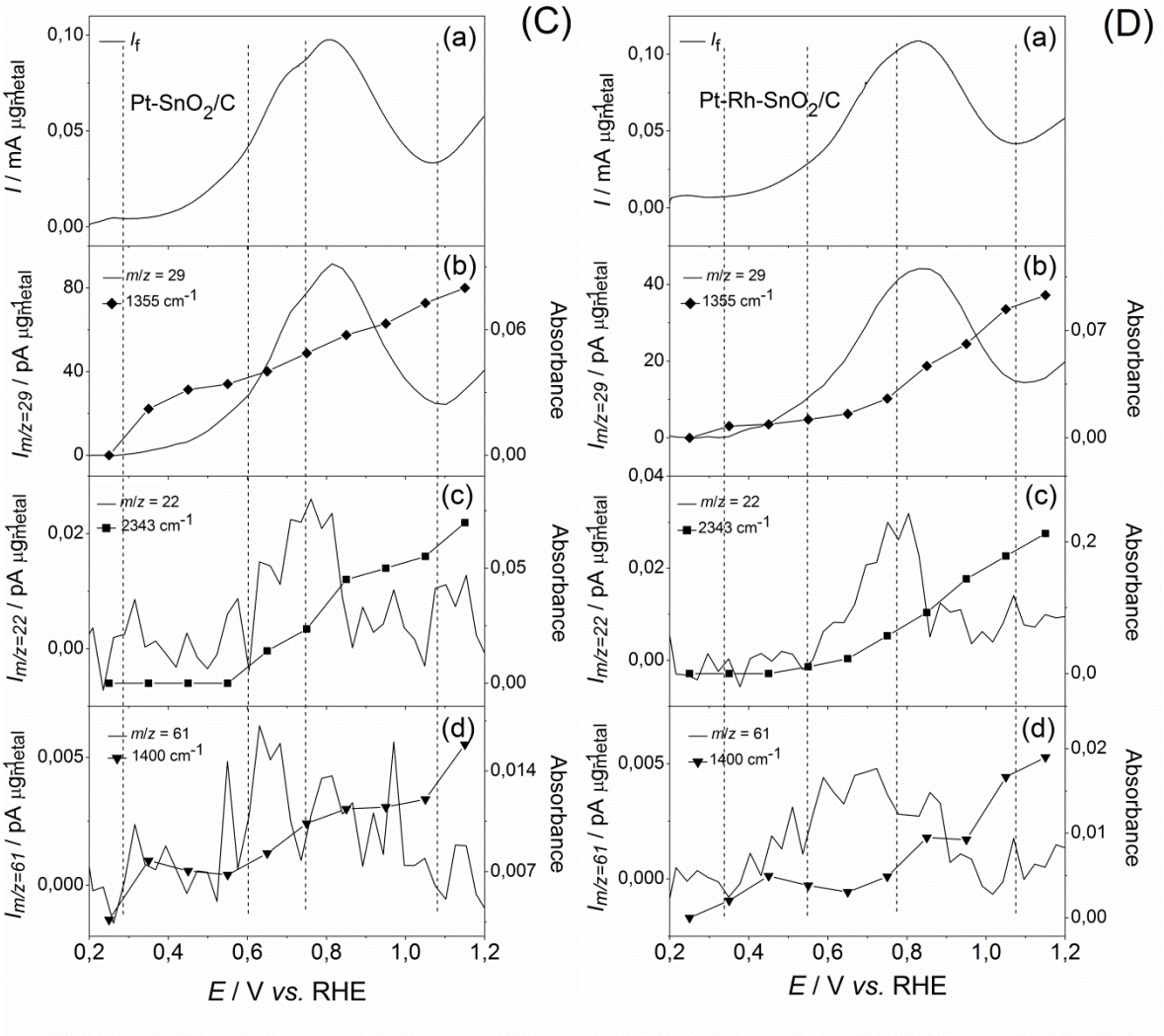

Fig. 36. (a) EOR cyclic voltammetry (in 0.5 M H_2SO_4 + 0.1 M EtOH) on (A) Rh/C, (B) Pt-Rh/C, (C) Pt-SnO_2/C and (D) Pt-Rh-SnO_2/C and corresponding MSCVs associated with EOR IR-bands (from Fig. 35): (b) *m/z* = 29 + 1355 cm^{-1}, (c) *m/z* = 22 + 2343 cm^{-1} and (d) *m/z* = 61 + 1400 cm^{-1} on Pt/C; v = 10 mV s^{-1}; T = 25°C.

Table 6. Onset potential values of the three defined potential regions highlighted in Fig. 33 and Fig. 36 on Pt/C, Rh/C, Pt-Rh/C, Pt-SnO_2/C and Pt-Rh-SnO_2/C during the potentiodynamic EOR recorded after a CA at E_{ad} = 0.05 V *vs.* RHE.

	Pt/C	Rh/C	Pt-Rh/C	Pt-SnO_2/C	Pt-Rh-SnO_2/C
Potential region onset	*E* / V *vs.* RHE				
(1)	0.36	0.28	0.35	0.29	0.34
(2)	0.59	0.56	0.53	0.60	0.55

(3)	0.79	0.69	0.75	0.75	0.77

The variations of the CO_2 current efficiency (CCE) against the potential is represented in Fig. 37. The CCE values were determined from potendiodynamic voltammetries and the corresponding mass-to-charge signal *m*/*z* = 22 between *E* = 0.5 and 0.9 V *vs.* RHE (0.1 V step) on Pt/C, Pt-Rh/C, Pt-SnO_2/C and Pt-Rh-SnO_2/C according to the procedure detailed in section II.7.1. Among the studied electrocatalysts, Pt-Rh-SnO_2/C demonstrates the highest CO_2 current efficiency on the whole potential range, while Pt/C and Pt-SnO_2/C displayed the lowest values in the potential range *E* = 0.6 - 0.7 V *vs.* RHE. Fig. 37 confirms quantitatively the qualitative comparison done in Fig. 35 which showed that the complete EOR was favored on Pt-Rh-SnO_2/C. A more detailed description of Fig. 37 is done in section IV.

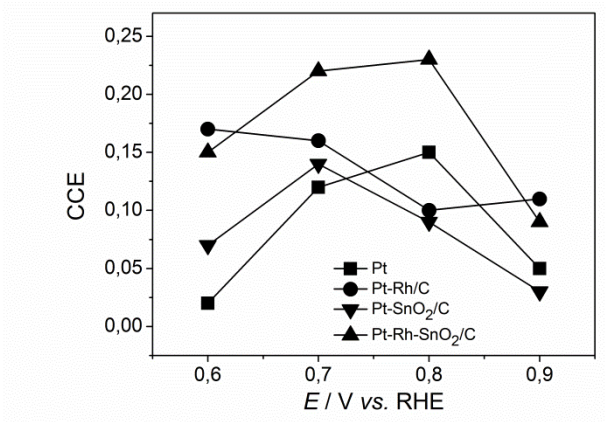

Fig. 37. (a) EOR CO_2 current efficiency (CCE) values calculated from cyclic voltammetries run in 0.5 M H_2SO_4 + 0.1 M EtOH (represented in Fig. 33 and Fig. 36) and corresponding MSCVs (in Fig. 33 and Fig. 36) on Pt/C, Pt-Rh/C, Pt-SnO_2/C and Pt-Rh-SnO_2/C.

III.2.6. Conclusions on the addition of transition metals to platinum

The influence of the addition of rhodium and tin oxide to platinum was investigated in regard to the potentiodynamic ethanol electrooxidation by on-line differential electrochemical mass spectrometry (DEMS) and *in situ* Fourier transform infrared (FTIR) spectroscopy. To that purpose, the study was carried out on home-made Pt/C, Rh/C, Pt-Rh/C, Pt-SnO_2/C and Pt-Rh-SnO_2/C characterized by ICP-AES, XRD and TEM. The three main products of the EOR: acetaldehyde, acetic acid and CO_2, were detected using the mass-to-charge signals *m*/*z* = 29, 22 and 61 and the IR-bands at 1355, 1400 and 2343 cm^{-1} respectively.

A modification of the hydrogen and oxygen region on platinum was induced by the addition of rhodium and tin oxide. These changes were explained by rhodium and, to a larger extent, tin oxide oxophilic character, as well as an enhanced dehydrogenation on Pt-Rh/C, Pt-

SnO_2/C and Pt-Rh-SnO_2/C. The initiation at lower potentials of the CO-stripping on the bi- and tri-metallic electrocatalysts in regard to Pt/C was evidenced by *in situ* FTIR and DEMS analyses: it was explained by the enhanced OH_{ad}-supply at low potentials on the electrocatalyst, thanks to the oxophilic tin oxide and rhodium moieties. A possible modification of platinum electronic configuration is also considered.

The *in situ* FTIR study revealed that the complete ethanol electrooxidation to CO_2 was intensified on Pt-Rh-SnO_2/C compared to the other electrocatalysts. This information was confirmed by a DEMS investigation which showed a slight shift of the EOR initiation on Pt-SnO_2/C and Pt-Rh-SnO_2/C and an enhanced CCE on Pt-Rh-SnO_2/C and, to a lower extent, on Pt-Rh/C, especially at "low" potential values (E < 0.8 V *vs*. RHE). While Rh promotes the cleavage of the C-C bond, SnO_2 provides OH-species at low potential and frees rhodium (and platinum) from the hydroxide adsorbates.

Chapter IV.

Influence of H- and OH-adsorbates on the ethanol oxidation reaction – A DEMS Study

This chapter presents a DEMS investigation on the role of pre-adsorbed H- and OH-adsorbates on the EOR on 20 wt.% Pt/C, Rh/C, Pt-Rh/C, Pt-SnO_2/C, Pt-Rh-SnO_2/C electrocatalysts. Previous studies on the influence of adsorbates on the ethanol electrooxidation are initially reviewed. Afterward, the results are introduced and further discussed regarding the EOR response after the pre-adsorption process. The objective of this investigation was to highlight the possible hindrance and enhancement of the EOR performed by the hydrogen and hydroxide adsorbates respectively on Pt/C and to examine whether a similar phenomenon was observed on the bi- and tri-metallic electrocatalysts.

IV.1. Influence of adsorbates on the oxidation of organic molecules

The influence of the presence of water adsorbates (H_{ad}, OH_{ad}) on the electrocatalyst surface on the initiation or even on the mechanism of oxidation of organic species has rarely been reviewed to date. On the one hand, studies on methanol and ethanol adsorbates electrooxidation demonstrated that their adsorption on the electrocatalyst is hindered in the UPD-region by the presence of hydrogen adsorbates [38,72,219–221]. On the other hand, it was observed that H_{ad}-species enhances formic acid adsorption [222]. In all cases, OH_{ad}-species were reported to boost the electrooxidation of organic species [220,222]. According to Bagotzky et al., the adsorption of organic species in the hydrogen region is maximal when the adsorption process requires a hydrogenation reaction (formic acid) whereas it is minimal when the adsorption proceeds through a dehydrogenation reaction [220]. However, although these studies demonstrated the impact of H_{ad}- and OH_{ad}-species on the electrocatalyst coverage in organic species, no MOR or EOR study highlighting the impact of these water adsorbates on the initiation or on the kinetics of the methanol or ethanol electrooxidation was found in the literature.

In the present study, the influence of pre-adsorbed hydrogen and hydroxide species on the ethanol oxidation reaction (EOR) has been investigated on home-made model EOR electrocatalysts (Pt/C, Rh/C, Pt-Rh/C, Pt-SnO_2/C and Pt-Rh-SnO_2/C). The H_{ad}- and OH_{ad}-adsorbates were formed by potentiostatic hold at E_{ad} = 0.05 and 1 V *vs.* RHE, whereas "water adsorbates-free" surfaces were prepared by potentiostatic hold at E_{ad} = 0.3 V *vs.* RHE. The home-made model electrocatalysts were firstly characterized by thermogravimetric analysis (TGA), inductively coupled plasma atomic emission spectrometry (ICP-AES), powder X-ray diffraction (XRD) and transmission electron microscopy (TEM) to determine the metal-to-carbon ratio and metal crystallite/nanoparticles size and distribution on the carbon support. The EOR was thoroughly studied by on-line differential electrochemical mass spectrometry (DEMS) using the mass-to-charge signals *m/z* = 22, *m/z* = 29 and *m/z* = 61, which are representative to CO_2, acetaldehyde and acetic acid formation respectively. The CO_2 current efficiency (CCE) during the electrooxidation reactions was determined after calibration of the mass-to-charge signal *m/z* = 22 according to the procedure detailed in section II.4.2.2.

IV.2. Hydrogen and hydroxide adsorption procedure

Adsorption of hydrogen and hydroxide species on the electrocatalysts surface was carried out by applying the desired potential (E_{ad} = 0.05 and 1 V *vs.* RHE respectively) to the working electrode through a 8 min-long chronoamperometry, while the 0.5 M H_2SO_4 supporting electrolyte was flowing to the working electrode. The solution was then switched to 0.5 M H_2SO_4 + 0.1 M EtOH during 4 min so as to allow a stabilization of the ionic baseline for the studied mass-to-charge signals before the following CVs started (see Fig. 38). For the

sake of comparison, CVs carried out after a CA at E_{ad} = 0.3 V *vs.* RHE were also investigated, as this potential is located in the so-called double layer region, which should prevent any hydrogen or hydroxide adsorption (adsorbate-free electrode).

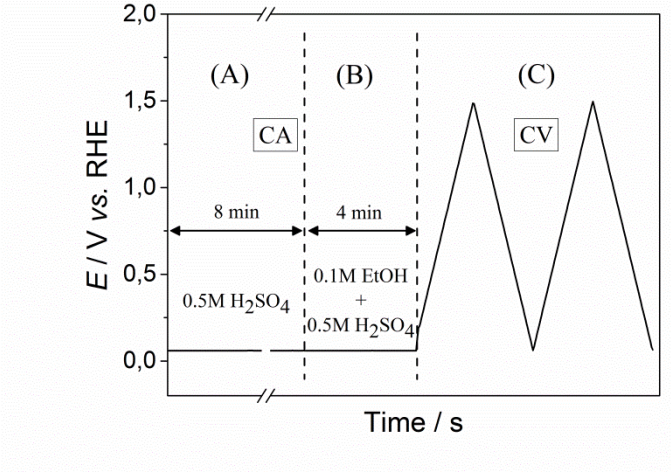

Fig. 38. Potential *vs*. time representation of (A) the adsorbates adsorption in 0.5 M H_2SO_4 (represented here at E_{ad} = 0.05 V *vs.* RHE), (B) the solution change in 0.5 M H_2SO_4 + 0.1 M EtOH and (C) the potentiodynamic ethanol oxidation reaction starting at E = 0.2 V *vs.* RHE.

IV.3. Potentiodynamic ethanol oxidation reaction

IV.3.1. On Pt/C

Fig. 39 presents a comparative study of the first scan of the potentiodynamic voltammograms obtained after a CA at E_{ad} = 0.05, 0.3 and 1 V *vs.* RHE. Apparent faster EOR kinetics can be observed during the CV recorded after the CA at E_{ad} = 1 V *vs.* RHE compared to the CV run after the CA at E_{ad} = 0.05 V *vs.* RHE. Also the associated ionic signals m/z = 29 (Fig. 39b), m/z = 22 (Fig. 39c) and m/z = 61 (Fig. 39d) present a shift toward negative potentials after the CA at E_{ad} = 1 V *vs.* RHE. Clearly, the OH_{ad}-species adsorption during the chronoamperometry at E_{ad} = 1 V *vs.* RHE enhanced ethanol oxidation to acetaldehyde at lower potentials. On the contrary, H-adsorbates formed at E_{ad} = 0.05 V *vs.* RHE do inhibit the reaction. Similarly, CO_2 (Fig. 39c) and acetic acid (Fig. 39d) production are also shifted negatively with the presence of OH-adsorbates. Moreover, it seems that ethanol complete electrooxidation into CO_2 is slightly hindered (in terms of amount produced) and that the mechanism leading to acetic acid as end-product is slightly favored. The result is not surprising as the OH_{ad} species required for the EOR and in particular for acetic acid production are provided during the CA at E_{ad} = 1 V *vs.* RHE; in that sense the electrode pre-oxidation facilitates acetic acid formation at lower potentials. These results are in agreement with the literature, as it was demonstrated that Pt-SnO_2/C electrocatalysts do not favor ethanol

complete oxidation into CO_2, although tin oxide brings hydroxide species at the electrocatalyst surface at lower potentials [30,98,101]. Interestingly, it can also be seen that the acetic acid formation starts at potentials as low as the acetaldehyde production, which could signify that adsorbed acetaldehyde is not required as reaction intermediate to generate acetic acid, as it is often proposed in the literature [21,22]. Finally, the backward scans are in all cases superposed, demonstrating that the pre-formation of such adsorbates cannot maintain durable EOR performance alteration. In all cases, the behavior monitored at E = 0.3 V *vs.* RHE is intermediate between the other two, suggesting that H_{ad} do inhibit the EOR whereas OH_{ad} do favor the reaction.

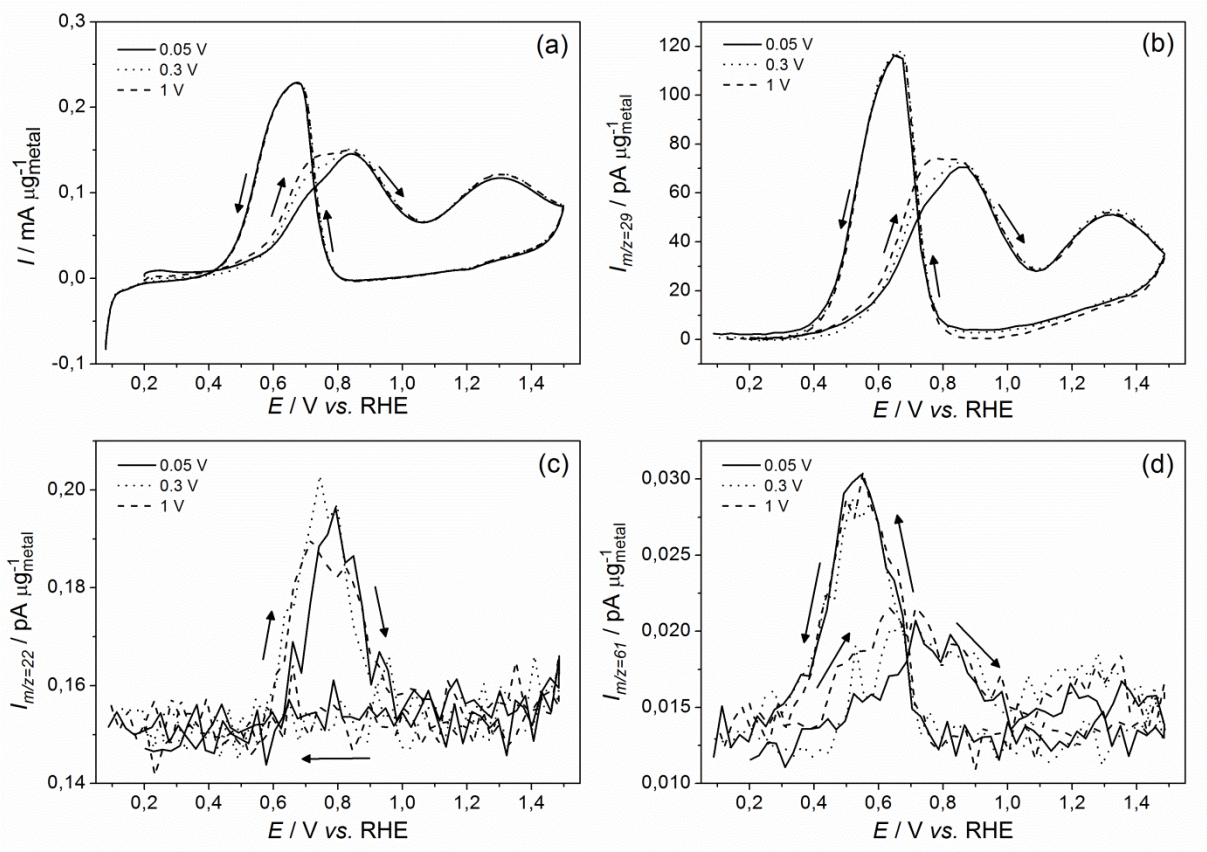

Fig. 39. (a) CV of the EOR in 0.5 M H_2SO_4 + 0.1 M EtOH after adsorption at E_{ad} = 0.05 (solid), 0.3 (dots) and 1 V *vs.* RHE (dash) and corresponding MSCV for mass-to-charge ratio (b) *m/z* = 29, (c) *m/z* = 22 and (d) *m/z* = 61 on Pt/C; v = 10 mV s^{-1}; T = 25°C.

This observation is further confirmed in Fig. 40 which displays the two first cycles of a representative potentiodynamic ethanol electrooxidation on Pt/C and their associated mass-to-charge signals *m/z* = 29, *m/z* = 22 and *m/z* = 61 obtained after a chronoamperometry at E_{ad} = 0.05 (Fig. 40a) and 1 V *vs.* RHE (Fig. 40b). Although ethanol electrooxidation initiates at the same potential (*ca.* E = 0.4 V *vs.* RHE) during the first and second scan, the ethanol oxidation reaction kinetics during the first positive scan is faster than during the following

one, after OH-species adsorption during the CA at E_{ad} = 1 V *vs.* RHE in 0.5 M H_2SO_4 (Fig. 40b). On the contrary, the hydrogen adsorption during the chronoamperometry at E_{ad} = 0.05 V *vs.* RHE seems to hinder ethanol electrooxidation kinetics, as the first scan is delayed compared to the second one (Fig. 40a). According to the literature [35,37,119], the presence of adsorbed hydrogen hinders ethanol adsorption on the electrocatalyst surface, thereby explaining the slower reaction rate during the first scan of the cyclic voltammetry in Fig. 40a. On the opposite, OH_{ad} likely enhances the adsorption/oxidation of organic molecules [223].

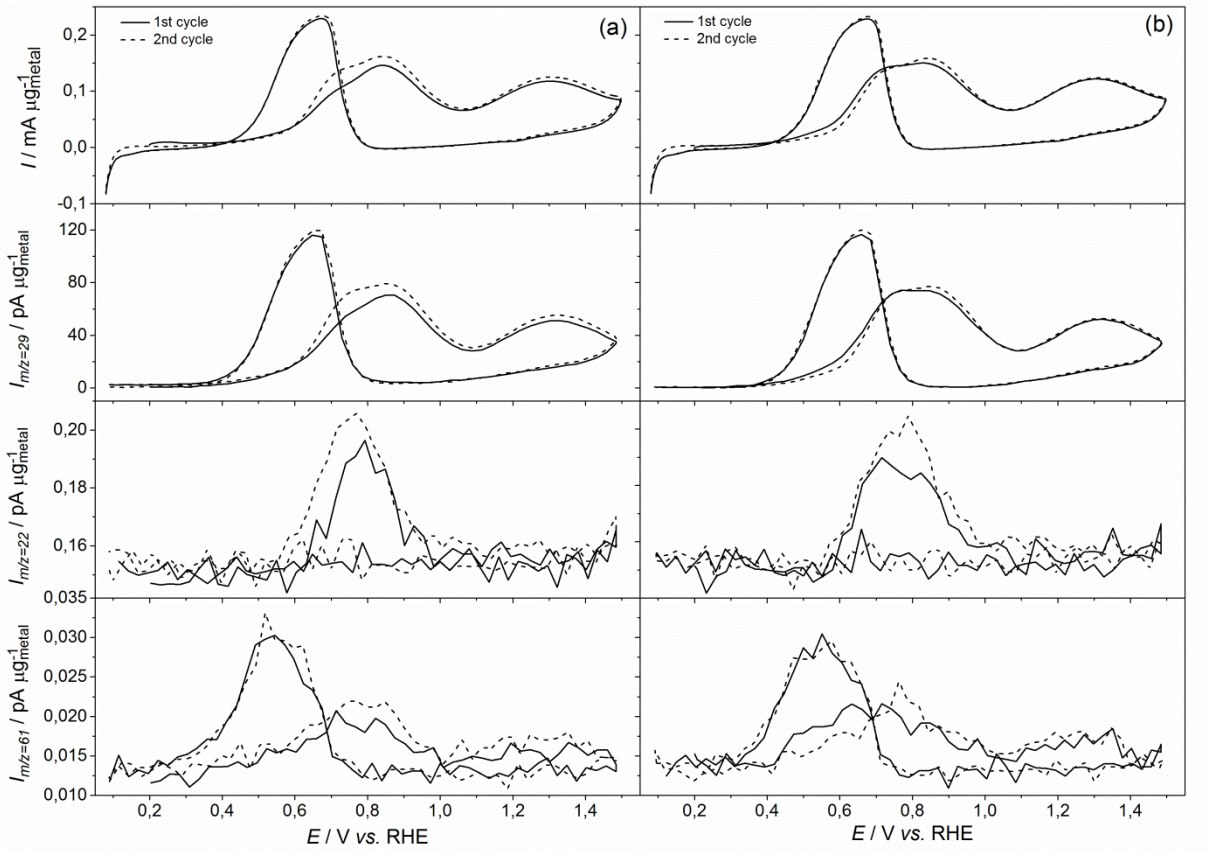

Fig. 40. (solid) First and (dash) second scan of the potentiodynamic EOR in 0.5 M H_2SO_4 + 0.1 M EtOH after adsorption at E_{ad} = (a) 0.05 and (b) 1 V *vs.* RHE and corresponding MSCV for mass-to-charge ratio *m/z* = 44, *m/z* = 22 and *m/z* = 61 on Pt/C; v = 10 mV s^{-1}; T = 25°C.

IV.3.2. On Rh/C

Fig. 41 compares cyclic voltammograms in 0.5 M H_2SO_4 + 0.1 M EtOH on Rh/C preceded by chronoamperometries carried out at E_{ad} = 0.05, 0.3 and 1 V *vs.* RHE. The EOR activity is intensified after hydrogen adsorption on the electrocatalyst surface (seen for E_{ad} = 0.05 V *vs.* RHE), although it remains very low in comparison to Pt/C. The EOR CVs for the two other adsorption potential values are inhibited by OH adsorption, OH_{ad} being very stable

on rhodium surface (the OH reduction peak is located at *ca.* E = 0.33 V *vs.* RHE *versus* E = 0.75 V *vs.* RHE on Pt/C – see Fig. 26) [224,225]. This observation is confirmed by the weak signals reported after E_{ad} = 0.3 and 1 V *vs.* RHE for the mass-to-charge signal m/z = 29 and 22 in Fig. 41b and Fig. 41c respectively. It can be noticed from the CV preceded by the CA at E_{ad} = 1 V *vs.* RHE that, although rhodium provides OH-species at low potentials, the EOR insignificantly proceeds to the generation of acetaldehyde (m/z = 29) and CO_2 (m/z = 22) and does not yield to acetic acid (m/z = 61 - not shown here). This behavior is contradictory with that of Pt/C. One assumption could be that ethanol can hardly displace OH-adsorbates on Rh/C surfaces (similarly to sulfate adsorbates [224,226]), conversely to what occurs on Pt/C and, as a consequence, cannot benefit from the electrocatalyst surface composition *a priori* favorable to acetic acid formation. Moreover, ethanol dissociative adsorption leading to CO_2 formation requires free electrocatalytic sites, which is, in our set of experiments, only encountered after the chronoamperometry carried out at E_{ad} = 0.05 V *vs.* RHE (surface pre-reduction).

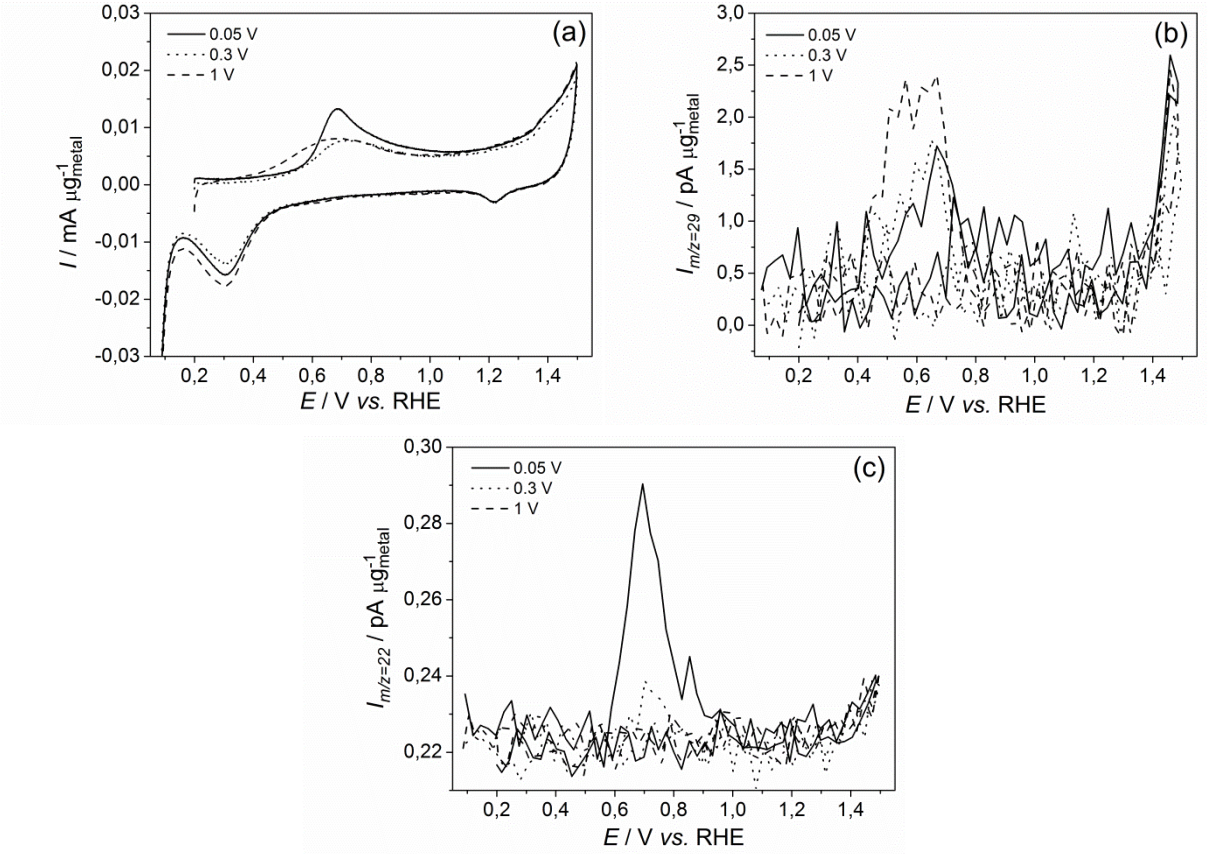

Fig. 41. (a) CV of the EOR in 0.5 M H_2SO_4 + 0.1 M EtOH after adsorption at E_{ad} = 0.05 (solid), 0.3 (dots) and 1 V *vs.* RHE (dash) and corresponding MSCV for mass-to-charge ratio (b) m/z = 29, (c) m/z = 22 on Rh/C; v = 10 mV s^{-1}; T = 25°C.

Further information can be obtained in Fig. 42 by comparing the first and second cycle of the potentiodynamic ethanol oxidation reaction on Rh/C preceded by hydrogen adsorption at E_{ad} = 0.05 V *vs.* RHE. As shown in Fig. 42a, the second cycle is very similar to the CV obtained after adsorption at E_{ad} = 1 V *vs.* RHE (shown in Fig. 41a). In Fig. 42b, the mass-to-charge signal *m*/*z* = 22 discloses a high CO_2 production (starting at *ca.* *E* = 0.56 V *vs.* RHE) during the first cycle compared to the second one where almost no CO_2 was detected.

The mass-to-charge signal *m*/*z* = 29 gives further information on the mechanism that operates during the two cycles. During the first cycle, quasi no acetaldehyde is detected (Fig. 42c) while, during the second one, a small but noticed amount of acetaldehyde emerged during the cyclic voltammetry. It seems that, during the first cycle, the EOR proceeds almost solely through its complete oxidation pathway leading to CO_2 formation and produces neither acetaldehyde nor acetic acid. On the contrary, a small amount of acetaldehyde and near-zero CO_2 could be detected during the second scan, similarly to the first scan of the CVs preceded by a chronoamperometry at E_{ad} = 0.3 and 1 V *vs.* RHE (Fig. 41). It can therefore be assumed that the presence of OH-adsorbates on the Rh/C surface inhibits considerably the complete EOR leading to CO_2 (by impeding ethanol adsorption) and even slightly encourages acetaldehyde formation (ethanol dissociative adsorption is no longer possible due to the overwhelming OH-adsorbates on rhodium surface). Finally, a large rise of the signal *m*/*z* = 29 is observed at high potential (*E* > 1.2 V *vs.* RHE, Fig. 42c), which can only correspond to acetaldehyde formation (a similar increase was obtained with signal *m*/*z* = 15 ($[CH_3^+]$) not shown here). This acetaldehyde formation is expected to come from the oxidation of C_2-species, only possible at high potential [185,227].

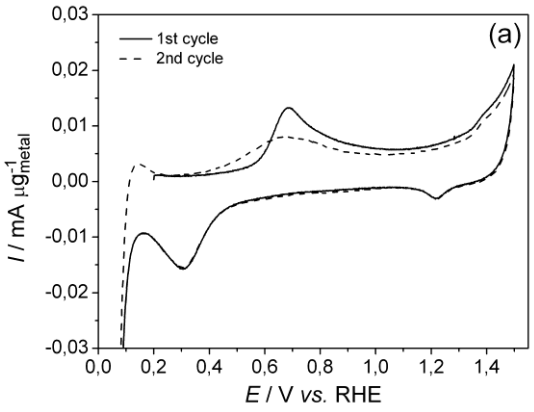

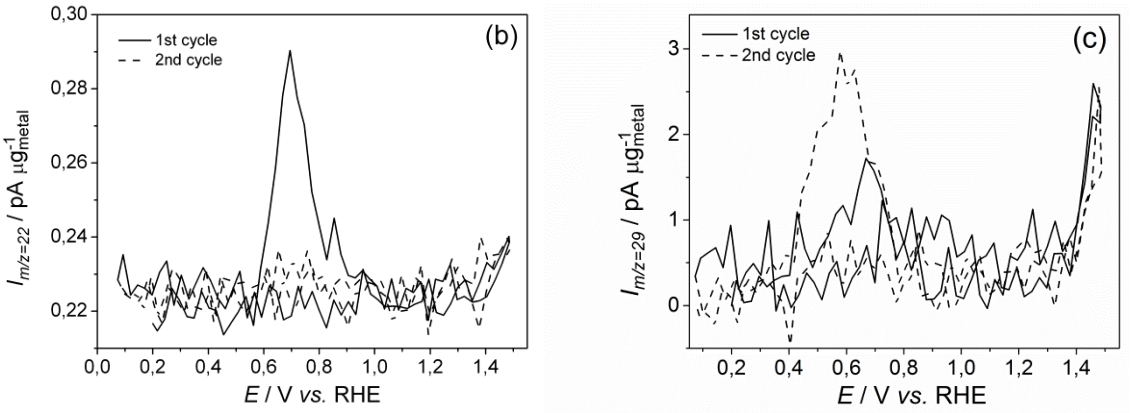

Fig. 42. (solid) First and (dash) second scan of the (a) potentiodynamic EOR in 0.5 M H_2SO_4 + 0.1 M EtOH after adsorption at E_{ad} = 0.05 V *vs.* RHE and corresponding MSCV for mass-to-charge ratio (b) *m/z* = 22 and (c) *m/z* = 29 on Rh/C; v = 10 mV s^{-1}; T = 25°C.

IV.3.3. On Pt based bi- and tri-metallic electrocatalysts

In Fig. 43, a particular attention is paid to the influence of the different chronoamperometries achieved prior to the cyclic voltammetries in 0.5 M H_2SO_4 + 0.1 M EtOH on Pt-Rh/C, Pt-SnO_2/C and Pt-Rh-SnO_2/C. On Pt-Rh/C, they obviously do not impact much the reaction initiation (Fig. 43a). As platinum and rhodium have opposite behaviors regarding the strength of H- and OH-adsorbates, the lack of adsorbate effect could be imputed to a combined effect of Pt and Rh metals lowering the stability of OH_{ad} and H_{ad} on Pt-Rh/C and thus easing their displacement by ethanol molecules. Similarly, the EOR on Pt-Rh-SnO_2/C (Fig. 43c) does not seem much influenced by the adsorbates. However, as for Pt/C, the EOR kinetics on Pt-SnO_2/C (Fig. 43b) is significantly hindered by hydrogen adsorbates. This is an indirect evidence that tin oxide does not help the surface dehydrogenation, and that such composite electrocatalyst likely operates through a bifunctional mechanism: Pt adsorbs ethanol and dehydrogenates it, whereas SnO_2 "only" provides OH_{ad} species (at lower potential than Pt).

During the negative scan, the initiation of the ethanol electrooxidation on Pt-Rh/C and Pt-Rh-SnO_2/C occurs at lower potential after the CA at E_{ad} = 1 V *vs.* RHE compared to the CVs obtained after E_{ad} = 0.05 and 0.3 V *vs.* RHE. This may reflect the higher stability of the OH-adsorbates on Rh surface or on Pt modified surface (electronic interactions between platinum and rhodium) which could impede ethanol electrooxidation. On the contrary, the EOR on Pt-SnO_2/C remains unchanged, even though hydroxide adsorbates are more stable on tin oxide. This can be interpreted by the fact that ethanol does not adsorb on SnO_2, which is just an oxophilic source of OH_{ad}-species as stated above.

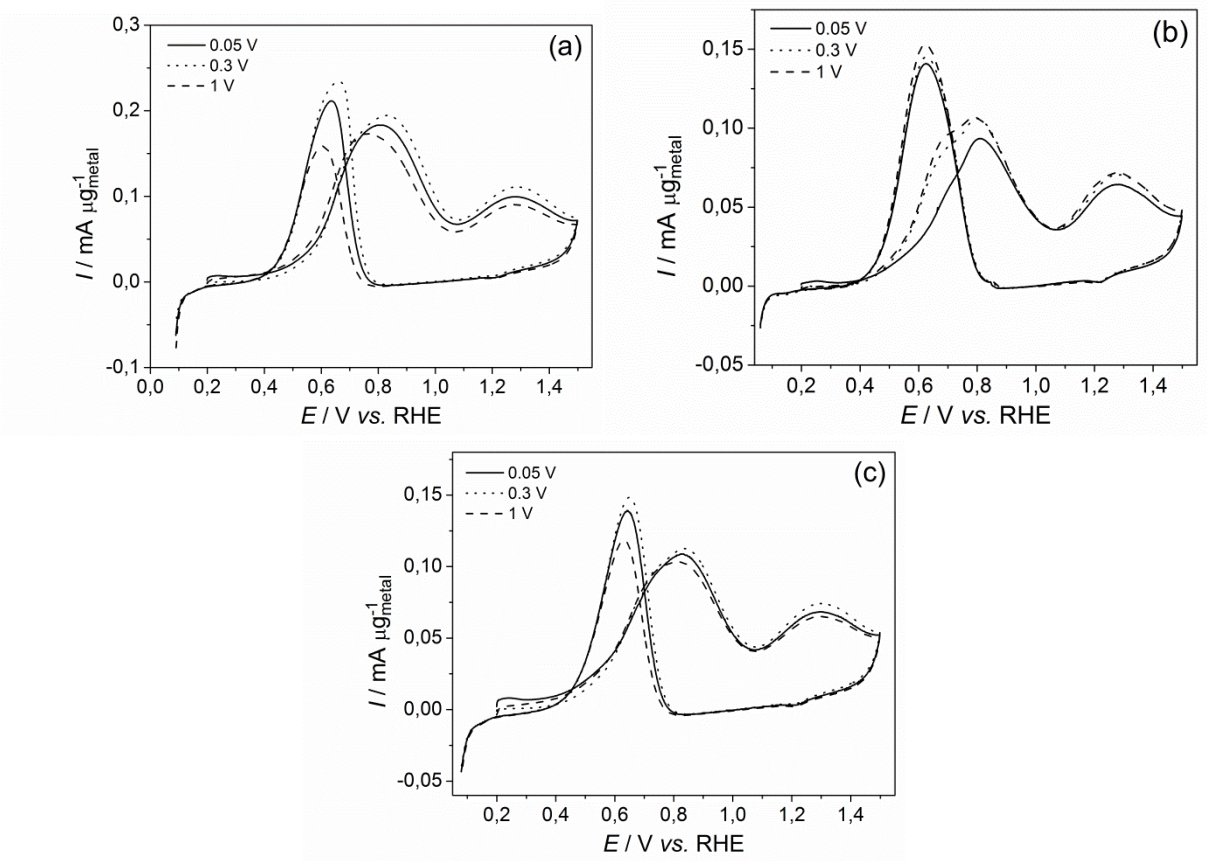

Fig. 43. CV of the EOR in 0.5 M H_2SO_4 + 0.1 M EtOH after adsorption at E_{ad} = 0.05 (solid), 0.3 (dots) and 1 V *vs.* RHE (dash) on (a) Pt-Rh/C, (b) Pt-SnO_2/C and (c) Pt-Rh-SnO_2/C; v = 10 mV s^{-1}; T = 25°C.

IV.4. EOR comparative study between the electrocatalysts

Fig. 44 compares the EOR after a chronoamperometry at E_{ad} = 0.05 V *vs.* RHE on Pt/C, Pt-Rh/C, Pt-SnO_2/C and Pt-Rh-SnO_2/C. The ethanol electrooxidation on Rh/C is ignored as the reaction electroactivity was too low in comparison to the other electrocatalysts. As shown in the inset of Fig. 44, the EOR initiates on all electrocatalysts at *ca.* E = 0.35 V *vs.* RHE. Nonetheless, a higher reaction electroactivity (normalized by the total metal mass) was recorded on Pt-Rh-SnO_2/C and on Pt-SnO_2/C compared to Pt/C until E = 0.62 V *vs.* RHE. Such faster current increase during the EOR at very low potential values can be explained by faster ethanol dehydrogenation kinetics (2 e^-) or by an enhanced ethanol electrooxidation toward acetic acid (4 e^-) or CO_2 (12 e^-).

Conversely, Pt/C clearly surpasses all the multi-metallic electrocatalysts at E > 0.62 V *vs.* RHE. Pt lower metal content in Pt-SnO_2/C (see Table 4) and Pt-Rh-SnO_2/C compared to Pt/C (which is the most electroactive pure metal in acid medium) could explain the larger

peak current at E = 0.88 V *vs.* RHE on the latter (the current is normalized to the total mass of metal). However, this explanation does not work for Pt-Rh/C, the Pt:Rh ratio of which is almost 1:1. Although the EOR activity is not very large on Rh alone (Fig. 41) compared to Pt (Fig. 39), the EOR on Pt-Rh/C exhibits currents as high as on Pt/C. This could be due to an alloy effect between the two metals and to a facilitation of the C-C bound breaking in the presence of Rh.

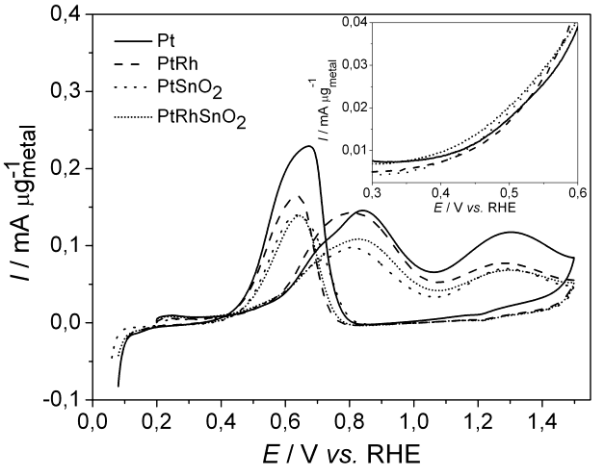

Fig. 44. (a) CV of the EOR in 0.5 M H_2SO_4 + 0.1 M EtOH after CA at E_{ad} = 0.05 V *vs.* RHE on Pt/C (solid), Pt-Rh/C (dash), Pt-SnO_2/C (dots) and Pt-Rh-SnO_2/C (short dots); v = 10 mV s^{-1}; T = 25°C.

Regarding the mass-to-charge signals m/z = 22, 29 and 61 (Fig. 45), acetaldehyde formation (m/z = 29) starts at *ca.* E = 0.27 V *vs.* RHE on Pt-Rh/C and E = 0.24 V *vs.* RHE on Pt-SnO_2/C and Pt-Rh-SnO_2/C versus E = 0.31 V *vs.* RHE on Pt/C. This observation agrees with the larger dehydrogenation on Pt-Rh/C, Pt-SnO_2/C and Pt-Rh-SnO_2/C highlighted in Fig. 26. These values are slightly lower than those depicting the faraday current onset, due to the non-quantitative formation of acetaldehyde which generates a too low current to be observable in Fig. 45. Acetic acid formation starts shortly after *ca.* E = 0.35 V *vs.* RHE on Pt-Rh-SnO_2/C and E = 0.32 V *vs.* RHE on Pt-Rh/C and Pt/C. Pt-SnO_2/C seems to ease acetic acid formation better than the other electrocatalysts at low potential (onset at *ca.* E = 0.28 V *vs.* RHE), because the SnO_2 moiety is capable to easily provide OH_{ad}-species to the acetaldehyde adsorbed at the Pt moiety. However, at higher potential, acetic acid formation seems more enhanced on Pt-Rh/C electrocatalyst. Conversely to the literature [30,101], our synthesized Pt-SnO_2/C electrocatalyst does not seem to favor the pathway leading to acetic acid formation compared to Pt/C. PtSnO_2/C peculiar physical structure (presence of larger nanoparticles and agglomerates) could explain these divergent results. Unfortunately, the few existing studies focused on the nanoparticles size effect [35,172] do not give evidence of a clear influence of the nanoparticles size on the EOR pathway (even less is known about the influence of agglomerates, except regarding CO oxidation [57,197]). Finally, CO_2 generation

seems slightly shifted negatively on Pt-based bi- and tri-metallic electrocatalysts compared to Pt/C. Indeed, CO_2 could be detected at potentials as low as E = 0.54 V *vs.* RHE on Pt-Rh-SnO_2/C versus E = 0.58 V *vs.* RHE on Pt-Rh/C and E = 0.61 V *vs.* RHE on Pt/C. CO_2 was also generated during the negative scan on Pt-SnO_2/C. Ionic (m/z = 22, 29 and 61) reaction onsets of all studied electrocatalysts (comprised Rh/C) are summarized in Table 7.

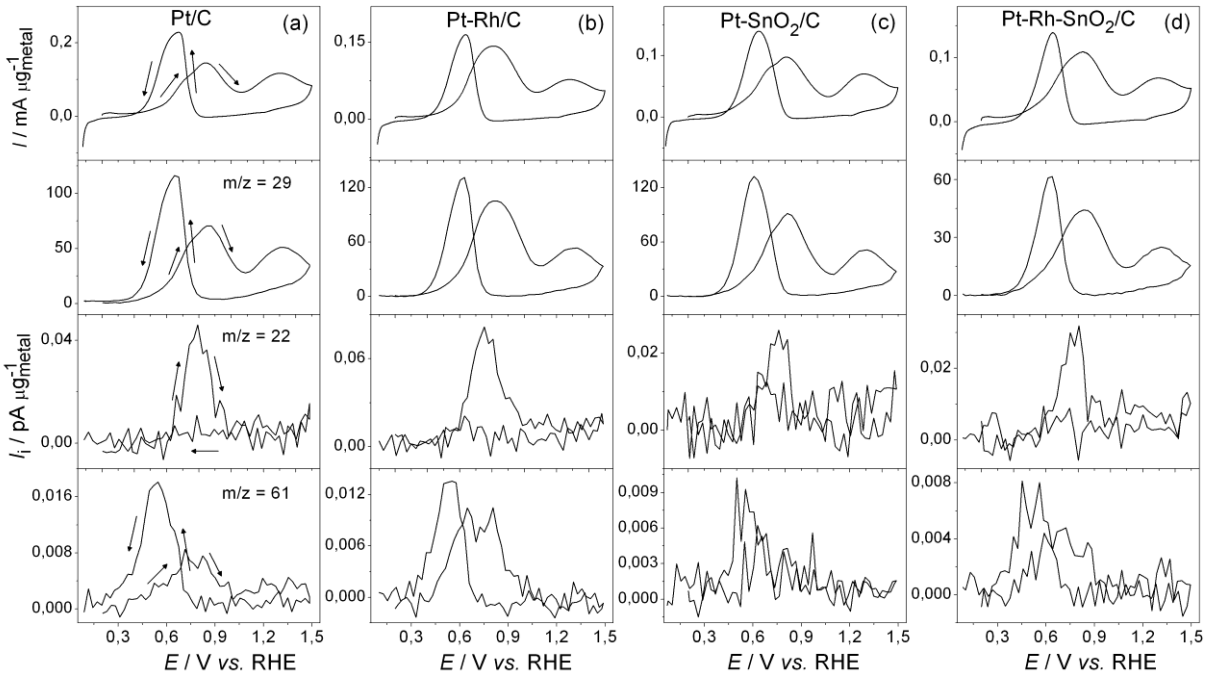

Fig. 45. CV of the EOR in 0.5 M H_2SO_4 + 0.1 M EtOH after adsorption at E_{ad} = 0.05 on (a) Pt/C, (b) Pt-Rh/C, (c) Pt-SnO_2/C and (d) Pt-Rh-SnO_2/C and corresponding MSCV for mass-to-charge ratio m/z = 29, m/z = 22 and m/z = 61; v = 10 mV s^{-1}; T = 25°C.

Table 7. Onset potential values of the mass-to-charge signals m/z = 22, 29 and 61 measured on Pt/C, Rh/C, Pt-Rh/C, Pt-SnO_2/C and Pt-Rh-SnO_2/C during the potentiodynamic EOR recorded after a CA at E_{ad} = 0.05 V *vs.* RHE.

	Pt/C	Rh/C	Pt-Rh/C	Pt-SnO_2/C	Pt-Rh-SnO_2/C
m/z			E / V *vs.* RHE		
29	0.31	0.27	0.27	0.24	0.24
22	0.61	0.56	0.58	0.59	0.54
61	0.35	-	0.33	0.28	0.35

IV.5. CO_2 current efficiency

The CO_2 current efficiency (CCE) was determined from potendiodynamic voltammetries and the corresponding mass-to-charge signal m/z = 22 between E = 0.5 and 0.9 V *vs.* RHE (0.1 V step) on Pt/C, Pt-Rh/C, Pt-SnO_2/C and Pt-Rh-SnO_2/C. Regarding the previous results of Fig. 45, the chronoamperometries at E_{ad} = 0.05, 0.3 and 1 V *vs.* RHE do impact the EOR and more specifically the CO_2 production. Consequently, the CCE variation versus the potential was evaluated after chronoamperometries at E_{ad} = 0.05, 0.3 and 1 V *vs.* RHE.

It can be noticed in Fig. 46 that the CCE evolution can be separated in two steps for all electrocatalysts: a first ascending phase between E = 0.6 and *ca.* 0.7 - 0.8 V *vs.* RHE (depending on the previous CA) where the CCE increases against the potential; a second one at E > 0.7 - 0.8 V *vs.* RHE where the CCE decays. The CCE rise in the first potential region can reasonably be explained by the growing adsorption of OH-adsorbates that facilitates the oxidation of adsorbed CO. A second reason could be the improved C-C bond breaking ability gained by the electrocatalyst with the potential increase (although previous studies reported ethanol dissociative adsorption at potentials as low as E = 0.05 V *vs.* RHE [185,227]). On the contrary, in the second potential region (E > 0.7 - 0.8 V *vs.* RHE), CO_2 generation is more and more hindered as the potential increases. It is believed that above a certain potential, the presence of adsorbates on the electrocatalyst surface prevents ethanol dissociative adsorption and *a fortiori* CO_2 generation. These adsorbates are supposedly OH_{ad} and ethanol intermediates [17,29] and are believed to sterically impede the ethanol dissociative adsorption. Fig. 46c shows the relative lower CCE values obtained when the potentiodynamic voltammetry is preceded by the CA at E_{ad} = 1 V *vs.* RHE in comparison to the CVs preceded by the CA at E_{ad} = 0.05 and 0.3 V *vs.* RHE. It is supposed that adsorbed hydroxide species did not have time to desorb completely from the electrocatalyst surface at the beginning of the CV and that the remaining OH_{ad}-species hinder ethanol dissociative adsorption and thus CO_2 generation. An accumulation of ethanol adsorbates on the electrocatalyst surface could also prevent ethanol dissociative adsorption (which likely requires more than two free neighboring electrocatalytic sites). This explanation is supported by the oxidation of CH_x- and C_2-adsorbates only at potentials as high as E = 0.9 V *vs.* RHE [185]. Identifying these ethanol adsorbates would require a thorough IR analysis and is beyond the scope of this study.

Among the studied electrocatalysts, Pt-Rh-SnO_2/C demonstrates the highest CO_2 current efficiency in all three protocols, while Pt/C and Pt-SnO_2/C displayed the lowest values. A higher CO_2 generation on Pt-Rh-SnO_2/C than on PtSnO_2/C evaluated by infrared techniques is also reported in the literature [123]. Low CCE values on Pt/C and Pt-SnO_2/C are also supported in the literature in other DEMS studies [30,98].

The influence of the chronoamperometries at E_{ad} = 0.05, 0.3 and 1 V *vs.* RHE in 0.5 M H_2SO_4 run before the potentiodynamic voltammetries on the CO_2 current efficiency is compared in Fig. 46a, Fig. 46b and Fig. 46c respectively. For each Pt-based electrocatalysts,

the CCE values are generally lower after the chronoamperometry at E_{ad} = 1 V *vs.* RHE, illustrating the observation done with Fig. 45. Although adsorbed OH-species are necessary to oxidize CO_{ad}, a large coverage of the electrocatalyst surface by the OH-adsorbates may hinder CO_{ad} formation coming from adsorbed acetaldehyde or direct ethanol dissociative adsorption. The CA at E_{ad} = 0.3 V *vs.* RHE seems to enhance CO_2 production during the following cyclic voltammetry. Although the original goal of this chronoamperometry was to start the cyclic voltammetry without any adsorbates at the electrocatalyst surface, the mandatory change of solution during the last four minutes of the CA may have, on the contrary, provoked ethanol dissociative adsorption into CO_{ad} before the beginning of the CV. These CO_{ad}-species then likely oxidized as soon as hydroxide molecules started adsorbing on the electrocatalyst surface. That could explain the higher CCE values in Fig. 46b and also why CO_2 generation starts at potentials as low as E = 0.5 V *vs.* RHE on Pt-Rh-SnO_2/C, which also corresponds to the beginning of OH_{ad} formation on the tri-metallic electrocatalyst (see Fig. 77).

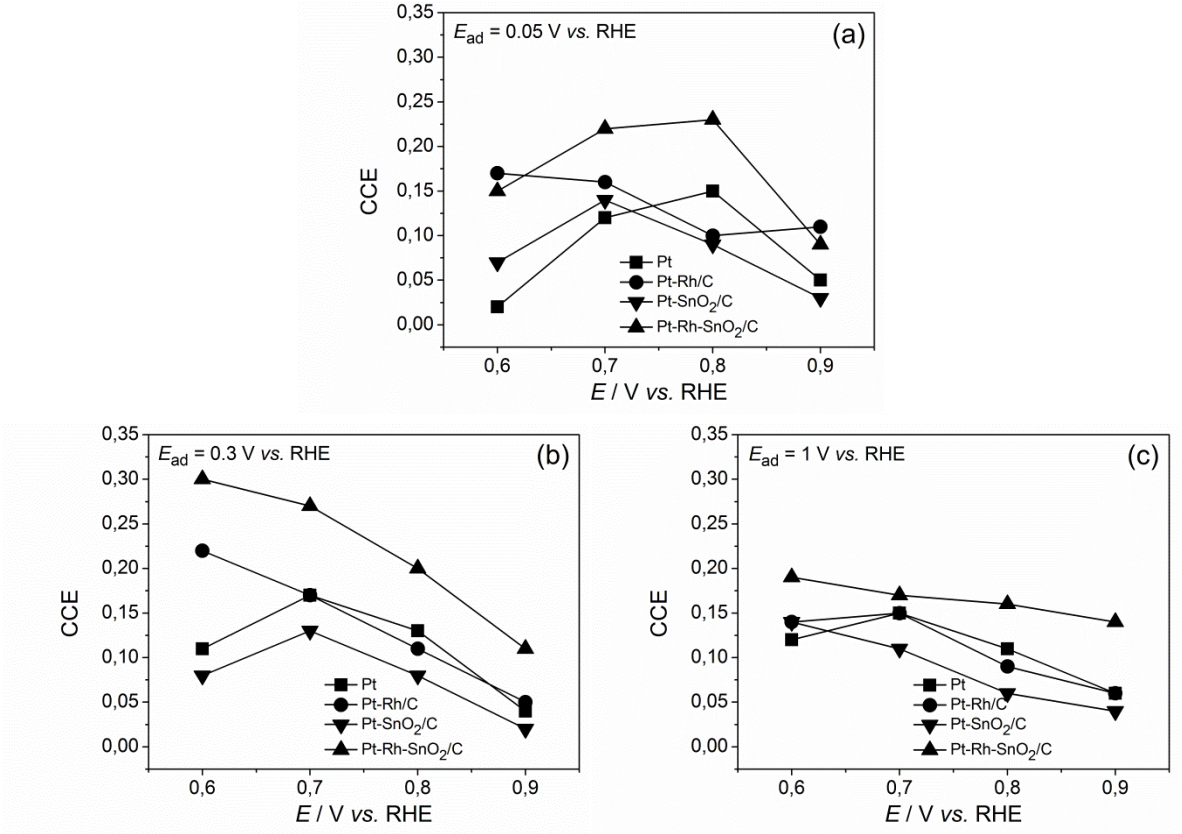

Fig. 46. Potentiodynamic EOR CO_2 current efficiency (CCE) values deduced from cyclic voltammetries in 0.5 M H_2SO_4 + 0.1 M EtOH on Pt/C, Pt-Rh/C, Pt-SnO_2/C and Pt-Rh-SnO_2/C preceded by CA at E_{ad} = (a) 0.05, (b) 0.3 and (c) 1 V *vs.* RHE.

IV.6. Zoom on the CA at E_{ad} = 0.05 V vs. RHE

IV.6.1. On Pt/C and Rh/C

The aim of this section is to demonstrate the difficulty for ethanol to displace adsorbed hydrogen species on Pt/C conversely to Rh/C. To that purpose, the presented figures show the evolution of the potential (left y-axis) and of the mass-to-charge signals (right y-axis) *m*/*z* = 29 ([CHO^+]) and *m/z* = 2 ([H_2^+]) against the time during the chronoamperometry carried out at E_{ad} = 0.05 V *vs.* RHE, followed by the voltamperogram in 0.5 M H_2SO_4 + 0.1 M EtOH (similarly to Fig. 38 but with the additional evolution of the MSCVs *m*/*z* = 2 and *m*/*z* = 29). The particularly interesting information here relies in the behavior of the signal *m*/*z* = 2 after the solution switch from 0.5 M H_2SO_4 to 0.5 M H_2SO_4 + 0.1 M EtOH after the first eight minutes of the CA. The mass-to-charge signal *m*/*z* = 29 (ascribed to ethanol) is used to evidence the solution switch after the first eight minutes of CA. As observed in Fig. 48a and Fig. 48b, the appearance of this signal is slightly delayed (which explains the non superposition of the vertical dashed line with the signal *m*/*z* = 29). This delay corresponds to the time required by the solution to flow in the capillaries, reach the electrochemical cell and be pumped inside the mass spectrometer.

First and foremost, the first decrease of the mass-to-charge signal *m*/*z* = 2 during the first eight minutes of the CA corresponds to a "normal" hydrogen generation response to the potential step from E_{ad} = 1 to 0.05 V *vs.* RHE (a first CA not shown in Fig. 47 was carried out at E_{ad} = 1 V *vs.* RHE in 0.5 M H_2SO_4 during 30 s to clean the electrocatalyst surface from potentially residual ethanol adsorbates coming from a previous CV in 0.5 M H_2SO_4 + 0.1 M EtOH). Contrary to the first step of the CA similar on Pt/C and Rh/C, the second step differs significantly on the two electrocatalysts: on Pt/C (Fig. 47a), the initial ionic (*m*/*z* = 2) current drop during the first eight minutes of the CA is followed by a slight rise/stabilization of the current appearing simultaneously to the signal *m*/*z* = 29, and may sign that a low amount of acetaldehyde is formed from ethanol dehydrogenation on Pt/C at E_{ad} = 0.05 V *vs.* RHE (a by-product of this reaction being H_2). But the high constant ionic (*m*/*z* = 2) current recorded on Pt/C is more believed to illustrate H_2 steady formation and thus ethanol difficulty to adsorb on the electrocatalyst. On the contrary, a further ionic (*m*/*z* = 2) current shrinkage is recorded on Rh/C (Fig. 47b). The latter phenomenon on Rh/C can be explained by the ethanol adsorption taking place quantitatively on the electrocatalyst surface which blocks rhodium electroactive sites and hinders dramatically the hydrogen generation.

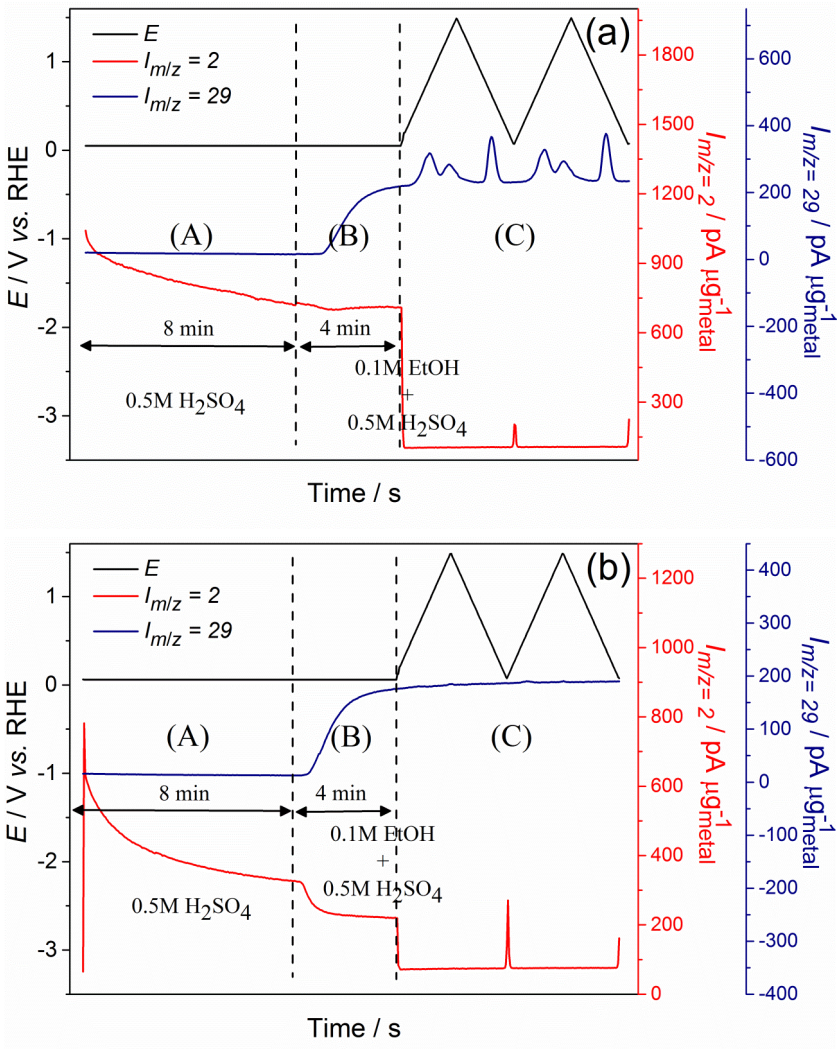

Fig. 47. Evolution of the potential and mass-to-charge ratio signals m/z = 2 and m/z = 29 *vs.* time on (a) Pt/C and (b) Rh/C during three consecutive steps: (A) hydrogen adsorption in 0.5 M H_2SO_4 at E_{ad} = 0.05 V *vs.* RHE, (B) the solution change in 0.5 M H_2SO_4 + 0.1 M EtOH and (C) the potentiodynamic ethanol oxidation reaction starting at E = 0.2 V *vs.* RHE.

IV.6.2. On Pt-based multi-metallic electrocatalysts

Like on Pt/C, the hydrogen generation does not seem impeded by the solution switch to 0.5 M H_2SO_4 + 0.1 M EtOH operated during the chronoamperometry at *ca.* E_{ad} = 0.05 V *vs.* RHE on Pt-Rh/C, Pt-SnO_2/C and Pt-Rh-SnO_2/C (as shown in Fig. 48 for Pt-Rh-SnO_2/C). The low increase/stabilization of the mass-to-charge signal m/z = 2 during step (B), similar to that of Pt/C (Fig. 47a), demonstrates once more that ethanol likely dehydrogetates into acetaldehyde forming in the process H_2, as by product.

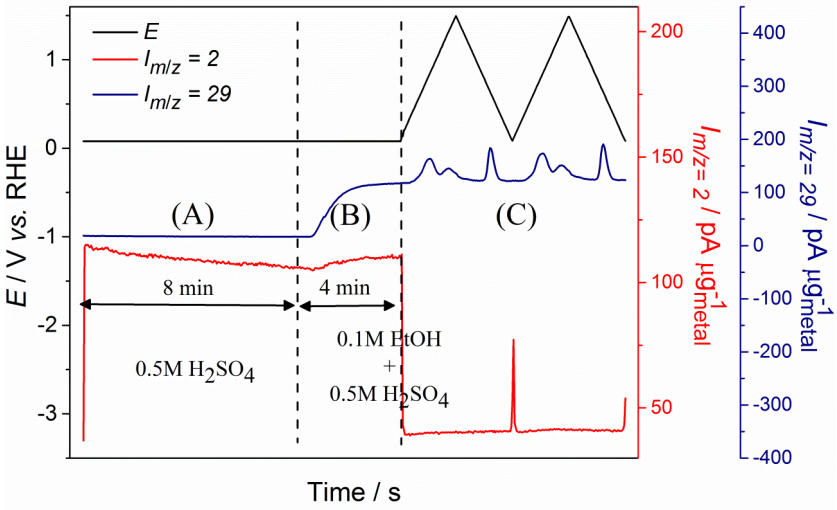

Fig. 48. Evolution of the potential and mass-to-charge ratio signals *m*/*z* = 2 and *m*/*z* = 29 *vs.* time on Pt-Rh-SnO_2/C during three consecutive steps: (A) hydrogen adsorption in 0.5 M H_2SO_4 at E_{ad} = 0.07 V *vs.* RHE, (B) the solution change in 0.5 M H_2SO_4 + 0.1 M EtOH and (C) the potentiodynamic ethanol oxidation reaction starting at *E* = 0.2 V *vs.* RHE.

IV.7. Potentiodynamic acetaldehyde oxidation reaction

IV.7.1. On Pt/C

Fig. 49 presents a comparative study of the first scan of the potentiodynamic voltammetries obtained after a CA at E_{ad} = 0.05, 0.3 and 1 V *vs.* RHE in 0.5 M H_2SO_4 + 0.1 M acetaldehyde. Similarly to the EOR, an initiation at lower potentials can be observed during the CV recorded after the CA at E_{ad} = 1 V *vs.* RHE compared to the one run after the CA at E_{ad} = 0.05 V *vs.* RHE. Moreover, the related mass-to-charge signals *m*/*z* = 22 (Fig. 49b) and *m*/*z* = 60 (Fig. 49c) display a negative shift after the CA at E_{ad} = 1 V *vs.* RHE. This behavior, comparable to the EOR, differs maybe only by the significant proximity of the CVs preceded by the CAs at E_{ad} = 0.3 and E_{ad} = 1 V *vs.* RHE. This proximity shows that it may not be so much the presence of OH-adsorbates that shifts negatively the AOR initiation, but the absence of H-adsorbates (which is the case after both surface treatment at E_{ad} = 0.3 and E_{ad} = 1 V *vs.* RHE). Indeed, the results strikingly show that H-adsorbates formed at E_{ad} = 0.05 V *vs.* RHE do inhibit the reaction at low potential. Likewise, CO_2 (Fig. 49b) and acetic acid (Fig. 49c) production are also shifted positively in the presence of H-adsorbates. The positive shift of the reactions initiation is likely imputed to a positive shift of the adsorption of hydroxide species required for the generation of CO_2 and acetic acid.

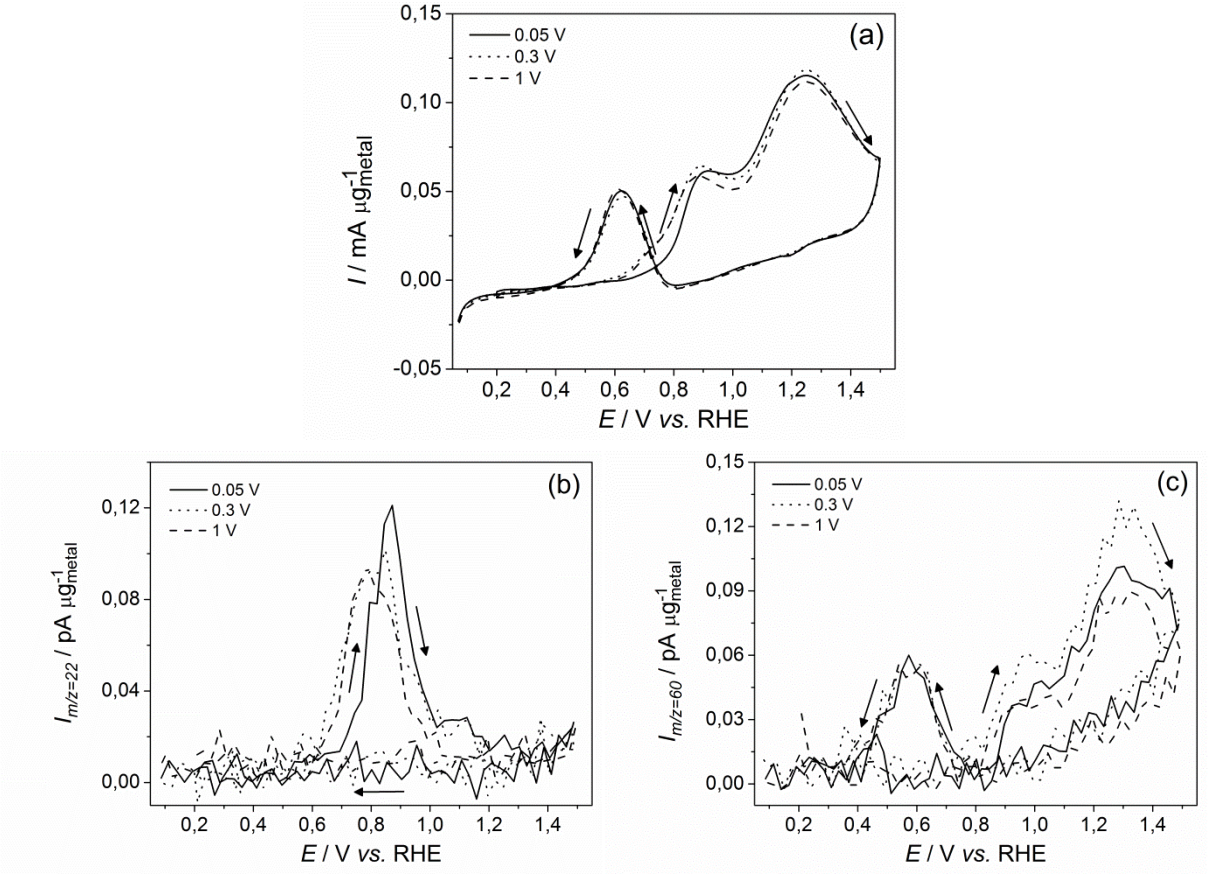

Fig. 49. (a) CV of the EOR in 0.5 M H_2SO_4 + 0.1 M acetaldehyde after adsorption at E_{ad} = 0.05 (solid), 0.3 (dots) and 1 V *vs.* RHE (dash) and corresponding MSCV for mass-to-charge ratio (b) *m/z* = 22 and (c) *m/z* = 60 on Pt/C; v = 10 mV s^{-1}; T = 25°C.

Fig. 50 shows the two first cycles of a representative potentiodynamic acetaldehyde electrooxidation on Pt/C and their associated mass-to-charge signals *m/z* = 22 and *m/z* = 60 obtained after a chronoamperometry at E_{ad} = 0.05 (Fig. 40a) and 1 V *vs.* RHE (Fig. 40b). Hydrogen adsorbates formation during the chronoamperometry at E_{ad} = 0.05 V *vs.* RHE obviously impedes the AOR initiation in a similar manner than it was observed with the EOR. On the opposite, as noticed for Fig. 49, OH-adsorbates do not seem to enhance acetaldehyde electrooxidation. The comparison between the first and second cycle of the CV shows that the initiation potential of the AOR remains constant (contrary to what was observed in Fig. 40b for the EOR). On the contrary, higher faraday and ionic (*m/z* = 22 and *m/z* = 60) currents are even reported during the second cycle compared to the first one. A consistent explanation would be that the OH_{ad}-species, like the H_{ad}-species, block the Pt sites for acetaldehyde adsorption/oxidation. As the hydroxile species are also used during the AOR initiation to form CO_2, the onset potential or the reaction would not be mechanically shifted toward positive potential as it is the case with H_{ad}-species. Another explanantion based on the "history" of the

electrode could rationalize the present results. Indeed, as shown later in chapter V, some acetaldehyde "strong adsorbates" do not react during the first potentiodynamic scan, but only during the second one. The presence of more acetaldehyde adsorbates at the beginning of the second scan could explain the higher currents registered during the latter than during the first sweep.

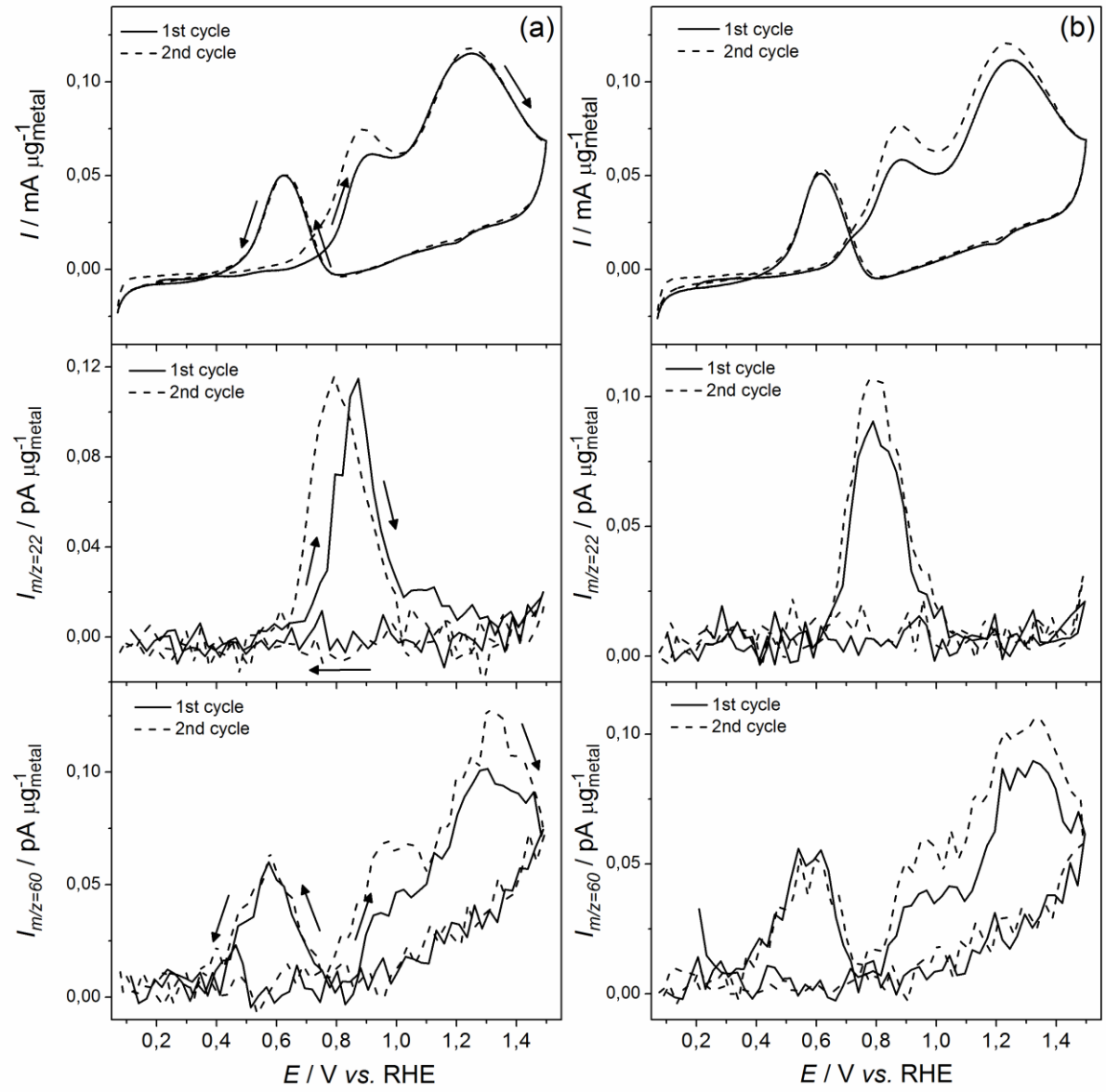

Fig. 50. (solid) First and (dash) second scan of the potentiodynamic acetaldehyde in 0.5 M H_2SO_4 + 0.1 M acetaldehyde after adsorption at E_{ad} = (a) 0.05 and (b) 1 V *vs.* RHE and corresponding MSCV for mass-to-charge ratio *m/z* = 22 and *m/z* = 60 on Pt/C; v = 10 mV s^{-1}; T = 25°C.

IV.7.2. On Rh/C

Fig. 51 displays potendiodynamic voltamperograms in 0.5 M H_2SO_4 + 0.1 M acetaldehyde on Rh/C preceded by CAs run at E_{ad} = 0.05 and 1 V *vs.* RHE in 0.5 M H_2SO_4. The results presented hereafter could not be repeated (by lack of time) and their interpretation is thus subjected to precaution.

Conversely to the EOR on Rh/C, the AOR activity does not differ significantly between the CVs obtained after hydrogen adsorption (seen for E_{ad} = 0.05 V *vs.* RHE) and OH_{ad} formation (at E_{ad} = 1 V *vs.* RHE) on the electrocatalyst surface: the reaction onsets are similar and only a slightly steeper rise in current can be observed for E_{ad} = 0.05 V *vs.* RHE. This observation is rather surprising as it was explained before that OH-adsorbates are very stable on rhodium electroactive surface. Yet, these results can be rationalized by an easier displacement of the OH-adsorbates by acetaldehyde molecules. The good superposition between the first and second cycle of the CV and MSCV from the signal *m*/*z* = 22 in Fig. 51b defends this assumption.

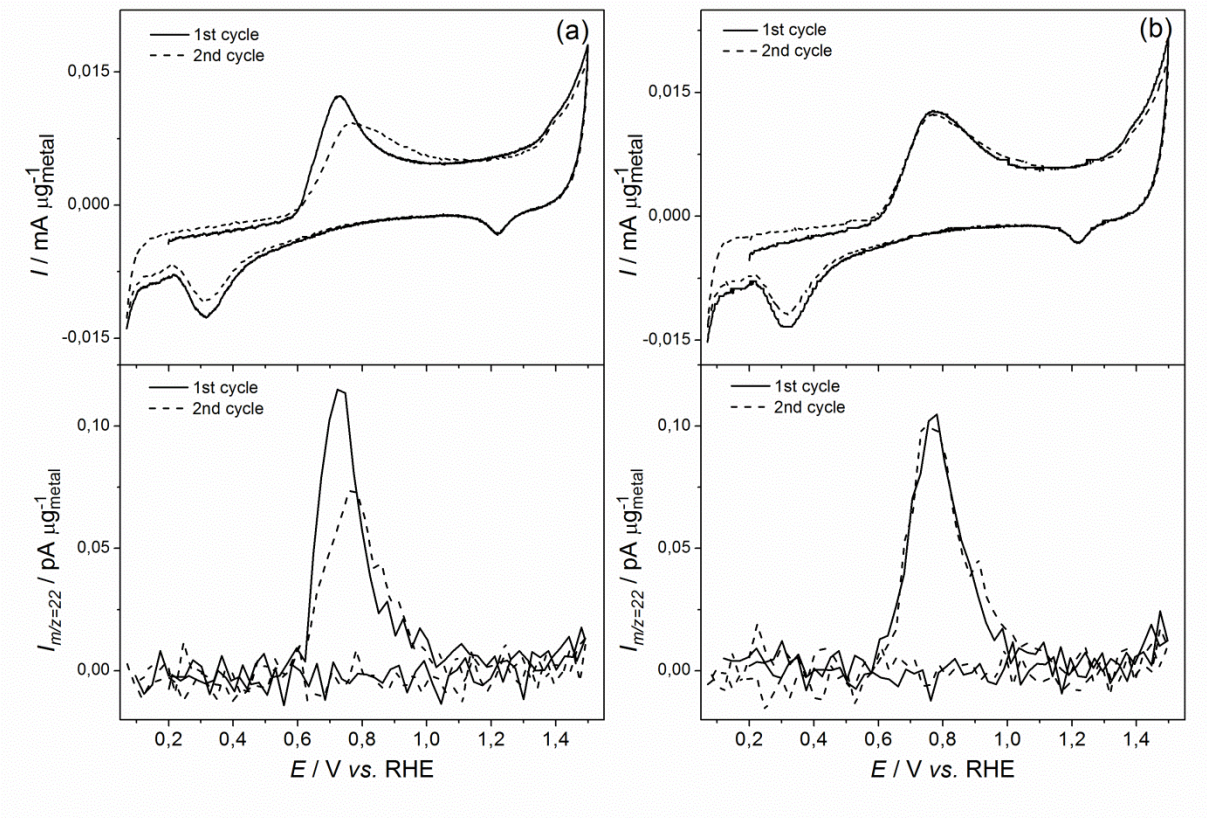

Fig. 51. (solid) First and (dash) second scan of the potentiodynamic acetaldehyde in 0.5 M H_2SO_4 + 0.1 M acetaldehyde after adsorption at E_{ad} = (a) 0.05 and (b) 1 V *vs.* RHE and corresponding MSCV for mass-to-charge ratio *m*/*z* = 22 on Rh/C; v = 10 mV s^{-1}; T = 25°C.

IV.7.3. On Pt-based electrocatalysts

The influence of H- and OH-adsorbates on the potentiodynamic AOR was also studied on Pt-Rh/C, Pt-SnO_2/C and Pt-Rh-SnO_2/C. Fig. 52 and Fig. 53 show the results obtained on Pt-Rh/C and Pt-Rh-SnO_2/C respectively. A slight negative shift was recorded on Pt-Rh/C for the cyclic voltammetry carried out after OH-adsorption (E_{ad} = 1 V *vs.* RHE) compared to the one run after the CA at E_{ad} = 0.05 V *vs.* RHE. This is confirmed with the corresponding MSCV of the signal m/z = 22 showing a similar small negative shift of the CO_2 production. On the opposite, the mass-to-charge signal m/z = 60 does not seem to be influenced by the surface treatment. As reported on Pt/C but contrary to Pt-Rh/C, the hydrogen adsorption seems to hinder intensively the AOR initiation on Pt-Rh-SnO_2/C (similar results were obtained on Pt-SnO_2/C, not shown here). Contrary to the EOR, the addition of rhodium to platinum is not sufficient to counter-balance the hindrance of the AOR initiation by hydrogen adsorbates but does inhibit their effect. As seen in section IV.3, the addition of SnO_2 to Pt does not favor the electrocatalyst surface dehydrogenation.

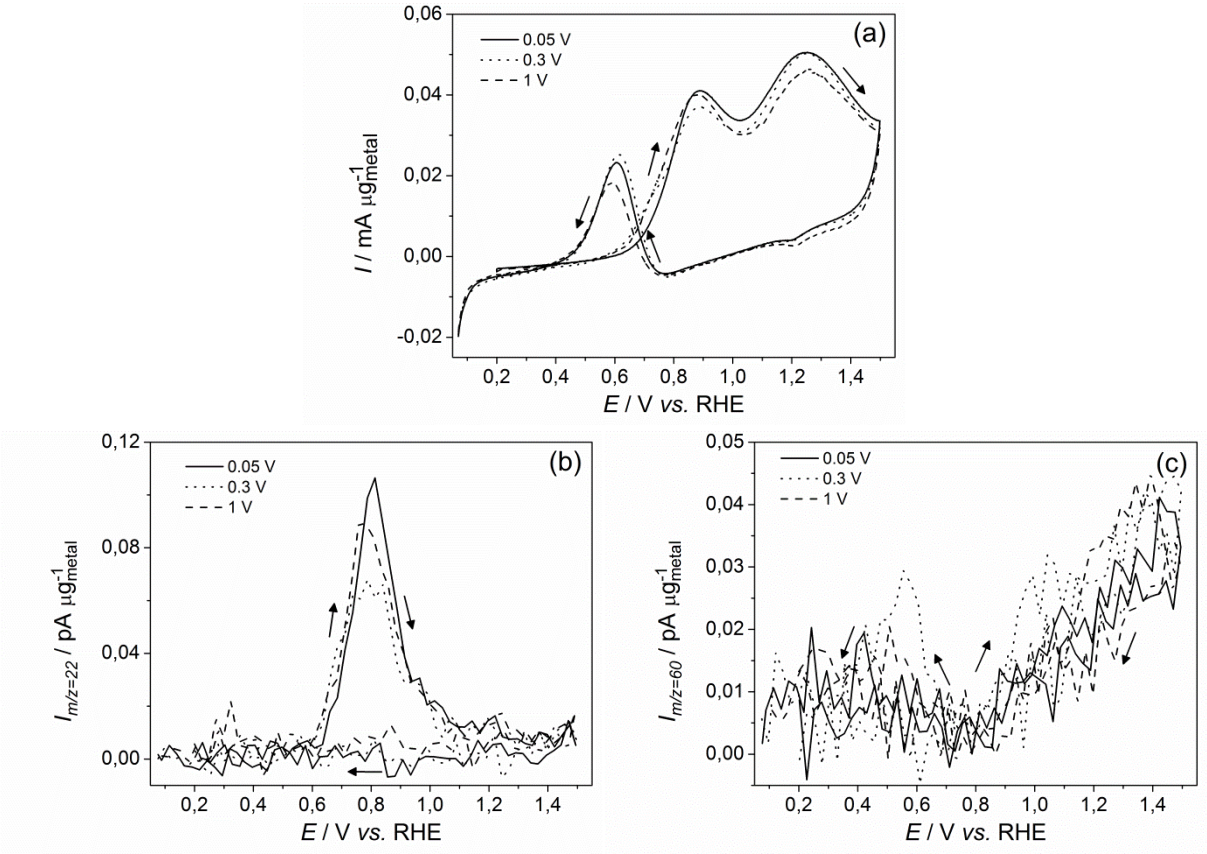

Fig. 52. (a) CV of the EOR in 0.5 M H_2SO_4 + 0.1 M acetaldehyde after adsorption at E_{ad} = 0.05 (solid), 0.3 (dots) and 1 V *vs.* RHE (dash) and corresponding MSCV for mass-to-charge ratio (b) m/z = 22 and (c) m/z = 60 on Pt-Rh/C; v = 10 mV s^{-1}; T = 25°C.

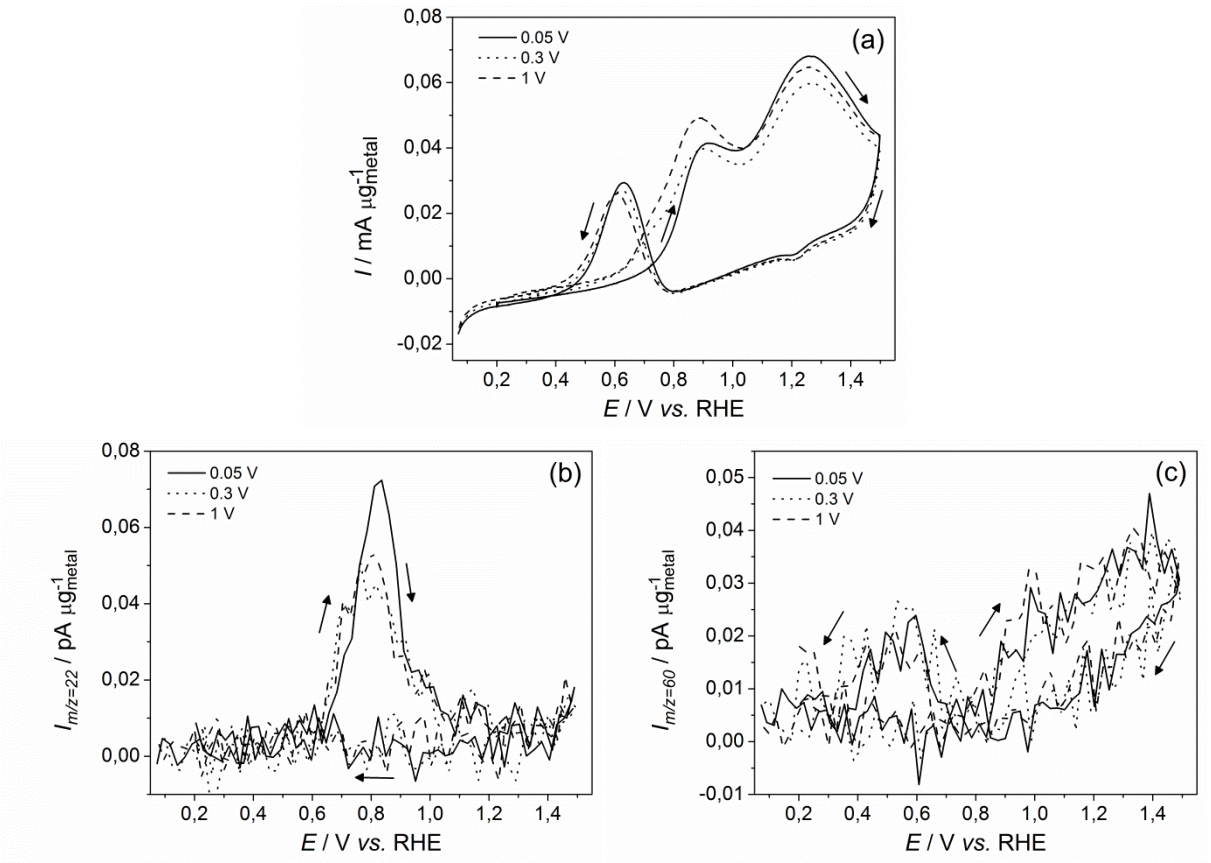

Fig. 53. (a) CV of the EOR in 0.5 M H_2SO_4 + 0.1 M acetaldehyde after adsorption at E_{ad} = 0.05 (solid), 0.3 (dots) and 1 V *vs.* RHE (dash) and corresponding MSCV for mass-to-charge ratio (b) m/z = 22 and (c) m/z = 60 on Pt-Rh-SnO_2/C; v = 10 mV s^{-1}; T = 25°C.

IV.8. Acetaldehyde potentiostatic adsorption at E_{ad} = 0.05 V vs. RHE

A similar representation of the potential and mass-to-charge signals m/z = 2 and m/z = 29 evolution against the time than those in section IV.5 and IV.6 can be found in Fig. 54 for Pt/C and Pt-SnO_2/C. These two graphs can be distinguished from those previously introduced for the ethanol adsorption by the larger ionic current values (right y-axis) of the signal m/z = 29 obtained with the acetaldehyde solution. As previously explained, the signal m/z = 29 is ascribed to the fragment [CHO^+] which can originate from both ethanol and acetaldehyde. However, as acetaldehyde presents a relative higher volatility compared to ethanol, at equal solution concentrations, more acetaldehyde is pumped in the mass spectrometer chamber than

ethanol, which induces larger ionic current values. Another difference remains in the quasi-stability of the signals m/z = 29 during the CVs (part (C) in Fig. 54) due to the absence of further acetaldehyde production contrary to the EOR.

Fig. 54a and Fig. 54b show that after the solution switch from 0.5 M H_2SO_4 to 0.5 M H_2SO_4 + 0.1 M acetaldehyde, contrary to what was observed in Fig. 47a and Fig. 48 with ethanol on Pt-based electrocatalysts, hydrogen generation shrinks markedly on Pt/C and Pt-SnO_2/C (similar results were obtained for Pt-Rh/C and Pt-Rh-SnO_2/C). This suggests that acetaldehyde adsorption does occur quantitatively at potentials as low as E_{ad} = 0.05 V *vs.* RHE on these electrocatalysts, contrary to ethanol. These two figures are contradictory with the interpretation of the results presented in section IV.6, which stated that the hindrance of the AOR initiation is caused by the hydrogen adsorbates. On the opposite, it seems in Fig. 54 that the electrocatalyst coverage by hydrogen species is markedly low at the beginning of the CV. The only explanation satisfying the results displayed in section IV.6 and in Fig. 54 is that the shift toward positive potentials of the AOR initiation is not due to hydrogen adsorbates. No explanation has been found until now to rationalize this behavior.

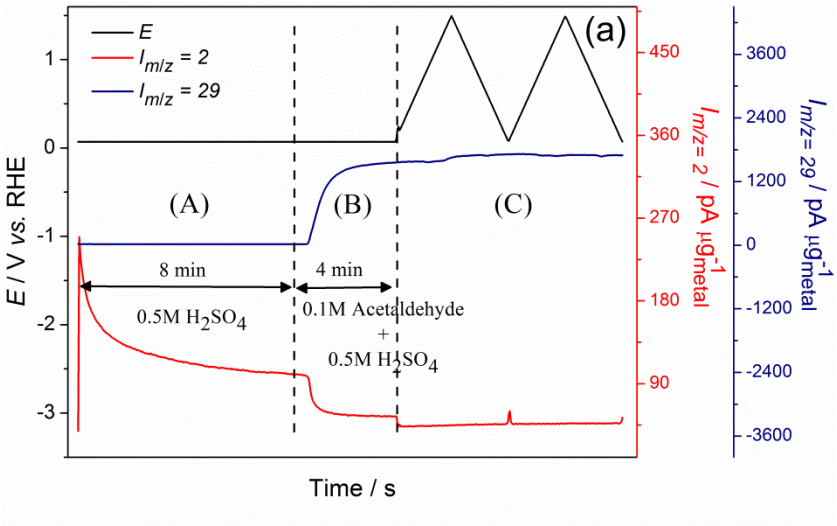

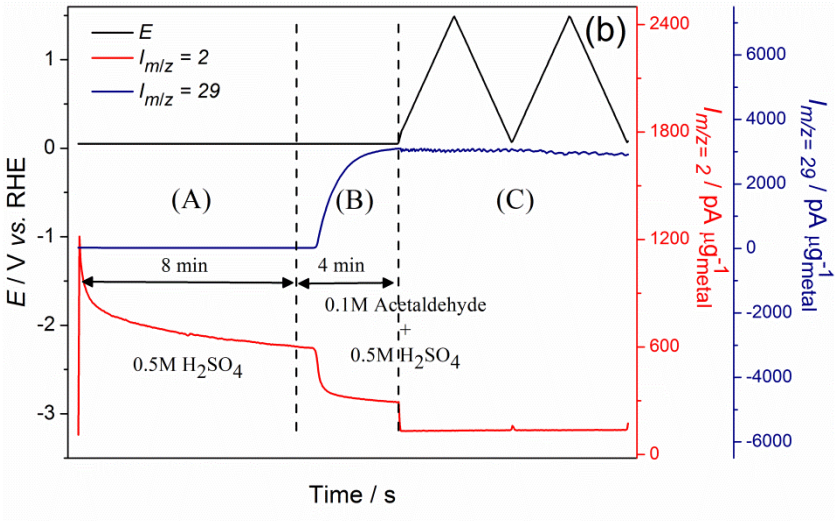

Fig. 54. Evolution of the potential and mass-to-charge ratio signals *m*/*z* = 2 and *m*/*z* = 29 *vs.* time on (a) Pt/C and (b) Pt-SnO_2/C during three consecutive steps: (A) hydrogen adsorption in 0.5 M H_2SO_4 at E_{ad} = 0.05 V *vs.* RHE, (B) the solution change in 0.5 M H_2SO_4 + 0.1 M acetaldehyde and (C) the potentiodynamic ethanol oxidation reaction starting at *E* = 0.2 V *vs.* RHE.

IV.9. Conclusions

The influence of the presence of H- and OH-adsorbates on the potentiodynamic ethanol electrooxidation was studied on home-made Pt/C, Rh/C, Pt-Rh/C, Pt-SnO_2/C and Pt-Rh-SnO_2/C by on-line differential electrochemical mass spectrometry (DEMS) in a flow cell system. Prior to the cyclic voltammetries, a chronoamperometry at E_{ad} = 0.05 and 1 V *vs.* RHE was applied in order to adsorb these species. For the sake of comparison, another adsorption potential was chosen at E_{ad} = 0.3 V *vs.* RHE, in the double layer region. The three main products of the ethanol oxidation reaction (EOR), acetaldehyde, acetic acid and CO_2, were detected using the mass-to-charge signals *m*/*z* = 29, 61 and 22, respectively.

The comparison of the first and second cycle of the CVs on Pt/C revealed a kinetics slow-down during the first scan following the CA at E_{ad} = 0.05 V *vs.* RHE, whereas a shift toward negative potentials was observed after the CA at E_{ad} = 1 V *vs.* RHE. These results were interpreted by the hindrance of the ethanol adsorption/electrooxidation due to H_{ad} and by an easier replacement of OH-adsorbates by ethanol molecules.

Results on Rh/C were opposite to platinum. The EOR did proceed almost entirely through its complete pathway toward CO_2 after hydrogen adsorption, while the activity was significantly lowered during the second scan of the CV preceded by the CA at E_{ad} = 0.05 V *vs.* RHE. A low EOR activity was also reported after the CA at E_{ad} = 0.3 and 1 V *vs.* RHE. The high OH_{ad} stability on Rh/C likely prevents their displacement by bulk ethanol molecules and thus their electrooxidation.

As for Pt/C, the EOR on Pt-SnO_2/C was hindered by H-adsorbates while the EOR on Pt-Rh/C and Pt-Rh-SnO_2/C did not show much influence of the adsorbates. The last result was explained by Pt and Rh opposite behaviors. The comparison between the electrocatalysts revealed a slightly lower EOR onset potential on Pt-SnO_2/C and Pt-Rh-O_2/C than on Pt/C, which was corresponding to ethanol better dehydrogenation into acetaldehyde. CO_2 generation was detected at lower potentials on Pt-Rh-SnO_2/C than on the other electrocatalysts. The CO_2 currency efficiency (CCE) was finally determined for each electrocatalyst and demonstrated higher values on Pt-Rh-SnO_2/C, regardless of the adsorption process preceding the cyclic voltammetries.

The potentiodynamic AOR study revealed a similar or even more dramatic hindrance of the oxidation reaction on Pt/C compared to EOR after the CA at E_{ad} = 0.05 V *vs.* RHE. On the contrary, the AOR on Rh/C was not impeded as much as the EOR after the potentiostatic treatment at E_{ad} = 1 V *vs.* RHE. These results suggest that acetaldehyde can more easily displace the OH-adsorbates than ethanol on Rh surfaces.

Finally, The representation *versus* time of the mass-to-charge ratio m/z = 2 gives further insight on the ability of both organic molecules to displace the hydrogen adsorbates: ethanol is unable to dislodge H_{ad} significantly on Pt/C (but can partially dehydrogenize and form H_2 as by-product), whereas this operation is successfully performed on Rh/C. Acetaldehyde can dehydrogenize quantitatively the electrocatalysts surface and that, independently of the electrocatalyst nature. These last results seem however in contradiction with the positive shift reported in the CV at E_{ad} = 0.05 V *vs.* RHE. More work would be necessary to unveil the remaining blur.

Chapter V.

Mass spectrometric investigation of ethanol and acetaldehyde adsorbates electrooxidation on Pt- and Rh-based electrocatalysts

This chapter aims at further understanding the EOR mechanism by means of ethanol and acetaldehyde stripping. A DEMS investigation is presented on the electrooxidation of ethanol and acetaldehyde adsorbates on home-made 20 wt.% Pt/C, Rh/C, Pt-Rh/C, Pt-SnO_2 and Pt-Rh-SnO_2/C. In the first place, a detailed overview of the literature is broached in this section. The results are then introduced and further analyzed in the light of pre-existing studies on this topic.

V.1. Ethanol and acetaldehyde adsorbates electrooxidation

Knowing the complexity in the interfacial processes taking place during bulk ethanol and acetaldehyde electrooxidation reaction, insight into these reactions may firstly be provided by studying the electrooxidation of adsorbed ethanol and acetaldehyde molecules on the surface of the electrocatalyst. Despite the apparent simplicity of the method, previous publications on the topic did yield divergent results regarding the nature of the ethanol adsorbates on Pt electrocatalysts [29,64,115,116,227–233]. According to Willsau et al. [229] the cleavage of the C-C bond of the ethanol molecule only occurs at high potentials during the potentiodynamic sweep following the adsorption process. It was also reported by Pastor and Iwasita [29] that more than 60 % of the adsorbates formed at E_{ad} = 0.3 V *vs.* RHE are C_2-species. On the contrary, Gootzen et al. [230] as well as Schmiemann et al. [231] proposed that ethanol adsorbs dissociatively into CO and CH_x. With regards to acetaldehyde, Wang et al. reported that the main adsorbate is CO which oxidizes at *ca.* E = 0.3 V *vs.* RHE while adsorbed C_2-species only constitute a small part of the adsorbed species [227]. The influence of the adsorption potential on the amount of ethanol and acetaldehyde adsorbates on bulk platinum and Pt/C was also evidenced in acidic [64,227,234] and alkaline [235] media.

The electrooxidation of ethanol or/and acetaldehyde adsorbates on other metals than Pt is scarce in the literature [116,232]. Mendez et al. investigated the reaction on rhodium [116] and found that the nature of the organic adsorbates seemed to be the same as on platinum. Besides, the authors noted the absence of ethane conversely to previous results on Pt [29,64]. An enhanced dehydrogenation of the ethanol molecule and an accentuated C-C bond breaking on rhodium compared to platinum were proposed. The only Pt-based bi-metallic electrocatalyst investigated in regard to the ethanol adsorbates stripping is Pt-Ru/C [232]. Conversely to Rh, no ethanol adsorbates could be observed on pure ruthenium surface. Besides, ethanol adsorbates stripping on Pt-Ru/C led to a smaller ethane production than on Pt/C. A slight negative shift of the onset potential of the CO-like adsorbates electrooxidation was also perceived on Pt-Ru/C against Pt/C.

This investigation is focused on the electrooxidation of ethanol and acetaldehyde adsorbates after their potentiostatic adsorption at distinct potentials on home-made 20 wt.% Pt/C, Rh/C, Pt-Rh/C, Pt-SnO_2/C and Pt-Rh-SnO_2/C electrocatalysts (their physical characterization can be found in section III). On-line differential electrochemical mass spectrometry (DEMS) was performed on thin-film electrodes in a flow cell system in order to identify and quantify the nature of the different adsorbates that are formed during the CAs in ethanol or acetaldehyde containing solutions and are oxidized (or reduced) during the following potentiodynamic sweep. The number of exchanged electrons per produced CO_2 molecule during the electrooxidation reactions was determined on Pt/C only, after calibration of the mass-to-charge signals m/z = 22 and m/z = 44. The ionic signals m/z = 15 and m/z = 30 were also respectively used to detect methane and ethane formation qualitatively. Finally, the influence of the adsorption potential on the adsorbates distribution was tentatively unveiled.

V.2. Ethanol and acetaldehyde adsorbates formation

Prior to the potentiodynamic stripping of ethanol and acetaldehyde adsorbates, a solution containing either bulk ethanol (0.5 M H_2SO_4 + 0.1 M EtOH) or bulk acetaldehyde (0.5 M H_2SO_4 + 0.1 M acetaldehyde) was kept flowing through the cell containing the working electrode during 8 min at fixed potential, allowing a maximum coverage at the electrocatalyst surface by the adsorbates. The solution was then switched to pure 0.5 M H_2SO_4 in order to flush the non-adsorbed organic residues. This operation lasted 20 min. In order to study the influence of the adsorption potential on the distribution of adsorbates at the surface of the electrocatalyst, the adsorption of ethanol and acetaldehyde was carried out at various potential values: E_{ad} = 0.05, 0.15, 0.3 and 0.5 V *vs.* RHE. Two different types of cyclic voltammetry procedures were recorded per adsorption potential in order to elucidate the influence of the reduction of adsorbed CH_x on the shape of the oxidation curves. While one CV started with a positive sweep from the initial potential at E = 0.2 V *vs.* RHE up to E = 1.5 V *vs.* RHE, before going back down to E = 0.05 V *vs*. RHE for 2 cycles, the other one initiated with a reduction sweep from the starting potential down to E = 0.05 V *vs*. RHE before the oxidation sweep to the higher vertex potential of E = 1.5 V *vs.* RHE (see Fig. 55). The notation "dir" (direct) and "indir" (indirect) will be used in the present text and in the figures to distinguish the CVs starting with a first oxidation (Fig. 55a) and reduction sweep (Fig. 55b) respectively.

The relative electrocatalyst surface coverage by the ethanol and acetaldehyde adsorbates was calculated using faraday and mass spectrometric data:

$$\Theta_{\mathrm{f,i}} = \frac{Q_{\mathrm{f,i}}}{Q_{\mathrm{f,CO}}} \qquad \text{Eq. V.1}$$

$$\Theta_{\mathrm{i}}^{44} = \frac{Q_{\mathrm{i}}^{44}}{Q_{\mathrm{CO}}^{44}} \qquad \text{Eq. V.2}$$

with $Q_{\mathrm{f,i}}$ and $Q_{\mathrm{f,CO}}$ the faraday charges corresponding to the electrooxidation reactions of ethanol (and acetaldehyde) adsorbates and to the stripping of a saturated CO_{ad} monolayer respectively and Q_{i}^{44} and Q_{CO}^{44} the ionic charges of the mass-to-charge signal m/z = 44 of the same reactions respectively.

The experiments were repeated three times on different days for the sake of reproducibility. The adsorbates surface coverage values presented hereafter are reproducible within ± 0.1; therefore, the results will be discussed qualitatively more than quantitatively.

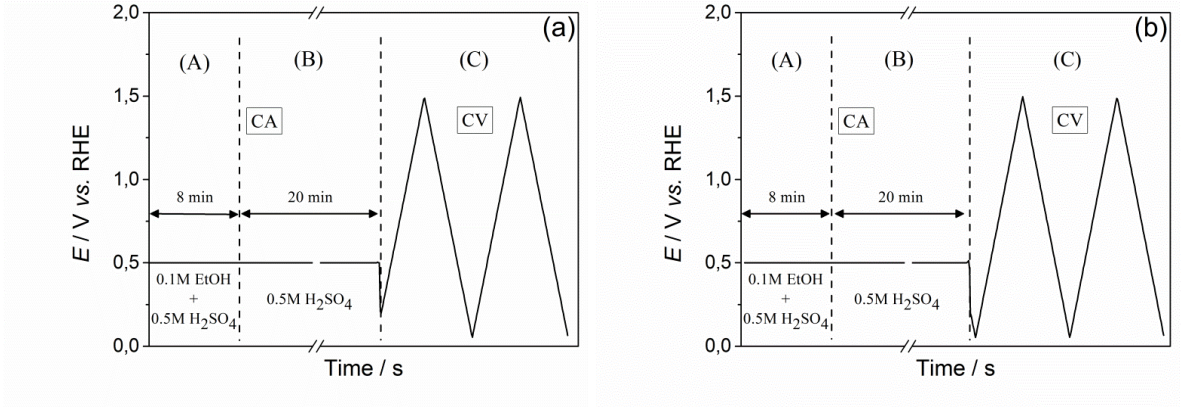

Fig. 55. Potential *vs.* time representation of (A) the adsorbates adsorption in 0.5 M H_2SO_4 + 0.1 M EtOH (represented here at E_{ad} = 0.5 V *vs.* RHE), (B) the flush of the solution in 0.5 M H_2SO_4 and (C) the adsorbates electrooxidation starting at E = 0.2 V *vs.* RHE with a first (a) positive (hereafter noted "direct") and (b) negative (hereafter noted "indirect") sweep.

V.3. On Pt/C

V.3.1. Ethanol adsorbates stripping

Fig. 56 shows cyclic voltammetries ran with a direct oxidative scan from E = 0.2 V *vs.* RHE after the adsorption at different adsorption potentials (see experimental section). Two oxidation regions can be identified: one at low potential (between *ca.* E = 0.5 and 0.8 V *vs.* RHE) which corresponds to the oxidation of adsorbed CO-like species and the other at high potential (E > 0.9 V *vs.* RHE), which starts in the hydroxide adsorption region and corresponds to the oxidation of strongly adsorbed species. As shown in Fig. 56, the maximum faraday charge corresponding to the oxidation between *ca.* E = 0.5 and 0.8 V *vs.* RHE is obtained upon adsorption at E_{ad} = 0.3 V *vs.* RHE. This result is not surprising as this potential is located in the double layer region where the electrocatalyst surface is free of any hydrogen or hydroxide adsorbates (see chapter IV). Besides that, this voltammogram displays a pre-peak between *ca.* E = 0.45 and 0.55 V *vs.* RHE not observable on the others. The voltammogram acquired after an adsorption process at E_{ad} = 0.15 V *vs.* RHE also demonstrates a quite large oxidation peak around E = 0.7 V *vs*. RHE: at E_{ad} = 0.15 V *vs.* RHE, *i.e.* at the positive limit of the hydrogen region, adsorbed hydrogen species are oxidized, leaving an essentially free Pt surface for the adsorption of ethanol, which adsorbates are subsequently oxidized at higher potential. On the contrary, at E_{ad} = 0.05 V *vs.* RHE, ethanol adsorption takes place in the hydrogen adsorption region, resulting in smaller ethanol coverage and therefore smaller ethanol stripping peak. The ethanol adsorption is however not completely inhibited at E_{ad} = 0.05 V *vs*. RHE; one reason could be that ethanol enables the cleavage of the Pt-H bonds (or the displacement of H_{ad}), but this result is contradictory with

[227] and chapter IV. Finally, the stripping CV resulting from ethanol adsorption at E_{ad} = 0.5 V *vs.* RHE shows limited coulometry in the oxidation peak between E = 0.5 and 0.9 V *vs.* RHE, evidencing that some of the adsorbates were already oxidized during the adsorption step.

Fig. 56b and Fig. 56c shows the corresponding mass-to-charge signals m/z = 22 and m/z = 44. Besides a quasi-similar onset potential (at E = 0.55 V *vs.* RHE) for the CO_2 generation, it can be noticed that no pre-peak is observed on those two figures for the electrooxidation of ethanol adsorbates after adsorption at E_{ad} = 0.3 V *vs.* RHE, although a pre-peak was found for the faradaic current (Fig. 56a). This indicates that the oxidation reaction corresponding to the pre-peak does not involve the generation CO_2, but would rather correspond to another product not detectable by the mass spectrometer. Cases et al. recorded a similar pre-peak on a Pt(111) surface after an adsorption of ethanol at E_{ad} = 0.2 V *vs.* RHE [162]. They attributed this pre-peak to a residue acting independently from the species oxidized during the following oxidation at *ca.* E = 0.55 V *vs.* RHE. On the contrary, Lai and Koper gave convincing evidences that this pre-peak could be ascribed to the oxidation of $CH_{x,ad}$-species to CO_{ad} [21].

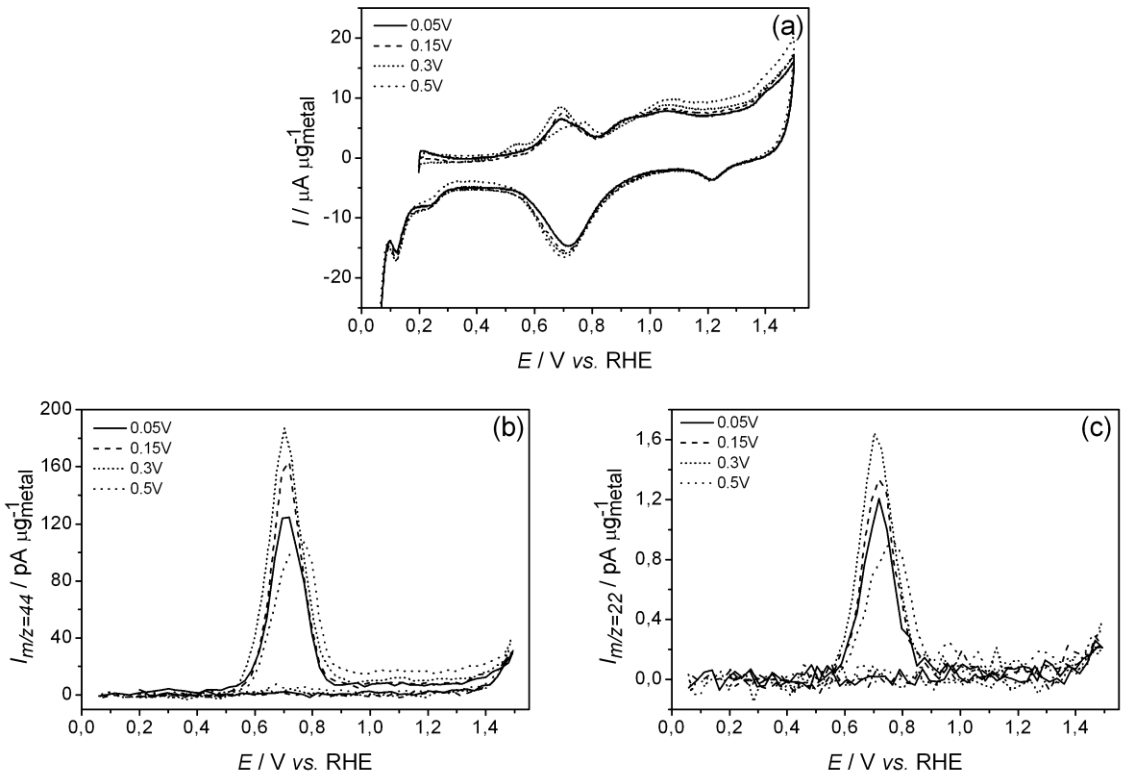

Fig. 56. (a) CV of the electrooxidation of ethanol adsorbates in 0.5 M H_2SO_4 after adsorption at E_{ad} = 0.05 (solid), 0.15 (dash), 0.3 (short dash) and 0.5 V *vs.* RHE (dots) and corresponding

MSCV for mass-to-charge ratio (b) *m/z* = 44 and (c) *m/z* = 22 on Pt/C; v = 10 mV s^{-1}; T = 25°C.

Fig. 57 shows indirect cyclic voltammetries ran first with a reduction scan from E = 0.2 V *vs.* RHE down to E = 0.05 V *vs.* RHE followed by a positive scan as in Fig. 56. A similar pattern of the oxidation taking place between *ca.* E = 0.5 to 0.8 V *vs.* RHE can be observed in comparison to the results in Fig. 56. Moreover, as it can be seen in Fig. 58, the relative coverage of the electrocatalyst surface (adsorbates oxidation charge normalized by CO stripping charge) by ethanol adsorbates does not significantly differ in the two cases. If CH_x-adsorbates were indeed oxidizing into CO_{ad} in the potential range E = 0.5 - 0.8 V *vs.* RHE, a decrease of the surface coverage would have been expected after the reduction of the $CH_{x,ad}$-species between E = 0.2 and 0.05 V *vs.* RHE. Moreover, the pre-peak observed after the adsorption step at E_{ad} = 0.3 V *vs.* RHE is once again observed in Fig. 57, suggesting that the $CH_{x,ad}$ reduction operating during the first negative scan did not have a significant impact on this pre-peak. Fig. 59 shows more clearly the comparison between the two potentiodynamic curves obtained after adsorption at E_{ad} = 0.3 V *vs.* RHE. A slight decrease of this pre-peak is witnessed after the reduction of the $CH_{x,ad}$-species, but this does not consist of sufficient evidence to prove that adsorbed CH_x do oxidize into CO_{ad} at these potentials. In order to clearly identify if this reaction corresponds to the pre-peak, it would be necessary to carry out not one but several cycles between E = 0.05 and 0.2 V *vs*. RHE in order to completely reduce CH_x-adsorbates, as it can be found in the literature [64,227].

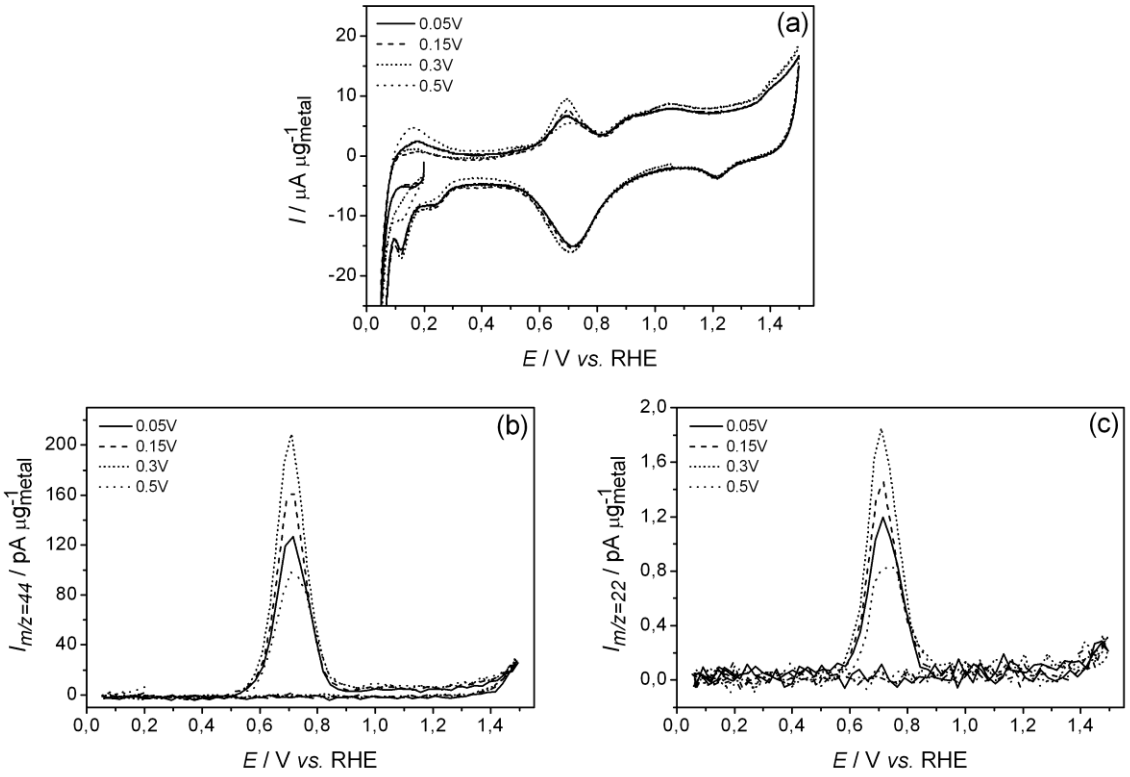

Fig. 57. (a) CV of the electrooxidation of ethanol adsorbates in 0.5 M H_2SO_4 with a first reduction scan after adsorption at E_{ad} = 0.05 (solid), 0.15 (dash), 0.3 (short dash) and 0.5 V *vs.* RHE (dots) and corresponding MSCV for mass-to-charge ratio (b) *m/z* = 44 and (c) *m/z* = 22 on Pt/C; v = 10 mV s^{-1}; T = 25°C.

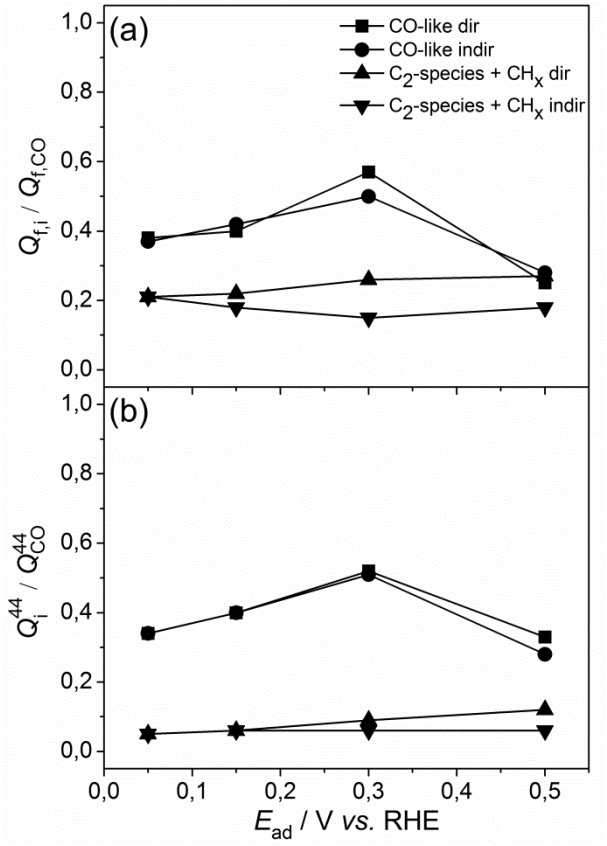

Fig. 58. Relative coverage of the Pt/C surface by ethanol adsorbates adsorbed at E_{ad} = 0.05, 0.15, 0.3 and 0.5 V *vs.* RHE deduced from (a) faraday charges and (b) ionic charges from the mass-to-charge signal *m/z* = 44.

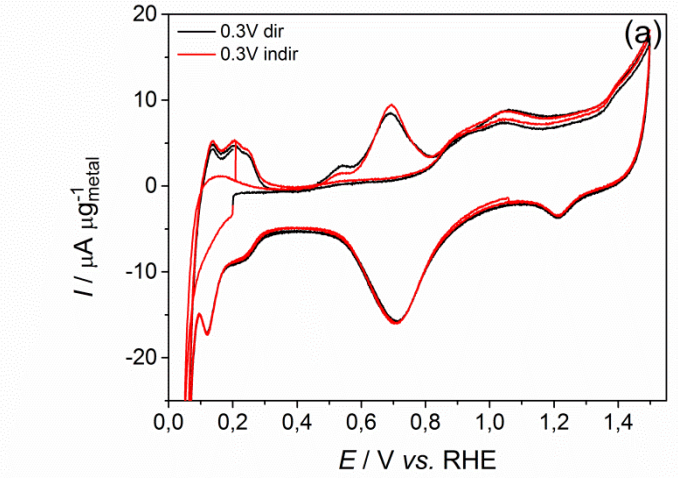

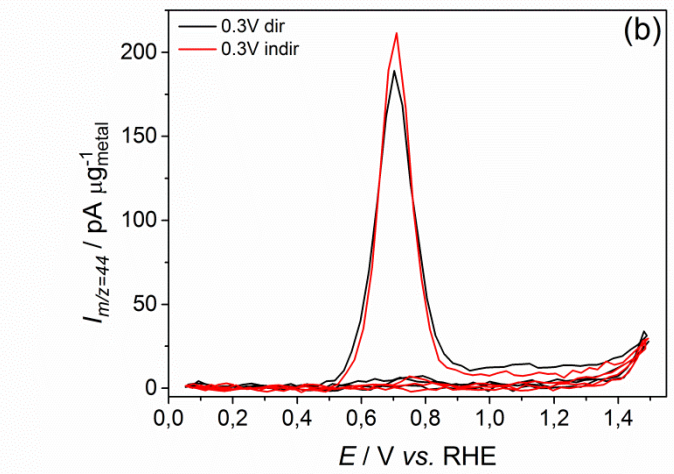

Fig. 59. (a) CV of the electrooxidation of ethanol adsorbates in 0.5 M H_2SO_4 after adsorption at E_{ad} = 0.3 V *vs.* RHE (black) without and (red) with a first reduction scan and the corresponding MSCV for mass-to-charge ratio (b) *m/z* = 44 on Pt/C; v = 10 mV s^{-1}; T = 25°C.

The number of transferred electrons per CO_2 molecule corresponding to the oxidation occurring between E = 0.5 and 0.8 V *vs.* RHE were calculated using Eq.II.13 and summarized in Table 8. It seems that whatever the adsorption potential, the number of exchanged electrons remains the same (≈ two electrons) and could only be ascribed to the oxidation of adsorbed CO, coming from ethanol dissociative adsorption, into CO_2.

Table 8. Number of electrons exchanged per CO_2 molecule during the electrooxidation of ethanol adsorbates between *ca.* E = 0.5 and 0.8 V *vs.* RHE and at E > 0.9 V *vs.* RHE without[(d)] and with[(i)] a first reduction scan.

	0.5 – 0.8 V *vs.* RHE		> 0.9 V *vs.* RHE	
E_{ad} / V *vs.* RHE	$n_{e^-}^{dir}$	$n_{e^-}^{indir}$	$n_{e^-}^{dir}$	$n_{e^-}^{indir}$
0.05	2.2	2.1	8.0	8.2
0.15	2.0	2.1	7.3	6.3
0.3	2.2	2.0	5.8	5.4
0.5	1.8	1.9	4.6	6.1

[dir]: without first reduction scan
[indir]: with first reduction scan

Interestingly, the adsorption potential also seems to impact the oxidation at high potential (E > 0.9 V *vs.* RHE). Indeed, as it can be observed in Fig. 58a, the coverage of the Pt/C surface by ethanol "strong absorbates" seems to increase with the rise of the adsorption potential, *e.g.* especially after adsorption at E_{ad} = 0.3 and 0.5 V *vs.* RHE. For the sake of clarity, it can be seen in Fig. 60 the first and second cycle of the curves corresponding to the ethanol adsorbates electrooxidation after adsorption at E_{ad} = 0.15 and 0.5 V *vs.* RHE. The

oxidation occurring after E = 0.9 V *vs.* RHE looks larger after adsorption at E_{ad} = 0.5 V *vs.* RHE. This could be enlighten by the fact that after adsorption at E_{ad} = 0.5 V *vs.* RHE, the adsorbed species oxidizing at lower potentials are already destabilized (and therefore desorb or (partially) oxidize during the adsorption step), freeing some Pt/C sites for "strongly adsorbed" species that oxidize only at high potential (E > 0.9 V *vs.* RHE).

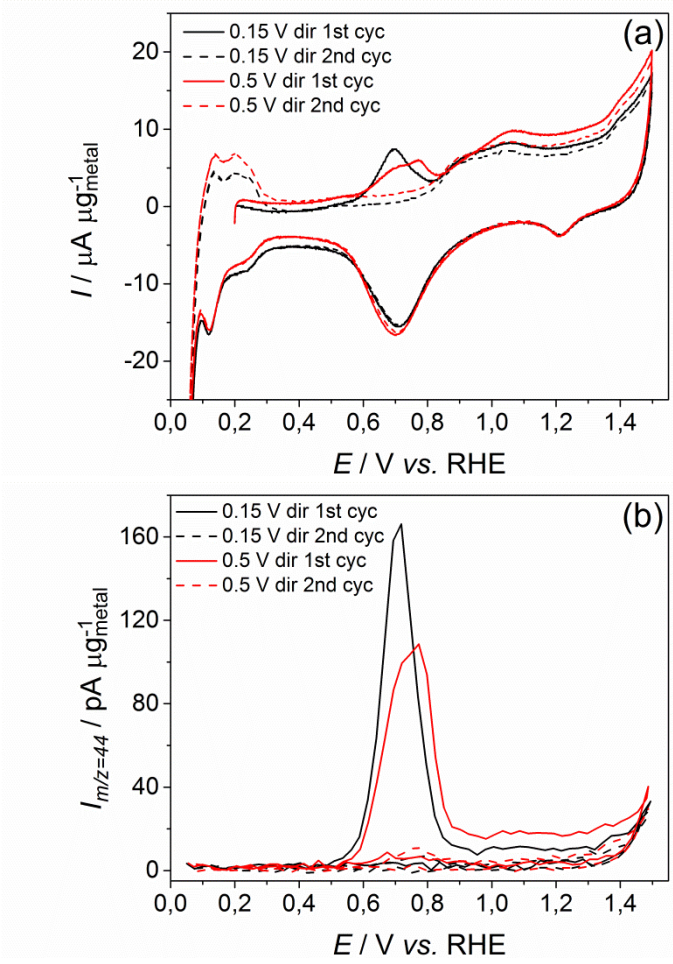

Fig. 60. (a) CV of the electrooxidation of ethanol adsorbates in 0.5 M H_2SO_4 after adsorption at (black) E_{ad} = 0.15 V *vs.* RHE and (red) E_{ad} = 0.5 V *vs.*RHE and the corresponding MSCV for mass-to-charge ratio (b) m/z = 44 on Pt/C; v = 10 mV s^{-1}; T = 25°C.

Fig. 61 shows a comparison between two CV of electrooxidation of ethanol adsorbates formed at E_{ad} = 0.5 V *vs.* RHE started either directly with a positive scan (dir) or after a negative scan (indir). It is clearly apparent that the oxidation current at high potentials is smaller in the latter case. This demonstrates that $CH_{x,ad}$ oxidation into adsorbed CO-like species (CO_{ad}, COH_{ad}) corresponds to this larger oxidation current monitored at high potential in the "direct" (dir) CV, whereas an initial negative sweep down to E = 0.05 V *vs.* RHE reduces $CH_{x,ad}$ and suppress such high-potential oxidation current. Similar results are obtained

with an adsorption process at E_{ad} = 0.3 V *vs.* RHE, but not at E_{ad} = 0.15 V *vs.* RHE and E_{ad} = 0.05 V *vs.* RHE; this can be rationalized by the fact that low adsorption potentials promote the "*in situ*" reduction of $CH_{x,ad}$-species (during the adsorption process) or simply forbid their formation. The CV of Fig. 60, relative to an adsorption potential of E_{ad} = 0.15 V *vs.* RHE, is a clear example of this scenario. This phenomenon is finally summarized in Fig. 58, where higher coverage values at high potentials were recorded after adsorption at E_{ad} = 0.5 V *vs.* RHE. Similar results can also be found in the literature for alkaline solutions [236].

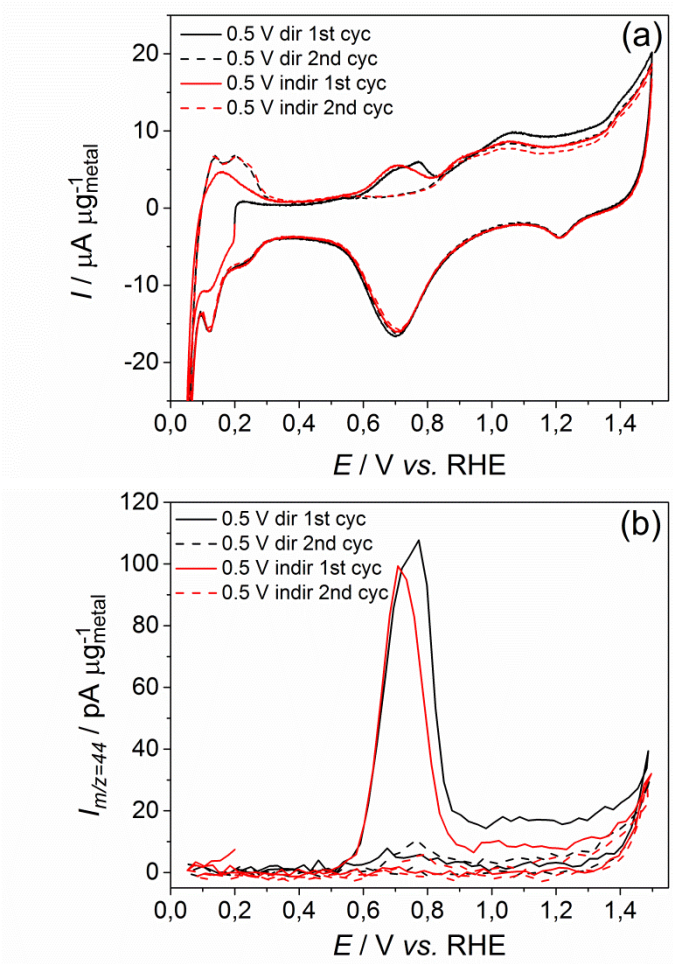

Fig. 61. (a) CV of the electrooxidation of ethanol adsorbates in 0.5 M H_2SO_4 after adsorption at E_{ad} = 0.5 V *vs.* RHE without a first reduction scan (black) and with a first reduction scan (red) and the corresponding MSCV for mass-to-charge ratio (b) *m/z* = 44 on Pt/C ; v = 10 mV s^{-1}; T = 25°C.

The number of electrons calculated for the "high-potential oxidation" at E > 0.9 V *vs.* RHE (see Table 8) is significantly higher than for the "low-potential oxidation" (0.5 < E < 0.8 V *vs.* RHE). As seen before, the oxidation of adsorbed CH_x-species seems to contribute

appreciably to this oxidation, in a process that firstly yields CO (Eq.V.3) and then CO_2 (Eq.V.4), in a maximum 7 electron-process overall (*i.e.* for $x = 3$: $CH_{3,ad}$):

$$CH_{x,ad} + H_2O \rightarrow CO_{ad} + (2+x)\ H^+ + (2+x)\ e^- \qquad \text{Eq. V.3}$$

$$CO_{ad} + 2\ OH^- \rightarrow CO_2 + H_2O + 2\ e^- \qquad \text{Eq. V.4}$$

Nonetheless, this reaction may not be the only one taking place at $E > 0.9$ V *vs.* RHE. When comparing the coverage values in Fig. 58a and Fig. 58b deduced from the calculated faraday and ionic charges, the relative part of adsorbed species oxidizing in CO_2 (Fig. 58b) is low compared to the overall adsorbed species oxidizing at high potentials (Fig. 58a). That suggests that another parallel mechanism could occur in this potential range, which does not involve CO_2 production.

The distribution of ethanol adsorbates on the Pt/C surface was not only assessed from the faraday charges (Fig. 58a) but also from the associated mass-to-charge signals $m/z = 22$ and $m/z = 44$ charges (Fig. 58b). The coverage values correspond to the species oxidizing in the potential range [0.5 V *vs.* RHE; 0.8 V *vs.* RHE] and for $E > 0.9$ V *vs.* RHE. It can be seen in both figures that, whatever the adsorption potential, the coverage of the electrocatalyst in ethanol adsorbates never reaches the charge obtained in a CO stripping CV. It can be assumed that, after an adsorption at $E_{ad} = 0.05$ V *vs.* RHE and to a lesser extent at $E_{ad} = 0.15$ V *vs.* RHE, the adsorbates besides CO_{ad}, $CH_{x,ad}$ and C_2-species are hydrogen adsorbates. Then, it could be reasonably supposed that part of the adsorbed CO already starts oxidizing when the adsorption occurs at $E_{ad} = 0.3$ V *vs.* RHE. When the adsorption occurs at $E_{ad} = 0.5$ V *vs.* RHE, most of the CO-like adsorbates are expected to oxidize during the 20 minutes in 0.5 M H_2SO_4 electrolyte following the adsorption in the ethanol containing solution and preceding the potentiodynamic voltammetry. Regardless of the adsorption potential, a larger steric effect of ethanol species compared to CO could explain that even at an optimal adsorption potential (0.15 V *vs.* RHE $< E_{ad} <$ 0.3 V *vs.* RHE), the ethanol adsorbates coverage never reaches CO coverage.

When comparing Fig. 58a and Fig. 58b, ethanol adsorbates coverage values deduced from the faraday and ion charges ($m/z = 44$) seem to correlate between $E = 0.5$ and 0.8 *vs.* RHE. Nonetheless, divergent results regarding the Pt/C coverage by strong adsorbates appear at high potentials, between the coverage values obtained with the calculated faraday and ionic charges from the mass-to-charge signal $m/z = 44$. Indeed, the ionic normalized charge values are 3-4 times lower than faraday ones. This may be indicative that two reactions (at least) are simultaneously occurring at high potentials: a minor one generating CO_2 and a major one (or more), the products of which are not detectable by mass spectrometry. These formed reaction intermediates/products are supposed to completely desorb from the electrocatalyst surface between $E = 0.9$ and 1.5 V *vs.* RHE, as nothing could be then detected by mass spectrometry

during the following negative and positive scan. This topic will be further discussed in the next section.

V.3.2. Acetaldehyde adsorbates stripping

The influence of the adsorption potential of bulk acetaldehyde on the profile of the stripping CV can be seen in Fig. 62. The largest oxidation occurring between E = 0.5 and 0.9 V *vs.* RHE corresponds to an acetaldehyde adsorption at E_{ad} = 0.15 V *vs.* RHE. This observation is supported in Fig. 63 by the relative coverage values in acetaldehyde adsorbates: a slightly higher coverage is monitored when the adsorption takes place at E_{ad} = 0.15 V *vs.* RHE. Similarly, when the CV starts with a negative scan (Fig. 64), the highest peak is also observed after adsorption at E_{ad} = 0.15 V *vs.* RHE. In both set of experiments, the oxidation charge between E = 0.5 and 0.8 V *vs.* RHE corresponding to the oxidation of adsorbates formed at E_{ad} = 0.5 V *vs.* RHE decreased drastically.

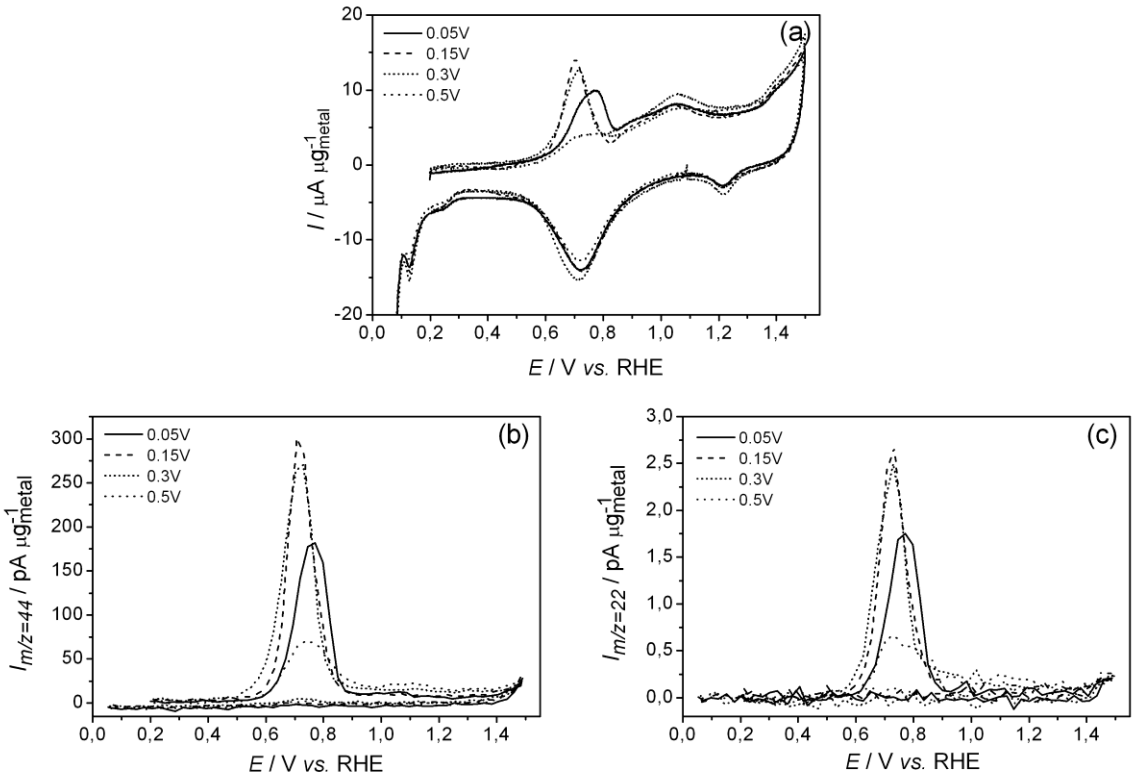

Fig. 62. (a) CV of the electrooxidation of acetaldehyde adsorbates in 0.5 M H_2SO_4 after adsorption at E_{ad} = 0.05 (solid), 0.15 (dash), 0.3 (short dash) and 0.5 V *vs*. RHE (dots) and corresponding MSCV for mass-to-charge ratio (b) *m/z* = 44 and (c) *m/z* = 22 on Pt/C; v = 10 mV s^{-1}; T = 25°C.

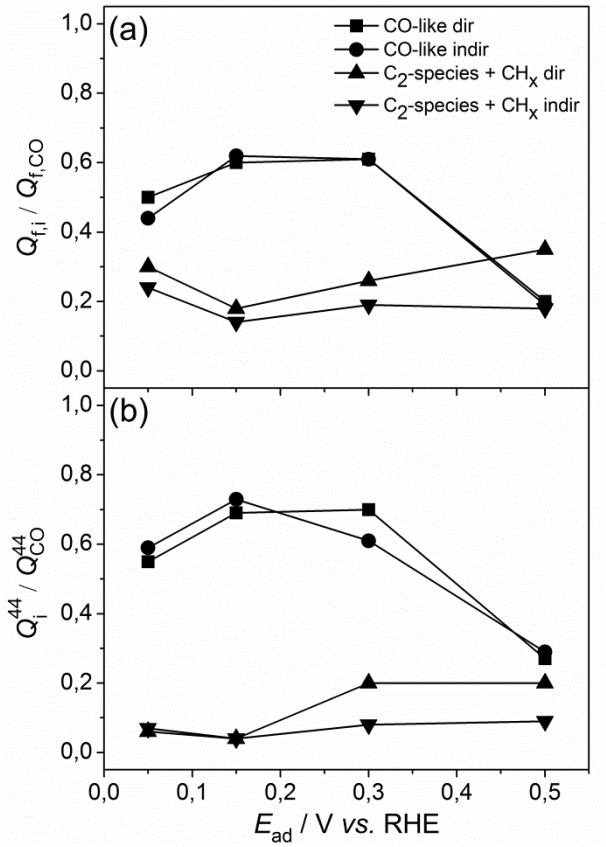

Fig. 63. Relative coverage of the Pt/C surface by acetaldehyde adsorbates adsorbed at E_{ad} = 0.05, 0.15, 0.3 and 0.5 V *vs.*RHE deduced from (a) faraday charges and (b) ionic charges from the mass-to-charge signal *m/z* = 44.

As it can be seen in Table 9, the oxidation of acetaldehyde adsorbates between *ca.* *E* = 0.5 and 0.8 V *vs.* RHE generates around two electrons, whatever the adsorption potential. These results, similar to the stripping of ethanol adsorbates, match with the electrooxidation of CO_{ad}-species into CO_2 in this potential region.

Table 9. Number of electrons exchanged per CO_2 molecule during the electrooxidation of acetaldehyde adsorbates between *ca.* 0.5 and 0.8 V *vs.* RHE and at *E* > 0.9 V *vs.* RHE without[(d)] and with[(i)] a first reduction scan.

	0.5 - 0.8 V *vs.* RHE		> 0.9 V *vs.* RHE	
E_{ad} / V *vs.* RHE	$n_{e^-}^{dir}$	$n_{e^-}^{indir}$	$n_{e^-}^{dir}$	$n_{e^-}^{indir}$
0.05	2.2	2.5	8.1	7.2
0.15	2.0	2.1	8.1	6.9
0.3	2.5	2.4	4.4	4.8

0.5	2.0	2.1	6.2	6.0

[dir]: without first reduction scan
[indir]: with first reduction scan

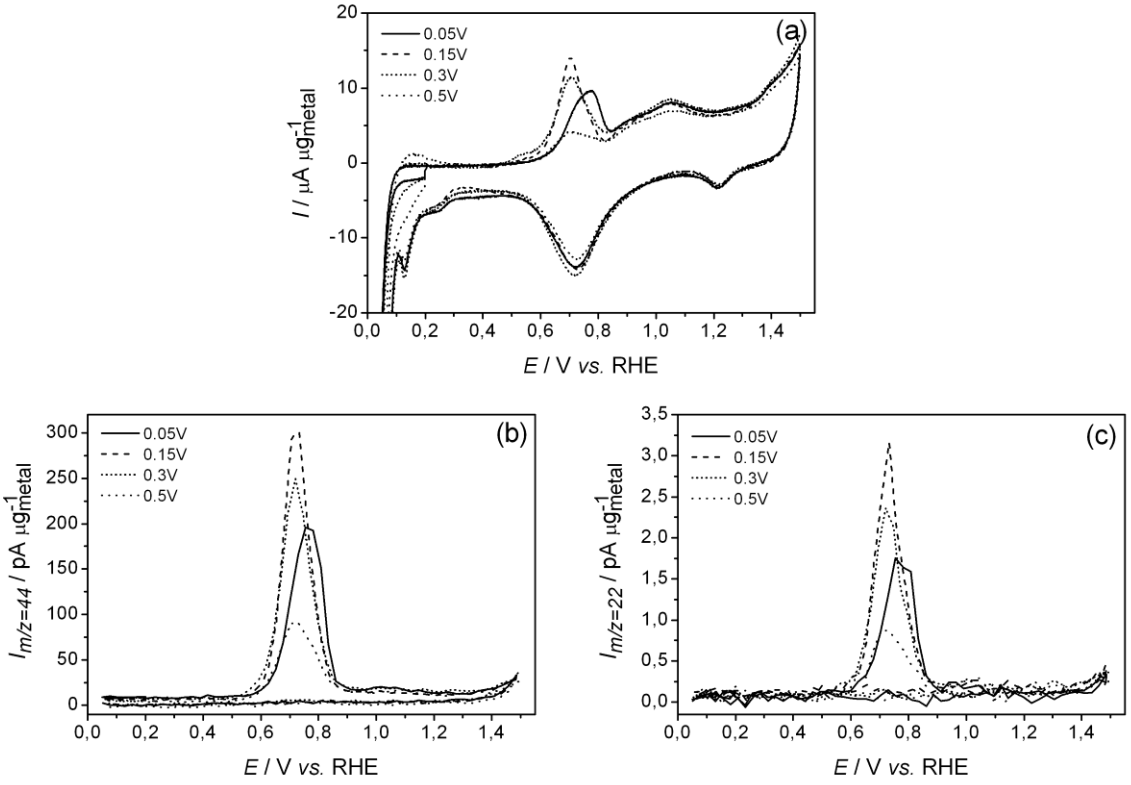

Fig. 64. (a) CV of the electrooxidation of acetaldehyde adsorbates in 0.5 M H_2SO_4 after adsorption at E_{ad} = 0.05 (solid), 0.15 (dash), 0.3 (short dash) and 0.5 V *vs.* RHE (dots) and corresponding MSCV for mass-to-charge ratio (b) *m/z* = 44 and (c) *m/z* = 22 on Pt/C; *v* = 10 mV s^{-1}; *T* = 25°C.

The coverage values of acetaldehyde adsorbates oxidizing at higher potentials (E > 0.9 V *vs.* RHE) are also displayed in Fig. 63. Like the ethanol adsorbates oxidation, the highest coverage in strong adsorbates corresponds to an adsorption at E_{ad} = 0.5 V *vs.* RHE. It could be conjectured that CO_{ad}-species are rapidly replaced by strong adsorbates during the adsorption at E_{ad} = 0.5 V *vs.* RHE, yielding a larger oxidation current at high potential during the following potentiodynamic sweep.

As seen in Fig. 65, the "high potential oxidation" charge of a stripping CV following an adsorption step at E_{ad} = 0.5 V *vs.* RHE and starting with an oxidation scan is much higher than when starting with a reduction scan. Like the ethanol adsorbates oxidation, the reduction of adsorbed CH_x-species during the initial negative scan impacts considerably the "high

potential oxidation" charge. This suggests again that $CH_{x,ad}$-species do oxidize at high potentials. Although slight variations are observed in the potential range [0.5 V *vs.* RHE; 0.9 V *vs.* RHE] between the two CV of Fig. 65, no distinct evidence of CH_x-adsorbates oxidation between E = 0.5 and 0.9 V *vs.* RHE could be claimed.

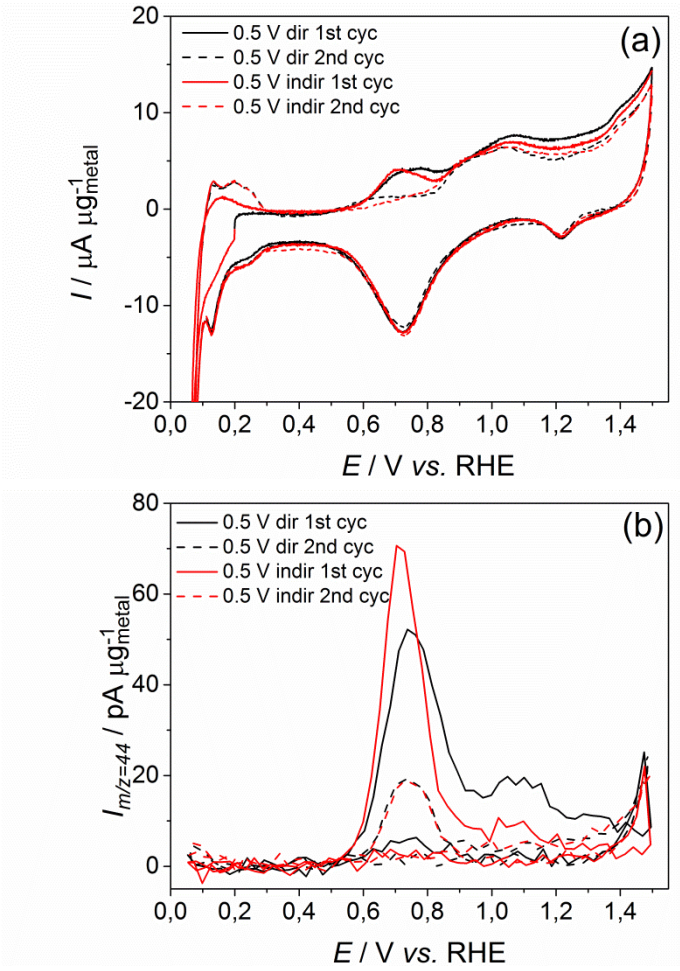

Fig. 65. (a) CV of the electrooxidation of acetaldehyde adsorbates in 0.5 M H_2SO_4 after adsorption at E_{ad} = 0.5 V *vs.* RHE (black) without and (red) with a first reduction scan and the corresponding MSCV for mass-to-charge ratio (b) m/z = 44 on Pt/C; v = 10 mV s^{-1}; T = 25°C.

Fig. 66b shows the change of the signal m/z = 15 *vs.* potential during an acetaldehyde adsorbates stripping CV after an adsorption step at E_{ad} = 0.05 V *vs.* RHE and starting by a reduction scan. The signal does not fluctuate at low potential during the first reduction scan, showing the absence of reduction of adsorbed CH_x-species into methane. This result was expected as $CH_{x,ad}$-species that possibly form during the adsorption step can constantly reduce in methane at an adsorption potential of E_{ad} = 0.05 V *vs.* RHE [227]. However, after the first cycle, the second reduction scan shows evidence of methane production, thus proving the formation of adsorbed $CH_{x,ad}$-species during the two scans. As the first oxidation at *ca.* E =

0.5 V *vs.* RHE mainly corresponds to CO-electrooxidation into CO_2, there is a high probability that $CH_{x,ad}$ formation occurs at E > 0.9 V *vs.* RHE from the cleavage of adsorbed C_2-species. Similarly, in Fig. 66c, the signal m/z = 30 does not fluctuate during the initial reduction scan, which shows the absence of ethane generation from adsorbed C_2-species. However, although the signal m/z = 30 presents a low signal/noise ratio, the second reduction scan clearly illustrates ethane production, hence attesting a modification in the nature of the adsorbed C_2-species operating most likely during the preceding oxidation scan at high potential. These two phenomena, which were not evidenced with ethanol adsorbates, also show that acetaldehyde adsorbates are much more strongly adsorbed than ethanol strong adsorbates and can remain at the surface of the electrocatalyst at potentials as high as E = 1.5 V *vs.* RHE.

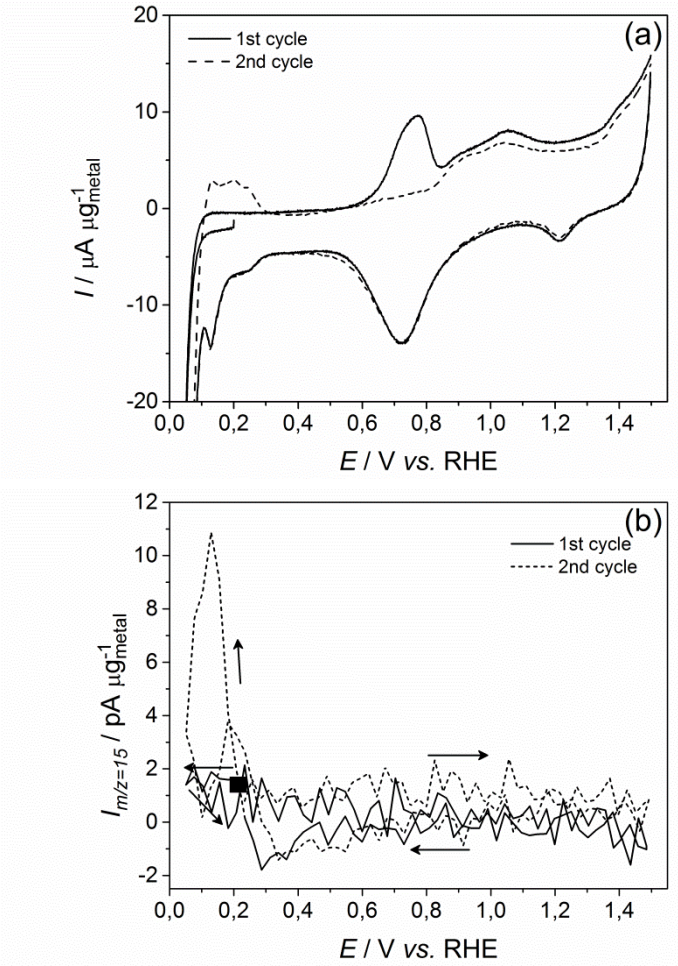

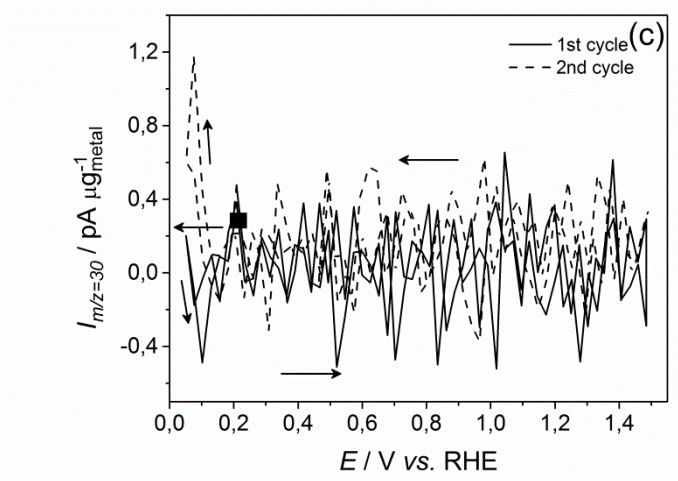

Fig. 66. (a) CV and related MSCV of the electrooxidation of acetaldehyde adsorbates in 0.5 M H_2SO_4 after adsorption at E_{ad} = 0.05 V *vs.* RHE with a first reduction scan for the mass-to-charge ratio (b) *m/z* = 15 and (c) *m/z* = 30 on Pt/C; (solid) 1st and (dash) 2nd cycle; *v* = 10 mV s^{-1}; *T* = 25°C.

V.3.3. Discussion

A comparison between the adsorption of ethanol and acetaldehyde adsorbates is broached in this section.

Both ethanol and acetaldehyde adsorbates electrooxidation show the same potentiodynamic pattern, revealing two different oxidation regions, respectively occurring between *E* = 0.5 and 0.8 V *vs.* RHE and at *E* > 0.9 V *vs.* RHE. The first reaction in the middle potential region undoubtedly corresponds to CO_{ad} electrooxidation into CO_2 [29,166,233,234]. This assertation is also supported by the calculation of the number of exchanged electrons (see Table 8 and Table 9). The oxidation of $CH_{x,ad}$-species in CO_{ad} during the pre-peak observed in the present study at *E* = 0.45 V *vs.* RHE after an adsorption at E_{ad} = 0.3 V *vs.* RHE, brought to light in [21], could not be certified, although some slight variation of this pre-peak between the cyclic voltammetries conducted with and without a first reduction scan were observed during the stripping of ethanol adsorbates.

It could be established from the present potentiodynamic results that $CH_{x,ad}$-species, or at least a part of them (*e.g.* those which do not oxidize into CO_{ad} in the pre-peak mentioned above), do oxidize at high potential (*E* > 0.9 V *vs.* RHE), most likely into CO_{ad}. The difference between the cyclic voltammetries carried out with and without a reduction scan provides a clear proof of it. Moreover, it was demonstrated in Fig. 66 that, in the case of acetaldehyde adsorbates oxidation, C_2-species do oxidize into $CH_{x,ad}$ at high potential in parallel to the oxidation of adsorbed CH_x-species into CO_{ad}. In addition, it was evidenced in Fig. 66c that the (same?) C_2-species are modifying their structure at *E* > 0.9 V *vs.* RHE

without cleaving their C-C bond, which results in ethane generation during the following reduction scan. Unfortunately, these concurrent reactions could not be confirmed with ethanol adsorbates oxidation in this study. Yet, Wang et al. demonstrated that a similar process occurs with ethanol adsorbates [227]: a CV carried out until E = 0.85 V *vs.* RHE displayed a larger methane production during the following reduction scan than during the reduction scan initiated at the beginning of the CV. It shows that there are indeed adsorbed C_2-species at least until potential as high as E = 0.85 V *vs.* RHE. It can be assumed that the C-C bond cleavage of these C_2-adsorbates takes place as the CO-like adsorbates oxidizes between E = 0.5 and 0.8 V *vs.* RHE and that the stability of these C_2-adsorbates is only ensured by the full coverage of the neighbor electroactive sites by CO_{ad}. When the latter start oxidizing, the C_2-adsorbates split into $CH_{x,a}$, and CO_{ad} (CO_{ad} further oxidizing into CO_2). Unveiling the nature of these C_2-species can hardly be discussed here and would require additional evidences, *e.g.* using Fourier Transform InfraRed (FTIR) spectroscopy. However, the ethoxi-species suggested in [29] could be a good candidate. Within the accuracy of our determination, the oxidation of $CH_{x,ad}$ into CO and furthermore into CO_2 could give rise to a significant number of electrons (up to 7 e^- per $CH_{x,ad}$).

In terms of adsorbate coverage values, Fig. 58 and Fig. 63 point towards a higher coverage of the electrocatalyst surface by the acetaldehyde adsorbates, whatever the adsorption potential. This behavior also observed by Wang et al. was imputed to the higher polarity of the acetaldehyde molecule, that eases its adsorption on Pt/C as well as its dissociation into CO_{ad} [63,227]. Regarding the present results, the higher polarity of the acetaldehyde molecule could explain the stronger binding of its adsorbates to the Pt/C surface, which literally "stick" to the electrocatalyst after incursion up to E = 1.5 V *vs.* RHE as well as the higher coverage in total acetaldehyde adsorbates. However, the higher CO_{ad} coverage could be a consequence of the latter and not from a higher dissociation power of the acetaldehyde molecule.

The distribution of ethanol and acetaldehyde adsorbates was seen to depend on the adsorption potential. At E_{ad} = 0.05 V *vs.* RHE, bulk acetaldehyde and ethanol adsorption seems slightly inhibited by H_{ad} but still manage to adsorb and dissociate into CO_{ad} at the surface of the Pt/C electrocatalyst. Dissociation into $CH_{x,ad}$ and then reduction in methane during the cyclic voltammetry following the adsorption process was not observable with the signal m/z = 15. This may be due to the low adsorption potential (E_{ad} = 0.05 V *vs.* RHE) favoring the on-time reduction of just formed $CH_{x,ad}$ in methane during the adsorption step. In the middle of the H_{upd} region, at E_{ad} = 0.15 V *vs.* RHE, the inhibition from adsorbed hydrogen species gets weaker, allowing increased coverage in ethanol and acetaldehyde adsorbates. In the latter case, the oxidation peak is even maximal. At E_{ad} = 0.3 V *vs.* RHE, the adsorption potential is located in the double layer region, thus explaining the largest oxidation of carbon monoxide issued from the ethanol adsorption. However, the fact that the CO_{ad} electrooxidation is already declining after acetaldehyde adsorption at E_{ad} = 0.3 V *vs.* RHE may indicate the partial desorption of these molecules during the adsorption step. In parallel,

the electrooxidation of strong adsorbates at high potentials (E > 0.9 V *vs.* RHE) is intensifying. This phenomenon is supposed to be greatly due to the rise in $CH_{x,ad}$ coverage, the species presumably oxidizing into CO_{ad} and then CO_2 as it can be seen when comparing the difference of coverage values between the cyclic voltammetries beginning without and with a first reduction scan in Fig. 58a and Fig. 63a. Finally, at E_{ad} = 0.5 V *vs.* RHE, the CO_{ad} coverage on Pt/C is shrinking, because the desorption/oxidation of CO_{ad} already occurs during the adsorption process at such "high" potential. The electrooxidation of strong adsorbates is therefore larger, the latter benefiting from the Pt sites freed by the desorbed/oxidized CO_{ad}-species.

V.4. On Rh/C

The adsorption/electrooxidation of ethanol adsorbates has also been studied on Rh/C following the same protocol (detailed in section VI.1). Unfortunately, due to time constraints, the experiments have only been partially accomplished on the electrocatalyst: solely one direct stripping-CV, after the CA at E_{ad} = 0.3 V *vs.* RHE, was carried out directly (without a first reduction scan from 0.2 to 0.05 V *vs.* RHE). Moreover, the results presented hereafter have not been repeated. As a consequence, the following interpretation of the results must be done with care.

Fig. 67 shows the different cyclic voltammetries run in 0.5 M H_2SO_4 after ethanol adsorbates adsorption in a 0.5 M H_2SO_4 + 0.1 M EtOH solution at E_{ad} = 0.05, 0.15, 0.3 and 0.5 V *vs.* RHE. The highest peak was recorded during the CV preceded by the CA at E_{ad} = 0.05 V *vs.* RHE and then shrinks together with the increase of the potential applied during the CAs. The corresponding mass-to-charge signal m/z = 44 (shown in Fig. 67b) supports this observation by displaying the largest CO_2 generation during the same CV. These results tend to demonstrate that ethanol adsorbates formation is eased at low potentials in the H_{UPD} region. In opposition to Pt/C, the ethanol molecules may be able to dislocate H_{ad}-species on Rh/C although its adsorption strength is similar on rhodium and platinum [237] (H_{UPD} is more weakly bounded to Rh than to Pt, as seen in the previous chapters). At higher adsorption potentials (E_{ad} = 0.3 and 0.5 V *vs.* RHE), ethanol adsorption can be hindered by OH_{ad} formation, species that are strongly adsorbed on rhodium [63]. Besides, CO_{ad} desorption/oxidation during the CA could already occur at these potentials. Finally, the competitive adsorption of ethanol with the sulfate anions (SO_4^{2-}, HSO_4^-) could also hinder ethanol adsorption at potentials between E = 0.2 and 0.5 V *vs.* RHE [116]. Indeed, according to Horanyl et al. and Zelenay et al., sulfate anions are strongly adsorbed on the rhodium surface [224,226] in this potential region.

At E > 1.2 V. *vs.* RHE, a large rise of the signal m/z = 44 is recorded in Fig. 67. This peak can be ascribed either to a CO_2 generation from the ethanol adsorbates electrooxidation

or/and to the carbon support corrosion. The distinction between the two reactions is not possible with the present data.

Finally, an interesting feature appears during the second negative scan in Fig. 67, which contrasts with the MSCVs obtained for the ethanol adsorbates electrooxidation on Pt/C (Fig. 57b): a reductive CO_2 formation is detected in the potential region between E = 0.15 and 0.4 V *vs.* RHE. This feature already reported in the literature [63] shows that some organic adsorbates still remain on the electrocatalyst surface after the first positive sweep. It can be assumed that they correspond to the adsorbates having partially oxidized into CO_2 during the previous positive scan at high potential (if the observed reaction is indeed CO_2 formation from ethanol adsorbates electrooxidation). To finish with, it can be noticed that this reductive CO_2 formation occurs simultaneously to OH-adsorbates reduction (see Fig. 26 and Fig. 67a).

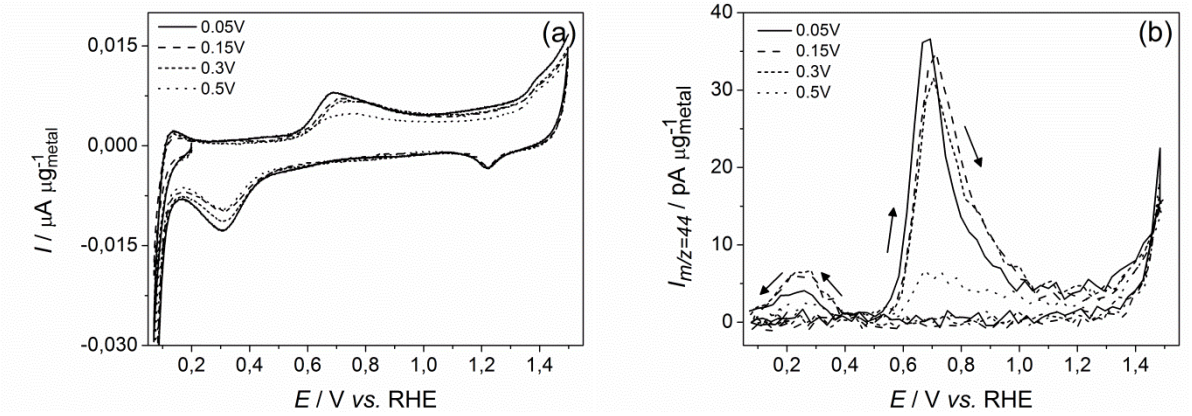

Fig. 67. (a) CV of the electrooxidation of ethanol adsorbates in 0.5 M H_2SO_4 after adsorption at E_{ad} = 0.05 (solid), 0.15 (dash), 0.3 (short dash) and 0.5 V *vs.* RHE (dots) and corresponding MSCV for mass-to-charge ratio (b) m/z = 44 and on Rh/C; v = 10 mV s^{-1}; T = 25°C.

Fig. 68 displays the first and second cycles of the cyclic voltammetry following the CA at E_{ad} = 0.3 V *vs.* RHE. Fig. 68a illustrates the difficulty to dissociate in two potential regions the adsorbates electrooxidation reactions, as it could be done for the ethanol adsorbates electrooxidation on Pt/C. In Fig. 68b, the good superposition of the first and second cycles in the very high potential region tends to show that the reaction at E > 1.2 V *vs.* RHE matches with the carbon support degradation. The absence of oxidative and reductive CO_2 formation during the second sweep evidences the complete adsorbates electrooxidation during the first scan. Then, the comparison between Fig. 68a and Fig. 68b shows that the faraday negative current (Fig. 68a) between 0.15 and 0.4 V *vs.* RHE mostly corresponds to OH_{ad} reduction: superposition of the first and second cycle of the CV (Fig. 68a) whereas the CO_2 is produced reductively solely during the first scan (Fig. 68b). Finally, a weak methane formation (ascribed to the signal m/z = 15 - in Fig. 68c) was detected during the first reduction scan of the CV, while no ethane generation (m/z = 30 - in Fig. 68d) could be noticed. Although the amount of methane is sensibly low (the peak is barely twice higher than the

noise), its presence suggests that the nature of the adsorbates is similar on Rh/C and Pt/C. The cyclic voltammetry represented in Fig. 68a and obtained after the CA at E_{ad} = 0.3 V *vs.* RHE was the only one demonstrating methane production. This result differs on Pt/C where two CVs, carried out after CA at E_{ad} = 0.3 and 0.5 V *vs.* RHE, could demonstrate methane production. The difference may be explained by the strong OH-species adsorption at E_{ad} = 0.5 V *vs.* RHE on Rh/C inhibiting ethanol adsorbates adsorption and thus methane production.

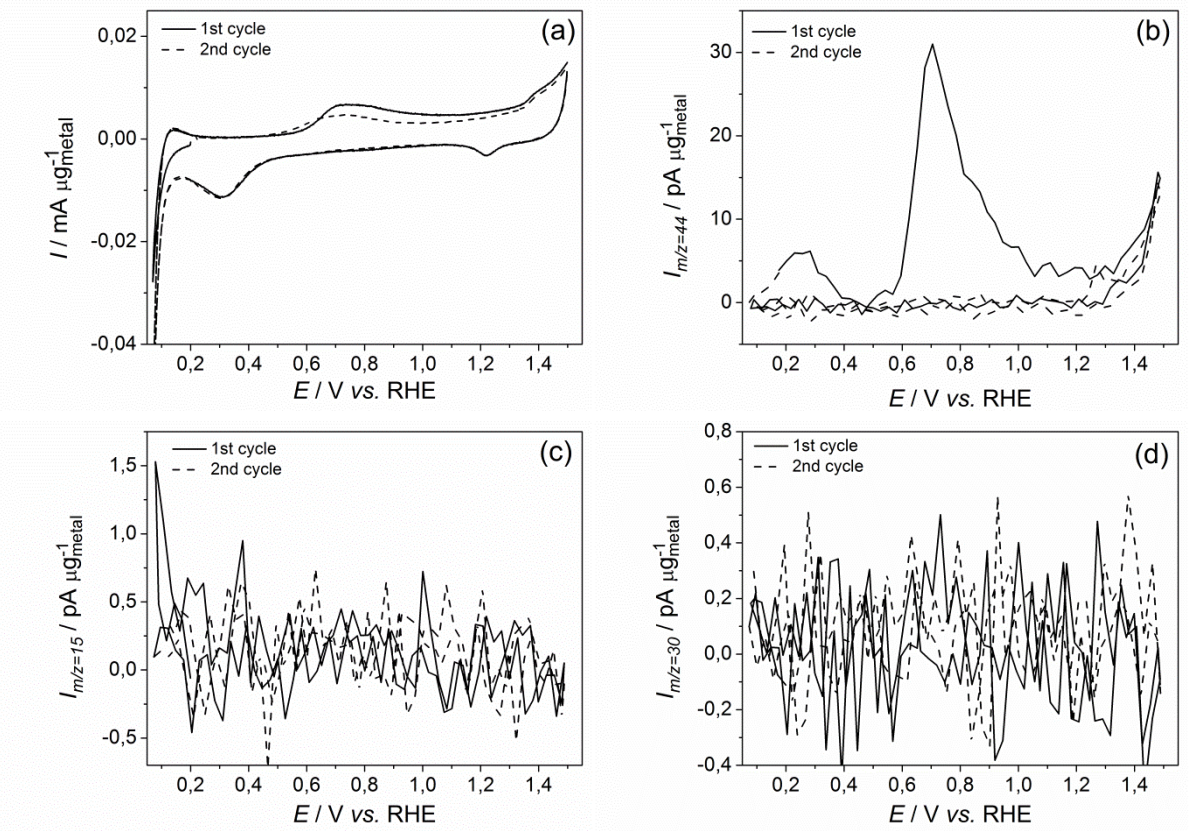

Fig. 68. (a) CV of the electrooxidation of ethanol adsorbates in 0.5 M H_2SO_4 after adsorption at E_{ad} = 0.3 V *vs.* RHE with a first reduction scan and the corresponding MSCV for mass-to-charge ratio (b) *m/z* = 44, (c) *m/z* = 15 and (d) *m/z* = 30 on Rh/C; v = 10 mV s^{-1}; T = 25°C.

V.5. On Pt-based electrocatalysts

V.5.1. Ethanol adsorbates stripping

The electrooxidation of ethanol adsorbates has also been carried out on Pt-Rh/C, Pt-SnO_2/C and Pt-Rh-SnO_2/C and was compared to Pt/C and Rh/C. Fig. 69 compares the CVs performed after a CA at E_{ad} = 0.3 V *vs.* RHE on the different electrocatalysts. The pre-peak observed for Pt/C in section VI.2 is apparent on Pt-Rh/C and maybe to a certain extent on Pt-

SnO_2/C too. However, no pre-peak is observable on Rh/C and the CV of Pt-Rh-SnO_2/C does not allow drawing any conclusion on the presence of this pre-peak. The related MSCV of the mass-to-charge m/z = 44 (Fig. 69b) shows a slight shift of the CO_2 generation onset on Pt-Rh/C (E = 0.47 V *vs.* RHE), Pt-SnO_2/C (E = 0.50 V *vs.* RHE) and Pt-Rh-SnO_2/C (E = 0.48 V *vs.* RHE) against Pt/C (E = 0.52 V *vs.* RHE). Besides, more than half of the charge from the CO_2 formation is located on the left-side of the dashed line for Pt-Rh/C and Pt-SnO_2/C. This information illustrates the rather small shift of the CO-like adsorbates in CO_2.

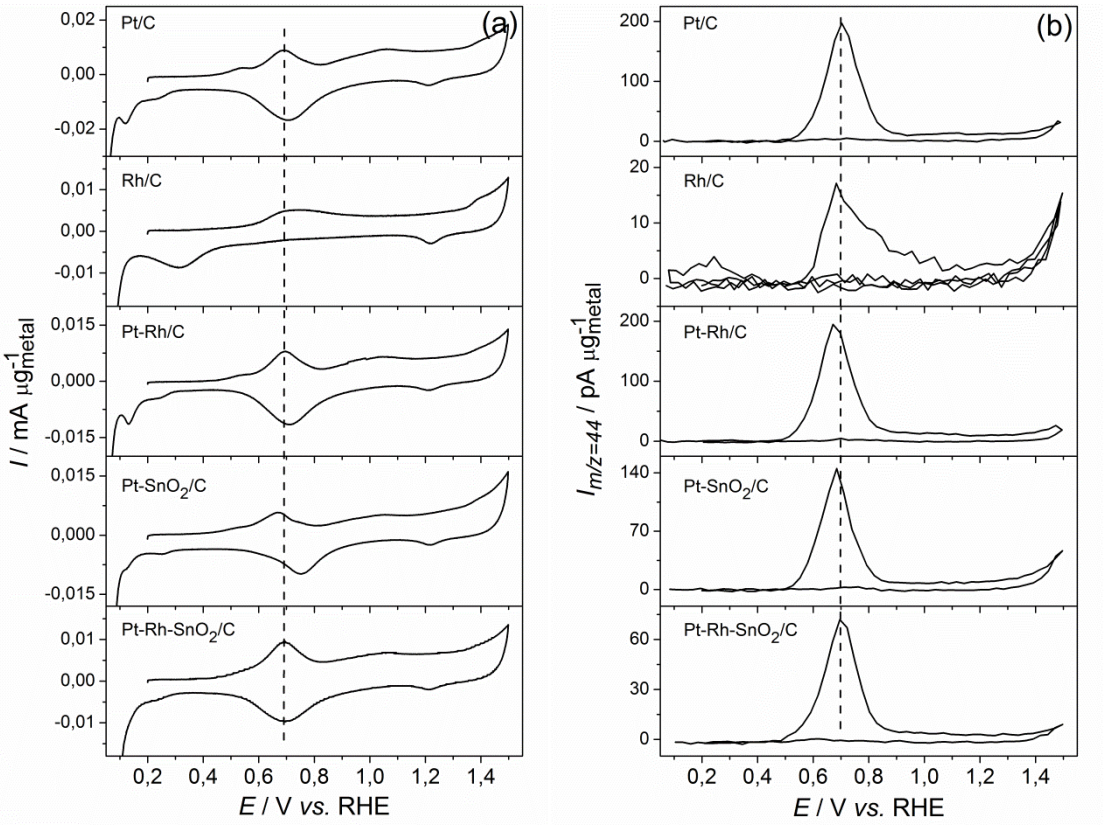

Fig. 69. (a) CV of the electrooxidation of ethanol adsorbates in 0.5 M H_2SO_4 after adsorption at E_{ad} = 0.3 V *vs.* RHE and the corresponding MSCV for mass-to-charge ratio (b) m/z = 44 on Pt/C, Rh/C, Pt-Rh/C, Pt-SnO_2/C and Pt-Rh-SnO_2/C; v = 10 mV s^{-1}; T = 25°C.

The electrocatalyst relative surface coverage by ethanol adsorbates has been investigated on Pt-Rh/C, Pt-SnO_2/C and Pt-Rh-SnO_2/C and has been compared to Pt/C. As the results on Rh/C were not repeated, no quantification of the relative coverage of the electrocatalyst surface has been accomplished. Fig. 70 shows the coverage by CO-like adsorbates deduced from the calculated faraday (Fig. 70a) and ionic (m/z = 44) charges (Fig. 70b).

First and foremost, it can be noticed the good proximity between the charge values deduced from the faraday and spectrometric measurements. A maximum coverage is reached

on Pt-Rh/C, Pt-SnO_2/C and Pt-Rh-SnO_2/C at E_{ad} = 0.15 V *vs.* RHE against E_{ad} = 0.3 V *vs.* RHE on Pt/C. It can be deduced that the ethanol adsorption is eased at quite low potential (E_{ad} = 0.15 V *vs.* RHE) on the bi-and tri-metallic electrocatalysts *versus* Pt/C. However, these results can be tempered by the fact that the coverage in ethanol coverage on the bi- and tri-metallic electrocatalysts is more or less the same than on Pt/C at lower adsorption potential (E_{ad} = 0.05 V *vs.* RHE).

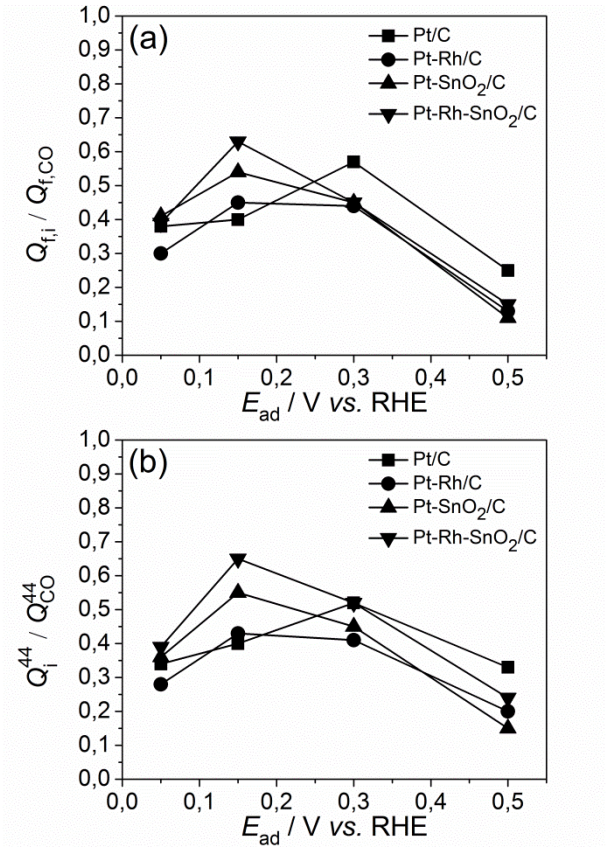

Fig. 70. Relative coverage of Pt/C, Pt-Rh/C, Pt-SnO_2/C and Pt-Rh-SnO_2/C electroactive surface by ethanol CO-like adsorbates (oxidizing at 0.4 V < E < 0.9 V *vs.* RHE) adsorbed at E_{ad} = 0.05, 0.15, 0.3 and 0.5 V *vs.*RHE deduced from (a) faraday charges and (b) ionic charges from the mass-to-charge signal m/z = 44.

Fig. 71 shows the relative coverage of the "strong adsorbates" oxidizing only at E > 0.9 V *vs.* RHE. While at high adsorption potentials (E_{ad} = 0.5 V *vs.* RHE) the coverage values are quite similar between the electrocatalysts, a larger discrepancy of the coverage values is obtained after adsorption at low adsorption potentials (E_{ad} = 0.05 and 0.15 V *vs.* RHE). Pt-SnO_2/C demonstrates at E_{ad} = 0.05 and 0.15 V *vs.* RHE the largest coverage in ethanol strong adsorbates and to some extent Pt-Rh-SnO_2/C at E_{ad} = 0.3 V *vs.* RHE. However regarding the values uncertainty (± 0.1), it was found wiser not to speculate on a hypothetical higher

adsorption on an apparent higher electrocatalyst coverage by "strong adsorbates" on Pt-SnO_2/C at low adsorption potentials.

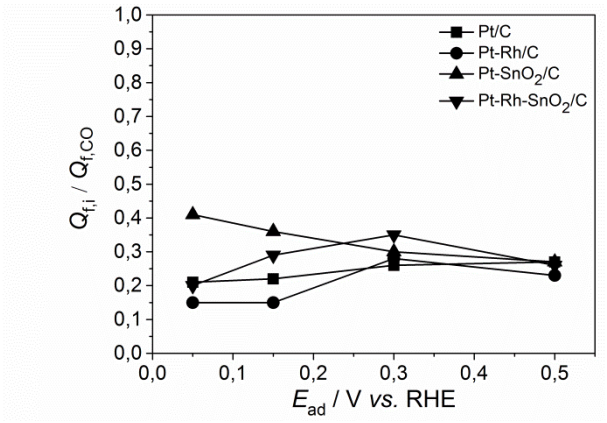

Fig. 71. Relative coverage of Pt/C, Pt-Rh/C, Pt-SnO_2/C and Pt-Rh-SnO_2/C electroactive surface by "strong ethanol adsorbates" (oxidizing at E > 0.9 V *vs.* RHE) adsorbed at E_{ad} = 0.05, 0.15, 0.3 and 0.5 V *vs.* RHE deduced from faraday charges.

V.5.2. Acetaldehyde adsorbates stripping

Fig. 72 shows comparative acetaldehyde adsorbates stripping-CVs between Pt/C, Pt-Rh/C and Pt-Rh-SnO_2/C after E_{ad} = 0.3 (Fig. 72a) and 0.05 V *vs.* RHE (Fig. 72b). No experiment was carried out on Rh/C and Pt-SnO_2/C. The CVs obtained after E_{ad} = 0.3 V *vs.* RHE are rather similar with one another. The presence of rhodium in Pt-Rh/C does not seem to help the oxidation of CO-like species (the results are even showing the opposite), whereas the combined addition of rhodium and tin oxide in Pt-Rh-SnO_2/C seems to help this oxidation reaction at low potentials (it is believed that tin oxide alone is responsible for CO_2 easier generation from CO_{ad}, Rh probably easing the C-C bond splitting): the onset potential is located at *ca.* E = 0.4 V *vs.* RHE on Pt-Rh-SnO_2/C against E = 0.45 V *vs.* RHE for the initiation of the pre-peak on Pt/C. At E_{ad} = 0.05 V *vs.* RHE (Fig. 72b), the differences between the electrocatalysts is more significant. The CO-like adsorbates start oxidizing on Pt-Rh/C and Pt-Rh-SnO_2/C at potentials lower than on Pt/C. This behavior is attributed to the shift toward positive potentials of CO_{ad} electrooxidation on Pt/C. Indeed, the dashed line centered on Pt/C shifts from E = 0.70 V *vs.* RHE in Fig. 72a to E = 0.77 V *vs.* RHE in Fig. 72b. These facts are supported by the associated mass-to-charge signals m/z = 44 in Fig. 72c and Fig. 72d. Moreover, it can be observed that the CO-like adsorbates stripping peak on Pt/C and Pt-Rh/C is more spread on the potential scale in Fig. 72b than in Fig. 72a thus showing that the oxidation occurs at a slower rate after the CV at E_{ad} = 0.05 V *vs.* RHE. This small shift and possible slower CO_{ad} oxidation kinetics could be due to the presence of hydrogen adsorbates

formed at E_{ad} = 0.05 V *vs.* RHE, which could inhibit hydroxide species adsorption, necessary for CO_{ad} oxidation into CO_2.

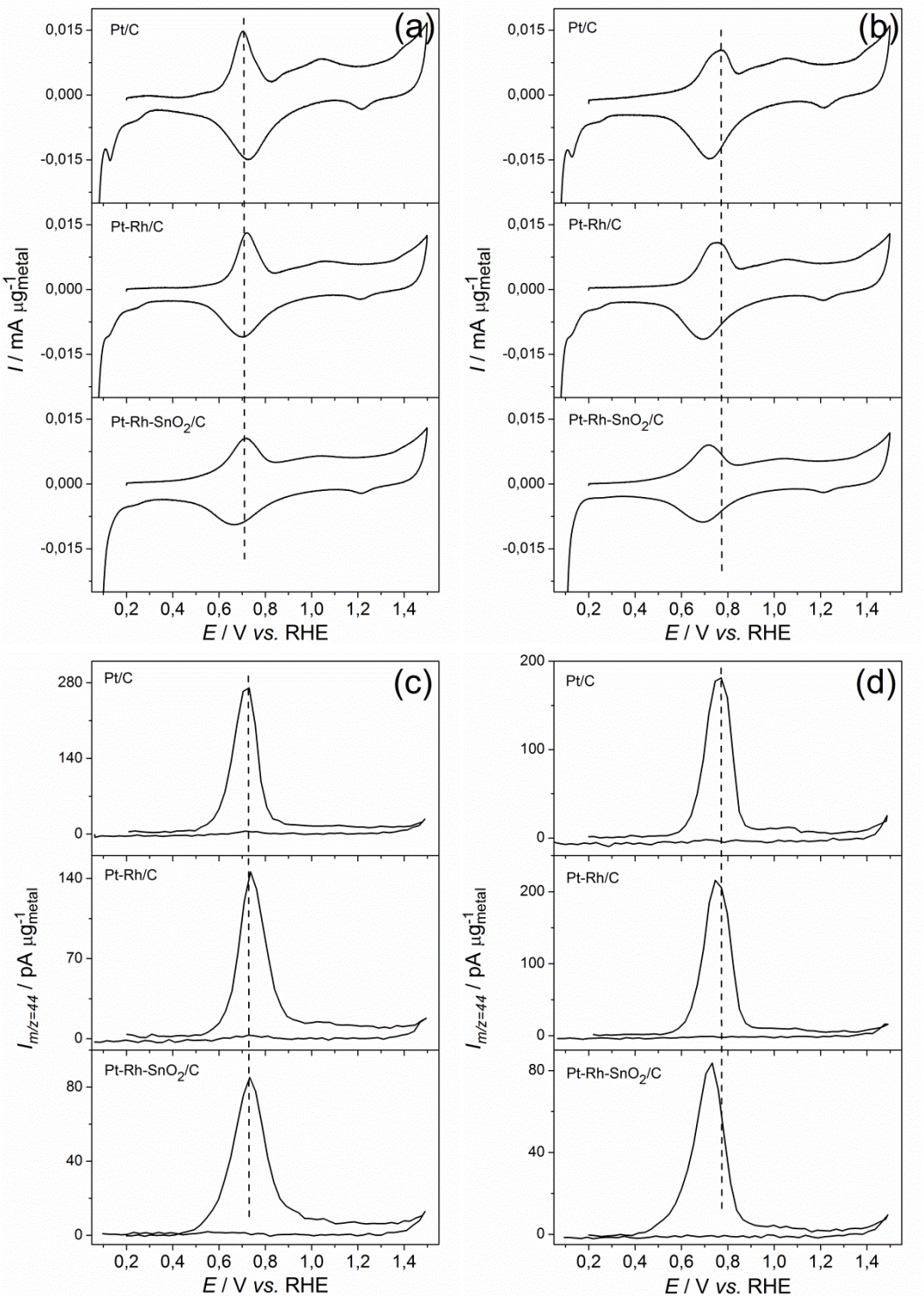

Fig. 72. (a) CV of the electrooxidation of acetaldehyde adsorbates in 0.5 M H_2SO_4 after adsorption at E_{ad} = (a) 0.3 and (b) 0.05 V *vs.* RHE and (c, d) the corresponding MSCV for mass-to-charge ratio *m/z* = 44 on Pt/C, Pt-Rh/C and Pt-Rh-SnO_2/C; v = 10 mV s^{-1}; T = 25°C.

The relative electrocatalyst coverage by acetaldehyde CO-like adsorbates is shown in Fig. 73. The profile of the curves is quite similar on Pt/C and Pt-Rh/C with a maximum coverage reached at E_{ad} = 0.15 V *vs.* RHE. Yet, the fact that the coverage decreases sharply at E_{ad} = 0.3 V *vs.* RHE on Pt-Rh/C, whereas a small plateau is formed on Pt/C between E_{ad} = 0.15 and E_{ad} = 0.3 V *vs.* RHE, indicates that the maximum CO_{ad}-species coverage may be reached at lower potential on Pt-Rh/C than on Pt/C. In contrast to the two electrocatalysts, the maximum coverage is already reached at E_{ad} = 0.05 V *vs.* RHE on Pt-Rh-SnO_2/C. It seems that the combined effect of Rh and SnO_2 addidition eases the adsorption of the CO-like adsorbates at low potentials and/or eases their electrooxidation at lower potentials (which would result in their electrooxidation/desorption during the CA and thus would lead to lower coverage values). The last explanation is supported by the CO-stripping results (Fig. 27) which evidences the lower onset potential on Pt-Rh-SnO_2/C compared to Pt/C and Pt-Rh/C.

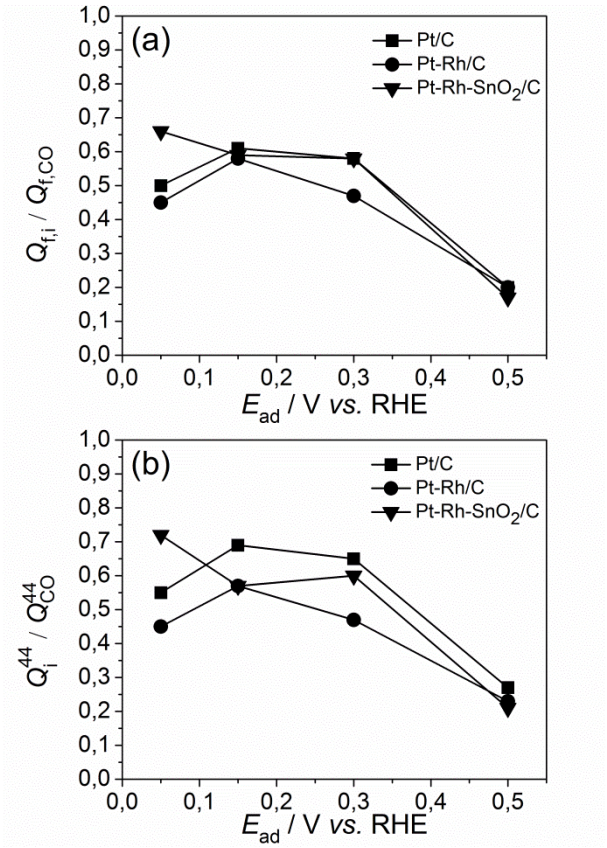

Fig. 73. Relative coverage of Pt/C, Pt-Rh/C and Pt-Rh-SnO_2/C electroactive surface by acetaldehyde CO-like adsorbates adsorbed at E_{ad} = 0.05, 0.15, 0.3 and 0.5 V *vs.*RHE deduced from (a) faraday charges and (b) ionic charges from the mass-to-charge signal *m/z* = 44.

The relative coverage by acetaldehyde "strong adsorbates" is presented in Fig. 74. No difference is observed between the three electrocatalysts, which all present the same tendency.

Alike Pt/C, the slight increase at E_{ad} = 0.3 and 0.5 V *vs.* RHE can be explained by the freeing of the electrocatalytic sites by CO-like adsorbates that already desorbs from the surface during the CA at these potentials. The slightly higher values at E_{ad} = 0.05 V *vs.* RHE could be assigned to a favored acetaldehyde non-dissociative adsorption due to the presence of hydrogen adsorbates on the electrocatalyst, which would result in an increase of non-active C_2-adsorbates as their presence was demonstrated in Fig. 66.

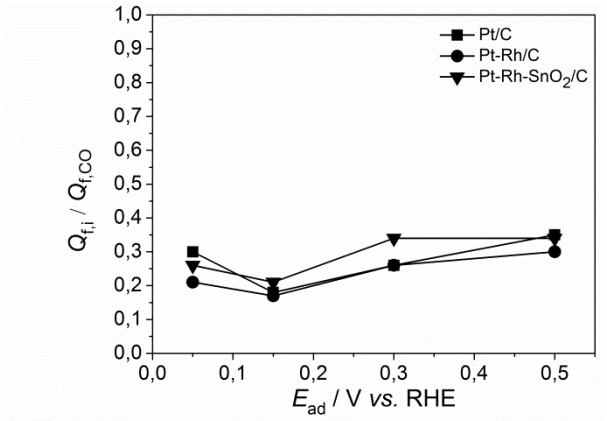

Fig. 74. Relative coverage of Pt/C, Pt-Rh/C and Pt-Rh-SnO_2/C electroactive surface by "strong acetalehyde adsorbates" (oxidizing at E > 0.9 V *vs.* RHE) adsorbed at E_{ad} = 0.05, 0.15, 0.3 and 0.5 V *vs.* RHE deduced from faraday charges.

V.6. Conclusions

Investigating ethanol and acetaldehyde adsorption on the different electrocatalysts allowed the understanding of both the EOR mechanism and the improvement brought by each component of the electrocatalysts.

Adsorption of bulk ethanol and acetaldehyde, followed by the potentiodymanic stripping of their adsorbates, has been performed at E_{ad} = 0.05, 0.15, 0.3 and 0.5 V *vs.* RHE and was studied by on-line DEMS. The aim of this study was to give further insights into the intermediates and products of the bulk ethanol and acetaldehyde electrooxidation and in their distribution on the Pt/C surface. It also enabled to evaluate the effect of the addition of rhodium or/and tin oxide in the Pt-based electrocatalysts on the adsorbates stripping.

The potentiodynamic electrooxidation of ethanol and acetaldehyde adsorbates could be separated in two potential regions. On the one hand, between E = 0.5 and 0.8 V *vs.* RHE, the prevailing reaction appears to be a CO_{ad} electrooxidation in CO_2. A pre-peak between *ca.* E = 0.45 and 0.55 V *vs.* RHE was formed after adsorbates adsorption at E_{ad} = 0.3 V *vs.* RHE,

which may correspond to the oxidation of adsorbed CH_x-species into CO_{ad}. Nonetheless, this reaction could not be evidenced based on the present experiments. On the other hand, at E > 0.9 V *vs.* RHE, the oxidation of adsorbed CH_x-species into CO_2 occurs in parallel to the oxidation of C_2-species into $CH_{x,ad}$. The latter reaction could however only be identified for the acetaldehyde adsorbates electrooxidation.

The number of exchanged electrons was in each potential region calculated after calibration of the mass-to-charge signals m/z = 22 and m/z = 44. The electrooxidation of CO_{ad} into CO_2 between E = 0.5 and 0.8 V *vs.* RHE, already known in the literature, was confirmed by the calculation of the number of exchanged electrons (2 e^-). The reaction taking place at high potential *(*E > 0.9 V *vs.* RHE) was found to generate between 4 and 8 electrons depending on the adsorption potential and could correspond to the oxidation of $CH_{x,ad}$ in CO_2 (up to 7 e^-).

CO_{ad}-species constitute the main bulk ethanol and acetaldehyde adsorbates after their adsorption at E_{ad} = 0.05, 0.15 and 0.3 V *vs.* RHE. For E_{ad} > 0.3 V *vs.* RHE, stronger adsorbates ($CH_{x,ad}$, C_2-adsorbates) start taking more Pt/C electroactive sites before becoming predominant at E_{ad} = 0.5 V *vs.* RHE.

The largest ethanol CO-like adsorbates oxidation peak was found for E_{ad} = 0.05 V *vs.* RHE on Rh/C. Rhodium higher dehydrogenation ability could explain this result. No charge calculation was carried out on the electrocatalyst. The operation is rendered difficult due to a possible overlap of the two adsorbates oxidation regions, as reported previously on Pt/C.

The CO_{ad} maximal oxidation charge reaches a maximum at lower potential on the Pt-based electrocatalysts than on Pt/C, both for acetaldehyde and ethanol adsorbates. Unfortunately, no potential onset shift toward lower potentials of the ethanol originated CO_{ad} stripping could be identified. On the contrary, the initiation of acetaldehyde CO-like adsorbates oxidation reaction occurred at lower potentials on Pt-Rh/C and Pt-Rh-SnO_2/C than on Pt/C after adsorption at E_{ad} = 0.05 V *vs.* RHE (the result was more biased at E_{ad} = 0.3 V *vs.* RHE).

Chapter VI.

Influence of the temperature for the ethanol oxidation reaction (EOR) on Pt/C, Pt-Rh/C and Pt-Rh-SnO_2/C

This chapter focuses on the influence of the temperature on the EOR mechanism on Pt/C, Pt-Rh/C and Pt-Rh-SnO_2/C. The first part will consist of an overview of the existing literature on the temperature effect on the ethanol electrooxidation on Pt and Pt-based electrocatalysts. Then, the experimental investigation will be broached. The results presented hereafter were obtained in a three-electrode setup with our polyol-made 10 wt.% electrocatalysts. A thorough analysis of these results is finally carried out in order to understand how the EOR mechanism is modified by increasing the temperature.

VI.1. Influence of the temperature on the EOR

Like most complex electrochemical reactions, the EOR is a temperature-dependent reaction [35,43,238–242]. Lima et al. recorded shifts of the EOR onset potential as well as of the CO_2 generation initiation on Pt/C and Pt-Rh/C with the increase of the temperature from 25°C to 60°C [35]. They ascribed the CO_2 generation at lower potentials at higher temperatures to the larger water activation and a lower Pt-CO bond strength when the temperature increases (up to 60°C). They also observed that the EOR onset shift between 25°C and 60°C was higher on Pt-Rh/C than on Pt/C, this result being explained by an enhanced bi-functional mechanism on the bimetallic electrocatalyst. Similarly, Behm et al. demonstrated that the CO_2 generation starts at lower potentials when the temperature increases [43]. According to the authors, the CCE increases together with the temperature: at the maximum investigated temperature (100°C), the maximum CCE equals *ca.* 45 % at *ca.* E = 0.5 V *vs.* RHE compared to barely 10 % at temperatures below 60°C. A thermal activation of the CO_{ad} electrooxidation explains the CO_2 generation at lower potentials, while the ease of the C-C bond breaking justifies the rise of the CCE values. Moreover, calculations of apparent activation energies revealed a slight decrease of the rate determining step (*rds*) with the potential rise. On the contrary, the *rds* at a given potential is unchanged whatever the temperature in the range 25°C - 100°C (the nature of the *rds* was not surveyed in this study). Conversely, Mahapatra et al. observed that the activation energy soars together with the potential in the temperature range 20°C-80°C [240]. By a brief comparison of the literature [43,77,240,243], the estimation of activation energy values brings conflicting results between the different studies. The importance of the experimental conditions in the determination of these values therefore appears primordial.

The aim of this chapter is precisely to investigate the influence of the temperature on the electrocatalytic EOR activity of bi-metallic Pt-Rh/C and tri-metallic Pt-Rh-SnO_2/C electrocatalysts, and to compare these with that of Pt/C. Potentiostatic and potentiodynamic studies were achieved on the 10 wt.% electrocatalysts, all prepared by a modified polyol method. A thorough potentiostatic study on the EOR kinetics was carried out by means of Tafel plots at 25°C, 40°C and 70°C. Steady-state EOR apparent activation energies were finally calculated in the potential range E = 0.4 – 0.7 V *vs.* RHE.

VI.2. Physical characterization

Fig. 75 displays representative XRD spectra of the 10 wt.% carbon-supported electrocatalysts. The sharpness of Pt/C and Pt-Rh-SnO_2/C patterns corresponds to well-crystallized nanoparticles in the fcc structure. More particularly, the sharp diffraction pattern of Pt/C could be related to a large average cristallite size, but the TEM data of Fig. 75 show that it is most probably caused by the presence of a few large or agglomerated nanoparticles.

The XRD pattern of Pt-Rh/C does not agree with a perfectly crystalline structure (in other words, Pt-Rh/C is either amorphous or with very small crystallites; this issue will be clarified below). An evaluation of the average cristallite size was carried out using the Scherrer's law on the (111) diffraction peak, as summarized in Table 10, together with the phases lattice parameters. It is wise stating that these 10 wt.% electrocatalysts were prepared prior to those characterized in chapter III, IV and V. At that time, the polyol method, and more specifically the dissolution of the rhodium salt ($RhCl_3$), was not optimally controlled (the mass of rhodium salt introduced in the synthesis solution was 50 wt.% higher than the optimal mass corresponding to a 10 wt.% metal loading)

The composition of Pt/C was determined by TGA: the synthesis indeed yield 10 wt.% electrocatalysts. ICP-AES measurements revealed the presence of 5.14 wt.% Pt and 4.95 wt.% Rh for Pt-Rh/C (10.1 wt.% $Pt_1Rh_{1.6}$/C) and 5.34 wt.% Pt, 2.21 wt.% Rh and 0.94 wt.% Sn for Pt-Rh-SnO_2/C (8.49 wt.% $Pt_1Rh_{0.79}(SnO_2)_{0.14}$/C).

Table 10. Structural proprieties of Pt/C, Pt-Rh/C and Pt-Rh-SnO_2/C electrocatalysts obtained by XRD and TEM

Electrocatalyst	Effective composition by ICP-AES	a / Å	d_{XRD} / nm	d_{Elec} / nm	d_N / nm	d_S / nm	d_V / nm
Pt/C	-	3.91	10	4.9	2.5	5.5	8.2
Pt-Rh/C	$Pt_1Rh_{1.6}$	3.88	1.2	2.0	2.4	2.6	2.8
Pt-Rh-SnO_2/C	$Pt_1Rh_{0.79}(SnO_2)_{0.14}$	3.91	3.3	6.2	3.2	3.5	3.7

a: lattice parameter; d_{XRD} : mean nanoparticle size (XRD); d_{Elec}: electrochemical mean particle size; d_N: number-averaged diameter (TEM); d_S: surface-averaged diameter (TEM); d_V: volume-averaged diameter (TEM)

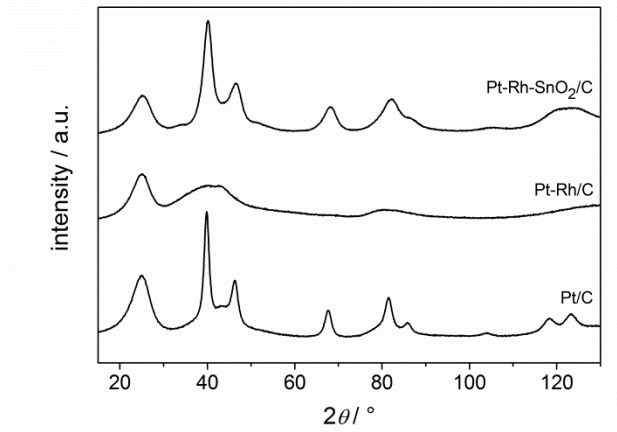

Fig. 75. XRD pattern of 10wt.% carbon supported Pt/C, Pt-Rh/C and Pt-Rh-SnO_2/C electrocatalysts prepared by the polyol method.

The electrocatalysts morphology and the particle size distribution (PSD) were further characterized by TEM. As seen in Fig. 76 and similarly to what was observed for the other electrocatalysts in Fig. 25, a uniform dispersion of relatively small nanoparticles on the

carbon support was obtained for all synthesized electrocatalyst compositions. The associated histograms in Fig. 76 reveal a narrow particle size distribution with a very similar mean particle size. The presence of some agglomerates was nonetheless observed on Pt/C.

Table 10 points out a discrepancy for the volume-averaged TEM diameter d_V and the mean crystallite size determined by XRD, d_{XRD}, both for Pt/C and Pt-Rh/C electrocatalysts; on the one hand, Pt/C suffers the presence of large particles and/or agglomerates, while, on the other hand, the smaller size extracted from the XRD data for Pt-Rh/C may be ascribed to an imperfect crystallization of the nanoparticles in these samples. In complement, d_{Elec} is in accordance with d_S for Pt/C and Pt-Rh/C but not for Pt-Rh-SnO_2/C. The inconsistency between d_{Elec} and d_S values was also observed in Table 4 for the tri-metallic electrocatalyst and was explained by an underestimation of the ECSA.

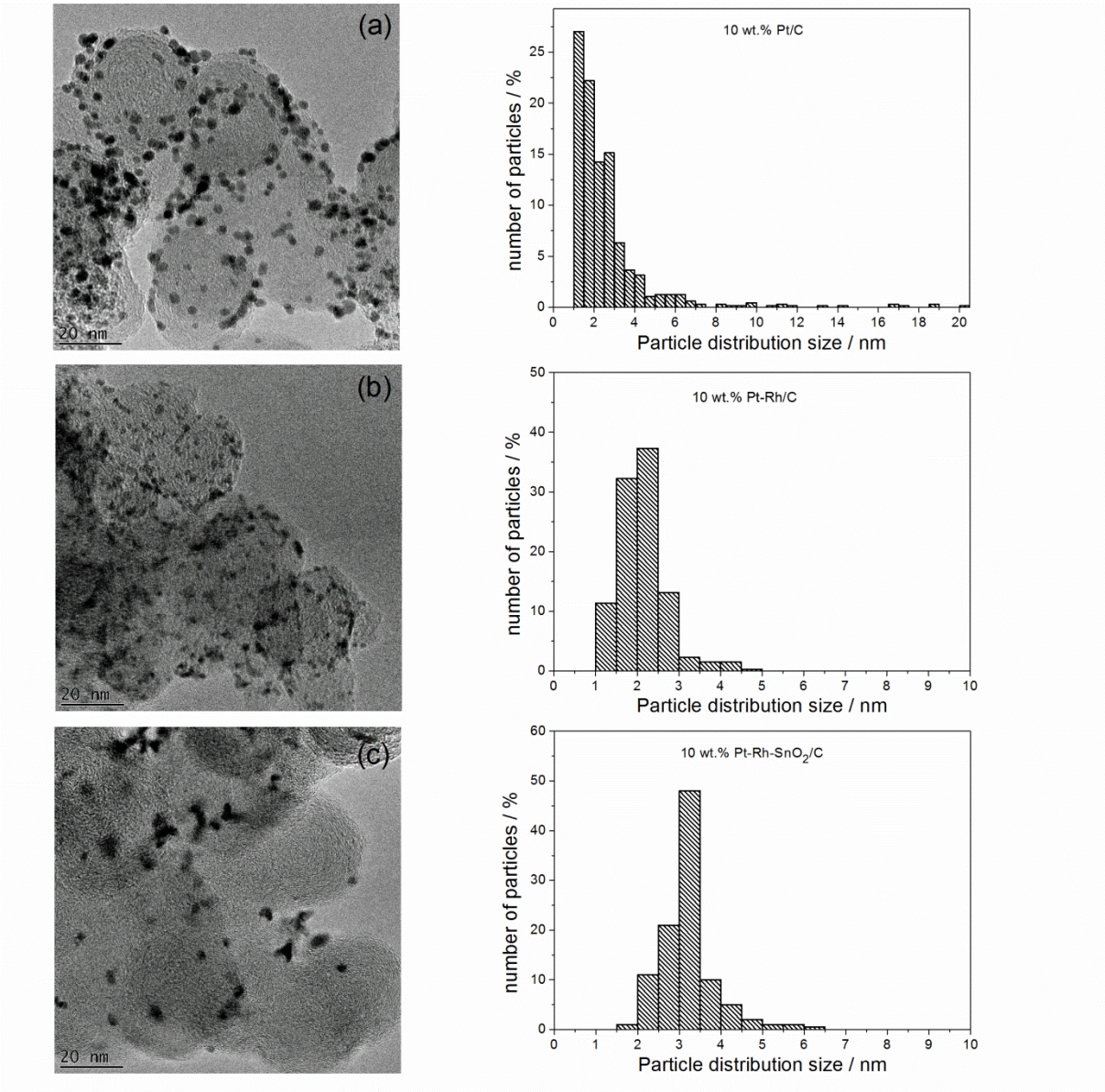

Fig. 76. Typical TEM images and associated particle size distribution of the 10 wt. % (a) Pt/C, (b) Pt-Rh/C and (c) Pt-Rh-SnO_2/C electrocatalysts.

VI.3. CVs in supporting electrolyte

Fig. 77 compares cyclic voltammograms on Pt/C (Fig. 77a), Pt-Rh/C (Fig. 77b) and Pt-Rh-SnO_2/C (Fig. 77c) obtained in supporting electrolyte (0.5 M H_2SO_4) at 25°C, 40°C and 70°C. The CVs at room temperature were already described in Fig. 26 on the 20 wt.% electrocatalysts, and, as such, will not be thoroughly detailled here. The usual features of the so-called oxygen region of Pt-based electrodes can be observed. In Fig. 77, at room temperature, the Pt oxide region (*i.e.* the region of water dissociation) initiates at E = 0.55 V

vs. RHE on Pt/C *versus* E = 0.44 V *vs.* RHE on Pt-Rh/C and E = 0.40 V *vs.* RHE on Pt-Rh-SnO_2/C. The usual features of the hydrogen region cannot be properly distinguished at room temperature (Fig. 77) due to the quite high value of the low-vertex potential (E = 0.1 V *vs.* RHE) chosen for this set of experiments. Only the initiation of hydrogen adsorption is clearly observable on the three electrocatalysts.

Fig. 77 reveals the metal oxide formation and water dissociation are greatly amplified for all electrocatalysts as the temperature increases to 40°C and 70°C; however, the onset potential of the process remains more or less the same. Faster water dissociation kinetics and place-exchange (on the electrocatalyst surface) could explain the current increase. Similarly, during the negative scan, the rise of the temperature intensifies extremely the oxide reduction current (in proportion to its increase in the positive scan) but does not impact the peak potential for Pt/C and Pt-Rh/C, which likely shows that the temperature does not influence the stability of the oxides at the surface of the two electrocatalysts. On the contrary, the shift toward positive potential of the oxide reduction peak on Pt-Rh-SnO_2/C could be attributed to the oxides lower stability on the electrocatalysts and especially on SnO_2. The rise of the temperature to 40°C and 70°C in Fig. 77a also generates a positive shift of the hydrogen adsorption on the Pt/C electrocatalyst (this observation on Pt/C could not be confirmed on Pt-Rh/C and Pt-Rh-SnO_2/C).

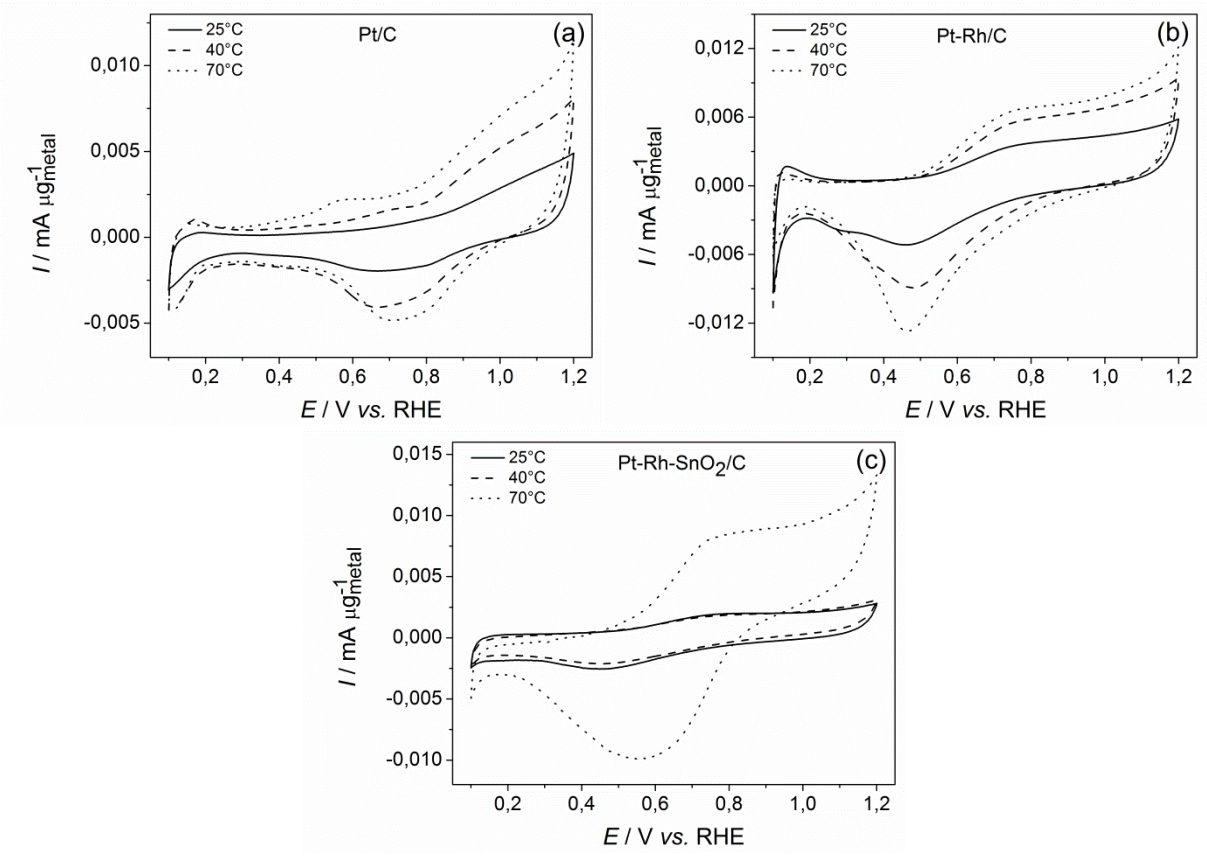

Fig. 77. CV in 0.5 M H_2SO_4 on (a) Pt/C, (b) Pt-Rh/C and (c) Pt-Rh-SnO_2/C at T = 25°C (full), 40°C (dash) and 70°C (dots); v = 10 mV s^{-1}.

VI.4. CO_{ad} monolayer electrooxidation

Fig. 78 displays comparative CO-stripping voltammograms at 25°C, 40°C and 70°C on Pt/C (Fig. 78a), Pt-Rh/C (Fig. 78b) and Pt-Rh-SnO_2/C (Fig. 78c). Similarly to Fig. 27, the CO-stripping initiates at lower potential on Pt-Rh-SnO_2/C and Pt-Rh/C than on Pt/C (see onset values summarized in Table 11). The effect of the temperature rise is the same on the three electrocatalysts: the CO-stripping potential onset shifts negatively with the increase of the temperature from 25°C to 70°C. Two effects can rationalize this observation: (i) it can be assumed that a rise of the temperature destabilizes CO_{ad} species thus lowering the M-CO (with M = Pt and Rh) adsorption strength; (ii) the easier generation of OH_{ad}-species (water dissociation is enhanced at higher temperature, which enables higher electrocatalyst coverage in OH_{ad} species at low potential) could also contribute to the CO_{ad} electrooxidation lower onset potential.

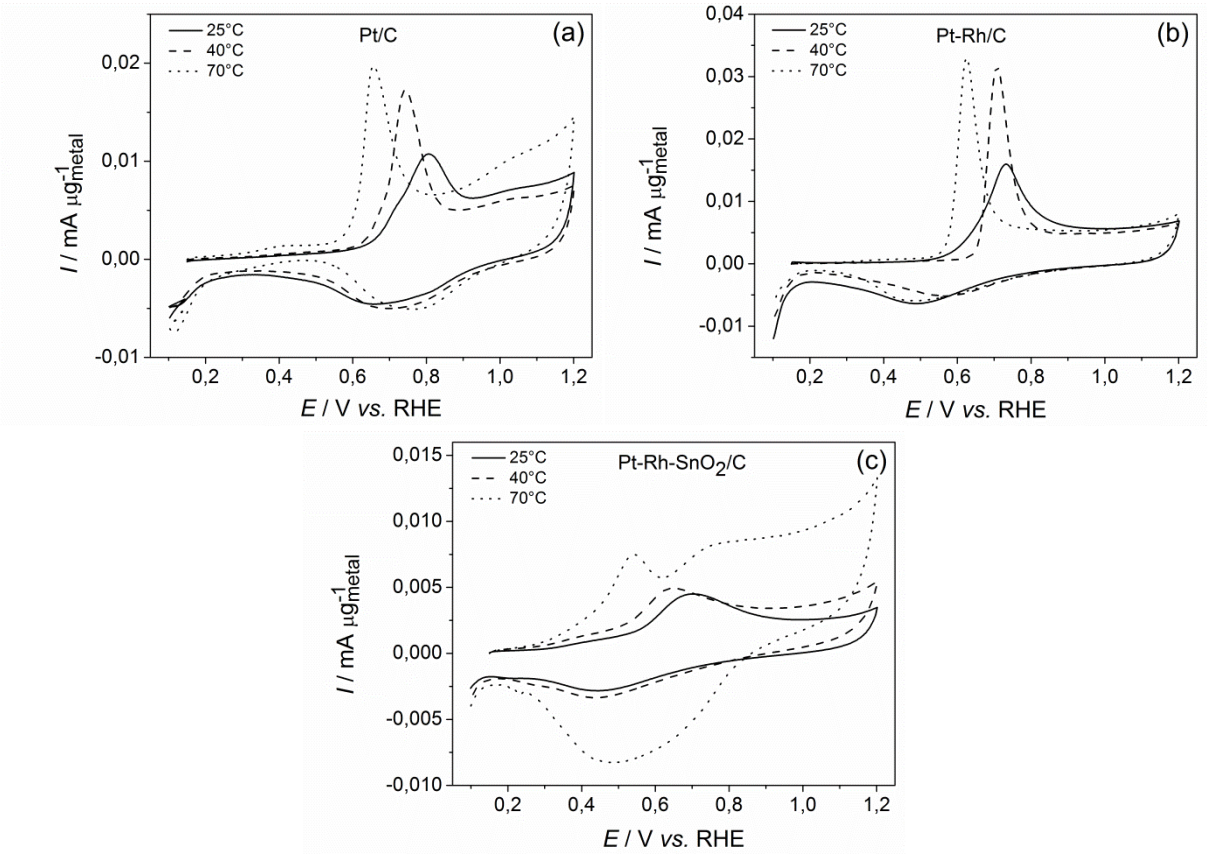

Fig. 78. CO-stripping CV in 0.5 M H_2SO_4 on (a) Pt/C, (b) Pt-Rh/C and (c) Pt-Rh-SnO_2/C; T = 25°C (full), 40°C (dash) and 70°C (dots); v = 10 mV s^{-1}.

Table 11. Values of the CO-stripping onset potential measured on Pt/C, Pt-Rh/C and Pt-Rh-SnO_2/C at 25°C, 40°C and 70°C.

	Pt/C	Pt-Rh/C	Pt-Rh-SnO_2/C
T / °C		*E* / V *vs.* RHE	
25	0.65	0.58	0.53
40	0.60	0.63	0.50
70	0.56	0.52	0.45

VI.5. Potentiodynamic EOR

Fig. 79 displays representative cyclic voltammograms relative to the EOR at 25°C, 40°C and 70°C on Pt/C, Pt-Rh/C and Pt-Rh-SnO_2/C. Like in Fig. 44, limited differences can be observed at room temperature between the EOR onset potentials of the three electrocatalysts: a lower potential onset of *ca.* 50 mV on Pt-Rh/C and 20 mV on Pt-Rh-SnO_2/C can be witnessed compared to Pt/C. However, the influence of the temperature plays a major role in the distinction of the EOR performances on the three electrocatalysts. Indeed, the EOR potential onset shifts negatively with the rise of the temperature from 25°C to 40°C and 70°C: the reaction overpotential on Pt/C falls from E = 0.64 V *vs.* RHE at 25°C to E = 0.53 V *vs.* RHE at 40°C and E = 0.49 V *vs.* RHE at 70°C. This shift may illustrate the enhancement of bulk ethanol adsorption/oxidation at low potentials with the rise of the temperature. The EOR overpotential shrinks even more drastically on Pt-Rh/C (from E = 0.59 to 0.45 V *vs.* RHE) and Pt-Rh-SnO_2/C (from E = 0.62 to 0.37 V *vs.* RHE) (all values are summarized in Table 12).

The influence of the temperature rise on the EOR is also evidenced during the backward (negative) scan on the three electrocatalysts (Fig. 79): the EOR starts at slightly more positive potentials and the kinetics speeds intensively up on the three electrocatalysts when the temperature increases. This observation can be rationalized by two combined effects: on the one hand, the faster oxide reduction frees the electrocatalysts surface more rapidly for the EOR and enables a faster initiation of the reaction; on the other hand, an enhancement of the reactions occurs during the EOR (ethanol dehydrogenation and acetic acid formation - see chapter III and IV).

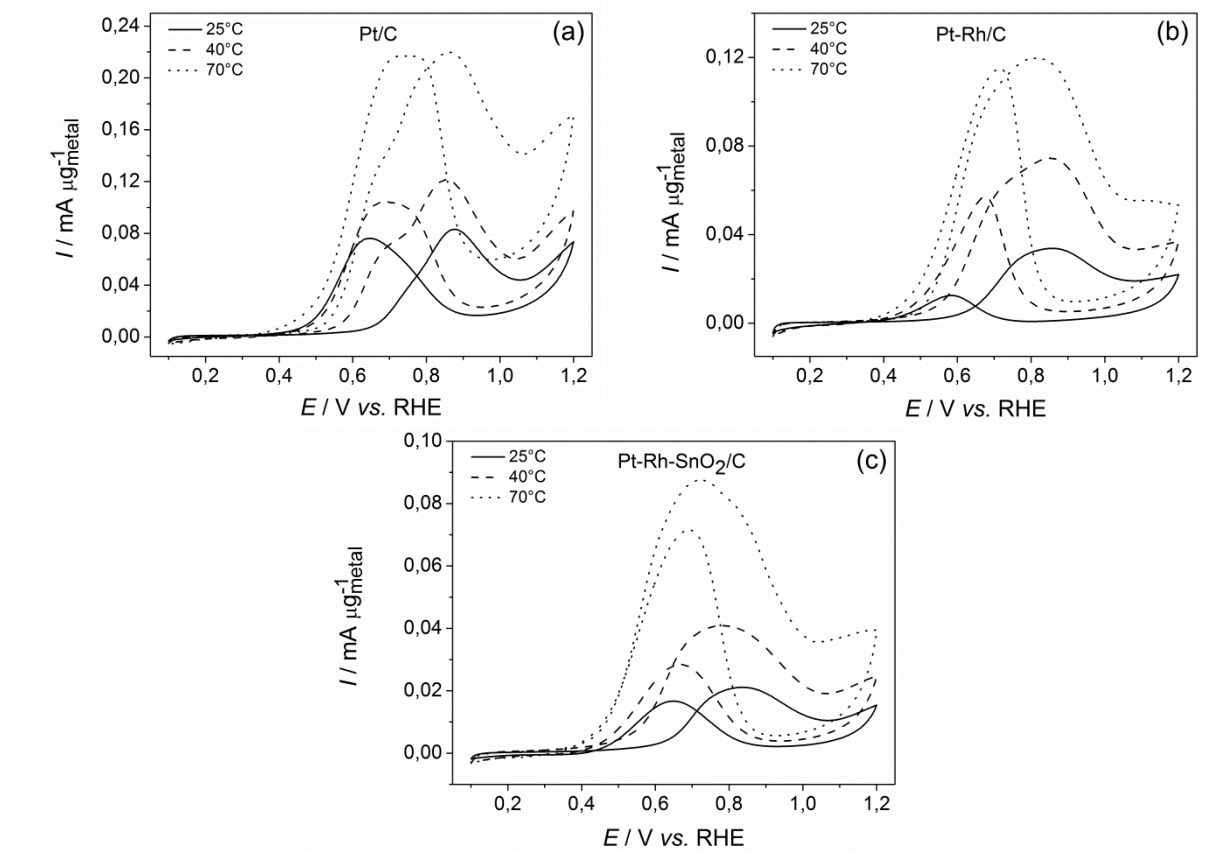

Fig. 79. CV in 0.5 M H_2SO_4 + 0.1 M EtOH of the EOR on (a) Pt/C, (b) Pt-Rh/C and (c) Pt-Rh-SnO_2/C; T = 25°C (solid), 40°C (dash) and 70°C (dots); v = 10 mV s^{-1}.

Table 12. EOR onset on Pt/C, Pt-Rh/C and Pt-Rh-SnO_2/C at 25°C, 40°C and 70°C.

	Pt/C	Pt-Rh/C	Pt-Rh-SnO_2/C
T / °C		E / V *vs.* RHE	
25	0.64	0.59	0.62
40	0.53	0.45	0.45
70	0.49	0.42	0.37

VI.6. Tafel plot

The Tafel plots in Fig. 80 have been reconstructed from successive 900 s-long potentiostatic polarizations (not represented here) between E = 0.4 and 0.7 V *vs.* RHE (0.1 V step) carried out in 0.5 M H_2SO_4 + 0.1 M EtOH at 25°C, 40°C and 70°C on Pt/C, Pt-Rh/C and Pt-Rh-SnO_2/C. The faraday current values of the Tafel plots were recorded at the end of each potential step. Table 13 summarizes the EOR Tafel slope values calculated using the four faraday current values between E = 0.4 and 0.7 V *vs.* RHE on Pt/C and Pt-Rh/C but using only the three first values for Pt-Rh-SnO_2/C. Indeed, it seems that the EOR is diffusion-

limited at lower potentials (from *ca.* E = 0.7 V *vs.* RHE) on Pt-Rh-SnO_2/C than on the other two electrocatalysts. The larger values estimation errors on Pt-Rh-SnO_2/C may be imputed to the proximity of the mass-transport limitation region with the potential values at which the chronoamperometries were carried out.

The rise of the temperature does not seem to impact much the rate determining step of the EOR on Pt/C and Pt-Rh/C in the studied temperature range. Indeed, the Tafel slope values remain quasi identical when the temperature increases from 25°C to 70°C. Several DEMS studies have already reported low CO_2 current efficiency (CCE) on Pt/C or Pt-Rh/C at room temperature, which illustrates the difficulty to break the C-C bond on these electrocatalysts [32,35,43]. As a matter of fact, the overall faraday current mainly corresponds to the dehydrogenation of the ethanol molecule into acetaldehyde (2 e^-) and into acetic acid formation (4 e^-) from the reaction between adsorbed acetaldehyde and OH_{ad}-species. It can thus be supposed that the rate determining step on Pt/C and Pt-Rh/C at room temperature is either controlled by ethanol dehydrogenation or by acetic acid formation, or by a combination of both.

The Tafel slope values for Pt-Rh-SnO_2/C are much higher than for Pt-Rh/C and Pt/C at each temperature (Table 13), which tends to demonstrate that the EOR rate limiting step differs for Pt-Rh-SnO_2/C compared to Pt-Rh/C and Pt/C (thus excluding the ethanol dehydrogenation or the acetic acid formation as *rds*). Therefore, the EOR could be controlled by the C-C bond breaking, as supported by the larger contribution of the complete ethanol electrooxidation into CO_2 to the overall faraday current on Pt-Rh-SnO_2/C (see chapiter III and IV). As the C-C bond breaking is a highly energetic reaction, it may further explain the larger EOR Tafel slope values for the tri-metallic electrocatalyst. Conversely to Pt/C and Pt-Rh/C, the EOR on Pt-Rh-SnO_2/C seems also dependent on the temperature. The significant drop of the Tafel slope values from 420 mV dec^{-1} (at 25°C) to 320 mV dec^{-1} (at 40°C) can either suggest a change in the reactions kinetics or a change in the rate determining step. The amplitude of the drop makes the latter more likely. But the large estimation error renders the conlusions purely hypothetical. The variation of the Tafel slope values from 320 mV dec^{-1} (at 40°C) to 350 mV dec^{-1} (at 70°C) is also imputed to the experimental uncertainties.

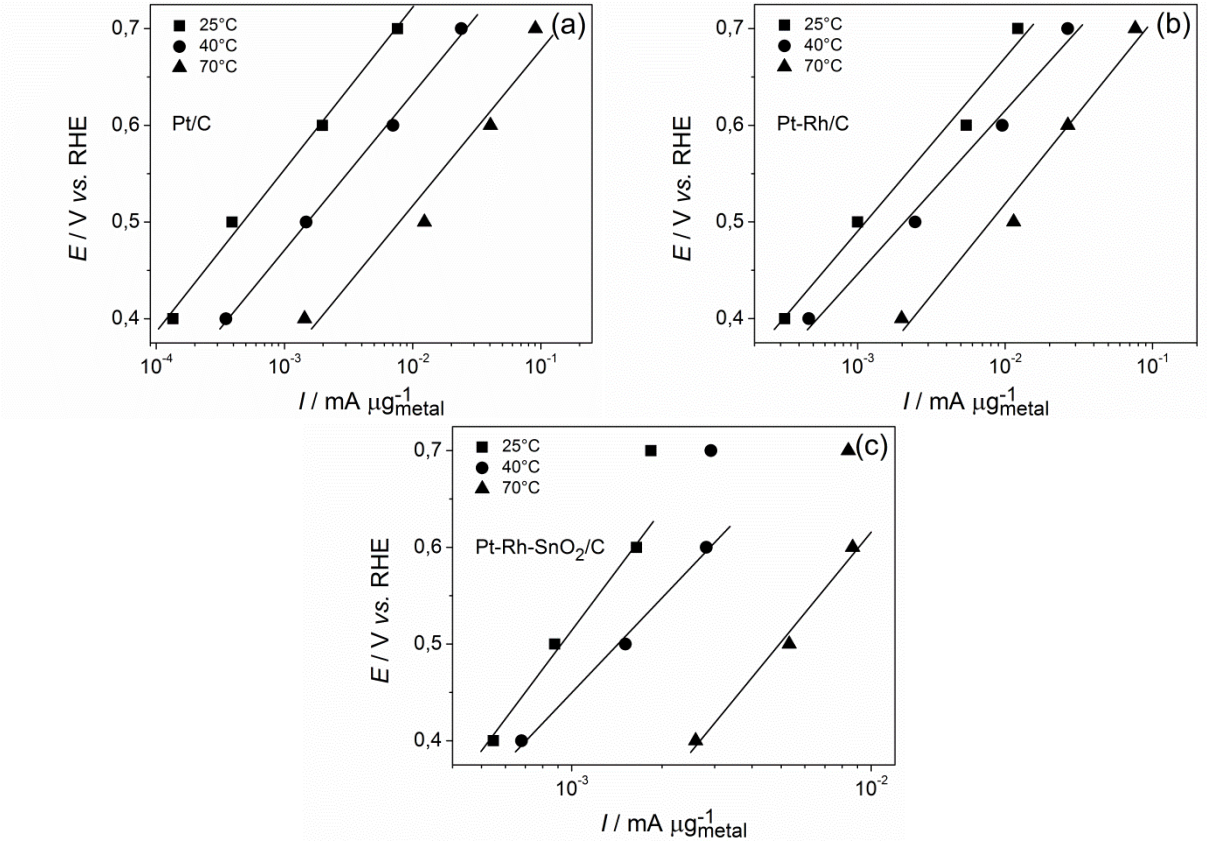

Fig. 80. Tafel plots of potentiostatic currents recorded after 900 s at potentials from 0.4 to 0.7 V *vs.* RHE (0.1 V step) in 0.5 M H_2SO_4 + 0.1 M EtOH on (a) Pt/C, (b) Pt-Rh/C and (c) Pt-Rh-SnO_2/C at 25°C, 40°C and 70°C.

Table 13. EOR Tafel slope values for Pt/C, Pt-Rh/C and Pt-Rh-SnO_2/C at 25°C, 40°C and 70°C, derived from the Tafel plots of Fig. 80.

	Pt/C	Pt-Rh/C	Pt-Rh-SnO_2/C
T / °C		E / mV dec^{-1}	
25	170 ± 10	180 ± 10	420 ± 20
40	160 ± 10	170 ± 10	320 ± 20
70	160 ± 10	190 ± 10	350 ± 30

VI.7. Apparent activation energy

Fig. 81 shows the Arrhenius plots of the EOR on Pt/C, Pt-Rh/C and Pt-Rh-SnO_2/C deduced from the steady-state current recorded after 900 s at potentials comprised between E = 0.4 and 0.7 V *vs.* RHE at 25°C, 40°C and 70°C. The corresponding apparent activation energy E_a was calculated for each electrocatalyst at each studied potential (E = 0.4, 0.5, 0.6

and 0.7 V *vs.* RHE) and summarized in Table 14 (E_a estimation error is ± 2 kJ mol^{-1}). A clear linear decrease against 1/*T* can be seen in Fig. 81, which demonstrates that only one rate determining step proceeds at each potential in the studied temperature range. This observation is however biased at E = 0.4 V *vs.* RHE on Pt-Rh/C and Pt-Rh-SnO_2/C, where the linear behavior is not as clear as at the other potentials.

At each potential over the studied temperature range, the apparent activation energy is larger on Pt/C ($19 \leq E_a \leq 28$ kJ mol^{-1}) than on Pt-Rh/C ($13 \leq E_a \leq 20$ kJ mol^{-1}) and to a larger extent on Pt-Rh-SnO_2/C ($13 \leq E_a \leq 15$ kJ mol^{-1}) (Table 14). Regarding the complexity of the EOR mechanism and without any present physical evidences on the reaction intermediates and products, interpreting the obtained E_a values can only remain purely hypothetic. The multiplicity of existing apparent activation energy values in the literature [42,43,77] and the dependence of these values on the experimental conditions make any quantitative comparison extremely difficult. However, a somehow reasonable qualitative analysis can still be done.

Considering the fluctuation of the apparent activation energy of the ethanol oxidation with the potential on Pt/C, it can be assumed that the nature of the rate determining step is potential-dependent. Except at E = 0.7 V *vs.* RHE, the apparent activation energies obtained for the EOR on Pt-Rh/C follow the same trend than on Pt/C. The lower values obtained on the bi-metallic electrocatalyst compared to Pt/C could sign that the energy barrier shrinks due to a more facile dehydrogenation of the ethanol molecule [35,119]. On the contrary, the apparent EOR activation energy on Pt-Rh-SnO_2/C seems to remain constant between E = 0.4 and 0.7 V *vs.* RHE, which could signify that the rate determining step remains the same in the studied potential range. The low values of E_a tend to exclude the C-C bond splitting as possible *rds*, while they suggest ethanol dehydrogenation and acetic acid formations as more probable candidates.

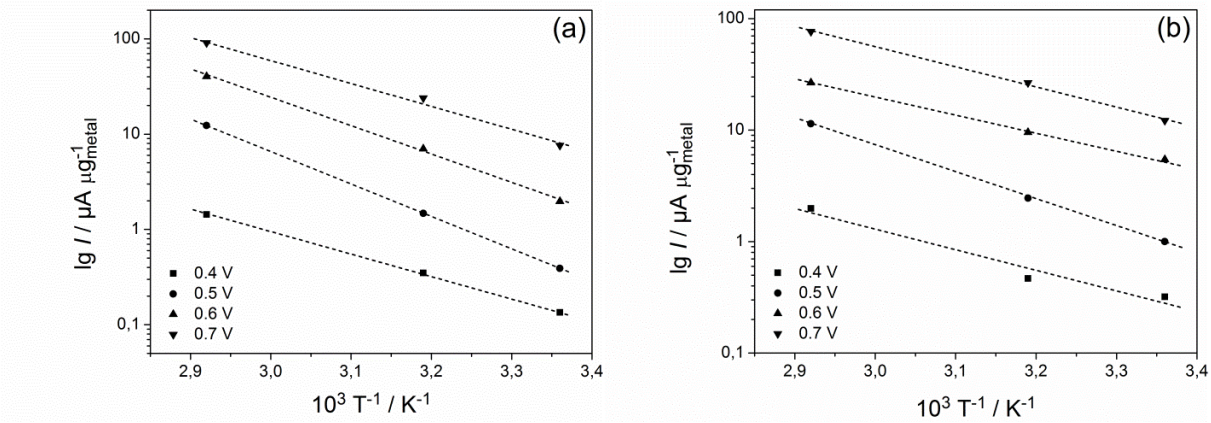

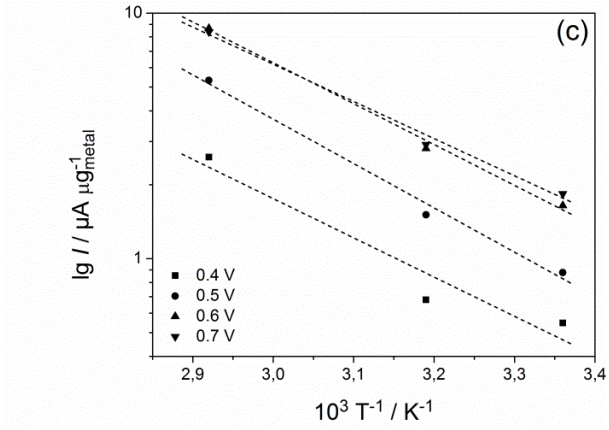

Fig. 81. Arrhenius plots of the of potentiostatic currents recorded after 900 s at potentials from E = 0.4 to 0.7 V *vs.* RHE (0.1 V step) in 0.5 M H_2SO_4 + 0.1 M EtOH on (a) Pt/C, (b) Pt-Rh/C and (c) Pt-Rh-SnO_2/C.

Table 14. Apparent activation energies for the ethanol oxidaton reaction on Pt/C, Pt-Rh/C and Pt-Rh-SnO_2/C deduced from the steaty-state current values recorded after 900 s at E = 0.4, 0.5, 0.6 and 0.7 V *vs.* RHE at 25°C, 40°C and 70°C.

	Pt/C	Pt-Rh/C	Pt-Rh-SnO_2/C
E / V *vs.* RHE		E_a / kJ mol^{-1}	
0.4	19 ± 2	15 ± 2	13 ± 2
0.5	28 ± 2	20 ± 2	15 ± 2
0.6	25 ± 2	13 ± 2	14 ± 2
0.7	20 ± 2	15 ± 2	13 ± 2

VI.8. Conclusions

This study on the influence of the temperature was carried out on 10 wt.% Pt/C, Pt-Rh/C and Pt-Rh-SnO_2/C electrocatalysts synthesized for the sake of this study.

Cyclic voltammetries in supporting electrolyte demonstrated the large amplification of the water dissociation reaction with the rise of the temperature on the three electrocatalysts, but no shift toward lower potential values of the reaction onset was recorded. On the contrary, the CO-stripping study revealed that CO_{ad} oxidation activates at lower potentials with the temperature rise, which was mainly imputed to the weakening of the metal-CO bond on the three electrocatalysts. Besides, a shift of the EOR initiation toward low potentials is observed when the temperature increases: the onset potential shift was about 150, 170 and 250 mV on Pt/C, Pt-Rh/C and Pt-Rh-SnO_2/C respectively between 25°C and 70°C.

A study on steady-state Tafel slopes and apparent activation energies E_a was also carried out in 0.5 M H_2SO_4 + 0.1 M EtOH between E = 0.4 and 0.7 V *vs.* RHE in the temperature range 25 - 70°C. Contrary to Pt/C and Pt-Rh/C electrocatalysts, which both

present a similar Tafel behavior at each temperature, the larger Tafel slope values monitored for Pt-Rh-SnO_2/C were ascribed to different rate determining steps and to a larger dependence to the temperature. The study of the EOR apparent activation energy revealed a higher influence of the applied potential on the *rds* for Pt/C than for Pt-Rh/C and Pt-Rh-SnO_2/C. The latter exhibits very similar activation energies between E = 0.4 and 0.7 V *vs.* RHE, which could sign the presence of a unique rate determining step on the studied potential range.

Discussion, conclusions and prospects

Discussion: Potendiodynamic EOR mechanism in acidic medium on Pt

To summarize the main results obtained in this work, a potentiodynamic EOR mechanism on Pt (in 0.5 M H_2SO_4 + 0.1 M EtOH) is proposed between E = 0.05 and 1.5 V *vs.* RHE, taking into account the adsorption modes from [29]:

1- E = 0.05 – 0.55 V *vs.* RHE

The non-dissociative ethanol adsorption followed by the molecule hydrogenation into acetaldehyde initiates at *ca.* E = 0.3 V *vs.* RHE (see Table 7 - m/z = 29) according to the reaction:

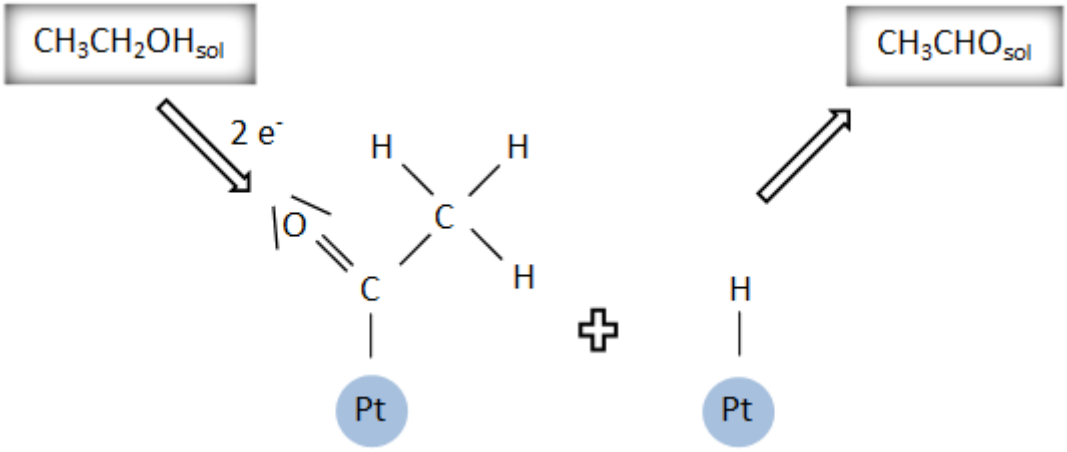

The reaction of the acetyl adsorbate with aqueous hydrogen species is not excluded, but was not represented here.

It is believed that, parallel to this reaction, ethanol adsorbs to form two other adsorbates generating either two electrons (dissociative adsorption by C-atom) or one electron (adsorption by O-atom). But due to a stronger adsorption force or/and to the lack of OH_{ad} on the electrocatalyst surface in this potential region, the adsorbates do not oxidize and block their electroactive sites:

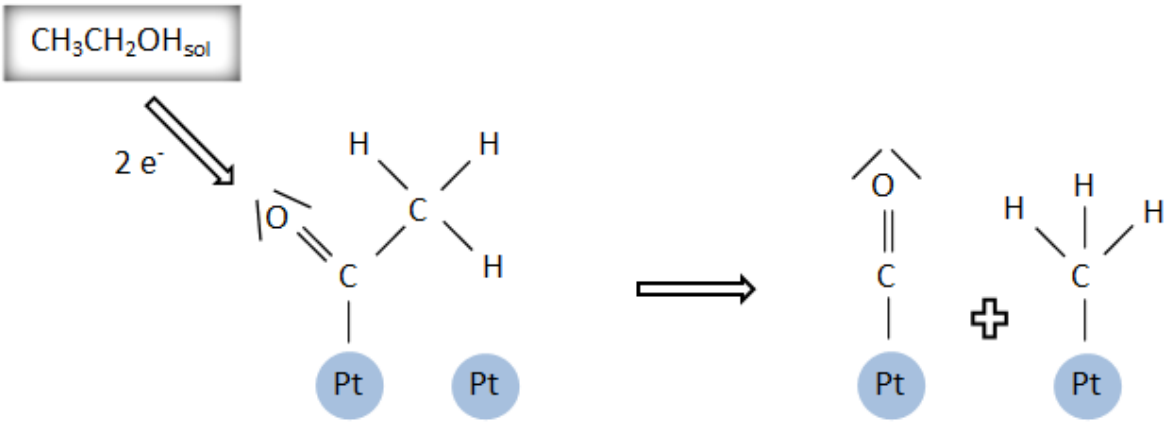

And

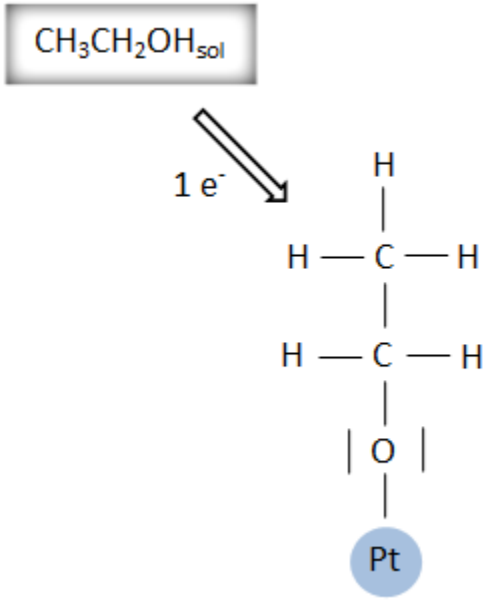

At *ca.* E = 0.35 V *vs.* RHE, ethyl acetate starts being detected by mass spectrometry (see Table 7 - m/z = 61). The proximity between acetaldehyde generation (m/z = 29) and the rise of the signal m/z = 61 is believed to be due to the direct formation of ethyl acetate from the ethanol adsorbates (its formation only requires ethanol in the solution):

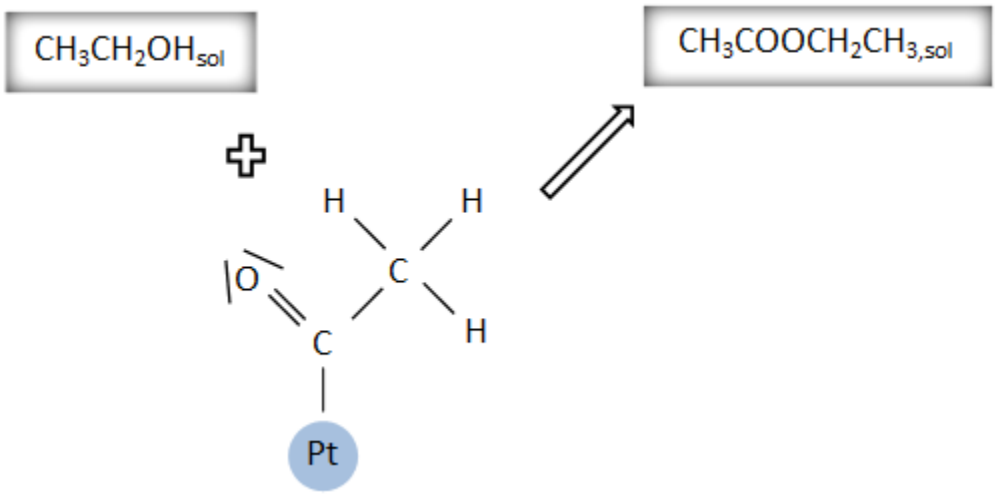

The difference of onset potentials between the two signals recorded in section IV could be explained by the fact that ethyl acetate is a much bigger molecule than ethanol and that its diffusion through the Gore-Tex membrane may be a slow process.

Another possible mechanism is the formation of acetic acid, which reacts with ethanol in the solution to form ethyl acetate as soon as the molecule leaves the electrocatalyst surface:

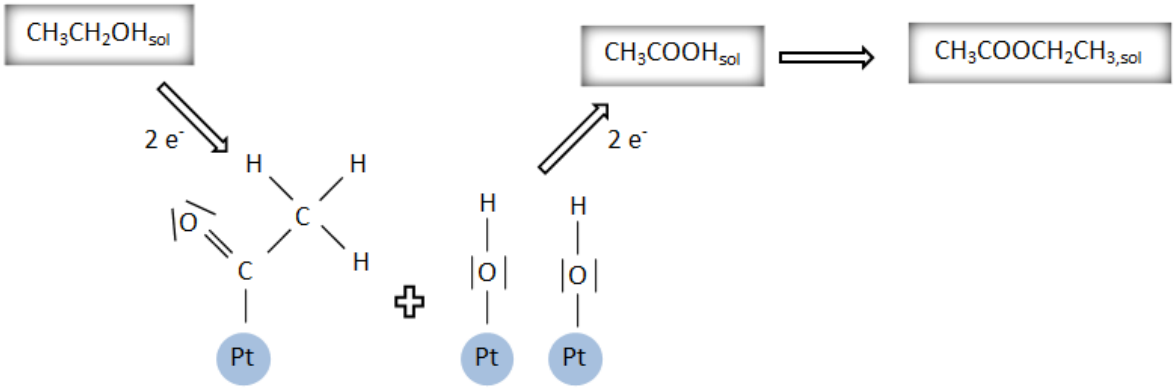

However, the fact that the mass-to-charge signal m/z = 60 remains flat between E = 0.05 and 0.6 V *vs.* RHE, while the signal m/z = 61 varies significantly tends to exclude the formation of acetic acid in this potential range (see Annex 2). Besides, at E = 0.35 V *vs.* RHE, quasi no OH_{ad} is present on the electrocatalyst surface which shall thus impede this reaction.

2- E = 0.55 – 1.1 V *vs.* RHE

CO_2 generation starts at *ca.* E = 0.55 – 0.6 V *vs.* RHE with the formation of OH-adsorbates necessary for the reaction:

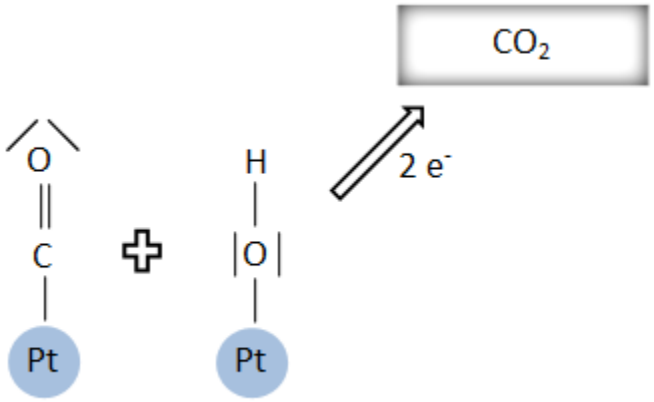

The low ethanol complete electrooxidation into CO_2 is often interpreted by the necessity to lower the dissociation energy of the C-C bond energy. The high energy required to cleave this bond should however not be interpreted by a potential threshold below which the dissociation cannot proceed, but more by the time it requires to dissociate on the electrocatalyst surface. Indeed, as seen in section VI, the dissociative adsorption can occur at potentials as low as E = 0.05 V *vs.* RHE. Performing a chronoamperometry in an ethanol solution at low potentials before starting the CV is an easy procedure which could give time to ethanol dissociative adsorption to take place and thus could raise the CCE.

In any case, lowering C-C dissociation energy is primordial. Reducing this energy would permit to balance acetaldehyde, ethyl acetate and CO_2 production.

3- E = 1.1 – 1.5 V *vs.* RHE

A second current rise starts at *ca.* E = 1.1 V *vs.* RHE. As discussed earlier, this current increase corresponds to the oxidation of strong adsorbates which are believed to be adsorbed by the O-atom. This reaction would generate directly ethyl acetate:

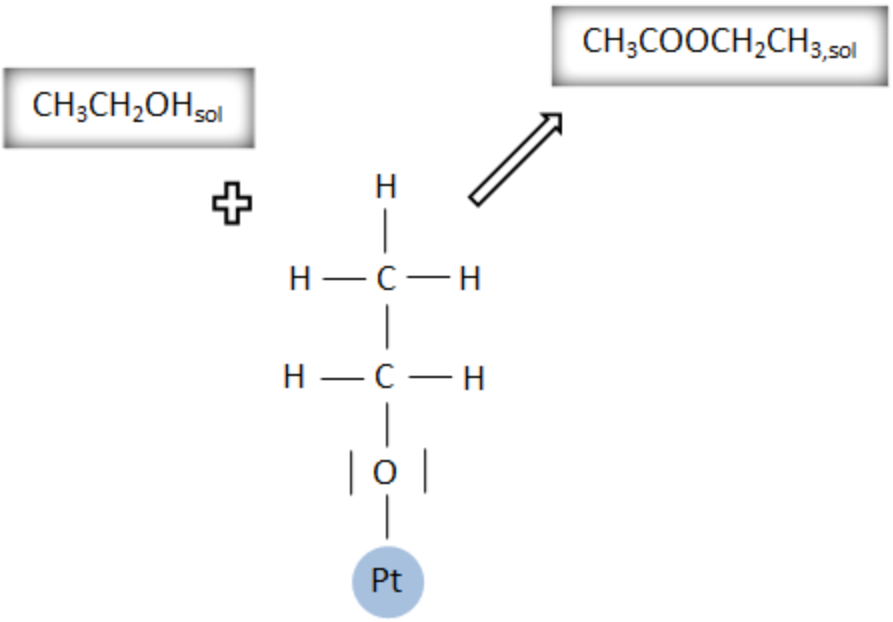

The intermediate acetaldehyde formation seems excluded due to the discriminating adsorption by the O-atom which hinders acetaldehyde formation:

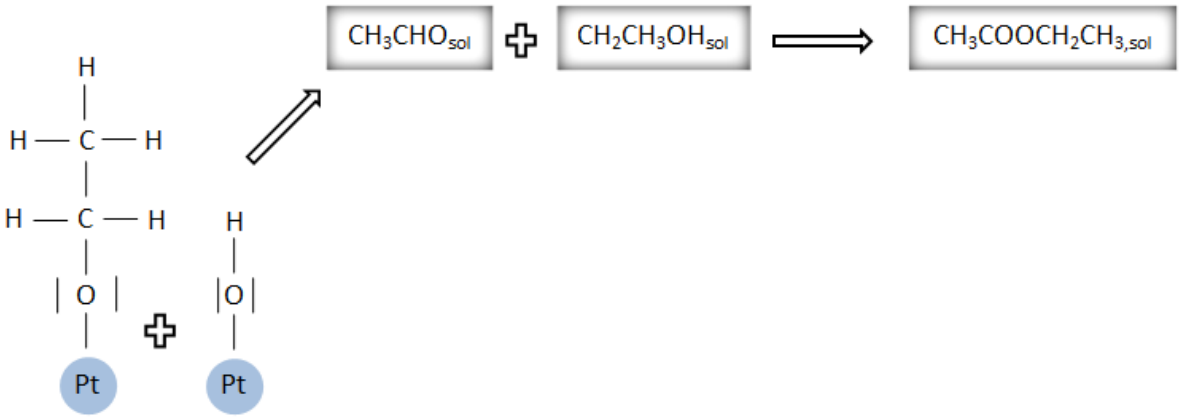

4- E = 1.5 – 0.05 V *vs.* RHE

During the reduction scan, OH_{ad} desorption/reduction at *ca.* E = 0.85 V *vs.* RHE frees Pt sites for ethanol adsorption/oxidation. The low or absence of CO_2 formation is due to the high amount of adsorbates at the electrocatalyst surface, which blocks ethanol dissociative adsorption. But the fact that CO_2 is in some cases detected during the reduction scan (see section III) shows that the adsorption by the C-atom can take place. Thus, it could lead to the same reactions as those occurring during the anodic scan between E = 0.05 – 0.55 V *vs.* RHE.

On the opposite, the adsorption by the O-atom is probable, but could be hindered by the presence of the OH-adsorbates which form an electronegative charged layer on the electrocatalyst (which could favor the adsorption by the electropositive C-atom).

Conclusions

The state of the art of the direct ethanol fuel cell (DEFC) does not permit any commercialization of this technology in the short-term. Its anodic reaction, the ethanol oxidation reaction is a slow process, which still requires overcoming several issues among which the high reaction overpotential and associated slow reaction kinetics. This thesis focused on the understanding of the EOR mechanism in acidic medium and of the enhanced performances demonstrated in previous studies on the carbon supported Pt-Rh-based electrocatalysts *versus* Pt/C.

This work primarily investigated the EOR on Pt/C and the influence of this electrocatalytic material structure (nanoparticles size and electrocatalyst layer thickness) on the products distribution. The results revealed that the complete ethanol electrooxidation is promoted by thicker electrocatalyst layers. The longer residence time of the reaction intermediates indeed favors the re-adsorption of the reaction intermediates and particularly of acetaldehyde, which can further oxidize.

A comparison between Pt/C with Pt-based Rh- and/or SnO_2-containing electrocatalysts was then performed to highlight the drawbacks/advantages from these multi-metallic electrocatalysts. The EOR onset potential was slightly shifted toward negative potentials on all studied bi- and tri-metallic electrocatalysts against Pt/C, which was illustrated by acetaldehyde earlier formation. Unfortunately, the intensified ethyl acetate formation on Pt-SnO_2/C, expected from previous results of the literature [30,78,100], could not be confirmed in this work. On the opposite, acetaldehyde was found to be the main reaction product. This raises the issue of the structural impact of the electrocatalysts on the EOR preferred pathway. Pt-Rh/C and, above all, Pt-Rh-SnO_2/C demonstrated the highest CO_2 current efficiency values, confirming rhodium superior ability in the C-C bond cleavage. Tin oxide oxophilic character guarantees the supply in OH-species to the electrocatalyst surface enabling CO_2 generation from adsorbed CO_{ad} at lower potentials than on Pt-Rh/C or Pt/C.

In a second approach, the influence of the presence of water adsorbates (H_{ad} and OH_{ad}) on the electrocatalysts surface was studied to evaluate their impact on the different steps/pathways of the EOR mechanism. The results highlighted the hindrance of ethanol adsorption due to hydrogen adsorbates on the electrocatalyst. Unlike tin oxide, the addition of rhodium seems to ease ethanol adsorption/dehydrogenation in the presence of adsorbed hydrogen. The AOR study supported these conclusions. The ethanol complete electrooxidation seemed slightly promoted after a CA at E_{ad} = 0.3 V *vs.* RHE. Ethanol dissociative adsorption may have been promoted during the last step of the potentiostatic process prior to the CV, which could have led to the presence of adsorbed CO on the electrocatalysts surface and could be at the origin of the larger CCE values.

The limits of the protocol used in this thesis are based on the uncertainty concerning the state of the electrocatalyst surface coverage. Although H_{ad} presence on the electrocatalyst

is convincing, thanks to the proofs of H_2 generation (brought by the mass-to-charge signals $m/z = 2$) until the very beginning of the CV, no such information could be brought for OH_{ad}-species. Most importantly, the presence of unwished ethanol adsorbates before the CV can be presumed.

The ethanol adsorbates stripping investigation revealed the presence of two types of adsorbates: CO-like adsorbates oxidizing in a medium potential region [E = 0.5 - 0.9 V *vs.* RHE) and "strong adsorbates" at E > 0.9 V *vs.* RHE. The identity of the latter is not clear yet. One certainty is that they are behind methane production occurring at low potentials, and thus, could be $CH_{x,ad}$ species. The applied protocol could unfortunately not unveil the doubt concerning the presence of C_2-adsorbates on the electrocatalyst.

The acetaldehyde adsorbates electrooxidation presents a similar CV pattern than ethanol adsorbates. One notable difference though relies in the discovery of the presence of C_2-adsorbates, which only activate after a first oxidation sweep. This phenomenon, not reported so far in the literature could be the object of further research: adapting the studied electrochemical window and reducing more thoroughly the presumed CH_x-adsorbates behind methane generation, could be ways to improve our understanding on that topic.

The study on the multi-metallic electrocatalysts did show a higher surface coverage by ethanol and acetaldehyde adsorbates than on Pt/C at lower adsorption potentials in the H_{UPD} region, which was explained by an eased displacement of the H_{ad}-species by the organic molecules for such complex Pt surfaces.

Finally, the study of the ethanol electrooxidation at different temperatures revealed a large negative shift of the reaction in the studied temperature range on all the electrocatalysts. Pt-Rh-SnO_2/C was apparently more sensitive to the temperature than Pt-Rh/C and Pt/C, as the current recorded on the latter was the largest up to E = 0.6 V *vs.* RHE. It was also assumed regarding the Tafel plots and activation energy calculation that all electrocatalysts were probably not subject to the same rate determining step. Besides this study, this chapter brought important information on the beneficial role of the temperature in the EOR electrocatalysis. However, the interpretation of the observed phenomena remains conjectural without lack of physical evidences.

Perspectives

This work provided interesting results regarding the ethanol electrooxidation on Pt-Rh-SnO_2/C and especially concerning the enhanced ability of this tri-metallic electrocatalyst to split ethanol C-C bond against Pt/C or Pt-SnO_2/C. However, it should not be forgotten that the finality beyond such works concerns the viability of a fuel cell as power source. As such, further research is still mandatory to nurse the hope that the DEFC can one day be commercialized and that it will not remain forever a research topic (even though very interesting!). Some burning issues concerning the anodic electrocatalyst need to be solved.

To start with, the enhanced performances demonstrated in this work particularly at operating temperatures (70°C) do not suffice to justify the use of rhodium as co-metal associated with platinum, as the former is even more expensive as the latter (and presumably less stable).

Then, MEA tests should be conducted to confirm the results mentioned earlier. These measurements are essential as they are much closer from the real operating conditions of a fuel cell, and could benefit from longer residence time of reaction intermediates in "real electrodes".

Above all, the question of durability of a Pt-Rh-SnO_2/C electrocatalyst has never been broached in this work. A study of the degradation rate and mechanism of such complex electrocatalyst should be achieved, if MEA tests of this electrocatalyst were conclusive.

About the EOR mechanism itself and from a fundamental prospective, more attention on the identity of the adsorbates oxidizing at high potentials (E > 0.9 V *vs.* RHE) should be carried out. Their behavior should also be more investigated at elevated temperatures (T > 60°C), as they constitute a real poison for the electrocatalyst (much more than CO_{ad}). If so, a way to efficiently remove them in DEFC systems shall be investigated too.

The notion of time broached in this thesis (with the study on the influence of the scan rate), which is of importance redarging the slow kinetics of the C-C bond breaking, could be more deeply investigated: a potentiostatic study at low potentials coupled with *in situ* FTIR could help see the formation rate of CO_{ad}…

Besides the CCE, the slow kinetics at low potentials is a real issue that could not be drastically improved by the addition of transition metals. Therefore, higher operational temperature in DEFC applications may be a short-term option, but then, the materials durability shall be checked.

It is hardly possible to discuss on the adsorption strength of the adsorbates on the different electrocatalysts without physical evidences: XPS analyses could give some insights on the nature of the effect of the metals associated to platinum and notably inform why they are positive.

Investigating different Pt nanoparticles structures could be worth its weight of gold. More studies could be for example focused on the influence of the nanoparticles size and shape on the different EOR pathways.

An EOR investigation on monocrystals combined with infrared techniques (FTIR, Raman…) would give new understandings on the EOR and, more specifically, on the electroactive sites and configurations where ethanol and its oxidation intermediates preferentially adsorb.

Active electrocatalysts supports (TiO_2, WO_x…) could modify the ethanol adsorbates adsorption energy or, for example, dehydrogenize efficiently the Pt metal surface…

The influence of the anions present in the electrolyte on the EOR and more specifically on the ethanol adsorption has not been studied [244], and this also would be worth a study.

This list is almost limitless and shows how long (and tortuous) the route to successful EOR in PEMFC is. Nevertheless, whatever the expected difficulties, I confess my interest to continue the work in the future as a part of the research community.

Appendix.

Electrooxidation of ethanol at room temperature on carbon-supported Pt and Rh-containing catalysts: a DEMS study

This annex introduces to a preliminary DEMS investigation on the EOR on 10 wt.% Pt/C and Pt-Rh/C electrocatalysts. The results presented hereafter highlight the better C-C bond cleavage on Pt-Rh/C *versus* Pt/C and are further commented in the light of pre-existing studies on the topic.

A1. CV in supporting electrolyte

Fig. 82 compares the cyclic voltammograms on Pt/C, Rh/C and Pt-Rh/C acquired at 10 mV s^{-1} in 0.5 M H_2SO_4 (physical characterization of the electrocatalysts can be found in section V.1.). The usual features of the hydrogen and oxygen region can be observed. The water dissociation initiates at 0.5 V *vs*. RHE on Pt-Rh/C versus 0.6 V *vs*. RHE on Rh/C and Pt/C. The water dissociation may operate at lower potential on Pt-Rh/C than on Pt/C because of rhodium oxophilic character. It also suggests that interactions between the two metals may impact the Pt electronic structure (unfortunately, the XRD data does not enable asserting this observation). During the negative scan, a shift toward lower potential was recorded on Rh/C and Pt-Rh/C compared to Pt/C for the reduction of the metal oxides reduction peak. This indicates that oxides are more stable on Rh-containing than on the Pt surface.[119] A second bump can even be observed on Pt-Rh/C which may correspond to the desorption/reduction of carbon oxide groups. Though not observable in Fig. 82, the same kind of feature was recorded on Pt/C[172] excluding therefore a possible distinctive metal oxides reduction on Pt and Rh nanoparticles.

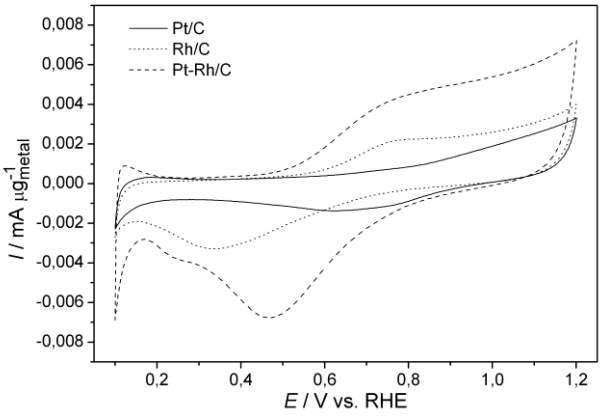

Fig. 82. Typical TEM images and associated particle size distribution of (a) Pt/C, (b) Rh/C, (c) Pt-Rh/C.

A2. CO stripping

A comparison of the CO stripping voltammograms obtained on Pt/C, Rh/C and Pt-Rh/C at 10 mV s^{-1} is shown in Fig. 83a. The CO stripping onset potential on Pt-Rh/C is located below those on Rh/C and Pt/C. Faster kinetics can as well be observed on the bimetallic electrocatalyst and on Rh/C than on Pt/C. It can be deduced that a ligand effect of Rh is operated on the Pt electronic structure. More precisely alloying Rh with Pt presumably leads to a down-shift of the Pt 5d-band center caused by the interactions in the lattice between

Pt and Rh atoms.[189] This phenomenon would result in a weaker adsorption of CO on Pt atoms of the alloy and thus in the acceleration of the kinetics on Pt-Rh/C. The presence of rhodium, which is an oxophilic metal, in the lattice also likely suggests a faster supply in OH^- species helping the oxidation of the adsorbed CO (bi-functional mechanism, often mentioned for CO and methanol oxidation reactions[188]).

Cyclic voltammograms on Pt/C and Pt-Rh/C in Fig. 83b and corresponding mass spectrometric signals *m/z* = 44 and *m/z* = 22, respectively displayed in Fig. 83c and Fig. 83d, show the good correlation between the faradaic and ionic currents. In order to quantify the CO_2 generation during the EOR, the calibration of the signal *m/z* = 22 was performed using the results presented in Fig. 83d. No mass spectrometric study on Rh/C was operated as the EOR activity on the latter is negligible.

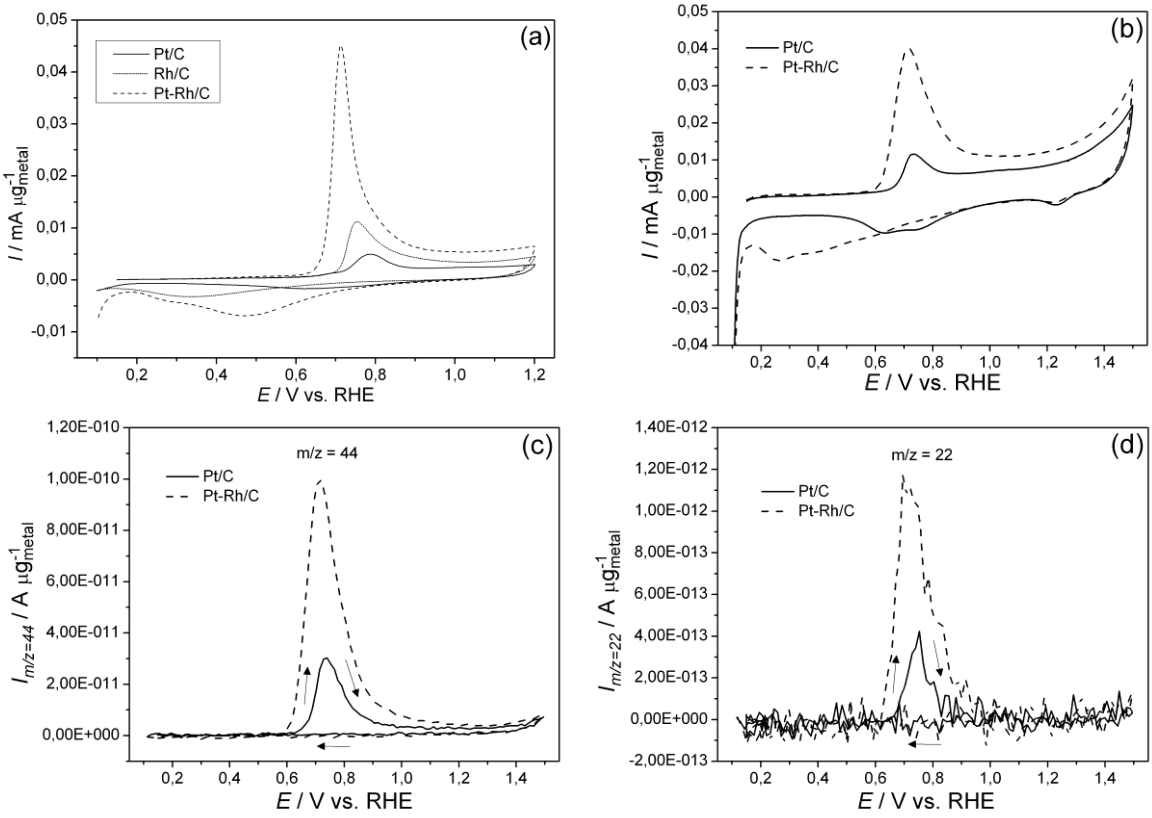

Fig. 83. CO-stripping CV in 0.5 M H2SO4 in (a) static and (b) flow electrolyte and corresponding MSCV for mass to charge ratio (c) *m/z* = 44 and (d) *m/z* = 22 of the CO stripping on (solid) Pt/C and (dash) Pt-Rh/C; v = 10 mV s^{-1}; T = 25°C.

A3. Potentiodynamic ethanol oxidation

Fig. 84a displays representative cyclic voltammograms relative to the EOR on Pt/C and Pt-Rh/C. Results on Rh/C are not shown in this part because of the negligible ethanol oxidation activity. A lower ethanol oxidation overpotential of *ca*. 0.1 V is witnessed for Pt-Rh/C compared to Pt/C. As a result, the performances on Pt-Rh/C seem slightly better than on Pt/C in the potential range up to 0.7 V *vs*. RHE. Moreover, Fig. 84a, Fig. 84b and Fig. 84c demonstrate a simultaneous increase of the faradaic and ionic currents of the mass to charge signals *m/z* = 44 ($[CH_3CHO^+]$) and *m/z* = 15 ($[CH_3^+]$), corresponding to CH_x ionization and to $[CH_3CHO^+]$ defragmentation in $[CH_3^+]$; this indicates that the faradaic current rise is mainly due to the oxidation of ethanol into acetaldehyde and not to major CO_2 production (the mass to charge signals *m/z* = 22 remains very small in comparison to the others). This observation is however valid only up to 0.5 V *vs*. RHE. Indeed, a rise of the signal *m/z* = 22 can then be observed in Fig. 84d from 0.5 V *vs*. RHE and 0.6 V *vs*. RHE on Pt-Rh/C and Pt/C respectively which illustrates the higher contribution of the total ethanol oxidation into CO_2 in the faraday current. When comparing this contribution between both electrocatalysts, the total oxidation of ethanol into CO_2 seems not only to start earlier on Pt-Rh/C than on Pt/C but also apparently in larger extent which illustrates an ease of the C-C bond cleavage with the addition of rhodium in the electrocatalyst. The enhancement of the faraday current due to the total ethanol oxidation into CO_2 (taking place from 0.5-0.6 V *vs.* RHE during the positive scan only) can also be noticed with the large height difference between the peaks from the positive and negative scan of the faraday current (Fig. 84a) which contrasts with the lower difference observed between the peaks of the ionic current from the signal *m/z* = 15 (Fig. 84b). Indeed, the CO_2 generation during the positive scan of the potentiodynamic voltammetry, which does not contribute to the ionic current from the signal *m/z* = 15, is at the origin of the amplification of the height difference between the faraday peaks from the positive and negative scan.

In Fig. 84, a different behavior on Pt/C and Pt-Rh/C can also be noticed when comparing the EOR peaks of the positive and negative scans. Indeed in agreement with the literature,[21,22,217] the negative peak corresponding to the EOR on Pt/C is almost always larger than the one obtained during the positive scan. However, in the case of Pt-Rh/C, the peak obtained during the negative scan is smaller than the one of the positive scan. Moreover, no change in the signal *m/z* = 22 is detected for both electrocatalysts during the negative scan. That suggests that the total oxidation of ethanol into CO_2 on Pt-Rh/C does occur during the positive scan but not during the negative scan. In addition, the current is lower during the negative scan on Pt-Rh/C because the ethanol oxidation onset is at lower potential. The reason for this may be the electrocatalyst surface blocking by OH^- species. Indeed as it was written earlier, the reduction of the adsorbed oxygen species on the electrocatalyst surface occurs at lower potential on Pt-Rh/C because of the presence of Rh. The peak is then obtained more or less at the same time on Pt/C and Pt-Rh/C probably because of the electrocatalyst surface blocking by C_2-species, mainly acetaldehyde.

Observing the signal *m/z* = 15 ($[CH_3^+]$) in Fig. 84b gives important information on the presence of CH_x species, although the presence of acetaldehyde for the same signal (defragmentation of this molecule into $[CH_3^+]$) corrupts the certainty of the interpretation. As can be seen at very low potential, in the hydrogen adsorption-desorption region, an increase of the ionic current is recorded during the negative scan followed by a decrease during the next positive scan; this is observed whatever the electrocatalyst. This phenomenon, already reported in the literature,[245] does not occur with the signal *m/z* = 29 (not presented here) corresponding mainly to the defragmentation of acetaldehyde molecule in $[CHO^+]$. That means that $[CH_3^+]$ certainly come from methane generation originated from the reduction of adsorbed CH_x species. The latter may result from the dissociative adsorption from a C_2-species, most likely acetaldehyde, occurring either during the negative scan or the previous positive scan. Assuming that detected $CH_{x,ad}$ comes from the dissociative adsorption of a C_2-species during the negative scan, there should also be some trace of adsorbed CO. Unfortunately this cannot be confirmed by DEMS measurements. An infrared study (FTIR, Raman…) could possibly enable to confirm the presence of CO_{ad} in the hydrogen region, which would give an indication about the moment of the formation of $CH_{x,ad}$.

The quantification of the ionic current of the signal *m/z* = 22 was then performed at each potential. Fig. 85 shows the evolution of the CO_2 current efficiency (CCE) together with the faradaic current and the ionic current of the signal *m/z* =22 on Pt/C and Pt-Rh/C. A maximal CCE of *ca*. 25% is reached at around 0.8 V *vs*. RHE on Pt-Rh/C while on Pt/C the CCE remains below 10 %. Though, the signal *m/z* =22 was noisy and could be source of uncertainties, the repeatability of the results on Pt-Rh/C was confirmed. As for Pt/C, the CCE varied between 5 and 10 % depending on the experiments, but never went above this value.

Though these results show undoubtedly a much higher production of CO_2 at room temperature on Pt-Rh/C than on Pt/C, the evolution of the faradaic current does not seem to be larger on the bimetallic electrocatalyst. On the contrary, it even seems that the kinetics is slightly lower on Pt-Rh/C than on Pt/C (the EOR peak obtained on Pt/C is somehow larger). This result is not contradictory with the literature;[35,75,119,118] indeed, as ethanol barely adsorbs on rhodium,[120] and knowing the Pt mass content in Pt/C is twice larger than in Pt-Rh/C, the higher production of CO_2 and thus of electrons on Pt-Rh/C does not compensate the supposedly higher production of acetaldehyde on Pt/C.

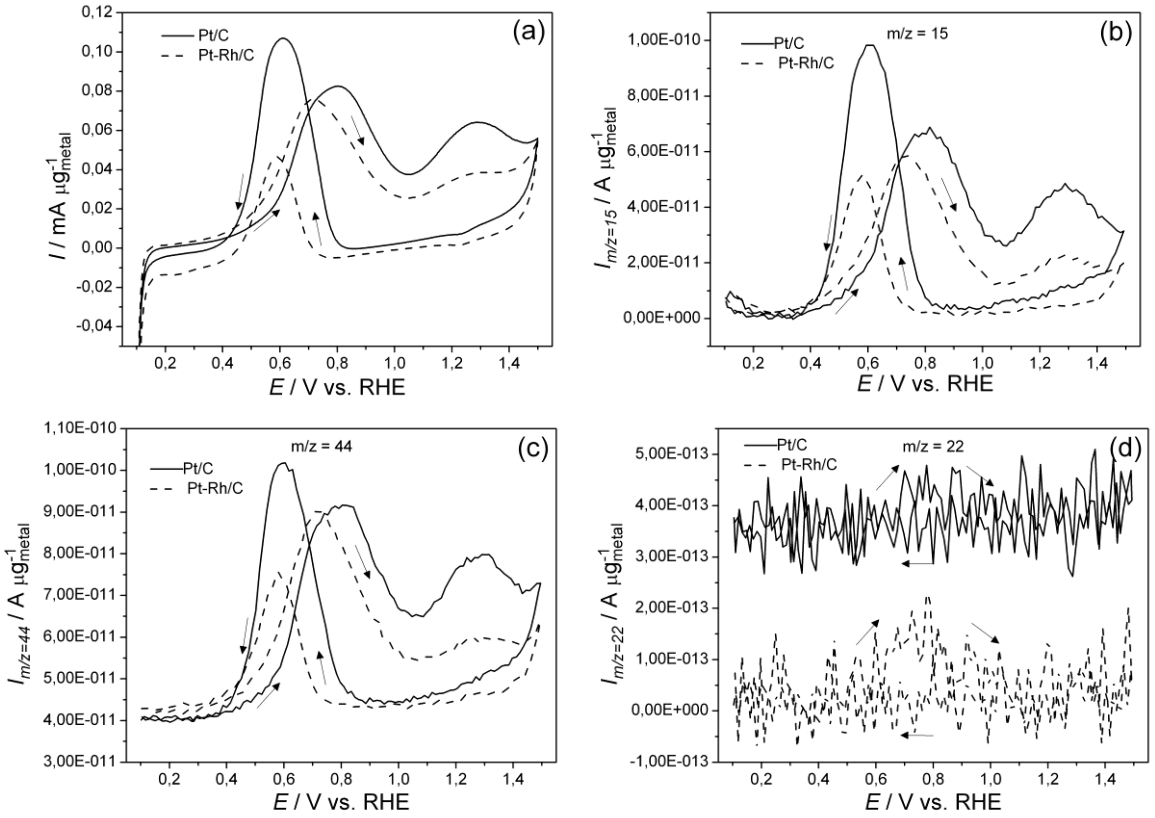

Fig. 84. (a) CV in 0.5 M H_2SO_4 + 0.1 M EtOH and MSCV for mass to charge ratio (b) *m/z* = 15, (c) *m/z* = 44 and (d) *m/z* = 22 of the EOR on (solid) Pt/C and (dash) Pt-Rh/C; *v* = 10 mV s^{-1}; *T* = 25°C.

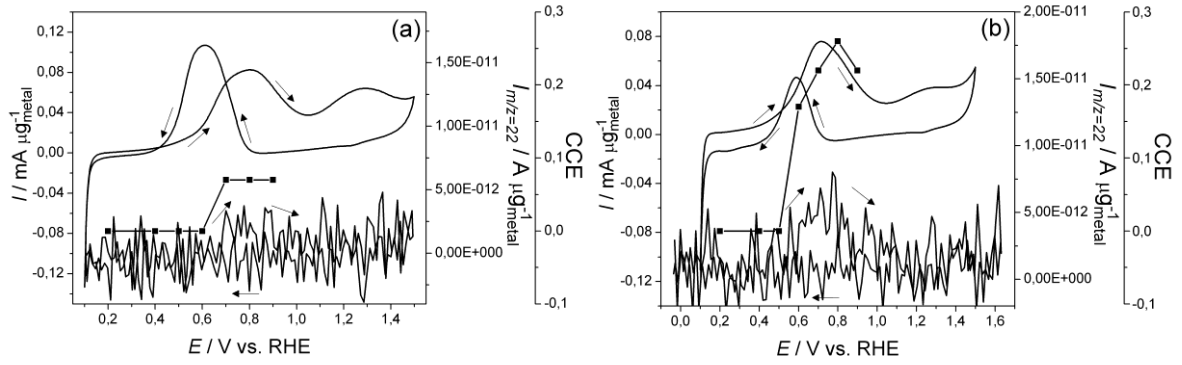

Fig. 85. EOR CV in 0.5 M H_2SO_4 + 0.1 M EtOH, MSCV for mass to charge ratio *m/z* = 22 and (line + symbol) CCE of the EOR on (left) Pt/C and (right) Pt-Rh/C.

A4. Potentiostatic ethanol oxidation

Fig. 86 exhibits the near-Tafel behavior of the two electrocatalysts in the potential range from 0.4 V *vs*. RHE to 0.7 V *vs*. RHE. It most likely corresponds to the adsorption of ethanol followed by its dehydrogenization into acetaldehyde. Indeed, it is admitted that the faradaic current generated during the EOR on Pt/C comes mainly from the dehydrogenation of ethanol that is to say from its oxidation into acetaldehyde (2 electrons). The formation of acetic acid (4 electrons) and the complete oxidation of ethanol into CO_2 (12 electrons) does not (or barely) occur at room temperature on Pt/C catalysts. As for the Pt-Rh/C, the total ethanol oxidation into CO_2 accounts for a maximal 20 % (at 0.7 V *vs*. RHE) of the overall ethanol oxidation and does not occur before 0.5 V *vs*. RHE according to the present DEMS results and before 0.4 V *vs*. RHE according to [35]. For this reason, it is assumed that the observed behavior for Pt-Rh/C mainly corresponds to the oxidation of ethanol in acetaldehyde. Thus, the difference of Tafel slope values could show a higher kinetics of the ethanol oxidation into acetaldehyde on Pt/C than on Pt-Rh/C. Huang et al.[246] obtained the same kind of results with other Pt-based electrocatalysts at low potential. The possible modification of the Pt electronic structure by Rh in Pt-Rh/C might have induced a slowdown of the ethanol dehydrogenation kinetics. Nevertheless, if the CO_2 production on Pt-Rh/C has any impact on its Tafel slope, it will logically reduce its inclination; as the CO_2 production implies the production of 12 e^- and is thus very slow compared to the formation of acetaldehyde.

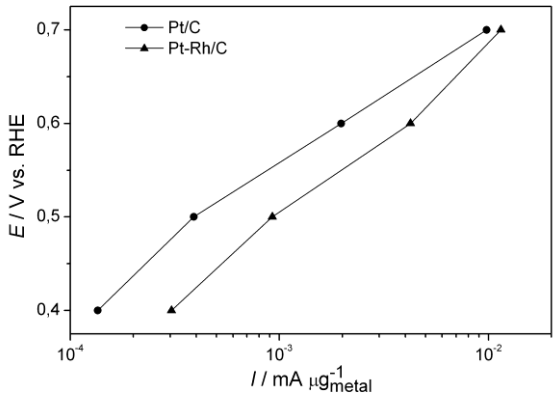

Fig. 86. Tafel plots of potentiostatic EOR currents (after 5 min) on (a) Pt/C and (b) Pt-Rh/C electrocatalysts in 0.5 M H_2SO_4 + 0.1 M EtOH at room temperature.

A5. Conclusions

Pt/C, Rh/C and Pt-Rh/C electrocatalysts were all synthesized by a modified polyol method. Their chemical composition was characterized by TGA, ICP-AES, XRD and TEM. A uniform dispersion of the metal nanoparticles on the carbon support as well as a narrow particle size distribution was reported. The presence of agglomerates on Pt/C could however be noticed.

The potentiostatic study of the EOR on Pt/C and Pt-Rh/C revealed higher kinetics in the potential range from E = 0.4 V *vs*. RHE to E = 0.7 V *vs*. RHE on Pt/C compared to Pt-Rh/C, though the EOR onset on Pt-Rh/C shifted toward lower potentials compared to Pt/C. This could be explained by the faster dehydrogenation of ethanol on Pt/C or by the sluggish CO_2 formation on Pt-Rh/C.

DEMS results showed a production of CH_x species at low potential on Pt/C and Pt-Rh/C coming from the dissociative adsorption of acetaldehyde during the negative scan. CO_{ad} is supposed to be also produced but a specific infrared study would be required to ascertain this assumption. A higher production of CO_2 during the ethanol oxidation was recorded on Pt-Rh/C than on Pt/C. That illustrates the good ability of Rh alloyed with Pt to break the C-C bond. After calibration of the signal m/z = 22, the CO_2 current efficiency (CCE) was quantified on both electrocatalysts. Pt-Rh/C exhibited a CCE up to 25 % of the faradaic current while the CCE on Pt/C was below 10 %. Nonetheless the faradaic peak current on Pt/C was still higher than on Pt-Rh/C. The lower amount of platinum in Pt-Rh/C could explain this phenomenon. However at practical potentials for fuel cells (E = 0.4 V *vs*. RHE - 0.6 V *vs*. RHE), Pt-Rh/C still represents a better activity than Pt/C. The addition of a third element may help getting better electrocatalytic performances.

Literature references

1. Statement of Yves-Louis Darricarrère, President of TOTAL Exploration & Production and TOTAL Gas & Power; Executive Vice President of TOTAL S.A.; Member of Executive Committee, TOTAL S.A., at CERAWeek energy conference 2012 in Houston, 06.03.2012.
2. Daimler AG, Ford Motor Compagny, General Motors Co., Honda Motor Co, Hyundai Motors Co., The Alliance Renault S.A. - Nissan Motor Co., and Toyota Motor Co., (n.d.).
3. Global leaders sign £31m plan to demonstrate the commercial case for hydrogen vehicles | Hydrogen London. http://www.hydrogenlondon.org/news/global-leaders-sign-31m-plan-to-demonstrate-the-commercial-case-for-hydrogen-vehicles/ (August 5, 2014).
4. M. S. Wilson and S. Gottesfeld, J. Electrochem. Soc. **139**, L28 (1992).
5. N. Kimiaie, K. Wedlich, M. Hehemann, R. Lambertz, M. Müller, C. Korte, and D. Stolten, Energy Environ. Sci. (2014).
6. G-energy Technologies, www.g-energy.com.
7. L. Dubau, L. Castanheira, F. Maillard, M. Chatenet, O. Lottin, G. Maranzana, J. Dillet, A. Lamibrac, J.-C. Perrin, E. Moukheiber, A. ElKaddouri, G. De Moor, C. Bas, L. Flandin, and N. Caqué, Wiley Interdiscip. Rev. Energy Environ. n/a (2014).
8. S. Shimpalee, D. Spuckler, and J. W. Van Zee, J. Power Sources **167**, 130 (2007).
9. P. Atkins and L. Jones, *Chemical Principles: The Quest for Insight 4th Edition*, W. H. Freeman & Co Ltd (2007).
10. Y. Wang, Electrochimica Acta **75**, 239 (2012).
11. F. Barbir, in *PEM Fuel Cells*, edited by F. Barbir (Academic Press, Burlington, 2005), pp. 17–32.
12. R. Palacios-Bereche, A. Ensinas, M. Modesto, and S. A. Nebra, Energy **70**, 595 (2014).
13. R. Raele, J. M. G. Boaventura, A. A. Fischmann, and G. Sarturi, Technol. Forecast. Soc. Change **87**, 205 (2014).
14. C. Lamy, A. Lima, V. LeRhun, F. Delime, C. Coutanceau, and J.-M. Léger, J. Power Sources **105**, 283 (2002).
15. W. Vielstich, H. A. Gasteiger, and H. Yokokawa, *Handbook of Fuel Cells: Vol.5 6 Advances in Electrocatalysis, Materials, Diagnostics and Durability*, Wiley (2009).
16. E. Antolini, J. Power Sources **170**, 1 (2007).
17. U. Schmiemann, U. Müller, and H. Baltruschat, Electrochimica Acta **40**, 99 (1995).
18. G. Andreadis and P. Tsiakaras, Chem. Eng. Sci. **61**, 7497 (2006).
19. S. Song, W. Zhou, Z. Liang, R. Cai, G. Sun, Q. Xin, V. Stergiopoulos, and P. Tsiakaras, Appl. Catal. B Environ. **55**, 65 (2005).
20. Y. H. Chu and Y. G. Shul, Fuel Cells **12**, 109 (2012).
21. S. C. S. Lai and M. T. M. Koper, Faraday Discuss. **140**, 399 (2009).
22. G. A. Camara and T. Iwasita, J. Electroanal. Chem. **578**, 315 (2005).
23. H. Wang, Z. Jusys, and R. J. Behm, J. Phys. Chem. B **108**, 19413 (2004).
24. M. H. Shao and R. R. Adzic, Electrochimica Acta **50**, 2415 (2005).
25. H.-F. Wang and Z.-P. Liu, J. Am. Chem. Soc. **130**, 10996 (2008).
26. L.-W. H. Leung, S.-C. Chang, and M. J. Weaver, J. Electroanal. Chem. Interfacial Electrochem. **266**, 317 (1989).
27. P. Gao, S.-C. Chang, Z. Zhou, and M. J. Weaver, J. Electroanal. Chem. Interfacial Electrochem. **272**, 161 (1989).
28. J. Willsau and J. Heitbaum, J. Electroanal. Chem. Interfacial Electrochem. **194**, 27 (1985).
29. T. Iwasita and E. Pastor, Electrochimica Acta **39**, 531 (1994).
30. H. Wang, Z. Jusys, and R. J. Behm, J. Power Sources **154**, 351 (2006).

31. L. Colmenares, H. Wang, Z. Jusys, L. Jiang, S. Yan, G. Q. Sun, and R. J. Behm, Electrochimica Acta **52**, 221 (2006).
32. D. A. Cantane, W. F. Ambrosio, M. Chatenet, and F. H. B. Lima, J. Electroanal. Chem. **681**, 56 (2012).
33. N. Fujiwara, K. A. Friedrich, and U. Stimming, J. Electroanal. Chem. **472**, 120 (1999).
34. F. Colmati, G. Tremiliosi-Filho, E. R. Gonzalez, A. Berná, E. Herrero, and J. M. Feliu, Faraday Discuss. **140**, 379 (2008).
35. F. H. B. Lima, D. Profeti, W. H. Lizcano-Valbuena, E. A. Ticianelli, and E. R. Gonzalez, J. Electroanal. Chem. **617**, 121 (2008).
36. T. Lopes, E. Antolini, and E. R. Gonzalez, Int. J. Hydrog. Energy **33**, 5563 (2008).
37. K. Bergamaski, J. F. Gomes, B. E. Goi, and F. C. Nart, Eclética Quím. **28**, 87 (2003).
38. H. Wang, Z. Jusys, and R. j. Behm, Fuel Cells **4**, 113 (2004).
39. T. Iwasita, F. C. Nart, and W. Vielstich, Berichte Bunsenges. Für Phys. Chem. **94**, 1030 (1990).
40. C. Lamy, E. M. Belgsir, and J.-M. Léger, J. Appl. Electrochem. **31**, 799 (2001).
41. K. Bergamaski, E. R. Gonzalez, and F. C. Nart, Electrochimica Acta **53**, 4396 (2008).
42. V. Rao, C. Cremers, U. Stimming, L. Cao, S. Sun, S. Yan, G. Sun, and Q. Xin, J. Electrochem. Soc. **154**, B1138 (2007).
43. S. Sun, M. C. Halseid, M. Heinen, Z. Jusys, and R. J. Behm, J. Power Sources **190**, 2 (2009).
44. R. Alcalá, M. Mavrikakis, and J. A. Dumesic, J. Catal. **218**, 178 (2003).
45. E. Vesselli, G. Coslovich, G. Comelli, and R. Rosei, J. Phys. Condens. Matter **17**, 6139 (2005).
46. S. Motoo and M. Watanabe, J. Electroanal. Chem. Interfacial Electrochem. **69**, 429 (1976).
47. S. Motoo, M. Shibata, and M. Watanabe, J. Electroanal. Chem. Interfacial Electrochem. **110**, 103 (1980).
48. M. Shibata and S. Motoo, J. Electroanal. Chem. Interfacial Electrochem. **194**, 261 (1985).
49. M. Watanabe, M. Shibata, and S. Motoo, J. Electroanal. Chem. Interfacial Electrochem. **187**, 161 (1985).
50. H. A. Gasteiger, N. M. Markovic, and P. N. Ross, J. Phys. Chem. **99**, 8945 (1995).
51. H. A. Gasteiger, N. M. Marković, and P. N. R. Jr, Catal. Lett. **36**, 1 (1996).
52. M. Arenz, K. J. J. Mayrhofer, V. Stamenkovic, B. B. Blizanac, T. Tomoyuki, P. N. Ross, and N. M. Markovic, J. Am. Chem. Soc. **127**, 6819 (2005).
53. E. Herrero, B. Álvarez, J. M. Feliu, S. Blais, Z. Radovic-Hrapovic, and G. Jerkiewicz, J. Electroanal. Chem. **567**, 139 (2004).
54. S. Mukerjee and J. McBreen, J. Electroanal. Chem. **448**, 163 (1998).
55. N. P. Lebedeva, A. Rodes, J. M. Feliu, M. T. M. Koper, and R. A. van Santen, J. Phys. Chem. B **106**, 9863 (2002).
56. K. J. J. Mayrhofer, M. Arenz, B. B. Blizanac, V. Stamenkovic, P. N. Ross, and N. M. Markovic, Electrochimica Acta **50**, 5144 (2005).
57. F. Maillard, S. Schreier, M. Hanzlik, E. R. Savinova, S. Weinkauf, and U. Stimming, Phys. Chem. Chem. Phys. **7**, 385 (2005).
58. P. N. Ross, K. Kinoshita, A. J. Scarpellino, and P. Stonehart, J. Electroanal. Chem. Interfacial Electrochem. **63**, 97 (1975).
59. P. N. Ross, K. Kinoshita, A. J. Scarpellino, and P. Stonehart, J. Electroanal. Chem. Interfacial Electrochem. **59**, 177 (1975).

60. C. Lu and R. I. Masel, J. Phys. Chem. B **105**, 9793 (2001).
61. F. Maillard, M. Eikerling, O. V. Cherstiouk, S. Schreier, E. Savinova, and U. Stimming, Faraday Discuss. **125**, 357 (2004).
62. E. P. Leão, M. J. Giz, G. A. Camara, and G. Maia, Electrochimica Acta **56**, 1337 (2011).
63. J. L. Rodríguez, E. Pastor, X. H. Xia, and T. Iwasita, Langmuir **16**, 5479 (2000).
64. J. Silva-Chong, E. Méndez, J. L. Rodríguez, M. C. Arévalo, and E. Pastor, Electrochimica Acta **47**, 1441 (2002).
65. S. Sun, M. Heinen, Z. Jusys, and R. J. Behm, J. Power Sources **204**, 1 (2012).
66. M. J. S. Farias, G. A. Camara, A. A. Tanaka, and T. Iwasita, J. Electroanal. Chem. **600**, 236 (2007).
67. J. M. Perez, B. Beden, F. Hahn, A. Aldaz, and C. Lamy, J. Electroanal. Chem. Interfacial Electrochem. **262**, 251 (1989).
68. T. Iwasita, B. Rasch, E. Cattaneo, and W. Vielstich, Electrochimica Acta **34**, 1073 (1989).
69. T. Iwasita and W. Vielstich, J. Electroanal. Chem. Interfacial Electrochem. **257**, 319 (1988).
70. D. S. Corrigan, E. K. Krauskopf, L. M. Rice, A. Wieckowski, and M. J. Weaver, J. Phys. Chem. **92**, 1596 (1988).
71. J. Wang, S. Wasmus, and R. F. Savinell, J. Electrochem. Soc. **142**, 4218 (1995).
72. V. M. Schmidt, R. Ianniello, E. Pastor, and S. González, J. Phys. Chem. **100**, 17901 (1996).
73. G. A. Camara, R. B. de Lima, and T. Iwasita, Electrochem. Commun. **6**, 812 (2004).
74. J. P. I. Souza, F. J. Botelho Rabelo, I. R. de Moraes, and F. C. Nart, J. Electroanal. Chem. **420**, 17 (1997).
75. J. P. I. de Souza, S. L. Queiroz, K. Bergamaski, E. R. Gonzalez, and F. C. Nart, J. Phys. Chem. B **106**, 9825 (2002).
76. S. Y. Shen, T. S. Zhao, and J. B. Xu, Int. J. Hydrog. Energy **35**, 12911 (2010).
77. F. Colmati, E. Antolini, and E. R. Gonzalez, J. Power Sources **157**, 98 (2006).
78. C. Lamy, S. Rousseau, E. M. Belgsir, C. Coutanceau, and J.-M. Léger, Electrochimica Acta **49**, 3901 (2004).
79. A. Kowal, M. Li, M. Shao, K. Sasaki, M. B. Vukmirovic, J. Zhang, N. S. Marinkovic, P. Liu, A. I. Frenkel, and R. R. Adzic, Nat. Mater. **8**, 325 (2009).
80. M. Li, A. Kowal, K. Sasaki, N. Marinkovic, D. Su, E. Korach, P. Liu, and R. R. Adzic, Electrochimica Acta **55**, 4331 (2010).
81. L. ZHAO, S. MITSUSHIMA, A. ISHIHARA, K. MATSUZAWA, and K. OTA, Chin. J. Catal. **32**, 1856 (2011).
82. G. García, N. Tsiouvaras, E. Pastor, M. A. Peña, J. L. G. Fierro, and M. V. Martínez-Huerta, Int. J. Hydrog. Energy **37**, 7131 (2012).
83. E. Lee, A. Murthy, and A. Manthiram, Electrochimica Acta **56**, 1611 (2011).
84. E. Higuchi, K. Miyata, T. Takase, and H. Inoue, J. Power Sources **196**, 1730 (2011).
85. K. Wang, H. A. Gasteiger, N. M. Markovic, and P. N. Ross Jr, Electrochimica Acta **41**, 2587 (1996).
86. V. R. Stamenković, M. Arenz, C. A. Lucas, M. E. Gallagher, P. N. Ross, and N. M. Marković, J. Am. Chem. Soc. **125**, 2736 (2003).
87. A. Velázquez-Palenzuela, F. Centellas, E. Brillas, J. A. Garrido, C. Arias, R. M. Rodríguez, and P.-L. Cabot, Int. J. Hydrog. Energy **38**, 16418 (2013).
88. E. Lee, A. Murthy, and A. Manthiram, J. Electroanal. Chem. **659**, 168 (2011).

89. X. Wang, J. Lian, and Y. Wang, Int. J. Hydrog. Energy **39**, 14288 (2014).
90. Y. Ishikawa, M.-S. Liao, and C. R. Cabrera, Surf. Sci. **463**, 66 (2000).
91. A. O. Neto, R. R. Dias, M. M. Tusi, M. Linardi, and E. V. Spinacé, J. Power Sources **166**, 87 (2007).
92. C. T. Hable and M. S. Wrighton, Langmuir **9**, 3284 (1993).
93. A. N. Haner and P. N. Ross, J. Phys. Chem. **95**, 3740 (1991).
94. B. Beden, F. Kadirgan, C. Lamy, and J. M. Leger, J. Electroanal. Chem. Interfacial Electrochem. **127**, 75 (1981).
95. S. A. Campbell and R. Parsons, J. Chem. Soc. Faraday Trans. **88**, 833 (1992).
96. B. Bittins-Cattaneo and T. Iwasita, J. Electroanal. Chem. Interfacial Electrochem. **238**, 151 (1987).
97. M. Watanabe, Y. Furuuchi, and S. Motoo, J. Electroanal. Chem. Interfacial Electrochem. **191**, 367 (1985).
98. L. Jiang, L. Colmenares, Z. Jusys, G. Q. Sun, and R. J. Behm, Electrochimica Acta **53**, 377 (2007).
99. H. Wang, Z. Jusys, and R. J. Behm, J. Power Sources **154**, 351 (2006).
100. S. Rousseau, C. Coutanceau, C. Lamy, and J.-M. Léger, J. Power Sources **158**, 18 (2006).
101. F. Vigier, C. Coutanceau, F. Hahn, E. M. Belgsir, and C. Lamy, J. Electroanal. Chem. **563**, 81 (2004).
102. A. V. Tripković, K. D. Popović, J. D. Lović, V. M. Jovanović, S. I. Stevanović, D. V. Tripković, and A. Kowal, Electrochem. Commun. **11**, 1030 (2009).
103. F. Delime, J.-M. Léger, and C. Lamy, J. Appl. Electrochem. **29**, 1249 (1999).
104. M. Hourani and A. Wieckowski, J. Electroanal. Chem. Interfacial Electrochem. **227**, 259 (1987).
105. C. K. Rhee, M. Wasberg, P. Zelenay, and A. Wieckowski, Catal. Lett. **10**, 149 (1991).
106. M. J. Weaver, S.-C. Chang, L.-W. H. Leung, X. Jiang, M. Rubel, M. Szklarczyk, D. Zurawski, and A. Wieckowski, J. Electroanal. Chem. **327**, 247 (1992).
107. T. H. M. Housmans, J. M. Feliu, and M. T. M. Koper, J. Electroanal. Chem. **572**, 79 (2004).
108. T. H. M. Housmans and M. T. M. Koper, Electrochem. Commun. **7**, 581 (2005).
109. L. W. H. Leung and M. J. Weaver, J. Phys. Chem. **93**, 7218 (1989).
110. W. Tokarz, H. Siwek, P. Piela, and A. Czerwiński, Electrochimica Acta **52**, 5565 (2007).
111. J.-H. Choi, K.-W. Park, I.-S. Park, W.-H. Nam, and Y.-E. Sung, Electrochimica Acta **50**, 787 (2004).
112. G. Y. Wang, L. Fang, F. F. Li, and S. Saipanya, Adv. Mater. Res. **953-954**, 1297 (2014).
113. I. Ávila-García, C. Ramírez, J. M. Hallen López, and E. M. Arce Estrada, J. Alloys Compd. **495**, 462 (2010).
114. F. H. B. Lima and E. R. Gonzalez, Electrochimica Acta **53**, 2963 (2008).
115. N. R. de Tacconi, R. O. Lezna, B. Beden, F. Hahn, and C. Lamy, J. Electroanal. Chem. **379**, 329 (1994).
116. E. Méndez, J. L. Rodríguez, M. C. Arévalo, and E. Pastor, Langmuir **18**, 763 (2002).
117. J. Greeley, J. K. Nørskov, and M. Mavrikakis, Annu. Rev. Phys. Chem. **53**, 319 (2002).
118. S. Sen Gupta and J. Datta, J. Electroanal. Chem. **594**, 65 (2006).
119. K. Bergamaski, E. R. Gonzalez, and F. C. Nart, Electrochimica Acta **53**, 4396 (2008).

120. M. Li, W.-P. Zhou, N. S. Marinkovic, K. Sasaki, and R. R. Adzic, Electrochimica Acta **104**, 454 (2013).
121. F. Colmati, E. Antolini, and E. R. Gonzalez, J. Alloys Compd. **456**, 264 (2008).
122. A. Kowal, M. Li, M. Shao, K. Sasaki, M. B. Vukmirovic, J. Zhang, N. S. Marinkovic, P. Liu, A. I. Frenkel, and R. R. Adzic, Nat. Mater. **8**, 325 (2009).
123. M. Li, A. Kowal, K. Sasaki, N. Marinkovic, D. Su, E. Korach, P. Liu, and R. R. Adzic, Electrochimica Acta **55**, 4331 (2010).
124. J. Zhang, M. B. Vukmirovic, K. Sasaki, A. U. Nilekar, M. Mavrikakis, and R. R. Adzic, J. Am. Chem. Soc. **127**, 12480 (2005).
125. L. C. Silva-Junior, G. Maia, R. R. Passos, E. A. de Souza, G. A. Camara, and M. J. Giz, Electrochimica Acta **112**, 612 (2013).
126. E. Higuchi, T. Takase, M. Chiku, and H. Inoue, J. Power Sources **263**, 280 (2014).
127. T. Vidaković, M. Christov, K. Sundmacher, K. S. Nagabhushana, W. Fei, S. Kinge, and H. Bönnemann, Electrochimica Acta **52**, 2277 (2007).
128. H. Boennemann and G. Khelashvili, ChemInform **41**, no (2010).
129. H. Bönnemann, W. Brijoux, R. Brinkmann, T. Joußen, B. Korall, and E. Dinjus, Angew. Chem. Int. Ed. Engl. **30**, 1312 (1991).
130. H. Bönnemann, U. Endruschat, J. Hormes, G. Köhl, S. Kruse, H. Modrow, R. Mörtel, and K. S. Nagabhushana, Fuel Cells **4**, 297 (2004).
131. S. Kinge and H. Bönnemann, Appl. Organomet. Chem. **19**, 750 (2005).
132. H. Bönnemann, R. Brinkmann, S. Kinge, T. O. Ely, and M. Armand, Fuel Cells **4**, 289 (2004).
133. E. Antolini, J. R. C. Salgado, R. M. da Silva, and E. R. Gonzalez, Mater. Chem. Phys. **101**, 395 (2007).
134. Y. Su, X. Xue, W. Xu, C. Liu, W. Xing, X. Zhou, T. Tian, and T. Lu, Electrochimica Acta **51**, 4316 (2006).
135. K. L. Ley, J. Electrochem. Soc. **144**, 1543 (1997).
136. K.-W. Park, J.-H. Choi, B.-K. Kwon, S.-A. Lee, Y.-E. Sung, H.-Y. Ha, S.-A. Hong, H. Kim, and A. Wieckowski, J. Phys. Chem. B **106**, 1869 (2002).
137. Y. Wang, J. Ren, K. Deng, L. Gui, and Y. Tang, Chem. Mater. **12**, 1622 (2000).
138. Z. Zhou, S. Wang, W. Zhou, G. Wang, L. Jiang, W. Li, S. Song, J. Liu, G. Sun, and Q. Xin, Chem. Commun. 394 (2003).
139. W. J. Zhou, W. Z. Li, S. Q. Song, Z. H. Zhou, L. H. Jiang, G. Q. Sun, Q. Xin, K. Poulianitis, S. Kontou, and P. Tsiakaras, J. Power Sources **131**, 217 (2004).
140. W. Zhou, Z. Zhou, S. Song, W. Li, G. Sun, P. Tsiakaras, and Q. Xin, Appl. Catal. B Environ. **46**, 273 (2003).
141. S. Liao, K.-A. Holmes, H. Tsaprailis, and V. I. Birss, J. Am. Chem. Soc. **128**, 3504 (2006).
142. E. V. Spinacé, M. Linardi, and A. O. Neto, Electrochem. Commun. **7**, 365 (2005).
143. H.-S. Oh, J.-G. Oh, Y.-G. Hong, and H. Kim, Electrochimica Acta **52**, 7278 (2007).
144. H.-S. Oh, J.-G. Oh, and H. Kim, J. Power Sources **183**, 600 (2008).
145. K.-S. Lee, H.-Y. Park, Y.-H. Cho, I.-S. Park, S. J. Yoo, and Y.-E. Sung, J. Power Sources **195**, 1031 (2010).
146. B. Liu, Z.-W. Chia, Z.-Y. Lee, C.-H. Cheng, J.-Y. Lee, and Z.-L. Liu, J. Power Sources **206**, 97 (2012).
147. H.-S. Oh, K. H. Lim, B. Roh, I. Hwang, and H. Kim, Electrochimica Acta **54**, 6515 (2009).

148. C. Bock, C. Paquet, M. Couillard, G. A. Botton, and B. R. MacDougall, J. Am. Chem. Soc. **126**, 8028 (2004).
149. Y.-J. Zhu and X.-L. Hu, Chem. Lett. **33**, 760 (2004).
150. M. Tsuji, M. Hashimoto, Y. Nishizawa, and T. Tsuji, Mater. Lett. **58**, 2326 (2004).
151. M. Watanabe, M. Uchida, and S. Motoo, J. Electroanal. Chem. Interfacial Electrochem. **229**, 395 (1987).
152. F. Bonet, V. Delmas, S. Grugeon, R. Herrera Urbina, P.-Y. Silvert, and K. Tekaia-Elhsissen, Nanostructured Mater. **11**, 1277 (1999).
153. D. Larcher and R. Patrice, J. Solid State Chem. **154**, 405 (2000).
154. F. Fievet, F. Fievet-Vincent, J.-P. Lagier, B. Dumont, and M. Figlarz, J. Mater. Chem. **3**, 627 (1993).
155. F. Fievet, J. P. Lagier, B. Blin, B. Beaudoin, and M. Figlarz, Solid State Ion. **32–33, Part 1**, 198 (1989).
156. L. Schultz, Masterarbeit (2012).
157. J. Turkevich, P. C. Stevenson, and J. Hillier, Discuss. Faraday Soc. **11**, 55 (1951).
158. X. Li, X. Qiu, H. Yuan, L. Chen, and W. Zhu, J. Power Sources **184**, 353 (2008).
159. B. Fultz and J. Howe, *Transmission Electron Microscopy and Diffractometry of Materials* (Springer Science & Business Media, 2012).
160. D. Bayer, Doktorarbeit (2014).
161. H. Baltruschat, J. Am. Soc. Mass Spectrom. **15**, 1693 (2004).
162. F. Cases, M. López-Atalaya, J. L. Vźquez, A. Aldaz, and J. Clavilier, J. Electroanal. Chem. Interfacial Electrochem. **278**, 433 (1990).
163. S. C. S. Lai and M. T. M. Koper, Faraday Discuss. **140**, 399 (2009).
164. F. Colmati, G. Tremiliosi-Filho, E. R. Gonzalez, A. Berná, E. Herrero, and J. M. Feliu, Phys. Chem. Chem. Phys. **11**, 9114 (2009).
165. M.-C. Morin, C. Lamy, J.-M. Léger, J.-L. Vasquez, and A. Aldaz, J. Electroanal. Chem. Interfacial Electrochem. **283**, 287 (1990).
166. J. Shin, W. J. Tornquist, C. Korzeniewski, and C. S. Hoaglund, Surf. Sci. **364**, 122 (1996).
167. S. C. Chang, L. W. H. Leung, and M. J. Weaver, J. Phys. Chem. **94**, 6013 (1990).
168. D. J. Tarnowski and C. Korzeniewski, J. Phys. Chem. B **101**, 253 (1997).
169. V. Pacheco Santos and G. Tremiliosi-Filho, J. Electroanal. Chem. **554–555**, 395 (2003).
170. V. Pacheco Santos, V. Del Colle, R. B. de Lima, and G. Tremiliosi-Filho, Electrochimica Acta **52**, 2376 (2007).
171. S. Chumillas, C. Busó-Rogero, J. Solla-Gullón, F. J. Vidal-Iglesias, E. Herrero, and J. M. Feliu, Electrochem. Commun. **13**, 1194 (2011).
172. J. Perez, V. A. Paganin, and E. Antolini, J. Electroanal. Chem. **654**, 108 (2011).
173. J. Gomes, D. Profeti, and L. J. Deiner, ChemElectroChem **1**, 655 (2014).
174. P. S. Ruvinskiy, A. Bonnefont, M. Bayati, and E. R. Savinova, Phys. Chem. Chem. Phys. **12**, 15207 (2010).
175. P. S. Ruvinskiy, A. Bonnefont, C. Pham-Huu, and E. R. Savinova, Langmuir **27**, 9018 (2011).
176. A. Schneider, L. Colmenares, Y. E. Seidel, Z. Jusys, B. Wickman, B. Kasemo, and R. J. Behm, Phys. Chem. Chem. Phys. **10**, 1931 (2008).
177. P.-Y. Olu, C. R. Barros, N. Job, and M. Chatenet, Electrocatalysis **5**, 288 (2014).
178. K. S. Freitas, B. M. Concha, E. A. Ticianelli, and M. Chatenet, Catal. Today **170**, 110 (2011).

179. F. Seland, R. Tunold, and D. A. Harrington, Electrochimica Acta **55**, 3384 (2010).
180. F. Gloaguen, F. Andolfatto, R. Durand, and P. Ozil, J. Appl. Electrochem. **24**, 863 (1994).
181. F. Maillard, E. R. Savinova, and U. Stimming, J. Electroanal. Chem. **599**, 221 (2007).
182. L. Palaikis, D. Zurawski, M. Hourani, and A. Wieckowski, Surf. Sci. **199**, 183 (1988).
183. A. Couto, M. C. Pérez, A. Rincón, and C. Gutiérrez, J. Phys. Chem. **100**, 19538 (1996).
184. Z. Jusys, J. Kaiser, and R. J. Behm, Phys. Chem. Chem. Phys. **3**, 4650 (2001).
185. A. Bach Delpeuch, M. Chatenet, C. Cremers, and T. Tübke, Electrochimica Acta **141**, 102 (2014).
186. H. Hitmi, E. M. Belgsir, J.-M. Léger, C. Lamy, and R. O. Lezna, Electrochimica Acta **39**, 407 (1994).
187. http://webbook.nist.gov/cgi/cbook.cgi?ID=C141786&Mask=200 (n.d.).
188. S. Mukerjee and R. C. Urian, Electrochimica Acta **47**, 3219 (2002).
189. J. Greeley, J. K. Nørskov, and M. Mavrikakis, Annu. Rev. Phys. Chem. **53**, 319 (2002).
190. G. Socrates, *Infrared and Raman Characteristic Group Frequencies: Tables and Charts* (John Wiley & Sons, 2004).
191. S. Watanabe, J. Inukai, and M. Ito, Surf. Sci. **293**, 1 (1993).
192. F. Kitamura, M. Takeda, M. Takahashi, and M. Ito, Chem. Phys. Lett. **142**, 318 (1987).
193. F. Kitamura, M. Takahashi, and M. Ito, Surf. Sci. **223**, 493 (1989).
194. L.-W. H. Leung and M. J. Weaver, J. Electroanal. Chem. Interfacial Electrochem. **240**, 341 (1988).
195. Y. Kinomoto, S. Watanabe, M. Takahashi, and M. Ito, Surf. Sci. **242**, 538 (1991).
196. T. Uchida, M. Osawa, and J. Lipkowski, J. Electroanal. Chem. **716**, 112 (2014).
197. F. Maillard, A. Bonnefont, M. Chatenet, L. Guétaz, B. Doisneau-Cottignies, H. Roussel, and U. Stimming, Electrochimica Acta **53**, 811 (2007).
198. F. Maillard, G.-Q. Lu, A. Wieckowski, and U. Stimming, J. Phys. Chem. B **109**, 16230 (2005).
199. T. Iwasita and F. C. Nart, Prog. Surf. Sci. **55**, 271 (1997).
200. F. C. Nart and T. Iwasita, J. Electroanal. Chem. **322**, 289 (1992).
201. A. Rodes, E. Pastor, and T. Iwasita, J. Electroanal. Chem. **376**, 109 (1994).
202. S.-C. Chang and M. J. Weaver, J. Chem. Phys. **92**, 4582 (1990).
203. F. M. Hoffmann, Surf. Sci. Rep. **3**, 107 (1983).
204. S. Watanabe, J. Inukai, and M. Ito, Surf. Sci. **293**, 1 (1993).
205. S. C. Chang, L.-W. H. Leung, and M. J. Weaver, J. Phys. Chem. **93**, 5341 (1989).
206. Y. Sawatari, J. Inukai, and M. Ito, J. Electron Spectrosc. Relat. Phenom. **64–65**, 515 (1993).
207. K. Kunimatsu, M. G. Samant, H. Seki, and M. R. Philpott, J. Electroanal. Chem. Interfacial Electrochem. **243**, 203 (1988).
208. P. W. Faguy, N. S. Marinković, and R. R. Adžić, J. Electroanal. Chem. **407**, 209 (1996).
209. T. Iwasita and F. C. Nart, J. Electroanal. Chem. Interfacial Electrochem. **295**, 215 (1990).
210. P. W. Faguy, N. Markovic, R. R. Adzic, C. A. Fierro, and E. B. Yeager, J. Electroanal. Chem. Interfacial Electrochem. **289**, 245 (1990).
211. R. Jinnouchi, T. Hatanaka, Y. Morimoto, and M. Osawa, Electrochimica Acta **101**, 254 (2013).
212. K. Kunimatsu, M. G. Samant, and H. Seki, J. Electroanal. Chem. Interfacial Electrochem. **258**, 163 (1989).

213. J.-M. Léger, S. Rousseau, C. Coutanceau, F. Hahn, and C. Lamy, Electrochimica Acta **50**, 5118 (2005).
214. K. Ito and H. J. Bernstein, Can. J. Chem. **34**, 170 (1956).
215. P. Gao, S.-C. Chang, Z. Zhou, and M. J. Weaver, J. Electroanal. Chem. Interfacial Electrochem. **272**, 161 (1989).
216. J. C. Morris, J. Chem. Phys. **11**, 230 (1943).
217. A. A. Abd-El-Latif, E. Mostafa, S. Huxter, G. Attard, and H. Baltruschat, Electrochimica Acta **55**, 7951 (2010).
218. A. B. Delpeuch, T. Asset, M. Chatenet, and C. Cremers, J. Electrochem. Soc. **161**, F918 (2014).
219. Z. Jusys and R. J. Behm, J. Phys. Chem. B **105**, 10874 (2001).
220. V. S. Bagotzky and Y. B. Vassiliev, Electrochimica Acta **11**, 1439 (1966).
221. Y. B. Vassiliev, V. S. Bagotzky, N. V. Osetrova, and A. A. Mikhailova, J. Electroanal. Chem. Interfacial Electrochem. **97**, 63 (1979).
222. A. Capon and R. Parsons, J. Electroanal. Chem. Interfacial Electrochem. **45**, 205 (1973).
223. A. Więckowski, Electrochimica Acta **26**, 1121 (1981).
224. G. Horányi and E. M. Rizmayer, J. Electroanal. Chem. Interfacial Electrochem. **201**, 187 (1986).
225. J. K. Nørskov, J. Rossmeisl, A. Logadottir, L. Lindqvist, J. R. Kitchin, T. Bligaard, and H. Jónsson, J. Phys. Chem. B **108**, 17886 (2004).
226. P. Zelenay, G. Horányi, C. K. Rhee, and A. Wieckowski, J. Electroanal. Chem. Interfacial Electrochem. **300**, 499 (1991).
227. H. Wang, Z. Jusys, and R. j. Behm, Fuel Cells **4**, 113 (2004).
228. M. Heinen, Z. Jusys, and R. J. Behm, ECS Trans. **25**, 259 (2009).
229. J. Willsau and J. Heitbaum, J. Electroanal. Chem. Interfacial Electrochem. **194**, 27 (1985).
230. J. F. E. Gootzen, W. Visscher, and J. A. R. van Veen, Langmuir **12**, 5076 (1996).
231. U. Schmiemann, U. Müller, and H. Baltruschat, Electrochimica Acta **40**, 99 (1995).
232. R. Ianniello, V. M. Schmidt, J. L. Rodríguez, and E. Pastor, J. Electroanal. Chem. **471**, 167 (1999).
233. T. Iwasita, R. Dalbeck, E. Pastor, and X. Xia, Electrochimica Acta **39**, 1817 (1994).
234. B. Beden, M.-C. Morin, F. Hahn, and C. Lamy, J. Electroanal. Chem. Interfacial Electrochem. **229**, 353 (1987).
235. D. Bayer, C. Cremers, H. Baltruschat, and J. Tübke, ECS Trans. **25**, 85 (2010).
236. C. Cremers, D. Bayer, J. O. Meier, S. Berenger, B. Kintzel, M. Joos, and J. Tübke, ECS Trans. **25**, 27 (2010).
237. S. Trasatti, J. Electroanal. Chem. Interfacial Electrochem. **39**, 163 (1972).
238. A. P. M. Camargo, B. A. F. Previdello, H. Varela, and E. R. Gonzalez, Quím. Nova **33**, 2143 (2010).
239. A. Yee, S. J. Morrison, and H. Idriss, J. Catal. **191**, 30 (2000).
240. S. S. Mahapatra, A. Dutta, and J. Datta, Electrochimica Acta **55**, 9097 (2010).
241. S. Sun, Z. Jusys, and R. J. Behm, J. Power Sources **231**, 122 (2013).
242. H. Wang, Z. Jusys, and R. J. Behm, J. Phys. Chem. B **108**, 19413 (2004).
243. V. Rao, Hariyanto, C. Cremers, and U. Stimming, Fuel Cells **7**, 417 (2007).
244. R. S. Ferreira Jr., V. R. Oliveira, R. G. C. S. Reis, G. Maia, and G. A. Camara, J. Power Sources **185**, 853 (2008).

245. D. Bayer, S. Berenger, M. Joos, C. Cremers, and J. Tübke, Int. J. Hydrog. Energy **35**, 12660 (2010).
246. Y. Huang, J. Cai, M. Liu, and Y. Guo, Electrochimica Acta **83**, 1 (2012).

Titre : Etude mécanistique de la réaction d'oxydation de l'éthanol sur électrocatalyseurs à base de Pt, Rh, SnO_2 sur support carboné en milieu acide

L'étude du mécanisme de la réaction d'oxydation de l'éthanol (EOR) a été réalisée sur des électrocatalyseurs bi- et tri-métalliques à base de Pt, Rh et SnO_2 sur support carboné à l'aide de méthodes électrochimiques couplées (DEMS, *in situ* FTIR). Deux importantes problématiques de l'EOR ont été abordées: la déshydrogénation de la molécule d'éthanol et la cassure de sa liaison C-C.

L'investigation de certains paramètres expérimentaux, comme l'épaisseur de la couche d'électrocatalyseur, a permis de démontrer q'une couche active épaisse conduit à une meilleure électrooxydation plus complète de l'éthanol en CO_2, mais également que l'empoisonnement de l'électrocatalyseur par de très forts adsorbats advient dans l'épaisseur de couche active.

Les performances de chaque électrocatalyseur ont été comparées entre elles et ont mis en évidence une meilleure sélectivité de l'EOR sur Pt-Rh-SnO_2/C, ainsi que l'engendrement de courants plus élevés à bas potentiel à température ambiante. La tendance est amplifiée à température plus élevée (T = 60 °C).

Mots clés : electrocatalyse ; réaction d'oxydation de l'éthanol ; cassure de la liaison C-C ; synthèse polyol ; pile à combustible

Title: Mechanistic study of the ethanol oxidation reaction on carbon supported Pt-, Rh- and SnO_2-based electrocatalysts in acidic medium

The study of the ethanol oxidation reaction (EOR) mechanism was performed on carbon supported bi- and tri-metallic Pt-, Rh-, SnO_2-based electrocatalysts *via* electrochemical coupled techniques (DEMS, *in situ* FTIR). Two of the most important issues related to the EOR have been broached: the dehydrogenation of the ethanol molecule and its C-C bond breaking.

The investigation of some experimental parameters, such as the thickness of the electrocatalyst layer, enabled demonstrating the better complete ethanol electrooxidation into CO_2 for large electrocatalysts layers, combined to the enhanced poisoning effect inside the catalyst layer by very strong adsorbates.

The performances of each electrocatalyst were compared and evidenced an improved selectivity of the EOR on Pt-Rh-SnO_2/C, as well as the generation of higher currents at low potential at room temperature. The tendency was amplified at elevated temperatures (T = 60 °C).

Keywords: electrocatalysis; ethanol oxidation reaction; C-C bond cleavage; polyol synthesis; fuel cell